Redox potential and mobility of contaminant oxyanions (As, Sb, Cr) in argillaceous rock during oxic and anoxic cycles

by

Ekaterina Markelova

A thesis
presented to the University of Waterloo
in fulfillment of the
thesis requirement for the degree of
Doctor of Philosophy
in
Earth Sciences

Waterloo, Ontario, Canada, 2017

Author's Declaration

I hereby declare that I am the sole author of this thesis. This is a true copy of the thesis, including any required final revisions, as accepted by my examiners.

I understand that my thesis may be made electronically available to the public.

Abstract

Electron transfer (redox) reactions are key processes in the biogeochemical functioning of natural systems. Redox reactions control the speciation and mobility of major elements (e.g., carbon, nitrogen, iron, and manganese) and environmentally important contaminants such as arsenic (As), antimony (Sb), and chromium (Cr). Nonetheless, the characterization of redox conditions and their effects on biogeochemical cycling and contaminant fate remain incompletely understood. The first part of this thesis focused on the interpretation of redox potential (E_H) measurements using results obtained in synthetic biogeochemical systems of increasing complexity under dynamic, redox-oscillating conditions. By progressively combining inorganic solutes, an organic electron donor (lactate), an aqueous electron acceptor (nitrate), a metabolically versatile heterotrophic bacterium (*Shewanella oneidensis*), and a solid-state electron acceptor (goethite), a full redox cascade from +500 to -350 mV (pH ~7.4) was reproduced in the laboratory. The experimental results revealed that a conventional Pt redox electrode responds to a variety of physical, chemical, and microbial factors. In particular, the presence of the bacteria always led to lower E_H readings. In contrast, measurements of E_H in argillaceous suspensions were insensitive to changes in chemical ratios of the redox-sensitive, but non-electroactive, couples, including O_2/H_2O, $CrO_4^{2-}/Cr(OH)_3$, $NO_3^-/NO_2^-/NH_4^+$, $HAsO_4^{2-}/H_3AsO_3$, and $Sb(OH)_6^-/Sb_2O_3$. Therefore, E_H measurements are shown to have limited usefulness in the natural systems depleted in electroactive redox couples, such as α-$FeOOH_{(s)}/Fe^{2+}_{(aq)}$.

The second part of the thesis focused on the behavior of oxyanion contaminants under redox-oscillating conditions in the argillaceous subsoil suspensions. Successive cycles of oxic and anoxic conditions were imposed on the argillaceous suspensions amended with a mixture of oxidized Cr(VI), As(V), Sb(V), and N(V). Oxyanion mobility was investigated under sterile conditions, with the addition of labile organic carbon (ethanol), and with the addition of a topsoil microbial inoculum. Speciation analyses revealed irreversible reduction: freshly reduced As(III), Sb(III), Cr(III), and N(III) were not re-oxidized during subsequent oxic periods. Microbially induced reduction transformations decreased aqueous concentrations of Sb and Cr via mineral precipitation, removed N via volatilization, but retained As in solution. Microorganisms exhibited two distinct strategies of contaminant reduction. The first strategy involved the simultaneous reduction of CrO_4^{2-}, $HAsO_4^{2-}$, and $Sb(OH)_6^-$ under aerobic and denitrifying conditions, as observed in the non-inoculated argillaceous suspensions. The second strategy involved respiratory reduction and followed the predicted thermodynamic order from highest to lowest energy production. In the argillaceous subsoil suspension enriched with topsoil inoculum,

the reduction of terminal electron acceptors proceeded in the following order: O_2, CrO_4^{2-}, NO_3^-, $HAsO_4^{2-}$, and $Sb(OH)_6^-$.

In the third part of the thesis, the oxyanion mobility observed in the argillaceous suspensions (representative of a saturated, clay-rich subsurface environment from depths > 20 m) was further compared to oxyanion mobility in topsoil suspensions (representative of a near-surface soil < 0.01 m enriched in (hydr)oxide phases). The key differences between the topsoil and subsoil systems were the abundance of oxyhydroxide Fe and Mn minerals and the range of E_H values developed during redox cycles. The results indicated that in the topsoil suspensions, strong redox cycling of Fe and Mn correlated closely with the observed oscillating mobility of As and Sb. This correlation suggests a crucial role of oxyhydroxide minerals acting not only as major sorbents, but also as oxidants ultimately controlling the reversibility of contaminant sequestration. Overall, the argillaceous matrix, in contrast to the topsoil matrix, is shown to provide a more suitable environment for contaminant sequestration, as it can withstand periodical redox oscillations without releasing contaminants back to the aqueous phase, at least at the time-scale of the experiments.

Résumé

Les réactions d'oxydoréduction (redox) sont inhérentes aux cycles biogéochimiques des systèmes naturels. En effet, les réactions redox contrôlent la spéciation et la mobilité des éléments majeurs comme le carbone (C), l'azote (N), le fer (Fe) et le manganèse (Mn) et des éléments traces comme l'arsenic (As), l'antimoine (Sb), et le chrome (Cr). Toutefois, notre compréhension du rôle que jouent les conditions redox sur les cycles biogéochimiques et la mobilité des éléments reste incomplète.

La première partie de cette thèse est consacrée à l'interprétation du potentiel redox (E_H) mesuré dans des systèmes de laboratoires en conditions oscillantes. L'approche choisie consiste à augmenter progressivement la complexité du système, d'abord en introduisant uniquement des solutés inorganiques, ensuite un donneur d'électron (lactate), puis un accepteur d'électron (nitrate), et enfin microorganisme hétérotrophe (*Shewanella oneidensis*). J'ai ainsi reconstruire, à un pH constant de 7.4, une cascade redox complète de +500 à -350 mV. Ces résultats expérimentaux montrent que l'électrode conventionnelle au platine (Pt) répond à une variété de facteurs physiques, chimiques et microbiens. En particulier, la présence de bactéries donne toujours lieu à une baisse du potentiel redox. Toutefois, en conditions abiotiques, par exemple dans des argiles, la mesure de E_H est peu utile, car elle ne reflète

pas l'activité des ions non électroactifs comme O_2/H_2O, $CrO_4^{2-}/Cr(OH)_3$, $NO_3^-/NO_2^-/NH_4^+$, $HAsO_4^{2-}/H_3AsO_3$, et $Sb(OH)_6^-/Sb_2O_3$, exception faite du couple Fe^{3+}/Fe^{2+}.

La seconde partie est consacrée au comportement géochimique des oxyanions en conditions d'oxydoréduction oscillantes, dans des suspensions argileuses. Des cycles successifs en conditions oxygénées et anoxiques ont été imposés à des suspensions dans lesquelles ont été ajoutés des sels oxydés de Cr(VI), d'As(V), de Sb(V), et de N(V). La mobilité de ces oxyanions a été étudiée d'abord en conditions stériles, puis en présence d'éthanol, et enfin en présence d'un inoculum de microorganismes provenant d'un sol naturel. La mesure de la spéciation de contaminants durant ces expériences montre une réduction est irréversible sous forme d'As(III), Sb(III), Cr(III), et N(III). Ces réductions, promues par l'activité microbienne, ont donné lieu à une précipitation réductive de Sb et Cr, à une volatilisation de N, mais à un maintien d'As réduit en solution. Je fais l'hypothèse que les microorganismes ont utilisé deux stratégies distinctes pour réduire les contaminants. La première consiste en la réduction simultanée de CrO_4^{2-}, $HAsO_4^{2-}$, et $Sb(OH)_6^-$ en conditions oxygénées et conditions où la réduction des nitrates est favorable – observées dans les suspensions sans inoculum. La seconde étant la respiration des oxydants en fonction de leur rendement thermodynamique respectifs. Dans la suspension activée par un inoculum d'un sol, l'ordre de consommation des accepteurs d'électron est le suivant : O_2, CrO_4^{2-}, NO_3^-, $HAsO_4^{2-}$, et $Sb(OH)_6^-$.

Dans la troisième et dernière partie, la mobilité des oxyanions en suspension argileuse a été comparée à celle observée précédemment dans des suspensions de sols naturels. La principale différence observée entre ces deux types de suspensions tient au rôle clé que joue, sur les gammes de potentiel redox développées et la présence d'(oxy)hydroxydes de Fe et de Mn. Les résultats montrent que les (oxy)hydroxydes de Fe et Mn contrôlent l'oscillation d'As et Sb au cours des cycles redox consécutifs, un comportement absent des expériences sur les argiles. Cela suggère que Fe et Mn agissent non seulement en tant que phases pour l'adsorption des éléments, mais aussi comme catalyseur des réactions d'oxydoréductions. Finalement, je conclus que les matrices argileuses, puisqu'elles ne favorisent pas l'oscillation entre les formes aqueuses et solides des contaminants, sont probablement un milieu stable pour le stockage des contaminants, même lorsqu'elles soumises à des oscillations du potentiel redox.

Acknowledgements

My Ph.D. thesis has greatly profited from the International Joint PhD/cotutelle program between two leading research groups in geochemistry, i.e., the Ecohydrology Research Group at the University of Waterloo and the ISTerre Geochimie group at the Université Grenoble Alpes. A combination of multidisciplinary and multicultural teamwork, with state-of-the-art equipment, under the supervision of leading experts, allowed me to develop and pursue my research interests in the field of biogeochemistry. During this period, I not only strengthened my passion for science, but also reassessed the meaning of life, with French wine consisting of "40% liquid and 60% dreams".

I extend my sincerest gratitude to my supervisors, Dr. Philippe Van Cappellen, Dr. Laurent Charlet, and Dr. Raoul-Marie Couture, for their guidance and access to research opportunities throughout the course of this degree. I appreciate the time spent with them during meetings and conferences in Canada, France, Norway, Belgium, Germany, Czech Republic, Netherlands, and Japan. I am especially grateful to Dr. Christopher T. Parsons, my unofficial committee member, for the insightful discussions on biogeochemistry and his invaluable help with the challenges associated with a cotutelle PhD. I also want to thank my committee member, Dr. David Blowes, for committing his time during meetings and ensuring I stayed on track with my timeline. I am indebted to Dr. Benoit Madé, my committee member and representative from Andra (the French National Radioactive Waste Management Agency), for giving me the freedom to explore my own ideas in line with the industrial interests. I also thank Dr. Grant Ferris, Dr. Matthew Lindsay, Dr. Mark Servos. and Dr. Alex Sobolev for agreeing to review my thesis and participate at my thesis defense.

My research progress was made possible thanks to collaboration, discussion, and technical support from Ecohydrology Research Group members. Special thanks to Dr. Christina M. Smeaton for her guidance and patience during microbial investigations; Igor Markelov for providing me with unwavering support and encouragement during difficult moments in research; Marianne Vandergriendt for assistance with IC, AFS, and lab safety; Shuhuan Li for performing XRD and adjustment of voltammetry; and Maria Mesquita for consulting on microbial sterilization. I am grateful to my friends who made my stay in Canada full of joy and support. Thank you to Adrian, Alena, Anzor, Anya, Chris, Christina, Christine, Danny, Fereidoun, Gabriel, Helen, Mark, Olzhas, Roma, Sasha, Taylor, Tatjana, Veronika, Zahra.

I would like to acknowledge the technical assistance provided to me at the ISterre by Delphine Tisserand during trainings for HPLC-ICP-OES, HPLC-AFS, and TOC; Sarah Bureau for support with

acidic digestion using HF and training for ICP-OES; and Nathaniel Findling for his help with XRD, XRF, and SEM. I am very grateful to my friends in France for distracting me from endless hours I was spending in the lab. Thank you to Ana, Ayumi, Bin, Caroline, Catalina, Claudia, Eric, Frans, Gosia, Ismael, Judith, Maor, Paul, Petya, Rita, Simon, Van, Vanya, Vitalik for living the life in its French style full of *les randonnées* in the beautiful Alpes.

I am grateful to Dr. Nele Bleyen and Dr. Hugo Moors from SCK-CEN (Belgian Nuclear Research Centre) for opening my eyes to the leakage of organics from the pH and E_H electrodes and providing insightful comments on microbial activity in the argillaceous matrices.

This research was funded by CERC (Canada Excellence Research Chairs) held by Dr. Van Cappellen and Andra through an R&D contract with Dr. Charlet.

Dedication

This thesis is dedicated to

my husband, colleague, and the best friend,

Igor Markelov

Table of Contents

List of Figures ..... **xiii**

List of Tables ..... **xviii**

Chapter 1: Introduction **1**

1.1 Background 2

1.1.1 Quantitative and Qualitative Complexity of Redox Potential (E_H) 3

1.1.2 Range of E_H in Saturated Near-Surface and Subsurface Systems 5

1.1.3 Uncertainties in Stability of Redox Conditions in Subsurface Repositories 8

1.1.4 Contaminant Mobility in Redox-Dynamic Systems 9

1.2 Research Objectives 12

1.3 Thesis Organization 12

1.4 Statement of Contributions to the Articles in Chapters 2-4 13

Chapter 2: Deconstructing redox potential (E_H) measurements: A systematic experimental approach **14**

2.1 Summary 15

2.2 Background 16

2.3 Materials and Methods 18

2.3.1 Reactor System 18

2.3.2 Increasing Complexity Experiments 19

2.3.3 Sampling and Analyses 21

2.4 Results and Discussion 22

2.4.1 Physical Mixing 22

2.4.2 Matrix Effects 22

2.4.3 Oxygen 23

2.4.4 Nitrogen Redox Transformations 25

2.4.5 Fe(III)/Fe(II) Redox Control 28

2.4.6 Microbial Effects 30

2.4.7 Redox Cascades 31

2.5 Conclusions 34

2.6 Supporting Information 35

Chapter 3: Mobility of oxyanion contaminants (Cr, As, Sb) in argillaceous suspensions during oxic and anoxic cycles **40**

3.1 Summary 41
3.2 Background 42
3.3 Materials and Methods 43
3.3.1 Argillaceous Sample, Synthetic Pore Water, and Contaminants 43
3.3.2 Experiments 44
3.3.3 Analyses 45
3.3.4 Biogeochemical Modelling 46
3.4 Results 51
3.4.1 Argillaceous Sample 51
3.4.2 Redox Potential (E_H) and pH Conditions 51
3.4.3 Microbial Activity 52
3.4.4 Dissolved Organic and Inorganic Carbon 53
3.4.5 Bulk Water Chemistry and Contaminant Dynamics 53
3.5 Discussion 55
3.5.1 Experimental Artifacts 55
3.5.2 Redox Conditions of the Argillaceous Suspension 56
3.5.3 Abiotic Sequestration of As, Sb, and Cr 56
3.5.4 Microbial Effect on the Mobility of As, Sb, Cr, and N 60
3.5.5 Oxyanion Interplay 69
3.5.6 Stability of Reduced Species 70
3.6 Conclusions 71
3.7 Supporting Information 72
3.7.1 Characterization of Argillaceous Matrix 72
3.7.2 Preparation and Injection of Soil Inoculum 80
3.7.3 Contaminant Speciation 80
Chapter 4: Contrasting contaminant mobility in topsoil and subsoil: Role of Fe- and Mn-oxyhydroxide minerals 84
4.1 Summary 85
4.2 Background 86
4.3 Materials and Methods 88
4.3.1 Compiled Experimental Dataset 88
4.3.2 Similarities and discrepancies between the two experiments. 88

4.3.3 Solid, Microbial, and Aqueous Analyses 90
4.3.4 Biogeochemical Modelling 91
4.4 Results and Discussion 92
4.4.1 Redox Oscillations in Topsoil and Oxic/Anoxic Oscillations in Subsoil 92
4.4.2 Reactivity of Fe and Mn in Topsoil and Subsoil Suspensions 98
4.4.3 Contaminant Sequestration by Topsoil and Subsoil Matrices 100
4.4.4 Contaminant Mobility under Oscillating Oxic/anoxic Conditions 105
4.5 Environmental Significance 108
Chapter 5: Conclusions 110
5.1 Novel Scientific Contributions 111
5.1.1 Interpretation of Redox Potential Measurements 111
5.1.2 Microbial Role in Redox Interplay Between As, Sb, and Cr 112
5.1.3 Contrasting Mineralogical Controls on Mobility of As, Sb, and Cr Mobility in Fe/Mn-rich and Clay-rich Matrices 112
5.1.4 Overall Contaminant Mobility under Redox-Oscillating Conditions 113
5.1.5 Biogeochemical Modelling of As, Sb, and Cr Mobility in Argillaceous Systems 114
5.2 Practical Recommendations and Avenue for Future Research 114
Chapter 6: Annex-I: On-off mobilization of contaminants in soils during redox oscillations.... 116
6.1 Summary 117
6.2 Background 118
6.3 Materials and Methods 120
6.3.1 Soil Sampling and Characterization 120
6.3.2 Experimental Design and Redox Oscillation Sequence 120
6.3.3 Aqueous Chemistry Analyses 121
6.3.4 Biogeochemical Modelling 121
6.4 Results and Discussion 123
6.4.1 Electron Balance 123
6.4.2 Fe^{II} and Mn^{II} Cycling in Solution 124
6.4.3 Mn^{II} and Fe^{II} Cycling in Solution in the Rresence of Contaminants 126
6.4.4 Chromium 126
6.4.5 Selenium 127
6.4.6 Antimony 127

6.4.7 Uranium 128
6.4.8 Arsenic 129
6.4.9 Behavior of Multiple Contaminants and the On-off Switch Mechanism 129
6.5 Supporting Information 132
6.5.1 Details on the Redox-Oscillating Reactor (ROR) Setup 132
6.5.2 Soil Characterization and Preparation 133
6.5.3 Complete Dataset for all Experiments 134
6.5.4 Supporting Information on Model Rates and Constants 137
6.5.5 Model Code 141
6.5.6 Model Sensitivity Analysis and Performance Metrics 142
Chapter 7: Annex-II: Geochemical codes for Chapter 3 145
7.1 Python Code for Calibration of PHREEQC Model (example for As model) 146
7.2 Python Code for Sensitivity Analysis 147
7.3 PHREEQC Code for O, N, As, Sb, and Cr Fate in Exp. IV 150
Bibliography 164

List of Figures

Figure 1-1. E_H-pH diagram showing regions of typical environmental systems superimposed on the stability fields for iron (Fe) and quinone (QH), as a model organic electron shuttle. Measured E_H data (light gray points) and environmental boundaries (a black frame) are constructed from the stability fields for various important ions including their actual measurements (H_2S/HS^-, $H_3PO_4/H_2PO_4^-/HPO_4^{2-}/PO_4^{3-}$, HSO_4^-/SO_4^{2-}, $H_2CO_3/HCO_3^-/CO_3^{2-}$, HNO_2/NO_2^-, NH_4^+/NH_4OH) (Becking et al., 1960). Figure reprinted from Tratnyek, Grundl, and Haderlein (2011). 5

Figure 1-2. E_H-pH diagram showing in-situ data for selected underground research laboratories (Table 1-1) plotted on top of the typical domain of saturated near-surface systems (grey area) demonstrated on Figure 1-1. 7

Figure 1-3. Shallow depth disposal concept designed for low-level long-lived radioactive waste (modified from ASN 2010) allowing gaseous mixing between surface and subsurface. In the French concept, long-lived radium-bearing waste contain both radionuclides and toxic chemicals leading to potentially high toxicity at low radioactivity (Andra, 2009). 9

Figure 2-1. Schematic diagram of the bioreactor system. Also shown is a conceptual representation of the processes occurring in the biotic goethite suspension under N_2 sparging (Exp. IV, see Table 2-1). 18

Figure 2-2. Measured time series of E_H (solid line), dissolved O_2 (dashed line), and concentrations of dissolved redox species: nitrate (squares), nitrite (circles), ammonium (triangles), and Fe (diamonds). "A-H" refers to the E_H subzones reached during air (white areas) and N_2 (grey areas) sparging. "Bio-pulse" (b.p.) refers to the inoculation with bacteria *S. oneidensis* MR-1 and "knee" identifies breakpoints in the E_H time series. A scaled up version of Figure 2-2 (c) is reproduced in Figure 2-5. Data for Exp. IV (d) are shown for the period 96 to 390 h; the data of E_H and $Fe^{2+}_{(aq)}$ for the entire experiment can be found in Figure 2-6. See text for complete discussion. 27

Figure 2-3. Redox cascade: compilation of measured E_H in the series of the four increasing complexity experiments. "A-H" refers to the E_H subzones identified in Figure 2-2. The definition of the redox zones (oxic, suboxic, and anoxic) is based on the experimental results; see text for a detailed discussion. 32

Figure 2-4. Schematic interpretation of main drivers of the redox cascade displayed on Figure 2-3. See text for discussion. 33

Figure 2-5. Scaled up time series of E_H (solid line) and concentrations of nitrate (squares), nitrite (circles), and ammonium (triangles) reproduced from Figure 2-2. Symbols correspond to results of duplicate measurements with 2σ uncertainty (within the symbol size unless indicated). The arrow "knee I" identifies breakpoint of E_H observed after depletion of nitrite. "C_1, C_2, F_1, G" refers to the E_H subzones reached during air (white areas) and N_2

(grey areas) sparging. "Bio-pulse" (b.p.) refers to the inoculation with bacteria *S. oneidensis* MR-1.....35

Figure 2-6. Time series of E_H, ATP, $Fe^{2+}_{(aq)}$, and $Fe^{2+}_{(s)}$ (HCl-extractable) concentrations in biotic AGW (Exp. III) and bacteria-goethite suspension (Exp. IV). ATP concentrations were an order of magnitude higher in Exp. III as compared to Exp. IV and are plotted on separate y-ordinates. "Bio-pulse" (b.p.) refers to the inoculation with bacteria *S. oneidensis* MR-1 in the beginning of both experiments (0 h) and at 144 h of Exp. IV. Time of Exp. IV was extended to 384 h by performing additional cycles of air (white areas) and N_2 (grey areas) sparging.....39

Figure 2-7. Calibration curve and correlation coefficient (r = 0.99) of ATP concentration (*x*) as a function of a cell number per 1 ml of solution (*y*) plotted against optical density (OD_{600}). Average concentration of ATP per a cell of *Shewanella oneidensis* MR-1 is $4.6\times0^{-10}\pm6.2\times10^{-11}$ nM $cell^{-1}$.....39

Figure 3-1. Conceptual models used to describe contaminant (e.g., Cr) mobility via redistribution of contaminant mass between aqueous and solid phases. The multi-reaction model of Zhang and Selim (2005) (A) is enhanced by reaction rates of contaminant reduction (B) built step by step upon the increasing complexity of experiments, where, K_{eq} is an equilibrium constant, k_f – rate constant of adsorption, k_b – rate constant of desorption, k_i – rate constant of irreversible sorption, k_{ab} – rate constant of abiotic reduction, k_{resp} – rate constant of microbial contaminant respiration, r_{max} – maximum rate of microbial contaminant reduction via detoxification or microbially produced soluble reductants. 48

Figure 3-2. Time series of ATP concentrations (squares connected by lines), redox potential (E_H) (solid line), and pH (dashed line) values. Antibiotics spikes are indicated by stars, whereas shaded and white areas indicate anoxic ($CO_2 + N_2$) and oxic ($O_2 + CO_2 + N_2$) periods, respectively.....52

Figure 3-3. Time series of modelled (line) and measured [As] (diamonds), [Sb] (circle), [Cr] (square), [NO_3^-] (right-pointing triangle), [NO_2^-] (left-pointing triangle) (a-d); modelled (line) and measured (circle) DOC concentration along with the estimated ethanol concentration (dashed line) (e-h); and measured DIC (square) and acetate-C concentrations (circle) (i-l). Shaded and white areas indicate anoxic ($CO_2 + N_2$) and oxic ($O_2 + CO_2 + N_2$) periods, respectively.....55

Figure 3-4. Time series of measured (symbols) and modelled aqueous (solid lines) and solid (dashed lines) speciation of As (a-d) and Sb (e-h). Kinetic and equilibrium formulations and parameters use in the model are presented in Table 3-2 and Table 3-4. Shaded and white areas indicate anoxic ($CO_2 + N_2$) and oxic ($O_2 + CO_2 + N_2$) periods, respectively.....58

Figure 3-5. Time series of measured (symbols) and modelled aqueous (solid lines) and solid (dashed lines) Cr and N speciation. Kinetic and equilibrium formulations and parameters use in the model are presented in Table 3-2 and Table 3-4. Shaded and white areas indicate anoxic ($CO_2 + N_2$) and oxic ($O_2 + CO_2 + N_2$) periods, respectively. 59

Figure 3-6. Redox scale showing the theoretical succession of redox potentials (E_H in mV) calculated for the initial experimental conditions (pH 6.9, activities of oxidized and reduced species) (Table 3-3). Potentially toxic CrO_4^{2-}, $HAsO_4^{2-}$, and $Sb(OH)_6^-$ can be reduced simultaneously likely via detoxification with no dependency on E_H (on the left) under aerobic and denitrifying conditions or successively as terminal electron acceptors (TEAs) via respiration following the thermodynamic order (i.e., E_H cascade) (on the right). An essential nutrient, NO_3^-, is exclusively reduced via the respiratory mechanism in the presence of microorganisms. 70

Figure 3-7. Comparison of contaminant removal from the aqueous phase (box with oblique line) with its accumulation in the solid phase (empty box) by the end of experiments (Table 3-10). Double arrow indicates loss of 21% Sb in Exp.IV. 78

Figure 3-8. Bulk wet chemistry time-series of aqueous Fe (a), SO_4^{2-} (b), Mn (c), Ca (d), Mg (e). Dissolved organic carbon (DOC) concentration leached from the pH and E_H electrodes as a function of Cl in Exp. I (squares) and Exp. II (hexagons) (f). Dashed lines represent linear function fit with significant ($p<0.005$) correlation coefficient of 0.99 for both experiments. Shaded areas indicate anoxic periods and white areas – oxic periods. 79

Figure 3-9. Estimated distribution of solid speciation of Cr, As and Sb by the end of the experiments....80

Figure 3-10. Time-series of aqueous contaminant speciation. Arsenic speciation was measured by the end of each half-cycle, Sb speciation on day 1, 24, 49, and Cr speciation on every sampling point. 81

Figure 3-11. Sensitivity analyses testing one at a time ("First") input parameters and by accounting for the sum of the interaction effects ("Total") controlling aqueous contaminant concentration. Parameter abbreviations are explained in Table 3-4....82

Figure 3-12. Polymerase chain reaction (PCR) of samples from Exp. III and IV indicating the presence of amplifiable DNA for prospective phylogenetic analyses....83

Figure 4-1. Measured E_H of the Aeric Humaquept topsoil (Germany) in response to precipitation during the period from June 2 to June 12 (1992). Reprinted with modifications from Schuring et al. (1999). 93

Figure 4-2. Time series of pH (dash line) and redox potential (solid line) with regard to the standard hydrogen electrode (E_H, SHE) measured in the experimental suspensions. The Topsoil-dynamic, Subsoil-abiotic, and Subsoil-biotic suspensions were exposed to oscillating oxic ($O_2/N_2/CO_2$) and anoxic (N_2/CO_2) conditions. The Topsoil-static suspension was maintained under constant oxic conditions. 95

Figure 4-3. Redox scale showing the theoretical succession of equilibrium redox potentials ($E_H°$ in mV) at pH 7 for dominant species of major nutrients (O, Mn, N, Fe) and contaminants (Cr, Sb, As). Oxidized Mn and Fe are demonstrated as manganite ($MnOOH_{(s)}$) and goethite (α-$FeOOH_{(s)}$), respectively. Calculations based on the thermodynamic values

given in (Bard et al., 1985; Filella and May, 2003; Nordstrom et al., 2014; Zotov et al., 2003) and are summarized in Table 4-4. 97

Figure 4-4. Time series of measured (symbols) and modeled (lines) dissolved Fe (circle) and Mn (rhombus) in the topsoil and subsoil suspensions. The results indicate the readily reducible mineral fraction in the topsoil matrix and the lack of redox reactive minerals in the subsoil matrix. 99

Figure 4-5. Time series of measured (symbols) and modeled (solid line) total aqueous concentrations of As (square), Sb (triangle), and Cr (circle) in topsoil and subsoil suspensions. Contaminant sequestration is reversible following oxic/anoxic cycles in the Topsoil-dynamic experiment and irreversible in the Subsoil-abiotic and Subsoil-biotic experiments. 103

Figure 6-1. Redox scale showing the theoretical succession of equilibrium redox potentials (E_H^o in V) and corresponding p*e* values calculated at pH 7.5 for dominant aqueous species of Cr, Mn, U, Se, Sb, As, Fe and C. Concentrations of dissolved contaminants are set to 5×10^{-4} M and those of Fe^{2+}, Mn^{2+}, and CO_3^{2-} to 1, 1 and 3 mM, respectively. 122

Figure 6-2. Measured (symbols) and modelled (solid lines) time-series of Sb (dark squares), As (circles), Cr (upward triangles), Mn (light squares), Fe (downward triangles), and DOC (diamonds) during 7 consecutive experimental half-cycles spanning 49 days. Measured E_H is indicated by a dotted line and shaded areas indicate half-cycles during which an anoxic headspace was imposed. 125

Figure 6-3. Measured (symbols) and modelled (solid lines) time-series of Cr (upward triangles), U (circles), Se (dark squares), Mn (light squares), Fe (downward triangles), and DOC (diamonds) during 7 consecutive experimental half-cycles spanning 49 days. Measured E_H is indicated by a dotted line and shaded areas indicate half-cycles during which an anoxic headspace was imposed. 128

Figure 6-4. Measured time-series of As^V (open squares), As^{III} (open diamonds), Se (dark squares), Mn (light squares), Fe (downward triangles), NO_3^- (solid circles), SO_4^{2-} (open circles), DOC (dark squares), and E_H (line) during 7 consecutive experimental half-cycles for experiments 0-Soil, 500-As and 500-Se. Shaded areas indicate half-cycles during which an anoxic headspace was imposed. Only As was measured during the "Soil only" experiment, with concentrations consistently < 1 μM. 134

Figure 6-5. Measured time-series of Sb (solid diamonds), As (light circles), Cr (upward triangles), Mn (light squares), Fe (downward triangles), DOC (dark squares), and E_H (line) during 7 consecutive experimental half-cycles for experiments 50-Sb, 50-Sb+As and 50-Sb+As+Cr. Shaded areas indicate half-cycles during which an anoxic headspace was imposed. Samples for NO_3^- and SO_4^{2-} could not analyze for these experiments due to instrument downtime. 135

Figure 6-6. Measured time-series of U (circles), Cr (upward triangles), Se (blue squares), Mn (light squares), Fe (downward triangles), NO_3^- (solid circles), SO_4^{2-} (open circles), DOC (dark

squares), and E_H (line) during 7 consecutive experimental half-cycles for experiments 500-U, 500-Cr and 500-Cr+Se+U. Shaded areas indicate half-cycles during which an anoxic headspace was imposed. 136

Figure 6-7. Sequence of the PHREEQC v3 section headings and keywords used to simulate element behavior during redox oscillations and produce Figure 6-2 and Figure 6-3 of the main text. 141

Figure 6-8. Proportion of total variance in modeled aqueous concentrations of As, Sb, Se, Cr and U explained by 10 parameters analyzed by the Extended Fourier amplitude sensitivity test (Extended FAST) sensitivity analysis method. “Main effect” denotes the part of total variance explained by a single parameter and “Interactions” the part explained by interactions with all other parameters. Parameter abbreviations are explained in Table 6-4. 142

Figure 6-9. Proportion of total variance in modeled aqueous concentrations of As, Sb, Se, Cr and U explained by 13 parameters analyzed by the Extended Fourier amplitude sensitivity test (Extended FAST) sensitivity analysis method. “Main effect” denotes the part of total variance explained by a single parameter and “Interactions” the part explained by interactions with all other parameters. Parameter abbreviations are explained in Table 6-4. 143

List of Tables

Table 1-1. The E_H and pH ranges reported for *in-situ* or in laboratory experiments with groundwater and rock materials found in the areas of selected underground research laboratories (URLs). The detailed E_H and pH data from listed references were used to construct Figure 1-2. 7

Table 2-1. Design of increasing complexity bioreactor experiments. 19

Table 2-2. Composition of the artificial groundwater (AGW) used in Experiments II, III, and IV. AGW was designed to mimic a groundwater capable of sustaining minimal microbial activity. 20

Table 2-3. Half reduction reactions of terminal electron acceptors used in the experiments with corresponding equilibrium constants (log K) accounting for reaction stoichiometry. Standard electron activity (pe^0) is calculated via Equation 1-4 and is expressed as standard state redox potentials (E^0) relative to the standard hydrogen electrode at pH 0 and pH 7 at 25 °C and unity of redox species. Calculations are based on values given in Brezonik and Arnold (2011). 24

Table 2-4. Comparison of measured and Nernstian redox potentials (E_H). Calculations are based on the measured chemical species concentrations (see Table 2-6) corrected for ion activities via Davies equation, experimental pH, and experimental temperature (30 °C) via Equation 1-1. Selected measured data represents the last sampling point within the E_H zones (A-H) identified in Figure 2-2. 28

Table 2-5. Summary of practical recommendations to the use of Pt electrode. 36

Table 2-6. Chemical concentrations, E_H, and pH measured at the last sampling point of the redox subzones (A-H) identified in Figure 2-2. LOD = limit of detection. 38

Table 3-1. Design of batch experiments comprising Tégulines sample (50 g L^{-1}) dispersed in 1 L of synthetic pore water (Table 3-6) and a mixture of As(V), Sb(V), and Cr(VI). 45

Table 3-2. Partition (or distribution) coefficient (Kd), equilibrium constant (log K), forward (k_f), backward (k_b), and irreversible (k_i) rate constants for As(V), As(III), Sb(V), and Cr(VI) sorption obtained by fitting experimental data to the multi-reaction model. 57

Table 3-3. Thermodynamic sequence based on the redox potentials (E_H) of half reduction reactions at the experimental pH (6.9), temperature (25 °C), and concentrations of reduced and oxidized species at the beginning of Exp. IV. Thermodynamic order of As and Sb reductions differs depending on pH ($E_H°'$ and $E_H°$) and products of Sb reduction. The observed experimental sequence of Sb reduction followed by As reduction, suggests Sb reduction to $Sb_2O_{3(s)}$, rather than to $Sb(OH)_3$. Calculations are based on the thermodynamic values given in Bard et al. (1985); Filella and May (2003); Nordstrom et al. (2014); Tratnyek and Macalady (2000); Zotov et al. (2003). 63

Table 3-4. The reaction network and kinetic formulations used in the biogeochemical models. 64

Table 3-5. Powder XRD mineralogy of argillaceous sample with the limit of detection (LOD) of 2%. 72

Table 3-6. Synthetic pore-water composition. 72

Table 3-7. ICP-OES elemental analysis of the initial argillaceous sample before experiments with the limit of detection (LOD) for As and Sb of 0.01 mg g^{-1}. 73

Table 3-8. Water content and particle size distribution of argillaceous sample. 73

Table 3-9. Actual initial aqueous concentrations (μM) of contaminants and nitrate in suspensions. 74

Table 3-10. Elemental composition following the complete acidic digestion of the solid samples measured before and after batch experiments (SD±0.01 mg g^{-1} of triplicates) with the limit of detection (LOD) of 0.01 mg g^{-1}. 74

Table 3-11. Solubility products of co-precipitation reactions. 74

Table 3-12. Kinetic and equilibrium parameters used in model formulations (Table 3-4). 75

Table 4-1. The key similarities in experimental conditions of topsoil and subsoil suspensions. 89

Table 4-2. Cationic and anionic composition of Saone river water and synthetic pore water. 90

Table 4-3. The key disparities in experimental conditions of topsoil and subsoil suspensions. 90

Table 4-4: Thermodynamic sequence based on the standard redox potential of half reduction reactions at pH 0 ($E_H°$) and pH 7 ($E_H°'$). Thermodynamic order of As and Sb reductions differs depending on pH and activities of redox species (E_H). Calculations are based on the thermodynamic values given in Bard et al. (1985); Filella and May (2003); Nordstrom et al. (2014); Tratnyek and Macalady (2000); Zotov et al. (2003), experimental pH (6.9) and concentrations of Cr, As, and Sb in the Subsoil-biotic experiment. Experiments depleted in Mn oxides (e.g., manganite, $MnOOH_{(s)}$) and Fe oxides (e.g., goethite, α-$FeOOH_{(s)}$) are indicated. 96

Table 4-5. Composition of the topsoil and subsoil matrices after total acidic dissolution and citrate-bicarbonate-dithionite (CBD) extractions (selected data). Concentrations of As and Sb were lower than the limit of detection (LOD) (0.01 mg g^{-1}). 98

Table 4-6. Partition coefficients (Kd) for sequestration of oxidized Cr, As, and Sb by topsoil and subsoil suspensions. For details on experimental conditions (e.g., pH, ionic strength) see Table 4-1 and Table 4-3. 100

Table 4-7. Multi-reaction sorption parameters of As(V), Sb(V), and Cr(VI) fitted to the time series of aqueous contaminant concentrations: equilibrium constant (log K), forward (k_f), backward (k_b), and irreversible (k_i) rate constants. Kinetically controlled reactions follow 1st-order rate equations. 101

Table 6-1. ICP-MS elemental analysis on initial soil after acid-digestion 133

Table 6-2. Water content, pH, carbon and particle size analysis sieving and sedimentation and after decarbonisation 133

Table 6-3. Redox reactions, their theoretical equilibrium redox potentials (E_H^0, in volts relative to the standard hydrogen electrode) and corresponding p*e* for dominant species at standard state and at pH 7.5. For the calculations at pH 7.5, concentrations of 5×10^{-4} M are set for Cr, Mn, U, Se, Sb, As, Fe and C. Fe and Mn are in equilibrium with ferrihydrite and birnessite, respectively, and the aqueous concentrations for Fe^{II} and Mn^{II} were set to 1×10^{-6} M. 137

Table 6-4. Kinetic formulations used in the model. 138

Table 6-5. Reaction parameters constrained by the model, which correspond to reactions #1-7 given in Table 6-4 and to reaction #28 in Table 6-6. 139

Table 6-6. Reactions for the formation of the various oxyanion species and their corresponding equilibrium constants added to the WATEQ4F database in PHREEQC. Solid phases allowed to form in the model are also listed. 140

Table 6-7. Pearson's correlation coefficient (r), root-mean-square error (RMSE), observation standard deviation (σ_{obs}) and RMSE:σ_{obs} ratio (RSR) calculated using modeled and measured contaminant concentrations time-series. 144

Chapter 1

Introduction

1.1 Background

Challenges to the long-term immobilization of contaminants in geologic repositories. Argillaceous formations are being investigated as potential geological hosts for radioactive waste disposal in 11 different Nuclear Energy Agency member countries, which are collectively referred to as the Clay Club (Nuclear Energy Agency, 1958). The mobility of radioactive (e.g., U, I, Pu, Am, Cm, Np, Tc, Th) and potentially toxic (e.g., As, Sb, Cr, Se, Hg, Be) contaminants present in such wastes is a key issue for safety risk assessment of the prospective disposal sites (Altmann, 2008; Andra, 2009). The low permeability and plasticity of argillaceous materials make them potential natural barriers to advective contaminant migration (Grambow, 2008). Despite physical stability of argillaceous formations, engineered repositories might be subjected to changes in temperature, geologic water saturation, or fresh water infiltration (Ewing et al., 2016). In these scenarios, physical retardation capacity is uncertain due to changes in redox conditions altering chemical interactions between the host rock and dissolved contaminants (Duro et al., 2014).

Redox-oscillating conditions have profound effects on aqueous contaminant concentrations in saturated topsoil (Hindersmann and Mansfeldt, 2014; Parsons et al., 2013a; Stewart et al., 2009; Thompson et al., 2006), suggesting they may also play a role in contaminant mobility in subsurface argillaceous environments. The collaborative project ReCosy between 32 European research institutes and universities was initiated in 2008 to address the problems of redox phenomena controlling the long-term release and retention of radionuclides within the repositories (Duro et al., 2014). In contrast to radionuclides, the mobility of potentially toxic chemicals has received insufficient recognition. Complex assemblages of toxic contaminants, argillaceous mineral matrices, and nutrients are rarely addressed systematically despite their relevance for waste management.

Research on the mobility of redox-sensitive contaminants is complicated by large uncertainties in the characterization of redox conditions (Laaksoharju et al., 2008). An improved interpretation of redox potential measurements as a proxy for redox conditions is required, as acknowledged by the ReCosy project deliverables (e.g., Gimeno et al. 2009). Therefore, before investigating the effect of redox-oscillating conditions on the mobility of potentially toxic chemicals (i.e., As, Sb, Cr) in the argillaceous environment, this thesis provides a reassessment of existing knowledge on redox potential measurements in natural geosystems.

1.1.1 Quantitative and Qualitative Complexity of Redox Potential (E_H)

The importance of electron transfer (redox) reactions in the biogeochemical functioning of natural systems has been emphasized and studied from various angles in electrochemistry (e.g., Liu et al. 2005), geochemistry (e.g., Parsons et al. 2013), agronomy (e.g., Husson 2013), microbial ecology (e.g., Rabaey et al. 2007), microbiology (e.g., Oktyabrskii and Smirnova 2012), biochemistry (e.g., Hewitt L.F. 1950), biotechnology (e.g., Kjaergaard 1977), and bioengineering (e.g., Myers et al. 2006). As a result, numerous attempts have been undertaken to characterize the redox conditions (or the redox state) as the overall tendency of a system to donate or accept electrons. One of the cost-effective and relatively fast approaches to describe the redox state of the system is by measuring the oxidation-reduction potential or redox potential (E_H).

The E_H can be calculated via the Nernst equation (Eq. 1-1) (referred to as the Nernstian E_H) or can be readily measured using redox probes (hereafter, E_H). Being an intensity parameter, E_H is measured as the potential difference between an inert sensing electrode, most commonly a platinum (Pt) electrode, and a reference electrode, commonly silver-based (e.g., $Ag^+|AgCl|Cl^-$), followed by a correction to the standard hydrogen electrode (SHE). The measured E_H (V) is related to the standard E_H° (V) and pH via the following relationship:

$$E_H = E_H^\circ + \frac{2.3\ RT}{nF} \log \frac{\{ox\}^a}{\{red\}^b} - \frac{2.3\ RTh}{nF} pH \qquad \text{(Eq. 1-1)}$$

where, n – the number of electrons and h – the number of protons transferred in the half reaction; {ox} and {red} – activity products of the oxidized and reduced side of the half reaction; a and b – corresponding stoichiometric coefficients; R – gas constant, 8.314 ($J \cdot mol^{-1} \cdot K^{-1}$); T – absolute temperature (K); F – Faraday's constant, 96490 ($C \cdot mol^{-1}$).

The electrode potential is related to a hypothetical measure of free energy of electron transfer (p*e*) through the expression:

$$E_H = \frac{2.3RT}{F} \cdot pe \qquad \text{(Eq. 1-2)}$$

Substituting for R, F, and T = 298.15 K (25 °C) in Eq. 1-2 yields:

$$E_H = 0.05916 \cdot pe \qquad \text{(Eq. 1-3)}$$

Further, standard p*e* is related to the corresponding equilibrium constant (log K) by the expression:

$$pe^\circ = \frac{\log K}{n} \qquad \text{(Eq. 1-4)}$$

Problems with the quantitative interpretation of redox potential. Developed in the early 20th century (Gillespie, 1920), redox electrodes have become ubiquitous tools for the characterization of soils, peat bogs, sea water, rivers, and lakes (Becking et al., 1960; Sato, 1960). However, over a century, E_H remains one of the most controversial parameters to interpret. The dilemma of E_H interpretation arises from the comparison of measured to calculated values, which seldom agree with each other (Essington, 2004; Gao et al., 2002; Lindberg and Runnells, 1984). This discrepancy is often equated to the temporal mismatch between the kinetic nature of both the electrode functioning and the redox disequilibria in solution versus the thermodynamic concept inherent to the Nernst equation. Although natural systems may approach a steady state, a true thermodynamic equilibrium is never achieved on the Earth's surface and subsurface, as life depends on redox gradients and redox disequilibria (Hostettler, 1984; Lindberg and Runnells, 1984; Morris and Stumm, 1967; Nordstrom, 2000).

In practice, the Nernstian concept is applicable only to truly reversible redox couples (Hewitt, 1950) that are electroactive (Peiffer et al., 1992). There is only a limited subset of naturally occurring inorganic redox couples, e.g., Fe(III)/Fe(II) and S(0)/S(-II), that have been shown to be electroactive and generate Nernstian E_H (Berner, 1963; Grundl and Macalady, 1989; Matia et al., 1991; Nordstrom et al., 1979; Silvester et al., 2005; Whitfield, 1974, 1969). Other major couples (e.g., H_2O/O_2, N_2/NH_4^+, N_2/NO_3^-, CH_4/CO_2) rarely correlate with the Pt electrode readings (Essington, 2004; Thorstenson, 1984).

Qualitative advantages of E_H measurements. It is the field of microbiology, rather than of geochemistry, that appears to historically have made more fruitful use of E_H measurements. Since Potter (1911) related the catabolic activity of yeast and bacteria accompanying oxidative organic matter decomposition to changes in E_H, microbial activity is frequently involved in E_H interpretation (Berner, 1963; Burrows, 1941; Gillespie, 1920; Husson, 2013; Opel et al., 2014; Whitfield, 1969). For example, continuous E_H measurements have been shown to provide qualitative information on the growth phase (exponential, cessation) (Hewitt, 1950; Hunting and Kampfraath, 2013; Oktyabrskii and Smirnova, 2012), physiological condition (starvation stress, heat shock, and osmotic shock) (Oktyabrskii and Smirnova, 2012), and genotype (Burrows, 1941; Gillespie, 1920; Hunting and Kampfraath, 2013; Whitfield, 1969) of bacteria.

At the time of writing, the consensus is that the features of E_H time-series encapsulate more meaning than the instantaneous values derived from the Nernst equation. For instance, Enright and Ferris (2016) demonstrated that long-range correlations of E_H time series can help distinguish microbial from chemical Fe(II) oxidation processes. Given that physical factors, such as temperature, barometric pressure, humidity, and gas solubility also affect the measured E_H values (Brezonik and Arnold, 2011), it is useful

to revisit physical, chemical, and microbial effects contributing to the long-standing issue of E_H interpretation.

1.1.2 Range of E_H in Saturated Near-Surface and Subsurface Systems

The E_H of saturated near-surface systems spans from +800 to -450 mV at pH 1.5 – 10 (Becking et al., 1960). The E_H-pH (or pe-pH, or Pourbaix) diagram (Table 1-1) indicates that such environmental E_H limits are within the thermodynamic stability field of water (H_2O/O_2 and H_2/H_2O) and overlap with the stability fields of inorganic iron ($Fe/Fe^{2+}/Fe_3O_4/Fe_2O_3/Fe^{3+}$) and organic quinone ($QH^{2-}/QH_2^-/QH_3/Q^-/QH$) redox couples. Despite the fact that equilibrium calculations of stability fields often do not reflect the true nature of kinetically driven redox systems, this E_H-pH diagram is useful for defining the conditions toward which a system tends to evolve.

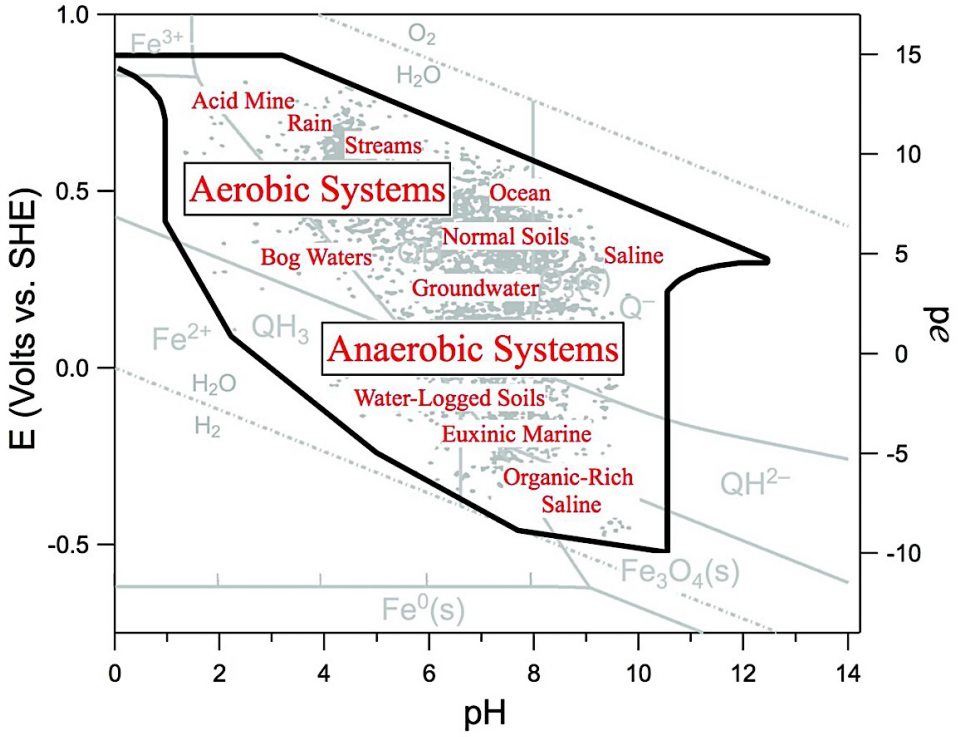

Figure 1-1. E_H-pH diagram showing regions of typical environmental systems superimposed on the stability fields for iron (Fe) and quinone (QH), as a model organic electron shuttle. Measured E_H data (light gray points) and environmental boundaries (a black frame) are constructed from the stability fields for various important ions including their actual measurements (H_2S/HS^-, $H_3PO_4/H_2PO_4^-/HPO_4^{2-}/PO_4^{3-}$, HSO_4^-/SO_4^{2-}, $H_2CO_3/HCO_3^-/CO_3^{2-}$, HNO_2/NO_2^-, NH_4^+/NH_4OH) (Becking et al., 1960). Figure reprinted from Tratnyek, Grundl, and Haderlein (2011).

Spatial and temporal variations of E_H are often documented for saturated near-surface (e.g., Roberts et al. 2010) and subsurface systems (e.g., Small et al. 2008). In near-surface systems (i.e., soils, peat bogs, sediments, groundwater, mine water), E_H is found to oscillate on diurnal (hours) and seasonal (months) frequency. Daily cycles in temperature induce changes in E_H ranging from 200 to 500 mV (Vorenhout et al., 2004). E_H oscillations related to changes in water regime (e.g., precipitation, snow melt, water table fluctuations) have been shown to reach up to 920 mV (Mansfeldt, 2003), while, cyclic changes in the level of UV irradiance affecting photosynthesis and redox changes in the Fe-system have also been recognized to impact E_H of natural environments (Becking et al., 1960; Melton et al., 2014).

Similarly to the susceptibility of E_H to temperature changes in the near-surface, a thermal stress caused by the disposal of heat-producing waste may alter E_H in the deep subsurface environments (Ewing et al., 2016). Therefore, E_H of subsurface horizons below the water table have been investigated primarily in the context of geological (e.g., clay rock, sedimentary rock, salt rock) disposal of radioactive waste (Duro et al., 2014; Gascoyne, 1997). In such complex engineered repositories within natural saturated host rock systems, E_H measurements are expected to respond to re-equilibration of the geological pore water under evolving thermal, hydrologic, and geochemical conditions (Laaksoharju et al., 2008).

Many underground research laboratories (URLs) are built below 100 m to perform site characterization and to test barrier materials under redox conditions close to those expected in the repository. I compiled the set of E_H-pH distribution from selected URL sites (data and references are tabulated in Table 1-1) and present it in Figure 1-2 to compare conditions of deep subsurface and near-surface systems. In contrast to near-surface saturated environments, the pH of deep subsurface is rarely acidic, rather it lies in the range from 6 to 12. On the other hand, the constructed E_H-pH diagram indicates that subsurface E_H is scattered from +537 to -620 mV, similarly to that of near-surface, although tending toward more reducing values. Such E_H-pH characteristics of subsurface are within the stability field of water and cover the stability fields of Fe minerals (e.g., pyrite, siderite, and goethite) (Sasamoto et al., 2011) and organic matter (e.g., reduced and oxidized quinones) (Tratnyek et al., 2011).

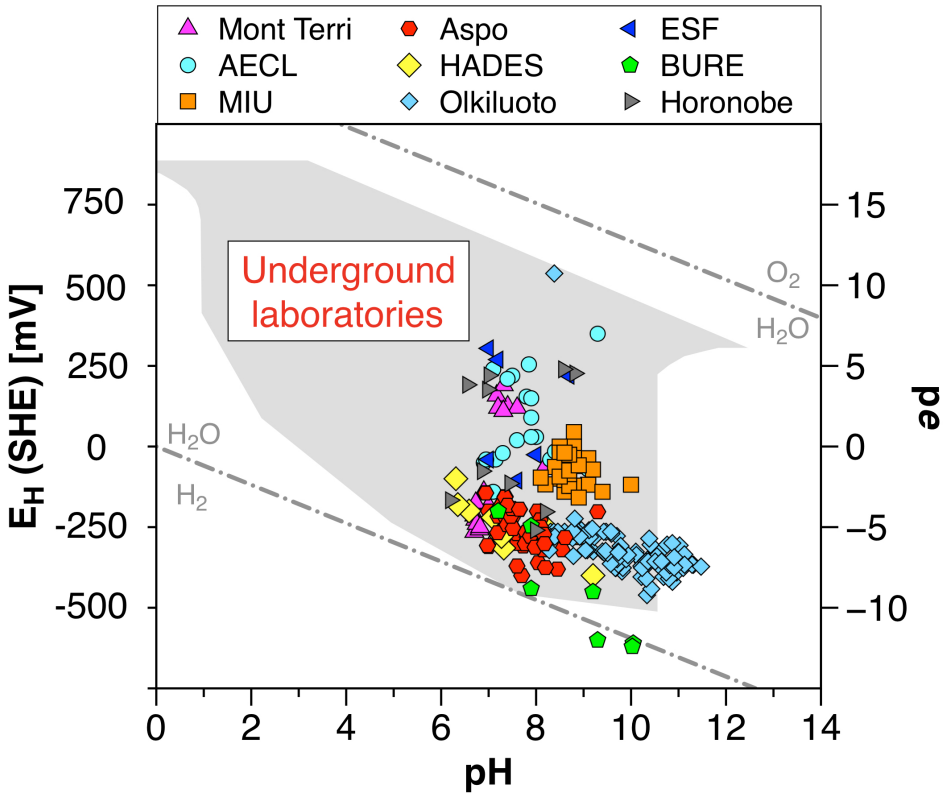

Figure 1-2. E_H-pH diagram showing in-situ data for selected underground research laboratories (Table 1-1) plotted on top of the typical domain of saturated near-surface systems (grey area) demonstrated on Figure 1-1.

Table 1-1. The E_H and pH ranges reported for *in-situ* or in laboratory experiments with groundwater and rock materials found in the areas of selected underground research laboratories (URLs). The detailed E_H and pH data from listed references were used to construct Figure 1-2.

URL	**Host rock, location** (OECD and NEA, 2013)	**pH**	**E_H**	**References**
BURE	Callovo-Oxfordian Argillites, Shale Meuse/Haute Marne, France	7.9 – 10.0	from +320 to -620 mV	(de Combarieu et al., 2007; Gaucher et al., 2009)
Mont Terri	Opalinus clay Mont Terri, Switzerland	6.7 – 8.8	from -190 to -265 mV	(Nagra, 2002; Pearson et al., 2003; Wersin et al., 2011)
HADES-URF [1]	Boom clay Mol/Dessel, Belgium	6.3 – 9.2	from -100 to -400 mV	(De Cannière et al., 1996; Zhang et al., 2008)

URL	Host rock, location, depth (OECD and NEA, 2013)	pH	E_H	References
AECL Underground Research Laboratory	Granite Lac du Bonnet, Canada	6.9 – 9.1	from +350 to -140 mV	(Gascoyne, 2004, 1997, 1989)
Aspo Hard Rock Laboratory	Granite Oskarshamn, Sweden	6.9 – 9.3	from – 143 to -400 mV	(Auqué et al., 2008; Laaksoharju et al., 2008, 1998)
Olkiluoto Research Tunnel	Granite Lansi-Suomi, Finland	8.3 – 11.5	from +537 to -460 mV	(Small et al., 2008)
ESF [3]	Welded tuff, Calico Hills Formation Yucca Mountain, United States	7.6 – 8.7	from +305 to -105 mV	(Daniels et al., 1982)
MIU [2]	Granite Gifu Prefecture, Japan	8.6 – 10.0	from +45 to -280 mV	(Fukuda et al., 2010; Iwatsuki et al., 2005)
Horonobe Underground Research Laboratory	Neogene sedimentary rock Hokkaido Prefecture, Japan	6.2 – 8.8	from +240 to -166 mV	(Ioka et al., 2011; Sasamoto et al., 2011)

[1] HADES-URF – High-Activity Disposal Experiment Site Underground Research Facility
[2] MIU – Mizunami Underground Research Laboratory
[3] ESF – Exploratory Studies Facility

1.1.3 Uncertainties in Stability of Redox Conditions in Subsurface Repositories

The assessment of the long-term performance of geological repositories relies on the stability of highly reducing conditions developed upon repository closure (Hedin and Olsson, 2016; Laaksoharju et al., 2008). The main oxygen scavengers are expected to be Fe systems of pyrite present in the bentonite matrix (Marty et al., 2010) or magnetite and siderite produced during steel canisters corrosion (El Mendili et al., 2014; Sakamaki et al., 2014). Furthermore, sulfidic systems comprising HS^-, pyrite, or mackinawite (Laaksoharju et al., 2008; Qi et al., 2014) have been considered to control the redox state of repository when bacteria remain active (Pedersen, 2002). Geochemical models based on Fe- and S- systems predict the development of reducing E_H (down to -700 mV) and significant pH_2 (Auqué et al., 2008; Duro et al., 2014, 2010; Ioka et al., 2011; Marty et al., 2010; Sakamaki et al., 2014; Sasamoto et al., 2011; Zhang et al., 2008).

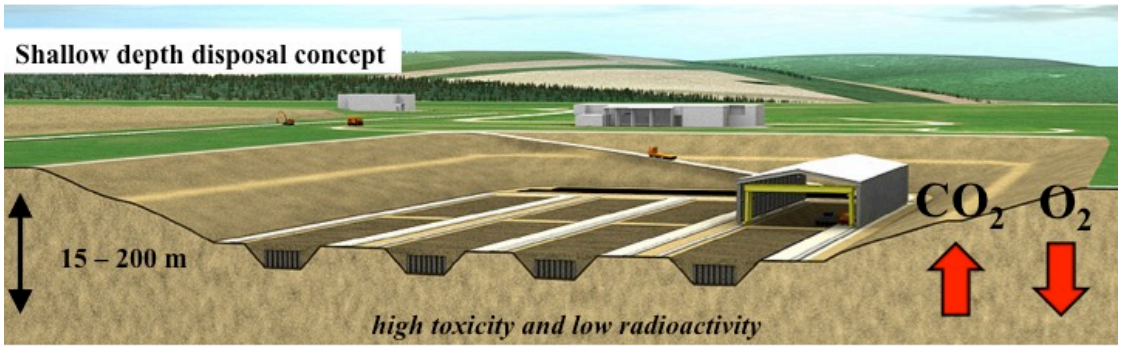

Figure 1-3. Shallow depth disposal concept designed for low-level long-lived radioactive waste (modified from ASN 2010) allowing gaseous mixing between surface and subsurface. In the French concept, long-lived radium-bearing waste contain both radionuclides and toxic chemicals leading to potentially high toxicity at low radioactivity (Andra, 2009).

However, the development of reducing conditions may take a several hundred years to evolve (Gascoyne, 1997). During the initial period of repository utilization, oxidizing perturbations in the vicinity of the repository may last from a few years to a hundred years (Figure 1-3) (Bildstein et al., 2005; Duro et al., 2014; Nagra, 2002; Stroes-Gascoyne et al., 2002). The intrusion of oxygenated groundwater (Swift and Bonano, 2016) or glacial water (Duro et al., 2014; Laaksoharju et al., 2008) into the repository site, as well as, water radiolysis catalyzed by gamma radiation in close proximity to the canisters (Rodwell et al., 2003; Song and Zhang, 2008) are potential causes of oxic conditions. Therefore, the examination of natural and engineered barrier materials in contact with the heterogeneous waste constituents under dynamic, redox-oscillating conditions can provide the necessary estimate of the long-term repository safety.

1.1.4 Contaminant Mobility in Redox-Dynamic Systems

In low-level waste (e.g., long-lived radium-bearing waste), potentially toxic chemicals (As, Sb, and Cr) are present along with radionuclides and maybe released into the environment in the case of repository failure (Andra, 2009). Inorganic contaminants often co-exist with redox-sensitive nutrients, such as dissolved organic carbon (DOC) and oxidized nitrogen (i.e., NO_3^-), with no exception for geologic repositories, where these nutrients are expected to leach from a bitumen matrix (Bertron et al., 2014). Once released, contaminant and nutrient mobility, bioavailability, and chemical reactivity is controlled by chemical speciation, which is, in turn, susceptible to dynamic changes in E_H, pH, mineralogy, and temperature (Borch et al., 2010). Further, these contaminants are of general geochemical interests as they are often released to the near-surface environment during metal mining, ore smelting, industrial processing, or shooting activities leading to the weathering of natural (e.g., pyroxenite, serpentinite,

arsenopyrite, scorodite, stibnite) (Godgul and Sahu, 1995; Wilson et al., 2010) and anthropogenic (e.g., tanned leather, semiconductor materials, bullets) (Bartlett, 1991) compounds.

Experiments in the field (e.g., irrigated rice fields, geothermal fields) and laboratory (e.g., soil and sediment suspensions) demonstrate that contaminant mobility fluctuates greatly with dynamic oxic and anoxic conditions (Hering et al., 2011; Hindersmann and Mansfeldt, 2014; Parsons et al., 2013a; Stewart et al., 2009; Thompson et al., 2006; Wilson et al., 2012). There is a good agreement between incubation experiments demonstrating As mobilization from soil and sediments under anoxic conditions, As sequestration under oxic conditions (Frohne et al., 2011; Mitsunobu et al., 2006; Parsons et al., 2013a), and Cr immobilization under anoxic conditions (Blowes et al., 2000; Butler et al., 2015; Frohne et al., 2015; Matern and Mansfeldt, 2016). However, less consistency is found for Sb behavior, with higher aqueous concentration under oxic conditions (Fawcett et al., 2015; Frohne et al., 2014; Mitsunobu et al., 2006) and in some experiments under anoxic conditions (Frohne et al., 2011; Hockmann et al., 2014). Finally, few experiments have considered contaminant mixtures pointing on potential complex interplay between co-existing redox-sensitive elements (Andrewes et al., 2000; Kourtev et al., 2009; Z. Wang et al., 2013).

Mineralogical control of contaminant mobility. In near-surface environments, fresh soils and sediments act as natural sinks for contaminants mainly due to contaminant sorption on Fe-, Mn-, and Al-oxyhydroxide minerals. Sorption efficiency differs for As, Sb, and Cr depending on contaminant speciation, pH, and the presence of competing ligands (e.g., phosphate, silicate, carbonate, natural organic matter). Oxyhydroxide Fe- and Mn- minerals are effective contaminant sorbents mainly in oxidizing environment and near-neutral pH (Schwertmann, 1991). Under reducing conditions, reductive dissolution of minerals driven either by abiotic (e.g., by sulfide) (Dos Santos Afonso and Stumm, 1992) or microbial processes (e.g., by iron-reducing bacteria) (DiChristina et al., 2005) can decrease specific surface areas and may cause a release of sorbed contaminants into environment. Significant correlation between reduced Fe(II) and aqueous contaminant concentrations has been widely reported (Hindersmann and Mansfeldt, 2014; Hockmann et al., 2014). As a result, the redox cycling of reductive dissolution and oxidative precipitation of contaminant-bearing minerals is often invoked as the main mechanism controlling contaminant mobility (Frohne et al., 2014; Islam et al., 2004; Mitsunobu et al., 2006; Parsons et al., 2013a; Stucker et al., 2013).

In contrast to the near-surface matrices, subsurface argillaceous formations consist principally of clay minerals (e.g., montmorillonite, illite, kaolinite, chlorite) (Grambow, 2016) and are depleted in reactive Fe- and Mn- oxyhydroxide phases. In such environments, contaminant mobility is potentially less

controlled by sorption and redox transformations. Although clays offer large surface areas with a variety of sites for As(V), Sb(V), and Cr(VI) sorption, such as broken clay edges or a cation bridging (Lin and Puls, 2000; Rai et al., 1989), oxyanions tend to persist in the aqueous phase due to electrostatic repulsion with negatively charged surface functional groups at near-neutral pH (Blowes et al., 2000).

Role of microbial processes on contaminant mobility. Microbial metabolism relies on the availability of redox-sensitive nutrients in groundwater and fracture minerals, thus, affecting the geochemical composition and environmental redox conditions. Microorganisms are abundant in the near-surface and are commonly found in subsurface to at least 1500 m (Pedersen, 2002). Across the depth profile of fractured granitic bedrock from the near-surface (-100 m) to deep subsurface (-1400 m), Laaksoharju et al. (2008) demonstrated the presence of active sulfate-reducing bacteria, heterotrophic methanogens, heterotrophic acetogens, and autotrophic acetogens.

This study highlighted that microbial activity plays important role in shaping geochemical systems even in deep, low-nutrient environments, thus, should not be ignored when predicting geochemical conditions of future repositories. A number of safety assessment already incorporate microbial processes into the predictive modelling (Duro et al., 2014; Hallbeck and Pedersen, 2012; Laaksoharju et al., 2008; Small et al., 2008; Zhang et al., 2008), however, the respective contributions of microbial and abiotic processes to overall contaminant sequestration capacity still remains uncertain.

Redox-sensitive contaminants, such as As, Sb, and Cr, can be reduced (e.g., Amend et al., 2014) and oxidized (e.g., Terry et al., 2015) by bacteria and archaea via enzymatic and non-enzymatic microbial processes. Enzymatically, microorganisms tend to reduce oxidized species to which they are exposed, either for energy, via reductive respiration in the presence of a suitable electron donor (e.g., organic carbon), or to mitigate toxic effects, via reductive detoxification (Campbell and Nordstrom, 2014; Zhu et al., 2014). Alternatively, contaminants can be reduced without a direct microbial activity (i.e., non-enzymatically) via oxidation of microbially produced glutathione (GSH) (Scott et al., 1993) or contaminant biosorption to the microbial cell wall (Viti et al., 2014). As a result, microbial reducing activity may either cause a decrease in contaminant mobility, as in the case of the reduction of soluble Cr(VI) and Sb(V) to sparingly soluble Cr(III) (Butler et al., 2015; Chen and Hao, 1998) and Sb(III) (Abin and Hollibaugh, 2014), or an increase, as in the case of As(V) reduction with a lesser sorption affinity of As(III) in the presence of competitive sorbing ligands (Burnol et al., 2007). The uncertainties in contaminant mobility can be tested on the case studies with respect to relevant to repository nutrient conditions and microbial diversity.

1.2 Research Objectives

The redox potential is considered as one of the major variables controlling the fate of redox-sensitive elements in saturated subsurface environment. Therefore, the primary objectives of this research were to reassess the characterization of redox potential measurements and to examine the effect of oscillating redox conditions on the biogeochemistry of relevant contaminants (As, Sb, Cr) and nutrients (C, N, Fe, Mn). The objectives of this research designed to address the corresponding knowledge gaps are the following:

- To evaluate the respective contributions of representative biogeochemical components of subsurface environments (i.e., solution-microbe-mineral) to redox potential (E_H) measurements by a Pt electrode.
- To investigate the mechanisms of oxyanion (Cr, As, Sb) sequestration in clay-rich suspension under successive oxic-anoxic conditions.
- To evaluate the reversibility of contaminant (Cr, As, Sb) sequestration under such conditions by comparing the contaminant fate in clay-rich suspension and Fe/Mn-rich suspension.

1.3 Thesis Organization

This thesis includes five chapters and annex associated with the research objectives identified above. The chapters are organized as a series of laboratory batch experiments progressing from less complex synthetic systems to more complex biogeochemical suspensions. To further interpret experiments, the increasing complexity approach is also applied to biogeochemical modelling, i.e., by fixing parameter values constrained from simple systems and using them unchanged in increasingly complex systems. Chapter 1 provides background information and identifies literature gaps in the field of redox potential interpretation and contaminant behavior in redox-dynamic environments. Chapter 2 presents a systematic study on deconstructing redox cascades and isolation of physical, chemical, and biological processes affecting E_H measurements. The experiments of increasing complexity aimed to characterize key representative components of subsurface water-mineral-microbial systems under redox-oscillating conditions. Chapter 3 presents a detailed study of contaminant mobility in the subsurface argillaceous suspensions with the focus on mineralogical and biological processes occurring under redox-oscillating conditions. Chapter 4 provides comparative analysis of two stand-alone studies of As, Sb, and Cr mobility in two different natural suspensions representing subsurface argillaceous (experiments of Chapter 3) and near-surface (experiments of a co-authored publication given in Annex-I) environments. Chapter 5 concludes by highlighting the novel scientific contributions provided by the thesis and summarizing practical

recommendations for future research in complex biogeochemical systems exposed to changes in redox conditions.

1.4 Statement of Contributions to the Articles in Chapters 2-4

Authors:

Ekaterina Markelova: Project design with the help of her supervisors and collaborators, experimental design, sample collection and instrumental analysis unless otherwise noted, theoretical calculations, modelling in Chapter 3, data interpretation and manuscript preparation.

Christopher Parsons: Project design, construction of bioreactors in Chapter 2 and 3, help with carrying out the experiments in Chapters 2-4. Prepared Figure 2-1.

Christina Smeaton: Assistance with experimental media preparation and calibration of ATP measurements in Chapter 2.

Igor Markelov: Assisance with the model design and performance of the model calibration and sensitivity analysis in Chapter 3.

Benoit Madé: Project design, manuscript writing.

Raoul-Marie Couture: Project design and co-supervision, data interpretation, manuscript writing, modelling work in Chapter 6.

Laurent Charlet: Project design and co-supervision, data interpretation, manuscript writing,

Philippe Van Cappellen: Project design and co-supervision, data interpretation, manuscript writing.

Collaborators:

Marianne Vandergriendt: analyzed samples for NO_3^- and NO_2^- in Chapter 2.

Shuhuan Li: performed XRD of goethite in Chapter 2.

Nathaniel Findling: performed XRD of an argillaceous sample in Chapter 3.

Chapter 2

Deconstructing redox potential

(E_H) measurements:

A systematic experimental approach

2.1 Summary

Redox electrodes are commonly used to measure the redox potential (E_H) of natural waters. However, interpretation of E_H measurements is challenging because redox equilibrium is rarely achieved. To improve the qualitative understanding of the factors affecting E_H measurements in natural systems, we performed a series of redox-oscillating batch experiments where we alternated sparging with air and N_2. Starting from a simple electrolyte solution, the stepwise addition of common groundwater solutes, metabolic substrates (nitrate and lactate), bacteria (*Shewanella oneidensis* MR-1), and goethite (α-$FeOOH_{(s)}$) increased the biogeochemical complexity in each subsequent experiment. This systematic approach allowed us to reproduce a full redox cascade from +500 to -350 mV (pH ~7.4) while isolating the influence of individual physical, chemical, and biological factors. Between +500 mV and +44 mV, the redox electrode primarily responded to the dissolved O_2 concentration. The addition of bacteria and solution matrix effects also markedly affected the E_H measurements, but variable nitrate (NO_3^-) and nitrite (NO_2^-) concentrations had no effect. Nitrate and nitrite reduction occurred between +44 mV and -55 mV, that is, at E_H values well below theoretical Nernstian E_H values associated with aqueous nitrogen redox couples. Upon depletion of NO_3^- and NO_2^-, E_H dropped to values below -200 mV. This decrease was interpreted as a microbial stress response to electron acceptor limitation, resulting in the extracellular release of reduced electron shuttle compounds. Nernstian E_H values were only observed below -250 mV when the α-$FeOOH_{(s)}/Fe^{2+}_{(aq)}$ couple was activated during microbial goethite reduction. Under all conditions, the presence of bacteria (i.e., *S. oneidensis* MR-I) lowered the measured E_H, whether or not terminal electron acceptors were available.

2.2 Background

Redox electrodes are widely used as simple and inexpensive monitoring devices to rapidly measure redox potentials (E_H or ORP). Although these electrodes have been used for over a century, the interpretation of the measured results remains controversial (Christensen et al., 2000; Gezahegne et al., 2007; Hunting and Kampfraath, 2013; Husson, 2013; Small et al., 2008). In a recent review of E_H and pH measurements, Husson (2013) noted that "according to the discipline, E_H gets measured on different scales and for various substrata: organelles, cells, plants, rhizosphere, bulk soil, sediments, soil solution, or water." Thus, the significance of redox potentials varies substantially between researchers from different disciplines, often with a selective focus on the contributions of chemical or biological factors when interpreting measured E_H values.

Despite the general acceptance of the ambiguities surrounding the interpretation of measured E_H (Small et al., 2008), there have been a number of recent studies providing new insights into the qualitative (Enright and Ferris, 2016; Hunting and Kampfraath, 2013; Oktyabrskii and Smirnova, 2012) and quantitative (Opel et al., 2014; Willey et al., 2012) application of redox electrodes, in studies showing that valuable information can be extracted from continuous E_H measurements. For instance, Enright and Ferris (2016) demonstrate that long-range correlations of E_H time series can help distinguish microbial from chemical Fe(II) oxidation processes. Thus, continuous monitoring of E_H variations, rather than single measurements, may hold most promise for the application of redox electrode measurements in complex environmental systems.

Not every redox couple is electroactive at the surface of the Pt electrode and several criteria must be met to generate a Nernstian E_H: (1) electrochemical equilibrium at the electrode surface, i.e. spontaneous reversibility of the redox reaction (Peiffer et al., 1992); (2) thermodynamic equilibrium between coexisting redox species and couples (Stumm and Morgan, 1996); (3) mono- or divalent transfer of electrons between the redox species (Nordstrom et al., 1979); (4) exchange currents of the redox couple greater than 10^{-7} amp cm^{-2}, which typically corresponds to concentrations of at least 10^{-5} mol L^{-1} for the oxidized and reduced species (Nordstrom et al., 1979). In other words, the concept of Nernstian E_H is applicable only for redox couples with oxidized and reduced species that can exchange electrons at the electrode surface during reversible oxidation and reduction. Otherwise, a redox couple is non-electroactive towards the electrode and, therefore, should not be expected to yield a Nernstian electrode response.

Throughout this paper, the potential of an aqueous solution computed with Equation 1-1 will be denoted as the Nernstian E_H, and the potential measured with a Pt redox electrode, and referenced against SHE, simply as E_H. Although the Pt electrode is non-selective, a few environmentally-relevant redox

couples, in particular Fe(III)/Fe(II) and S(0)/S(-II), are able to generate Nernstian E_H (Berner, 1963; Enright and Ferris, 2016; Nordstrom et al., 1979; Opel et al., 2014; Whitfield, 1974). Peiffer et al. (1992) suggest that a single redox couple may control the electrode voltage if its rate constant and/or activities are two orders of magnitude higher than that of the other redox couples. Otherwise, in aqueous systems lacking a master redox couple, the electrode voltage is a combination of the simultaneous electrochemical signals generated by all redox couples present in the electrode-solution system (Peiffer et al., 1992). In addition, the Pt electrode is highly susceptible to a variety of physical conditions and chemical matrix effects that further contribute to the generation of mixed potentials (Peiffer et al., 1992). Thus, while the electrochemical signals recorded by the Pt electrode may potentially yield meaningful information about an aqueous system, the cumulative responses of the electrode substantially complicate the interpretation of measured redox voltages.

Water-saturated environmental systems (e.g., surface water bodies, aquatic sediments, aquifers, wastewater treatment plants) are comprised of multiple components (solid/aqueous/gaseous, biotic/abiotic, organic/inorganic), and are often exposed to dynamic environmental conditions (e.g., variations in temperature, pH, salinity, water flow velocity, dissolved oxygen saturation) that affect redox potential measurements. The complexity and interdependence of the processes in such systems do not readily allow for the quantitative, and even qualitative, evaluation of factors contributing to observed E_H values. Although the effects of variable pH, temperature, water table depth, availability of energy substrates, terminal electron acceptors (TEAs), and microbial activity have been widely addressed in the literature (Fiedler and Sommer, 2004; Hunting and Kampfraath, 2013; Husson, 2013; Oktyabrskii and Smirnova, 2012), how individual factors and processes contribute to measured E_H values remains uncertain (Opel et al., 2014). Specifically, I hypothesized that the Pt electrode would responds to a variety of physical, chemical, and microbial influences, whose respective contributions to E_H values could be assessed in a synthetic biogeochemical system.

The approach was to record continuous redox potential measurements in a series of synthetic systems assembled from the following representative components of a water-saturated, subsurface environment: artificial groundwater (AGW), heterotrophic bacteria (*Shewanella oneidensis* MR-1), aqueous TEA (nitrate), aqueous primary electron donor (PED) (lactate), and solid-phase TEA (goethite). These components are combined in batch reactors to create systems of increasing complexity, starting from a simple electrolyte solution and ending with a multi-phase, solution-microbe-mineral biogeochemical system, via intermediate steps. In each experiment, oxic/anoxic-oscillating conditions are imposed by alternating the sparging of air and N_2 gas in the reactors. The resulting continuous E_H data

series are then interpreted in terms of the respective contributions of physicochemical (stirring rate, dissolved oxygen saturation, physisorption), geochemical ($NO_3^-/NO_2^-/NH_4^+$ and α-$FeOOH_{(s)}/Fe^{2+}_{(aq)}$), and microbial (metabolites, ATP levels) factors and processes.

2.3 Materials and Methods

2.3.1 Reactor System

A batch reactor system (Applikon Biotechnology) (Parsons et al., 2013a; Thompson et al., 2006) with a working solution volume of 1 L and a headspace of 0.25 L was used (Figure 2-1). The body was made from borosilicate glass, all other components were stainless steel. The reactor was covered by aluminum foil to exclude light. Temperature and gas inflow were precisely controlled; temperature, pO_2, pH, and E_H were monitored continuously. Programmable inflows of air and N_2 were delivered via mass flow controllers. To avoid evaporative losses, gas inflows were humidified prior to addition, while gas outflow passed through an Allihn condenser at 5 ^oC. Temperature was maintained constant with a heating blanket and an internal liquid cooling loop, which was actuated by a Pt-100 temperature sensor and a PID control algorithm.

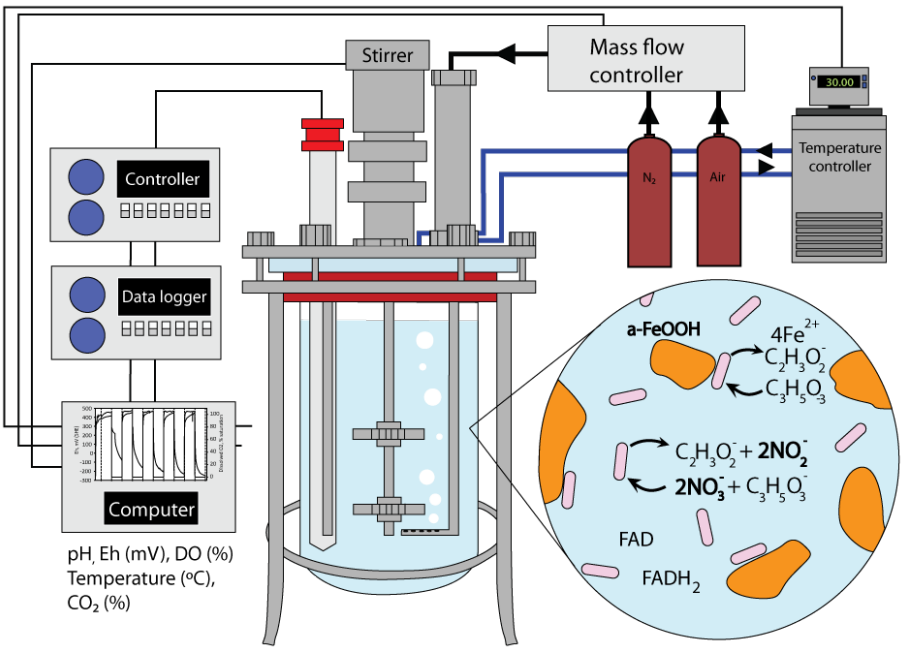

Figure 2-1. Schematic diagram of the bioreactor system. Also shown is a conceptual representation of the processes occurring in the biotic goethite suspension under N_2 sparging (Exp. IV, see Table 2-1).

The continuous measurement of pO_2 was performed using a low drift polarographic sensor with a detection limit to 0.1 mg L^{-1} and an accuracy of ±0.1%. The combined open-junction pH/E_H electrode used an argental reference (Ag|AgCl – 3 M KCl) and pre-pressurized liquid electrolyte (Mettler Toledo InPro 3253i/SG). Automatic adjustments of measured E_H values to the experimental temperature and SHE were performed via a multi-parameter transmitter (Mettler Toledo M800). Prior to all experiments the pH/E_H electrode was autoclaved and gently polished to erase the electrode's "history" (Aldous and Compton, 2011; Nordstrom et al., 1979). E_H and pH readings were then verified against Zobell's ORP standard solution and commercial pH buffers (A&C American Chemicals Ltd). For a concise summary of practical recommendations for the use of Pt electrodes we refer the reader to Table 2-5.

2.3.2 Increasing Complexity Experiments

Four batch experiments (Exp. I, II, III and IV) of increasing complexity were designed to assess the response of the Pt electrode to chemical, mineralogical, and microbial constituents representative of subsurface environments (Table 2-1). The reactors underwent four 48-hour cycles of alternating air and N_2 inflows (30 ml min^{-1} each) at constant temperature (30±0.1 °C) and stirring speed (300 rpm) for at least 8 days. All experiments were initiated with air sparging; time zero was defined as the first time the inflow was switched to N_2. All chemicals were of reagent grade from Sigma-Aldrich, EMD Chemicals, Fisher Scientific, or Acros Organics and solutions were prepared in Milli-Q water (resistivity of 18.2 MΩ cm^{-1}).

Table 2-1. Design of increasing complexity bioreactor experiments.

Factors tested	Exp. I	Exp. II	Exp. III	Exp. IV
Oxygen saturation: air (g) and N_2(g) sparging	+	+	+	+
Chemical matrix: artificial groundwater (AGW)*		+	+	+
Microbial presence: *S. oneidensis* MR-1			+	+
Mineral presence: goethite (α-FeOOH)				+

***** AGW – artificial groundwater (composition is given in Table 2-2).

In Exp. I, a simple 0.05 mol L^{-1} KCl electrolyte solution was prepared (>99%, EMD Millipore). The corresponding ionic strength (0.05 M) is within the range found for groundwater (Appelo and Postma, 2005). An ionic strength of ≥ 0.005 M is deemed necessary to reach electrochemical equilibrium with the redox electrode and thus to acquire stable readings (Grundl and Macalady, 1989). The artificial groundwater (AGW, Table 2-2) in Exp. II, was designed to mimic a typical saturated subsurface environment (0.05 mM PO_4^{3-}, 0.6 mM SO_4^{2-}, 0.1 mM NH_4^+, 0.4 mM Mg^{2+}) capable of sustaining microbial activity. The AGW contained nitrate as TEA (1 mM NO_3^-) and lactate as excess PED (18 mM

$C_3H_5O_3^-$). The ionic strength of AGW was 0.05 M, equal to Exp. I, and MOPS was used as a pH buffer (pH 7.41±0.01). In contrast to most microbial culture studies, which often use rich growth media, AGW did not contain trace elements (e.g., Co, Ni, B, Mo, Zn, Mn, Cu, Se), basal salts ($FeSO_4$, EDTA), vitamins or amino-acids (Cruz-García et al., 2007; Krause and Nealson, 1997; Marsili et al., 2008; Pinchuk et al., 2011) to avoid potential effects of these components on the redox measurements. Sterile conditions during Exp. II were ensured by addition of a broad-acting mixture of antibiotics (Sigma-Aldrich: kanamycin and streptomycin sulfates at 30 µg ml^{-1} and 50 µg ml^{-1}, respectively (Mesquita, 2013)) targeting Gram-positive, Gram-negative bacteria, and fungi.

Table 2-2. Composition of the artificial groundwater (AGW) used in Experiments II, III, and IV. AGW was designed to mimic a groundwater capable of sustaining minimal microbial activity.

Chemical	**mmol L^{-1}**
KH_2PO_4	0.05
$MgSO_4$, $7H_2O$	0.6
$MgCl_2$	0.4
NH_4Cl	0.1
KOH	8.0
KNO_3	1.0
Na-$C_3H_5O_3$	18.0
MOPS ($C_7H_{15}NO_4S$)	20.0

In Exp. III, AGW was inoculated with a heterotrophic bacterium: *S. oneidensis* MR-1 was chosen as a model facultative anaerobe capable of respiration using a wide range of aqueous and solid-phase TEAs, including O_2 (DiChristina, 1992), NO_3^- (Cruz-García et al., 2007), and goethite (Hartshorne et al., 2007). Microbial inoculum was prepared from a bacterial glycerol stock (ATCC 700550) stored at -80 °C, grown aerobically in Luria Bertani (LB) broth to late log phase (16 hours), centrifuged at 3500 rpm, washed with AGW, and inoculated into the reactor to achieve a cell density of 10^7 cells ml^{-1} (OD_{600} = 0.01). The cell density was determined by calibrating optical density (600 nm) measurements against direct cell counts by epifluorescence microscopy (Figure 2-7) (Hobbie et al., 1977). Use of AGW yielded relatively slow nitrate reduction rates (0.015 h^{-1}) that are more representative of subsurface environments than the growth rates typically achieved in laboratory culture experiments (>0.1 h^{-1}) (Cruz-García et al., 2007).

In Exp. IV, 5 g L^{-1} of pure goethite (α-FeOOH) was dispersed in AGW inoculated with *S. oneidensis* MR-1. Goethite was synthesized following Varanda et al. (2002) and Cornell & Schwertmann (2003). Briefly, a ferric iron salt ($Fe(NO_3)_3 \cdot 9H_2O$, EMD Chemicals) was dissolved in Milli-Q water. The pH was then raised from 3 to 10 with KOH to precipitate ferrihydrite. The suspension was heated for 2 days at 40 °C and then for 3 days at 60 °C before being poured into dialysis bags (7 Spectra/Por Dialysis Membrane MWCO:1000). Dialysis was performed in a Milli-Q water bath (10 L), replaced every day for 7 days until bath conductivity decreased from 2118 to 0.88 μS cm^{-1}. The purified precipitate was freeze-dried, ground, and identified as goethite by XRD (PANalytical Empyrean II with Cu-α cathode tube). The targeted cell density of *S. oneidensis* MR-1 in Exp. IV was the same as in Exp. III (10^7 cells ml^{-1}).

2.3.3 Sampling and Analyses

E_H, pH, temperature, and dissolved O_2 were measured continuously every minute for the duration of the experiments. All other variables were measured at least every 24 hours. Aliquots were filtered through 0.2 μm pore size filters (Supor®polyethersulfone). A portion of the filtrate was used for the immediate determination of ammonium (NH_4^+) and ferrous iron ($Fe^{2+}_{(aq)}$), while the rest was kept frozen (-20 ^oC) for later nitrate (NO_3^-) and nitrite (NO_2^-) analyses. Measurements of ATP were performed immediately on filtered and unfiltered samples to determine the extracellular and total ATP fractions, respectively (Hammes et al., 2010). The microbial ATP fraction was estimated as the difference between total and extracellular ATP concentrations.

A Dionex ICS-5000 ion chromatograph equipped with an AG11 HC analytical column was used for the determination of the NO_3^- and NO_2^- concentrations (DL = 11 μM, SD < 1%). Concentrations of N-NH_4^+ (DL = 2 μM, SD < 3%) and $Fe^{2+}_{(aq)}$ (DL = 4 μM, SD < 1%) were measured colorimetrically on a UV-vis spectrophotometer (Bolleter et al., 1961; Viollier et al., 2000). Aqueous and surface-bound Fe^{2+} were analyzed using a modification of the standard ferrozine assay (Lovley and Phillips, 1986; Stookey, 1970; Viollier et al., 2000). The surface-bound $Fe^{2+}_{(s)}$ was released by diluting 0.5 ml of the experimental suspension in 5 ml of 0.5 N HCl and digested for 1 hour with agitation, followed by centrifugation and filtration. ATP concentrations were used as a proxy for microbial activity (Hammes et al., 2010; Karl, 1980); they were measured using a commercial assay kit (Promega BacTiter-Glo Microbial Cell Viability Assay) and a Flexstation 3 Multi detection reader (Molecular devices). The ATP analyses were conducted in triplicate with a detection limit of 0.1 nM and a relative standard deviation of < 5%.

2.4 Results and Discussion

The full data set of NO_3^-, NO_2^-, NH_4^+, $Fe^{2+}_{(aq)}$, ATP concentrations, and measured values of pH and E_H are provided in Table 2-6. The redox potentials of the TEAs for respiration by *S. oneidensis* are listed in Table 2-3. The theoretical Nernstian E_H values for various redox couples, based on the chemical solution compositions measured in Exp. I, Exp. II, Exp. III, and Exp. IV, are listed in Table 2-4. The effect and relative importance of various physical, chemical, and microbial influences on the E_H signal isolated within the experimental series are described below, subsectioned by the influencing factor.

2.4.1 Physical Mixing

Physical mixing promotes homogeneity of the experimental solutions and suspensions, and enhances mass transfer to and from the electrode surface. However, there is no general agreement on how to optimize stirring speed for E_H measurements (Altmaier et al., 2011; Cubas et al., 2007; Ratusznei et al., 2003) and often this important variable is not reported (Parsons et al., 2013a; Thompson et al., 2006). In preliminary tests, we evaluated the effect of the stirring speed on the E_H measurements in 0.05 M KCl solution. A decrease of the stirring speed from 500 to 0 rpm caused the E_H values recorded by the Pt electrode to drop slightly by 6±1 mV during N_2 sparging, but to increase by 120±2 mV during air sparging.

The sensitivity of E_H measurements to the stirring rate during N_2 sparging probably reflects diffusion of very small amounts of O_2 across the boundary layer surrounding the electrode (i.e., the Nernst diffusion layer) (Helm et al., 2010). Even under vigorous N_2 sparging, aqueous solutions contain trace levels of O_2 in the absence of chemical or biological O_2 scavenging agents (e.g., *S. oneidensis*). We suggest that at a lower stirring rate, less trace O_2 accumulates at the electrode surface causing a lower E_H reading. In contrast, in well aerated KCl solution (i.e., during air sparging), the electrode is susceptible to the formation of a Pt-oxide coating (Schuring et al., 1999). The oxide persistence at the electrode surface is likely to increase under a lower stirring rate or in stagnant water, resulting in higher E_H values imposed by the redox potentials of the PtO/PtO_2/Pt couples (Schuring et al., 1999). All reactor experiments presented here were conducted at a constant stirring rate of 300 rpm, which was necessary to avoid sedimentation of goethite in Exp. IV.

2.4.2 Matrix Effects

Switching between air and N_2 sparging in the KCl electrolyte solution (Exp. I) caused reproducible E_H changes between +501±1 and +113±5 mV, respectively (Figure 2-2 (a)). The E_H values in the abiotic AGW (Exp. II) were systematically lower than those of the corresponding air and N_2 periods in KCl solution, as can be seen by the E_H differences in subzones A_{1-2} versus B_{1-2} and D_{1-2} versus E_{1-2} (Figure

2-2 (a-b)). Concentrations of NO_3^- and NH_4^+ in Exp. II remained constant and no NO_2^- was detected (Figure 2-2 (b)). The E_H differences between Exp. I and Exp. II were, therefore, attributed to constituents of AGW other than the nitrogen compounds. Testing the Pt electrode response to individual AGW constituents under air sparging subsequently revealed that addition of MOPS (pH buffer) caused an instantaneous decrease of measured E_H by 132 mV. One likely explanation is physisorption of MOPS' sulfonic functional group ($-SO_3^-$) to the electrode surface. The interaction between anionic functional groups and the positively charged Pt surface modifies the electrochemical structure of the Nernst diffusion layer which may cause a shift in E_H (Hauch and Georg, 2001). Awad et al. (2011) demonstrated that the adsorption of SO_2 on Pt discs causes a potential shift of -130 mV during oxygen reduction. This shift is comparable to the E_H differences observed in Figure 2-2 between Exp. I and Exp. II during air (-138 mV) and N_2 (-80 mV) spargin.

Changes to E_H measurements caused by the physisorption of both redox-sensitive and redox-inert species at the electrode surface are referred to as matrix effects (E_{Matrix}) (Peiffer et al., 1992) or electrode poisoning (Grundl and Macalady, 1989; Perry and Denuault, 2015). Although the exact mechanism of electrode poisoning by MOPS could not be established, our results show that MOPS can strongly modify non-Nernstian E_H electrode readings. Good's pH buffers (e.g., MES, PIPES, HEPES) (Good et al., 1966) all feature sulfonic functional groups. Given their widespread use in biological and biogeochemical studies their interference with redox electrode measurements should be recognized. Furthermore, while the effects of redox sensitive moieties in natural organic matter on E_H measurements are widely recognized, e.g., quinones in humic acids (Aeschbacher et al., 2010; Klüpfel et al., 2014), our results suggest that non-redox active organosulfur compounds may also influence E_H measurements. Organosulfur compounds, including cysteine, methionine, penicillin, and products of organic matter sulfurisation, are common constituents of soils and sediments (Couture et al., 2013b; Nriagu and Soon, 1985).

2.4.3 Oxygen

In the presence of excess PED (here, lactate), the redox potential is expected to follow the sequence of reduction reactions of the limiting TEAs (here, O_2, NO_3^-, and $FeOOH_{(s)}$), from higher to lower E_H (Table 2-3). In systems open to the atmosphere, O_2 is the strongest common oxidant and its reduction to H_2O should in principle set the value of E_H (Schuring et al., 1999). However, laboratory and field studies (Becking et al., 1960; Essington, 2004) systematically report measured E_H values in aerated environments that are lower than the Nernstian E_H of the O_2/H_2O couple. Indeed, the observed E_H (+500 mV) of the aerated KCl solution (98% DO saturation) in Exp. I is well below the theoretical Nernstian E_H for the

O_2/H_2O couple at near-neutral pH (>800 mV) (Table 2-3). Upon inoculation with *S. oneidensis* MR-1 (Exp. III), the dissolved O_2 saturation during air sparging dropped to 86±6 %, most likely due to O_2 consumption by microbial respiration (Figure 2-2 (c)). Under these conditions, the measured E_H (+305 mV) was also substantially lower than Nernstian E_H (+698 mV).

Table 2-3. Half reduction reactions of terminal electron acceptors used in the experiments with corresponding equilibrium constants (log K) accounting for reaction stoichiometry. Standard electron activity (pe^0) is calculated via Equation 1-4 and is expressed as standard state redox potentials (E^0) relative to the standard hydrogen electrode at pH 0 and pH 7 at 25 °C and unity of redox species. Calculations are based on values given in Brezonik and Arnold (2011).

Half-reaction	log K	pe^0 (pH 0)	E^0, mV (pH 0)	E^0, mV (pH 7)
Oxygen reduction				
$O_{2(aq)} + 4H^+ + 4\ \bar{e} \rightarrow 2H_2O$	86.0	21.5	1268	816
$O_{2(aq)} + 2H^+ + 2\ \bar{e} \rightarrow H_2O_2$	26.3	13.2	686	272
Nitrate reduction				
$NO_3^- + 2H^+ + 2\ \bar{e} \rightarrow NO_2^- + H_2O$	28.4	14.1	834	420
$NO_3^- + 10H^+ + 8\ \bar{e} \rightarrow NH_4^+ + 3H_2O$	119.2	14.9	881	191
Nitrite reduction				
$NO_2^- + 8H^+ + 6\ \bar{e} \rightarrow NH_4^+ + 2H_2O$	90.6	15.1	893	203
Goethite reduction				
$\alpha\text{-}FeOOH_{(s)} + 3H^+ + 1\ \bar{e} \rightarrow Fe^{2+}_{(aq)} + 2H_2O$	13.0	13.0	769	-360

Despite the commonly observed disparity between measured E_H and Nernstian E_H of the O_2/H_2O couple, strong correlation ($r^2 = 0.98$) between O_2 saturation and E_H values obtained in this study agrees with correlation demonstrated by Ishizaki et al. (1974), who suggested that when dissolved O_2 present in aqueous systems, Pt electrode responds to pO_2 at constant pH. Although the Pt electrode is designed to be inert to most redox reactions, Pt is a catalytically active metal for reaction with O_2 (Schuring et al., 1999). The O_2/H_2O redox couple, which requires a 2-electron transfer per O atom, is kinetically limited with a low rate constant for the electron transfer across the electrode surface on the order of 5×10^{-11} m s^{-1} (Schuring et al., 1999). Therefore, it is more likely that the intermediate redox couple O_2/H_2O_2, which only requires a 1-electron transfer per O atom, is the electroactive couple controlling the electrode response (Sato, 1960).

In agreement with previous studies (Barcelona et al., 1989; Holm et al., 1987), we estimate that for dissolved O_2 in equilibrium with the atmosphere (2.58×10^{-4} M) and a H_2O_2 concentration of 10^{-7} M (Frevert, 1984), the O_2/H_2O_2 couple yields a Nernstian E_H of +496±1 mV, which agrees well (within 1%) with the measured E_H of the aerated KCl solution in Exp. I. Moreover, the lowest E_H measured under air

sparging, +270 mV in both the AGW of Exp. III and the bacteria-goethite suspension of Exp. IV (Figure 2-2 (c-d)), matches the theoretical minimum Nernstian E_H of the O_2/H_2O_2 couple. Therefore, during electrode exposure to aerated conditions in our study, E_H was likely controlled by the O_2/H_2O_2 couple.

2.4.4 Nitrogen Redox Transformations

The NO_3^- added in Exp. III (1011 μM) was completely depleted during the first period of N_2 sparging (Figure 2-2 (c)). At the same time, NO_2^- was detected and the NH_4^+ concentration increased slightly from 68 to 89 μM. The changes in aqueous nitrogen speciation are qualitatively consistent with nitrate reduction coupled to lactate oxidation, whereby *S. oneidensis* MR-1 uses NO_3^- for respiration via the dissimilatory reduction to ammonium (DRNA) pathway (Cruz-García et al., 2007). To match the 1:1 NO_3^-:NH_4^+ stoichiometry of DNRA, a larger increase in NH_4^+ would have been expected in Exp. III. Contrasting results were obtained for the bacteria-goethite suspension of Exp. IV, where the NO_3^- concentration initially remained fairly stable (±180 μM), decreasing only slightly until the start of the last N_2 sparging period (290 h). At that point, NO_3^- consumption accelerated causing a complete depletion of NO_3^- while NO_2^- increased to 285 μM (Figure 2-2 (d)). Subsequently, NO_2^- was consumed and, by 338 h, had become undetectable, whereas NH_4^+ accumulated to 1115 μM. The near 1:1 molar ratio between the NO_3^- consumed and the NH_4^+ accumulated in Exp. IV matches the stoichiometry of DNRA.

The missing NH_4^+ in Exp. III can be explained by NH_4^+ assimilation into growing biomass (Cruz-García et al., 2007). Microbial ATP concentrations reached much higher levels in Exp. III compared to Exp. IV. During the first N_2 sparging period of Exp. III, microbial ATP rose from 23 to 138 nM (Figure 2-6). In contrast, the maximum microbial ATP concentration at the end of Exp. IV was only 5.2 nM. Based on the changes in microbial ATP, we estimate that biomass growth in Exp. III was at least 20 times higher than in Exp. IV. Microbial ATP concentrations calibrated against known *S. oneidensis* cell numbers ($4.6\pm0.6\times10^{-10}$ nM cell^{-1}, see calibration curve in Figure 2-7) imply that the biomass should have reached 2×10^{11} cells L^{-1} by the end of the first N_2 sparging period of Exp. III. Using the nitrogen content of *Escherichia coli* (24 fg N cell^{-1}) (Fagerbakke et al., 1996), the corresponding nitrogen assimilation by the newly formed biomass would have been around 0.4 mM, which would account for a large fraction of the missing NH_4^+ in Exp. III.

Microbial growth in Exp. IV remained limited, despite a second inoculation of *S. oneidensis* at 144 h. The decision to perform the second inoculation was taken because microbial ATP became undetectable (≤0.1 nM) after 32 h, indicating the collapse of the microbial population. Following the inoculation at 144 h, the microbial ATP concentration again decreased until, after 288 h, it began to rise

(Figure 2-6), indicating a recovery of the microbial population and its activity. This observation was coincident with the consumption of NO_3^- and, at a later stage, the build-up of $Fe^{2+}_{(aq)}$. The absence of detectable reduction of NO_3^- and formation of $Fe^{2+}_{(aq)}$ during the first 288 h of Exp. IV confirmed the lack of significant microbial activity prior to the last period of N_2 sparging.

During reduction of NO_3^- and NO_2^- in Exp. III and Exp. IV, the measured E_H continuously decreased and reached negative values. Upon the depletion of NO_2^- an abrupt drop in E_H occurred during both experiments (Figure 2-2, Figure 2-5). Although the E_H drop coincided with the end of NO_2^- respiration in both experiments, the measured E_H values were quite different: -10 mV in Exp. III and -100 mV in Exp. IV. Discontinuities in E_H are frequently observed in E_H time series recorded during biological wastewater treatment and in bioreactor experiments with NO_3^- as electron acceptor (Al-Ghusain and Hao, 1995; Guo et al., 2007; Kjaergaard, 1977; Parsons et al., 2013a; Wareham et al., 1993). Such discontinuities are colloquially referred to as "nitrate knees" and generally occur in the E_H range between +100 and -140 mV (Koch and Oldham, 1985; Tanwar et al., 2008; Wareham et al., 1993). The wide range of E_H values at which nitrate knees are observed, however, suggests that they are not under the direct thermodynamic control of the reduction reactions involving NO_3^- or NO_2^-.

The measured E_H values in Exp. III and Exp. IV were significantly more reducing than predicted with the Nernst equation for the various nitrogen redox couples (Table 2-4), which is also commonly observed for natural waters (Essington, 2004; Kumar and Riyazuddin, 2012; Lindberg and Runnells, 1984; Schuring et al., 1999; Włodarczyk et al., 2007). The negative E_H biases for the NO_3^-/NO_2^-, NO_2^-/NH_4^+, and NO_2^-/NH_4^+ couples, were up to 600, 325 and 293 mV, respectively. The lack of agreement between Nernstian and measured E_H is expected as nitrogen redox couples ($NO_3^-/NO_2^-/N_2O/NH_4^+$) are known to be non-electroactive (Langmuir, 1990; Schuring et al., 1999). Thus, nitrogen transformations affect measured E_H values indirectly by altering the metabolic activity of the bacteria utilizing NO_3^- and NO_2^- as substrates (Hunting and Kampfraath, 2013) (see section 2.4.6 *Microbial Effects*).

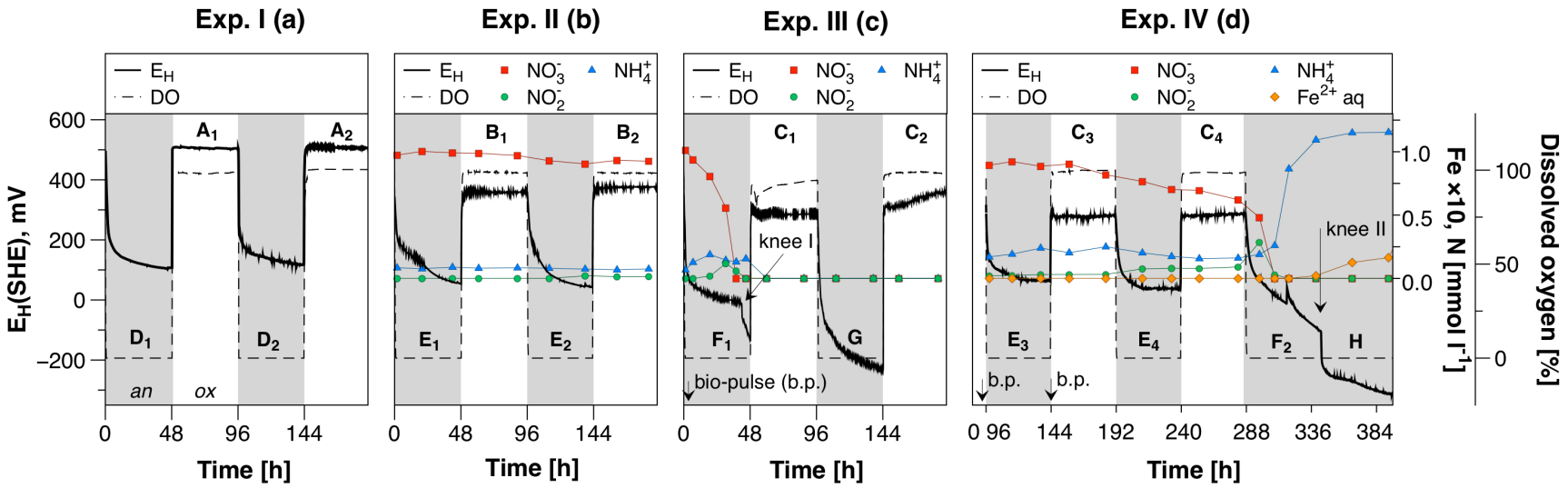

Figure 2-2. Measured time series of E_H (solid line), dissolved O_2 (dashed line), and concentrations of dissolved redox species: nitrate (squares), nitrite (circles), ammonium (triangles), and Fe (diamonds). "A-H" refers to the E_H subzones reached during air (white areas) and N_2 (grey areas) sparging. "Bio-pulse" (b.p.) refers to the inoculation with bacteria *S. oneidensis* MR-1 and "knee" identifies breakpoints in the E_H time series. A scaled up version of Figure 2-2 (c) is reproduced in Figure 2-5. Data for Exp. IV (d) are shown for the period 96 to 390 h; the data of E_H and $Fe^{2+}_{(aq)}$ for the entire experiment can be found in Figure 2-6. See text for complete discussion.

Table 2-4. Comparison of measured and Nernstian redox potentials (E_H). Calculations are based on the measured chemical species concentrations (see Table 2-6) corrected for ion activities via Davies equation, experimental pH, and experimental temperature (30 °C) via Equation 1-1. Selected measured data represents the last sampling point within the E_H zones (A-H) identified in Figure 2-2.

E_H zones	Measured E_H, mV	Nernstian E_H, mV					
		O_2/H_2O	O_2/H_2O_2	NO_3^-/NO_2^-	NO_3^-/NH_4^+	NO_2^-/NH_4^+	α-$FeOOH_{(s)}/Fe^{2+}_{(aq)}$
A_1	502	766	497	–	–	–	–
A_2	501	763	495	–	–	–	–
B_1	360	768	500	654	329	220	–
B_2	372	767	499	652	328	220	–
C_1	287	698	475	373	290	262	–
C_2	310	760	462	360	274	245	–
C_3	277	776	507	448	334	297	307
C_4	282	774	506	410	330	304	324
D_1	108	574	125	–	–	–	–
D_2	118	574	125	–	–	–	–
E_1	55	588	139	654	329	220	–
E_2	45	588	139	653	329	222	–
E_3	64	595	146	453	336	296	307
E_4	42	595	146	435	334	301	305
F_1	-10	579	130	409	315	283	–
F_2	-5	582	136	170	253	277	299
G	-230	551	102	361	275	247	–
H	-315	579	130	389	252	207	-333

2.4.5 Fe(III)/Fe(II) Redox Control

Prior to 288h, the goethite (α-FeOOH) particles in the bacteria-mineral suspension of Exp. IV did not appear to affect the redox electrode readings: the E_H values measured in subzones C_3 and C_4 (+279±2 mV), and E_3 and E_4 (+53±11 mV) of Exp. IV were within 6 % of those observed during periods of air sparging in Exp. III (C_1 and C_2: +298±11 mV) and N_2 sparging periods in Exp. II (E_1 and E_2: +50±5 mV), respectively (Figure 2-2). Until 288 h, no $Fe^{2+}_{(aq)}$ was detected, suggesting the absence of microbial Fe(III)

reduction (Figure 2-6). After 288 h, over a relatively long period (96 h) of N_2 sparging, about 3 μmol g^{-1} of surface-bound $Fe^{2+}_{(s)}$ was generated, which is equivalent to 15 μmol per litre suspension. However, the production of $Fe^{2+}_{(s)}$ did not cause changes in measured E_H. This observation is in agreement with the E_H measurements reported by Silvester et al. (2005) in goethite suspensions with adsorbed $Fe^{2+}_{(s)}$. These authors suggest that the anodic electrode current is responsive to aqueous $Fe^{2+}_{(aq)}$, but not to adsorbed $Fe^{2+}_{(s)}$ species (Silvester et al., 2005). Thus, given that in saturated soils and sediments the majority of Fe(II) produced during Fe(III) reduction is prevented from accumulating in solution by sorption and precipitation reactions, E_H measurements may not be a reliable indicator of the onset of microbial Fe reduction.

During the final stage of Exp. IV (subzone H, Figure 2-2 (d)), a release of up to 4 μM $Fe^{2+}_{(aq)}$ to solution was observed. The appearance of $Fe^{2+}_{(aq)}$ was accompanied by a pronounced drop in E_H (knee II in Figure 2-2 (d)). Following the drop, the measured E_H values (-315 mV) closely matched the calculated Nernstian E_H (-333 mV) for the $FeOOH_{(s)}/Fe^{2+}_{(aq)}$ couple at pH 7.55 (Table 2-4). Although the estimated concentration of $Fe^{3+}_{(aq)}$ (10^{-8} M) in equilibrium with goethite was well below the commonly assumed minimum electroactivity criterion (10^{-5} M), $Fe^{3+}_{(aq)}$ activities smaller than 10^{-7} M have been shown to result in Nernstian E_H (Macalady et al., 1990; Silvester et al., 2005). A Nernstian response of the Pt electrode to various Fe(III)/Fe(II) redox couples has been widely demonstrated, not only in acidic waters (Gezahegne et al., 2007; Grundl and Macalady, 1989; Langmuir, 1990; Nordstrom, 2011; Nordstrom et al., 1979), but also at neutral pH (Grenthe et al., 1992; Holm and Curtiss, 1989; Kumar and Riyazuddin, 2012; Macalady et al., 1990; Matia et al., 1991). In synthetic solutions of pH > 4, it has been proposed that the heterogeneous Fe(III)/Fe(II) couple enables the exchange current by coating the electrode with amorphous colloidal material (Macalady et al., 1990).

The α-$FeOOH_{(s)}/Fe^{2+}_{(aq)}$ redox couple meets several of the requirements to be electroactive, including reversibility of the redox reaction, a one electron transfer, and a high rate constant for the electron transfer across the electrode surface (5×10^{-5} m s^{-1}) (Schuring et al., 1999) wich allows for high exchange currents at the electrode surface. Our results thus agree with the long-held view that the Fe(III)/Fe(II) couples control E_H measurements with the Pt electrode, when detectable $Fe^{2+}_{(aq)}$ is present in solution (Grundl and Macalady, 1989). The results further suggest that under such conditions the E_H measurements are not sensitive to the presence of MOPS, consistent with redox potential measurements reported by Macalady et al. (1990) which were insensitive to matrix effects.

2.4.6 Microbial Effects

Non-Nernstian contributions of microorganisms to E_H measurements have mainly been extensively investigated by microbiologists (Oktyabrskii and Smirnova, 2012; Williams et al., 2010) and electrochemists (Opel et al., 2014; Xie et al., 2010). Continuous E_H measurements have been reported to yield qualitative information on the growth status (e.g., exponential and cessation) (Hunting and Kampfraath, 2013; Oktyabrskii and Smirnova, 2012), physiological condition (e.g., starvation stress, heat shock, and osmotic shock) (Oktyabrskii and Smirnova, 2012), and genotype (e.g., *Micrococcus luteus, Paracoccus pantotrophus*, and *Aminobacter aminovarans*) (Hunting and Kampfraath, 2013) of bacteria in liquid culture. Moreover, microorganisms have been shown to cause changes in E_H via the extracellular secretion of redox compounds (e.g., low-molecular weight thiols (Oktyabrskii and Smirnova, 2012) and quinone derivatives (Xie et al., 2010)), as well as redox inactive components (e.g., phospholipids (Das and Sligar, 2009)). In addition, E_H changes have been observed following cell lysis (Hunting and Kampfraath, 2013). Therefore, resident microbial communities may contribute to E_H distributions in natural waters not only by catalyzing biogeochemical redox reactions, but also through the release of metabolites into the surrounding environment (Becking et al., 1960).

The inoculation of 10^7 cells ml^{-1} of *S. oneidensis* MR-1 in Exp. III resulted in E_H values under air sparging that were 90 mV lower than under the sterile, but otherwise identical, conditions of Exp. I and Exp. II (Figure 2-2). These lower E_H values did not appear to be directly related to the level of aerobic respiration. The measured E_H during air sparging in Exp. III (C_1 = +287 mV) was similar to that in Exp. IV (C_3 = +277 mV), although both the O_2 saturation (86% versus 98%) and ATP concentrations (~50 nM versus undetectable, Figure 2-6) implied higher O_2 respiration in Exp. IV. That is, the E_H values measurements apparently responded to the presence of the bacteria, rather than their activity *per se*. This is in line with the observation that even inactive or dead microorganisms are capable of driving redox reactions (Park et al., 2005).

As noted earlier, in the biotic AGW (Exp. III) and the bacteria-goethite suspension (Exp. IV) the measured E_H values were much more reduced than the Nernstian E_H values calculated based on the aqueous nitrogen speciation (Table 2-4). We suggest that aqueous NO_3^- and NO_2^- affected the measured E_H indirectly by powering the cellular metabolic machinery, which in turn resulted in the extracellular excretion of organic byproducts that interact with the redox electrode (Hunting and Kampfraath, 2013). We further speculate that the large decreases E_H values reached during the N_2 sparging in Exp. III (subzones F_1 and G, Figure 2-2 (c)) may have been caused by the release of organic reductants by the cells

as a stress response to the complete depletion of the nitrogenous TEAs (Konhauser, 2007; Oktyabrskii and Smirnova, 2012).

In the absence of aqueous TEAs, *S. oneidensis* can survive via fermentation (Pinchuk et al., 2011) and the dissimilatory reduction of solid-phase TEAs such as α-$FeOOH_{(s)}$ (Beliaev et al., 2005). The bacteria can access the latter by secreting extracellular electron shuttles, such as flavins (Marsili et al., 2008; von Canstein et al., 2008). The depletion of NO_3^- and NO_2^- in Exp. III may have triggered a pulse release of flavins (e.g., riboflavin, FMN, FAD) (von Canstein et al., 2008) as the cells initiated a search for alternative TEAs. In support of this hypothesis, the mid-peak potential -219 mV (FMN and FAD) and -208 mV (riboflavin) at neutral pH are close to the E_H value of -232 mV observed in subzone G of Exp. III (Figure 2-2 (c)). It is important to note, however, that no measurements of extracellular electron shuttles were performed and, thus, the proposed hypothesis calls for further work.

2.4.7 Redox Cascades

Based on the combined results of the four experiments at pH 7.6±0.4, we divide the entire range of measured E_H into three redox zones: oxic ($+270 < E_H < +500$ mV), suboxic ($+40 < E_H < +270$ mV), and anoxic ($-350 < E_H < +40$ mV) as shown in Figure 2-3. The figure also displays the E_H records from subzones A-H of Figure 2-2 arranged as a redox cascade with relatively stable E_H plateaus separated by steps of about 150 mV. The oxic E_H range in Figure 2-3 is defined by the E_H values measured in the aerated solutions under abiotic and biotic conditions (i.e., subzones A_{1-2}, B_{1-2}, C_{1-4}). The suboxic E_H range corresponds to the E_H measurements in the abiotic solutions under N_2 sparging (subzones D_{1-2}, E_{1-2}), when trace dissolved O_2 concentrations were below the detection limit (0.1 mg L^{-1}) of the oxygen sensor (Grenthe et al., 1992; Ishizaki et al., 1974). Truly anoxic conditions required the removal of dissolved O_2 by *S. oneidensis* to below the half-saturation constant of aerobic respiration (~0.01 mg L^{-1}) (Wang and Van Cappellen, 1996). These conditions were reached in subzones F_{1-2}, G and H. The E_H ranges assigned to the redox zones in the experiments described here agree with E_H values reported for microbial systems where active aerobes are typically found in the range $+200 < E_H < +400$ mV and anaerobes in the range $-400 < E_H < +50$ mV (Hewitt, 1950).

With the exception of the α-$FeOOH_{(s)}/Fe^{2+}_{(aq)}$ couple, which imposed a Nernstian E_H control below -250 mV in the bacteria-goethite suspension (Exp. IV), no other master redox couple could be identified in the E_H range from +500 to -250 mV, implying that, above -250 mV, measured E_H values either reflect mixed redox potentials (E_{mix}) or as yet unidentified master redox couple(s). We hypothesize that this may also hold true for most E_H values above -250 mV measured in natural waters. Stable E_H measurements, such as those of the plateaus of the redox cascade in Figure 2-3, should therefore not be

taken as an indication that thermodynamic equilibrium has been reached among coexisting redox couples, or between the solution and the electrode surface (Peiffer et al., 1992; Stumm and Morgan, 1981).

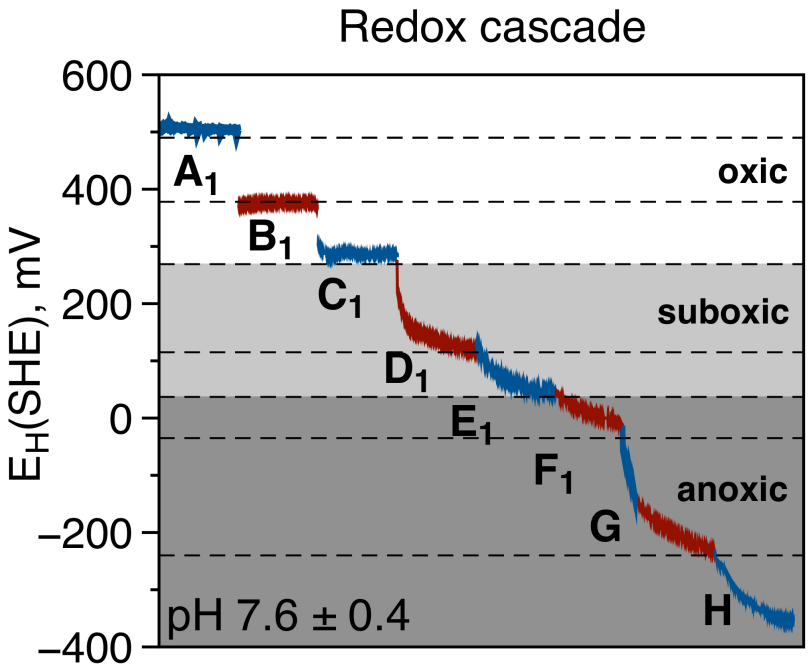

Figure 2-3. Redox cascade: compilation of measured E_H in the series of the four increasing complexity experiments. "A-H" refers to the E_H subzones identified in Figure 2-2. The definition of the redox zones (oxic, suboxic, and anoxic) is based on the experimental results; see text for a detailed discussion.

The experimental E_H range, from +500 to -350 mV (Figure 2-3), covers that of E_H values typically measured in natural subsurface environments, including waterlogged soils and sediments (Becking et al., 1960). In contrast to measurements made in the field or on natural samples, the observations accrued in the increasing complexity experiments enable us to start isolating the roles of individual physical, chemical, and biological factors on the measured E_H data and, hence, to deconstruct the redox cascade of Figure 2-3. The proposed interpretation of the cascade is summarized in Figure 2-4.

The E_H range from +500 to +44 mV, which comprises the oxic plus suboxic redox zones, encompasses the entire range of (non-zero) dissolved O_2 concentrations, from a maximum value of 7.5 mg O_2 L^{-1} during the periods of air sparging in Exp. I to values at or below detection (0.1 mg L^{-1}) during N_2 sparging in the abiotic solution of Exp. II. In addition to differences in O_2 concentration, the presence of MOPS and bacteria were a source of E_H variability. Together, the results suggest that matrix effects and microorganisms significantly impact redox potential measurements, and may help explain the relatively low redox potentials reported in oxic and suboxic aqueous environments. Changes in NO_3^- and NO_2^-

concentrations, however, did not influence the E_H, despite the variable NO_3^- to NO_2^- ratios in the periods C_{1-4} of Exp. III and Exp. IV.

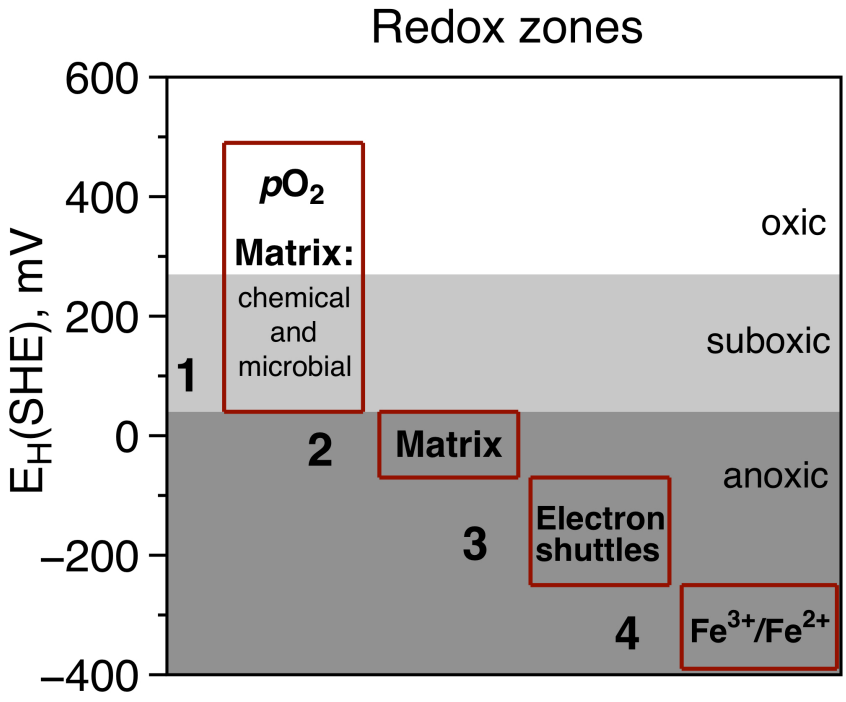

Figure 2-4. Schematic interpretation of main drivers of the redox cascade displayed on Figure 2-3. See text for discussion.

During microbial NO_3^- and NO_2^- reduction in Exp. III and Exp. IV, E_H ranged from +44 to -55 mV (subzones E_{1-4} and F_{1-2}). The corresponding 100 mV variation in E_H was possibly linked to the release of extracellular compounds by the bacteria. The exact nature of this microbially mediated matrix effect on E_H measurements needs to be determined, however. The E_H range from -55 to -200 mV during Exp. III (subzone G) occurred after the aqueous TEAs (NO_3^- and NO_2^-) were completely consumed and, therefore, the bacteria were left without terminal electron acceptor to enable respiration. We ascribe this E_H range to the extracellular release of cytochromes and riboflavin under starvation stress conditions (Hartshorne et al., 2007; Marsili et al., 2008). The most reducing conditions reached in the experiments correspond to subzone H in Exp. IV, when goethite reduction took place and $Fe^{2+}_{(aq)}$ was detected. Under these conditions, a thermodynamic control of E_H by the α-$FeOOH_{(s)}/Fe^{2+}_{(aq)}$ couple prevailed.

2.5 Conclusions

Redox potentials measured with a Pt electrode (range +500 to -350 mV) were recorded in redox-oscillating batch reactors of increasing biogeochemical complexity designed to include some key representative components of subsurface water-mineral-microbial systems. By systematically investigating different combinations of biogeochemical components it became possible to begin unraveling the effects of individual factors on the measured E_H values. The interplay of intermittent O_2 supply, solution matrix effects, mixed potentials, microbial effects and, under Fe reducing conditions, a Nernstian response of the electrode to the ferric-ferrous iron redox couple explains the observed trend of fairly stable E_H measurements separated by relatively abrupt transitions, that is, a redox cascade. The addition of the metabolically versatile bacterium *S. oneidensis* to the experimental systems always caused a lowering of the E_H readings. The results of this study yield hypotheses about the nature of geomicrobial effects on E_H measurements that can inform future research. In particular, we speculate that meaningful information on the responses of natural microbial communities to changes in their surrounding environmental conditions could be extracted from continuous time-series E_H data. Overall, our results imply that temporal or spatial redox cascades in environments such as waterlogged soils, sediments, and aquifers, cannot be explained solely as a succession of thermodynamic equilibria involving the major terminal electron acceptor redox couples.

2.6 Supporting Information

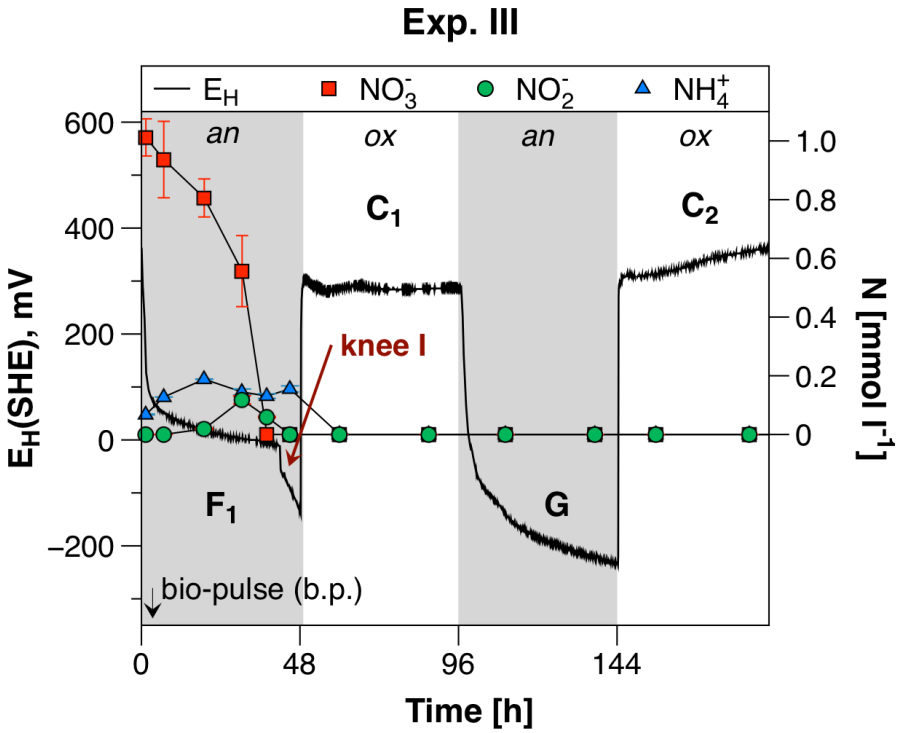

Figure 2-5. Scaled up time series of E_H (solid line) and concentrations of nitrate (squares), nitrite (circles), and ammonium (triangles) reproduced from Figure 2-2. Symbols correspond to results of duplicate measurements with 2σ uncertainty (within the symbol size unless indicated). The arrow "knee I" identifies breakpoint of E_H observed after depletion of nitrite. "C_1, C_2, F_1, G" refers to the E_H subzones reached during air (white areas) and N_2 (grey areas) sparging. "Bio-pulse" (b.p.) refers to the inoculation with bacteria *S. oneidensis* MR-1.

Table 2-5. Summary of practical recommendations to the use of Pt electrode.

Recommendation	Action	Reference
Correction for temperature with respect to the standard hydrogen electrode (SHE)	For example, at 20 °C the correction value of 211 mV should be added to the E_H value measured by the Pt electrode with an Ag|AgCl – 3 M KCl reference electrode. The correction value is calculated as the difference in the potentials of SHE (439 mV, tabulated) and the reference electrode (228 mV, tabulated) at a specific temperature.	(Appelo and Postma, 2005)
Test for the electrode accuracy against a standard solution	For example, at 20 °C the E_H value of ZoBell's standard solution measured by the Pt electrode (Ag|AgCl – 3 M KCl) is 250 mV. The correction of the measured value for SHE results in E_H(SHE) = 461 mV (250 mV + 211 mV), which is 18 mV higher than the tabulated E_H(SHE) of ZoBell's solution (443 mV). The difference between theoretical and practical potentials of ZoBell's solution is commonly accepted up to ±30 mV. The correction of measured E_H by addition/subtraction of observed difference (e.g, -18 mV in this example) is recommended.	(Schuring et al., 1999)
Monitoring of pH and E_H in situ	Measured E_H should be recorded along with pH under the same conditions. Further correction of E_H readings to the pH of interest should account for the actual ratio of H^+ to e^-, which is not necessarily equal to 1 (59 mV). Interference of the E_H signal due to proximity of the pH and E_H reference electrodes can be overcome by using a common reference electrode for both measurements.	(Becking et al., 1960; Hewitt, 1950)

Recommendation	Action	Reference
Electrode cleaning	A soft material (e.g., glass fibre, lapping pads) can be used to polish the Pt surface to erase the electrode "history" of Pt-oxides and prevent the drift of electrochemical potential.	(Aldous and Compton, 2011; Nordstrom et al., 1979)
Stabilization of sample flow velocity	In batch suspensions flow velocity can be controlled by adjusting the stirring speed, which should be recorded along with E_H data. In systems where flow velocity may not be easily controlled (e.g., measurements within rivers), the electrode surface should be shielded from changes to flow.	(Garske and Schock, 1986)
Addition of an inert electrolyte to water samples with low ionic strength less than 0.005 M	The addition of 9 mM NaCl to water sample improves electrode performance likely due to a combination of the decreased internal resistance and increased exchange current facilitated by the presence of chloride ions adsorbed at the Pt surface.	(Grundl and Macalady, 1989; Peiffer et al., 1992)

Table 2-6. Chemical concentrations, E_H, and pH measured at the last sampling point of the redox subzones (A-H) identified in Figure 2-2. LOD = limit of detection.

E_H zones	pH	E_H mV	O_2 mol l^{-1}	NO_3^- µmol l^{-1}	NO_2^- µmol l^{-1}	NH_4^+ µmol l^{-1}	$Fe^{2+}_{(aq)}$ µmol l^{-1}	ATP nmol l^{-1}
A_1	7.45	502	2.7×10^{-4}	–	–	–	–	–
A_2	7.49	501	2.7×10^{-4}	–	–	–	–	–
B_1	7.41	360	2.7×10^{-4}	991	<LOD	89	–	–
B_2	7.42	372	2.7×10^{-4}	929	<LOD	80	–	–
C_1	7.82	287	2.7×10^{-4}	<LOD	<LOD	<LOD	–	50.6
C_2	8.04	310	2.7×10^{-4}	<LOD	<LOD	<LOD	–	26.6
C_3	7.28	277	2.7×10^{-4}	818	31	250	<LOD	1.35
C_4	7.31	282	2.7×10^{-4}	481	285	260	<LOD	0.3
D_1	7.63	108	1×10^{-16}	–	–	–	–	–
D_2	7.64	118	1×10^{-16}	–	–	–	–	–
E_1	7.41	55	1×10^{-16}	991	<LOD	89	–	–
E_2	7.41	45	1×10^{-16}	932	<LOD	68	–	–
E_3	7.28	64	1×10^{-16}	922	23	192	<LOD	–
E_4	7.29	42	1×10^{-16}	765	75	201	<LOD	–
F_1	7.55	-10	1×10^{-16}	556	118	144	–	82.6
F_2	7.44	-5	1×10^{-16}	<LOD	30	866	<LOD	1.9
G	8.02	-230	1×10^{-16}	<LOD	<LOD	<LOD	–	46.7
H	7.55	-315	1×10^{-16}	<LOD	<LOD	157	98	5.2

*Oxygen concentrations were estimated assuming equilibrium with atmospheric air (A – C) and with N_2 gas (D – H).

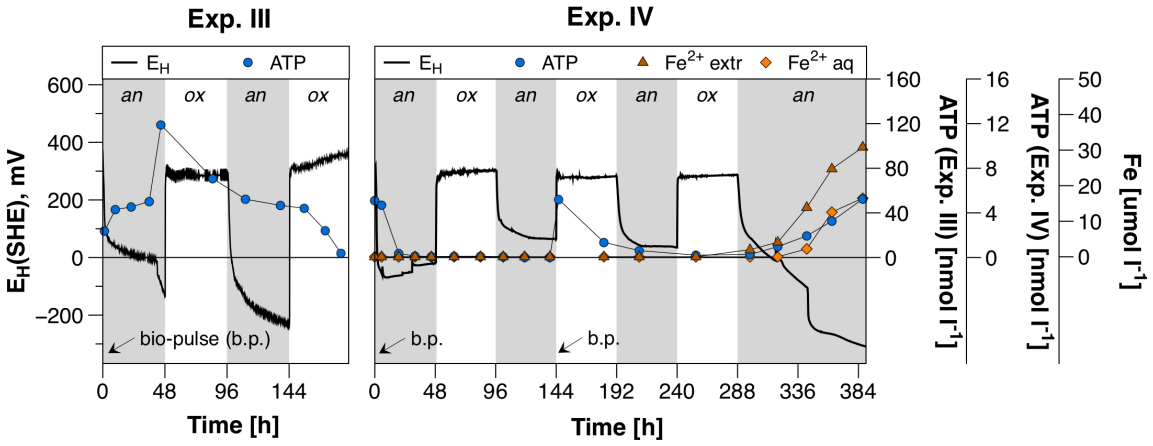

Figure 2-6. Time series of E_H, ATP, $Fe^{2+}_{(aq)}$, and $Fe^{2+}_{(s)}$ (HCl-extractable) concentrations in biotic AGW (Exp. III) and bacteria-goethite suspension (Exp. IV). ATP concentrations were an order of magnitude higher in Exp. III as compared to Exp. IV and are plotted on separate y-ordinates. "Bio-pulse" (b.p.) refers to the inoculation with bacteria *S. oneidensis* MR-1 in the beginning of both experiments (0 h) and at 144 h of Exp. IV. Time of Exp. IV was extended to 384 h by performing additional cycles of air (white areas) and N_2 (grey areas) sparging.

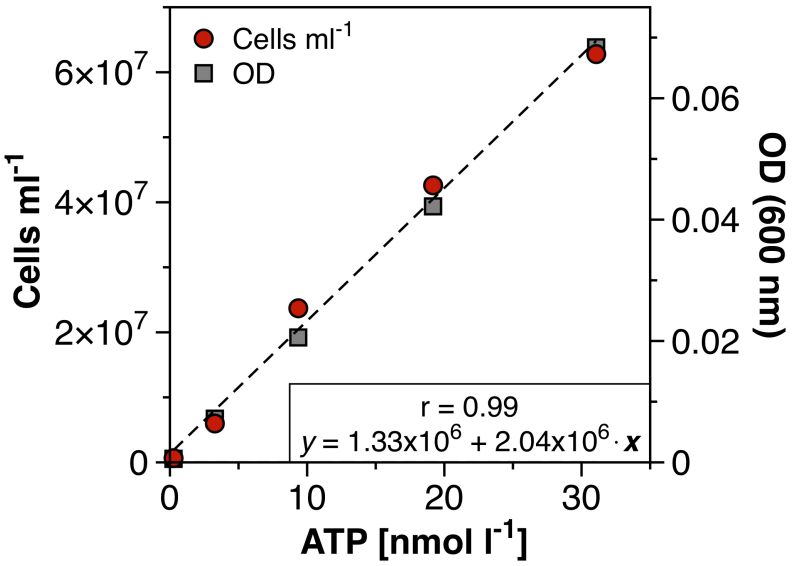

Figure 2-7. Calibration curve and correlation coefficient (r = 0.99) of ATP concentration (x) as a function of a cell number per 1 ml of solution (y) plotted against optical density (OD_{600}). Average concentration of ATP per a cell of *Shewanella oneidensis* MR-1 is $4.6\times0^{-10}\pm6.2\times10^{-11}$ nM cell^{-1}.

Chapter 3

Mobility of oxyanion contaminants (Cr, As, Sb) in argillaceous suspensions during oxic and anoxic cycles

3.1 Summary

Argillaceous formations are considered promising repositories for wastes containing inorganic contaminants. The sequestration capacity of an argillaceous natural barrier to contaminant migration may change because of environmental perturbations, such as, variable redox conditions and microbial activity. Here, we used a system of bioreactors to impose 7 successive week-long cycles of oxic and anoxic conditions on argillaceous suspensions amended with a mixture of oxidized arsenic (As), antimony (Sb), chromium (Cr), and nitrogen (N). We tested oxyanion mobility under sterile conditions, with the addition of labile organic carbon (ethanol), and with the addition of a soil microbial inoculum. Experimental results were reproduced in a numerical model providing a dataset of kinetic rate laws and equilibrium reaction parameters. Under sterile conditions, Cr(VI) was reduced to Cr(III), while As, Sb, and N remained oxidized in the solution. In contrast, when the indigenous microbial community was not inhibited, all elements underwent reduction regardless of the addition of ethanol. Inoculation with soil microorganisms increased contaminant reduction rates and altered the reduction mechanisms presumably from detoxification to respiration. The results suggest that when reduced via detoxification, contaminants do not obey thermodynamic driving force and are reduced simultaneously under aerobic and denitrifying conditions. In contrast, reduction via respiratory pathways mainly follows the sequence predicted by thermodynamics, with the exception of As and Sb reduction. The measured redox potential (E_H) oscillated between imposed oxic (+350±21 mV) and anoxic (+283±65 mV) conditions and did not respond quantitatively to the wide range of the redox transformations of the $HAsO_4^{2-}/H_3AsO_3$, $Sb(OH)_6^-/Sb_2O_3$, $CrO_4^{2-}/Cr(OH)_3$, and NO_3^-/NO_2^- couples. Despite relatively high E_H values, freshly reduced As(III), Sb(III), Cr(III), and N(III) were not re-oxidized during subsequent oxic periods. We hypothesize that the mineralogy and microbiota of the argillaceous sample did not catalyze contaminant re-oxidation processes resulting in irreversible contaminant reduction. Therefore, the argillaceous formation investigated stands out as a suitable environment for contaminant retention, as it can withstand periodic redox oscillations without releasing contaminants back to the aqueous phase.

3.2 Background

Argillaceous formations are being investigated as potential geological hosts for radioactive waste disposal (Grambow, 2016). Contaminant (e.g., As, Sb, Cr) mobility within such formations is a key issue for safety risk assessments of the prospective disposal sites (Altmann, 2008). Beneficial properties of argillaceous materials, such as low permeability and plasticity (Grambow, 2008), are considered in conjunction with uncertainties in chemical interaction with dissolved contaminants (Duro et al., 2014). In contrast to radionuclides, which are extensively studied in argillaceous systems (e.g., Claret et al., 2010; Wittebroodt et al., 2008), chemical mobility and reactivity of potentially toxic elements has been primarily investigated in near-surface environments rich of Fe oxyhydroxide minerals (Couture et al., 2015; Fawcett et al., 2015; Frohne et al., 2015; Lindsay et al., 2011).

In this chapter, I aimed to evaluate the sequestration capacity of a Tégulines argillaceous sample towards dissolved arsenic (As), antimony (Sb), and chromium (Cr) in the presence of nitrate (NO_3^-), which is a common component in leachate from waste backfill (Bertron et al., 2014). Similarly to other elements, which may be present in anionic forms, oxidized species of these contaminants are of concern due to their high mobility and low sorption affinity on typically negatively charged clay surfaces (Tournassat et al., 2007). At near-neutral pH, oxidized As, Sb, and Cr are expected to be present as oxyanions (primarily $HAsO_4^{2-}$, $Sb(OH)_6^-$, CrO_4^{2-}) and persist in the aqueous phase in the absence of positively charged Fe or Al minerals (Couture et al., 2013a; B. Manning and Goldberg, 1997).

Under reducing conditions, characteristic of subsurface disposal sites (Duro et al., 2014; Grambow, 2008), reduced uncharged species ($H_3AsO_3^0$, $Sb(OH)_3^0$, $Cr(OH)_3^0$) are potentially mobile within the argillaceous matrix (Vodyanitskii, 2010; Wilson et al., 2010). Moreover, contaminant fate is uncertain under redox-oscillating conditions, which are known to influence contaminant mobility in near-surface environments (Couture et al., 2015; Hockmann et al., 2014; Parsons et al., 2013a). Therefore, the sequestration capacity of argillaceous matrices must be evaluated under temporally variable redox conditions, which may be experienced in subsurface repositories due to thermal, hydrologic, and geochemical perturbations (Gascoyne, 1997).

High chemical heterogeneity of radioactive waste introduces a challenge to comparative estimates of the sequestration capacity towards a single element or a mixture of coexisting redox-sensitive elements. It is recognized that the biogeochemical cycles are more intricate when multiple contaminants coexist (Andrewes et al., 2000; Couture et al., 2015; Stucker et al., 2014). Therefore, effective remediation, in addition to assessment of environmental perturbations, requires comprehensive understanding of potential interplay between coexisting elements. The type of interaction is likely to vary according to environmental

conditions and may include both biotic and abiotic mechanisms. A direct competition for sorption sites and co-precipitation in the abiotic environment may be concurrent with microbial influences in natural systems (Pedersen, 1996).

The two main objectives of this research were to (1) quantify the potential effects of redox perturbations on the sequestration capacity of an argillaceous barrier material for oxyanions, and (2) examine the interdependence of the biogeochemical cycles of those coexisting elements. I present a series of batch experiments using argillaceous suspensions focusing on the effects of oxic *vs* anoxic and biotic *vs* abiotic conditions in a system of bioreactors. The role of additional labile organic C (ethanol) as a primary electron donor in the redox reactions is also evaluated.

I hypothesized that (1) successive oxic/anoxic conditions imposed to the argillaceous suspension would increase contaminant mobility, (2) microbial activity would decrease contaminant mobility, and (3) the coexistence of redox-sensitive species would be controlled by thermodynamics.

The approach chosen is to perform sequential experiments of increasing complexity while applying a comprehensive biogeochemical sampling and analysis protocol. Observed geochemical patterns were interpreted using kinetic and thermodynamic modelling of increasing complexity with parameter values determined and used unchanged from relatively simple to more complex models. I provide a diagnostic and prognostic tool for the quantitative simulation of biogeochemical processes driving contaminant mobility in argillaceous systems.

3.3 Materials and Methods

3.3.1 Argillaceous Sample, Synthetic Pore Water, and Contaminants

A sample of the Tégulines argillaceous sample was collected from the Gault formation in north-eastern France at 22.5 m depth and preserved under anaerobic conditions prior to use in experiments. For the characterization of the mineral composition of the argillaceous sample by powder X-ray diffraction (XRD), the sample dried undisturbed under an O_2-free atmosphere in a glove box (Jacomex BS 531, EP20Ra-nm purification, 100% N_2, < 1 ppm O_2). It was further ground by hand in the agate mortar to about 1-3 μm particle fractions and analyzed using a Bruker Axs D8 diffractometer. Results were obtained using a Cu-target X-ray tube analysing $K\alpha_{1+2}$ lines with a solXE detector. The X-ray diffraction patterns were treated by Rietveld refinement using BGMN software (Bergmann et al., 1998). Elemental composition was determined by inductively coupled plasma optical emission spectrometry (ICP-OES) (Varian 720 ES) after total acidic dissolution (HNO_3 + HF + H_3BO_3 + H_2O_2) (Cotten et al., 1995). Concentrations of reactive Fe, Mn, and Al present as amorphous oxides were estimated following citrate-

bicarbonate-dithionite (CBD) extraction (Jackson et al., 1986). Zeta-potential and the particle size distribution were analysed by laser granulometry (Malvern Instruments Zetasizer Nano).

Argillaceous sample was sieved through a 1 mm mesh, dispersed in synthetic pore water (50 g L^{-1}), and equilibrated, with agitation, for 7 days under anoxic conditions prior to oxyanion spikes. The synthetic pore water (Table 3-6) mimics the solution composition in contact with the host rock formation in the absence of oxygen (O_2) (Gaucher et al., 2009). The oxyanion mixture was prepared by dissolving high purity analytical compounds of $Na_2HAsO_4 \cdot 7H_2O$ (≥98%, SIGMA), $KSb(OH)_6$ (≥99%, Fluka), K_2CrO_4 (≥99%, SIGMA-ALDRICH), and $NH_4(NO_3)$ (≥99%, ROTH). Individual stock solutions of As, Cr, and N were combined and added to the pre-equilibrated experimental suspension, while Sb was spiked separately to prevent precipitation of $NaSb(OH)_6$ at high stock concentration of Na (Ilgen et al., 2014).

3.3.2 Experiments

Batch experiments were performed using a bioreactor system based on a design by Thompson et al. (2006). Briefly, each reactor contained a suspension volume of 1 L with a headspace of about 300 ml and was incubated in the dark (Parsons et al., 2013). Electrodes, mechanical agitation, and sampling ports were installed via the reactor head-plate and a water jacket ensured temperature control (25±1 °C). Solid polymer open junction pH and redox potential (E_H) electrodes (Mettler-Toledo Xerolyt Solid) were connected to field-effect transistor (FET) instrumental amplifiers with high input impedance. The E_H and pH data were recorded using an Agilent 34970A Data Logger every 2 minutes. Measured E_H was corrected for the reference electrode's standard voltage (+207 mV) relative to the standard hydrogen electrode (SHE) at 25°C and referred to a Ag/AgCl (3 M KCl), reference electrode.

Experimental time zero is the time of injection of the oxyanion mixture to a pre-equilibrated suspension under anoxic conditions. Redox oscillations were induced by alternate sparging of anoxic (1% CO_2 + 99% N_2) and oxic (1% CO_2 + 79% N_2 + 20% O_2) gas mixtures for periods of 7 days for a total experimental time of at least 7 weeks. Sampling was performed at regular intervals on the 1st, 2nd, 4th, and 7th day of each anoxic and oxic period using gas-tight sterile syringes. Suspensions were subsampled, immediately centrifuged, and filtered through 0.2 μm (cellulose hydrophilic membrane, Chromafil RC, ROTH) in the glove box. A part of the supernatant was flash frozen with liquid nitrogen and stored at -80 °C prior to aqueous speciation analysis. The rest of the supernatant was acidified with ultrapure HNO_3 to pH < 3 and stored at 4 °C for total aqueous concentration analysis.

Table 3-1. Design of batch experiments comprising Tégulines sample (50 g L^{-1}) dispersed in 1 L of synthetic pore water (Table 3-6) and a mixture of As(V), Sb(V), and Cr(VI).

Factors tested	Exp. I	Exp. II	Exp. III	Exp. IV
Mineralogy	+	+	+	+
Microbial presence and activity		+	+	+
Labile organic carbon addition			+	+
Microbial activity of enriched community				+

Each batch experiment included the argillaceous sample and synthetic pore water amended with the oxyanion mixture: 500 μM As(V), 500 μM Sb(V), 500 μM Cr(VI), and 500 μM N(V). Due to variability in assessing the solution volume in a continuously stirred suspension, final contaminant concentration values from the amendments varied by 10%. Actual spiked concentrations are provided in Table 3-10. In total four experiments were performed (Table 3-1): (I) a sterile control under abiotic conditions (sterilization of argillaceous sample at 121 °C and use of microbial inhibitors Na-azide, streptomycin, and kanamycin sulfates from Sigma-Aldrich); (II) an experiment with the argillaceous sample without additional treatment; (III) an experiment with additions of ethanol as a source of labile organic C and electrons (Wu et al., 2007); (IV) an experiment during which microbial diversity was boosted by adding a soil inoculum (See Appendix B), while still adding ethanol at the beginning each anoxic period. The quantity of ethanol (≥99.8%, SIGMA-ALDRICH) added at the beginning of each anoxic period was calculated based on the dissolved organic carbon concentration, to reach a total concentration of 20 mM. Soil inoculum has been extracted from the redox fluctuation zone. Previous characterization of the microbial ecology at this field site has demonstrated the presence of a broad diversity of aerobic and anaerobic bacteria (Parsons et al., 2013a). Details on the preparation and injection of soil inoculum are provided on page 80.

3.3.3 Analyses

All standards and reagents were of analytical grade and all solutions were prepared in Milli-Q water (resistivity of 18.2 MΩ cm^{-1}). Anion concentrations (NO_3^-, NO_2^-, SO_4^{2-}, Cl^-, and $C_2H_3O_2^-$) were determined by ion chromatography (Metrohm 761 Compact IC) and total aqueous concentrations of Na, K, Ca, Mn, Fe, S, As, Cr, Sb were measured by ICP-OES (Varian 720 ES). Hereafter, I refer to aqueous concentrations of those elements using square brackets. Certified multi-elemental solutions (Sigma-Aldrich) were used for quality control with measured concentrations within 10% of their certified values. Aqueous speciation of Cr was assessed using UV-Vis spectrophotometry at 272 and 373 nm (Rai et al.,

2007; Zydorczak et al., 2012). Speciation of aqueous Sb was measured by high performance liquid chromatography (HPLC) coupled to ICP-OES according to Lintschinger et al. (1997). Briefly, a Hamilton anion exchange column (PRP-X100, 4.1 9 150 mm, 10 mm) was used with a mobile phase of 20 mM EDTA (Fluka), 2 mM KHP (Sigma-Aldrich) (pH 4.3) at a flow rate of 1.5 ml min^{-1} for separation of Sb(V) and Sb(III) peaks. Aqueous speciation of As(V) and As(III) was performed using the same column and mobile phase of KH_2PO_4:K_2HPO_4 (Merck) at pH 6.25 prior to detection on ICP-OES (Roig-Navarro et al., 2001).

Dissolved organic C (DOC) and inorganic C (DIC) concentrations were determined on a carbon analyzer (Shimadzu TOC-Vcsn). Further characterization of DOC was performed by measurement of the raw absorbance at 254 nm using a UV-vis spectrophotometer (Agilent 8453E UV-Visible). The SUVA (specific UV absorbance) was calculated by dividing absorbance at 254 nm by DOC concentration (Cory and McKnight, 2005).

Solid-phase concentrations of oxidized As, Sb, and Cr were determined on samples collected on the last day of each experiment. The samples were analyzed by ICP-OES after leaching with 0.1 M Na_2CO_3 solution (Panichev et al., 2005), using a method that has been previously applied to extract other oxidized oxyanions (e.g., V(V) and U(VI)) (Liger et al., 1999; Mampuru et al., 2015). Concentrations of reduced As, Sb, and Cr species were estimated by difference between total concentrations and those of extractable oxidized species (Panichev et al., 2005).

Microbial activity was estimated using adenosine triphosphate (ATP) concentration as a proxy (Hammes et al., 2010; Karl, 1980). ATP concentration was determined by measuring luminescence levels (Lumat LB 9507 Berthold Technologies) after application of a BacTiter-Glo Microbial Cell Viability Assay kit (Promega).

3.3.4 Biogeochemical Modelling

Biogeochemical modelling was performed to identify key geochemical processes and limiting factors by reproducing observed aqueous and solid contaminant concentration and speciation as a function of time. Argillaceous suspensions investigated in the bioreactor experiments are complex systems comprising a heterogeneous mineral matrix, a mixture of dissolved contaminants (As, Sb, Cr), native (argillaceous) and foreign (soil-extracted) microbial communities, as well as, added organic carbon (ethanol). To maintain the simplicity of the models while describing the observations, an increasing complexity approach was applied was used in modelling. That is, derived parameter values from the first, simple experiments, were fixed and used unchanged in the models for the complex ones. Thus, the model of every consecutive

experiment was entirely based on the model of the previous experiment, supplemented by one additional reaction only.

Contaminant fate in the least complex experiment (Exp. I) was quantitatively assessed by fitting the multi-reaction model (Zhang and Selim, 2005) to the time series of As, Sb, and Cr concentrations. This model was initially created as an extended version of the equilibrium Freundlich approach to account for time-dependent sorption of contaminants on heterogeneous mineral matrix (Selim and Zhang, 2013). Furthermore, competitive effects are incorporated with each model reaction when multiple contaminants coexist in the suspension. This model (Figure 3-1, A) was chosen to describe As, Sb, and Cr sequestration by the argillaceous mineral matrix in this study.

Models were run for each contaminant and parameter values of reversible equilibrium sorption (K_{eq}), adsorption (k_f), desorption (k_b), and irreversible sorption (k_i) implicitly accounted for the presence of competing ions (i.e., $HAsO_4^{2-}$, $Sb(OH)_6^-$, CrO_4^{2-}, HCO_3^-, SO_4^{2-}). However, derived values are site-relevant for suspension density (50 g L^{-1}), contaminant concentration (500 μM), pH (7.1±0.1), ionic strength (0.05 M), temperature (25 °C), and reaction time (~ 50 days) of the experiments.

The numerical solution of the multi-reaction model was obtianed by solving a set of nonlinear equations in PHREEQC v.3.1.7 (Parkhurst and Appelo, 2013) (see code on page 150). The WATEQ4F database was used as a starting point, which was augmented with the additional constants selected from literature (Table 3-11). To my knowledge, this is the first time that the reaction scheme of Zhang and Selim (2005) is implemented in PHREEQC. This allowed to improve the model by accounting for solid-solution interactions defined in WATEQ4F database. An optimization algorithm was implemented in Python (see code on page 146). The scipy.optimize package (Jones et al., 2001) was used to minimize the root-mean-square error (RMSE) and select the subset of parameters yielding the best fit between the model and the data.

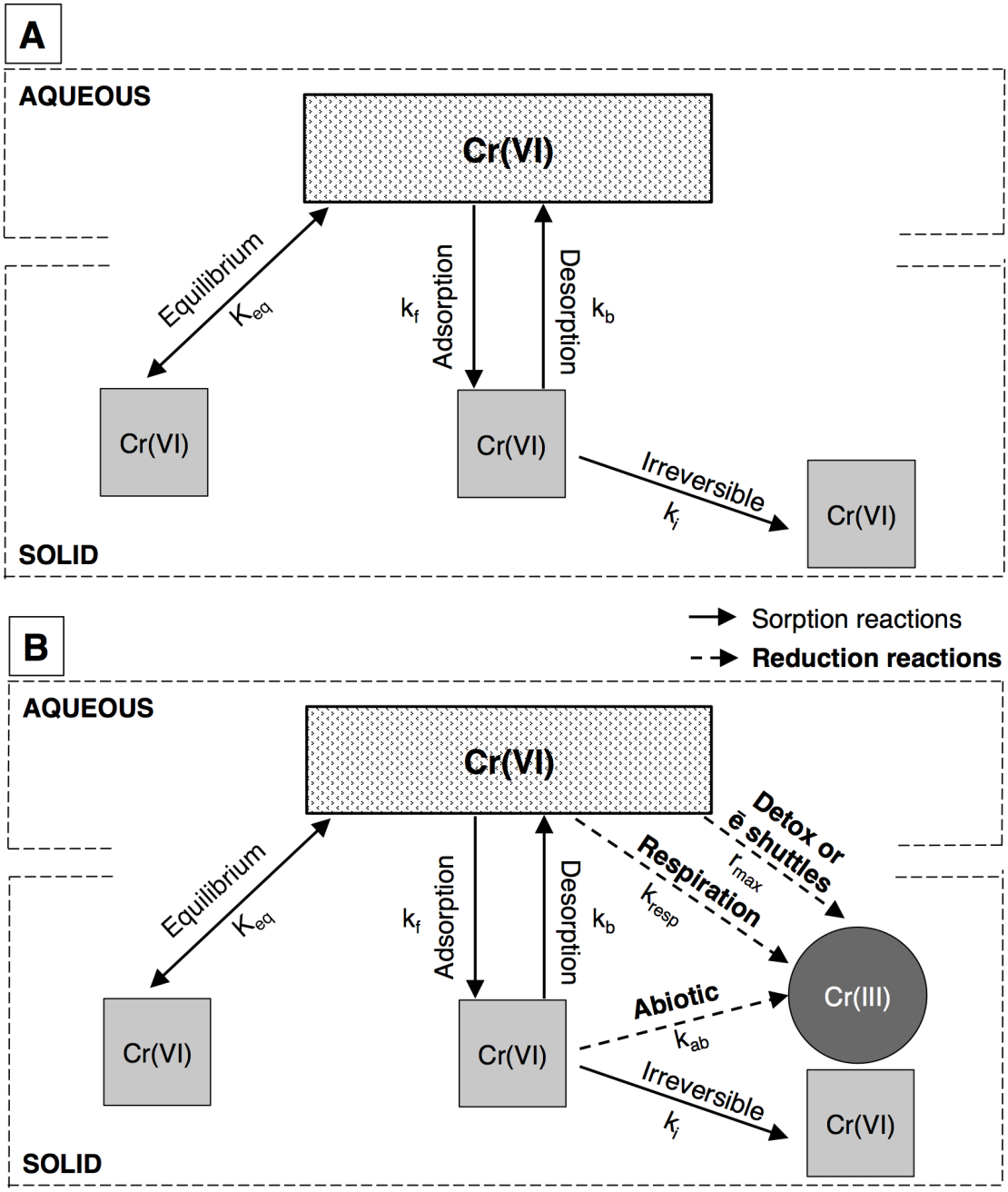

Figure 3-1. Conceptual models used to describe contaminant (e.g., Cr) mobility via redistribution of contaminant mass between aqueous and solid phases. The multi-reaction model of Zhang and Selim (2005) (A) is enhanced by reaction rates of contaminant reduction (B) built step by step upon the increasing complexity of experiments, where, K_{eq} is an equilibrium constant, k_f – rate constant of adsorption, k_b – rate constant of desorption, k_i – rate constant of irreversible sorption, k_{ab} – rate constant of abiotic reduction, k_{resp} – rate constant of microbial contaminant respiration, r_{max} – maximum rate of microbial contaminant reduction via detoxification or microbially produced soluble reductants.

Ordinary differential equations (ODEs) of kinetic rate laws used in the model of Exp. I for Cr, As, and Sb are the following (rate formulations are given in Table 3-4):

Chromium

$$\frac{d\mathrm{CrO_4^{2-}}}{dt} = -\mathrm{R_f^7} + \mathrm{R_b^8} \quad \text{Eq. 3-1}$$

$$\frac{d{\equiv}\mathrm{SOH_2^+CrO_4^{2-}}}{dt} = \mathrm{R_f^7} - \mathrm{R_b^8} - \mathrm{R_i^9} - \mathrm{R_{ab}^{10}} \quad \text{Eq. 3-2}$$

$$\frac{d(\equiv\mathrm{SOH_2^+CrO_4^{2-}})_i}{dt} = \mathrm{R_i^9} \quad \text{Eq. 3-3}$$

$$\frac{d\mathrm{Cr(OH)_{3(s)}}}{dt} = \mathrm{R_{ab}^{10}} \quad \text{Eq. 3-4}$$

Arsenic

$$\frac{d\mathrm{HAsO_4^{2-}}}{dt} = -\mathrm{R_f^{15}} + \mathrm{R_b^{16}} \quad \text{Eq. 3-5}$$

$$\frac{d{\equiv}\mathrm{SOHAsO_4}}{dt} = \mathrm{R_f^{15}} - \mathrm{R_b^{16}} - \mathrm{R_i^{17}} \quad \text{Eq. 3-6}$$

$$\frac{d(\equiv\mathrm{SOHAsO_4})_i}{dt} = \mathrm{R_i^{17}} \quad \text{Eq. 3-7}$$

Antimony

$$\frac{d\mathrm{Sb(OH)_6^-}}{dt} = -\mathrm{R_f^{26}} + \mathrm{R_b^{27}} \quad \text{Eq. 3-8}$$

$$\frac{d(\equiv\mathrm{SO})_2\mathrm{Sb(OH)_4^-}}{dt} = \mathrm{R_f^{26}} - \mathrm{R_b^{27}} - \mathrm{R_i^{28}} \quad \text{Eq. 3-9}$$

$$\frac{d((\equiv\mathrm{SO})_2\mathrm{Sb(OH)_4^-})_i}{dt} = \mathrm{R_i^{28}} \quad \text{Eq. 3-10}$$

The more complex contaminant behavior of Exp. II, compared to Exp. I, was modelled by the calibration of additional parameter values to account for microbial contaminant reductions via detoxification or oxidation of microbially produced soluble reductants. Because contaminant reduction involved a microbial step, the rates were formulated based on the modified Monod kinetics (e.g., Van Cappellen and Wang, 1996). Assuming a pseudo steadystate of microbial activity and unlimited supply of intracellular reductants, the rate of contaminant detoxification is expressed as (e.g., Cr):

$$\mathrm{R_{detox}^{11}} = \mathrm{r_{max}^{CrO_4^{2-}}} \cdot \left(\frac{[\mathrm{CrO_4^{2-}}]}{\mathrm{K_{m\,(detox)}^{CrO_4^{2-}}} + [\mathrm{CrO_4^{2-}}]} \right) \quad \text{Eq. 3-11}$$

where, r_{max} is the maximum rate of contaminant reduction, and K_m is a half saturation constant. Sorption and reduction reactions were assumed to occur in parallel. The model of Exp. III was identical to that of Exp. II with fixed parameter values between the experiments.

Finally, the last and most complex Exp. IV was modelled by adding rates of microbial contaminant reduction via respiration. A full conceptual model is presented in Figure 3-1 (B). In contrast to contaminant reduction via detoxification, microbial respiration was inhibited by the presence of alternative electron acceptors (e.g., O_2) and dependent on the concentration of extracellular organic carbon (e.g., acetate). Therefore, the rate of contaminant respiration is formulated as (e.g., Cr):

$$R_{resp}^{12} = k_{resp}^{CrO_4^{2-}} \cdot [CH_3COO^-] \cdot \left(\frac{[CrO_4^{2-}]}{K_{m\,(resp)}^{CrO_4^{2-}} + [CrO_4^{2-}]} \right) \left(\frac{K_{in}^{O_2}}{K_{in}^{O_2} + [O_2]} \right) \quad \text{Eq. 3-12}$$

where, k_{resp} is a rate constant of contaminant respiration, $[CH_3COO^-]$ – limited concentration of acetate (small compared to K_m of acetate), K_{in} – inhibition constant of O_2, which represents critical concentration above which O_2 increasingly suppresses the reaction. The models simulated cycles of oxic and anoxic conditions by alternating the equilibrium headspace composition controlled by $O_{2(g)}$ (0.2 atm) and $CO_{2(g)}$ (0.01 atm), respectively. Equilibrium with pCO_2 and calcite was imposed to maintain constant pH. The ODEs used in the model of Exp. IV for Cr, As, and Sb are the following:

Chromium: Eq. 3-2, 3-3 and additional equations

$$\frac{d\mathrm{CrO_4^{2-}}}{dt} = -R_f^7 + R_b^8 - R_{detox}^{11} - 2.66\, R_{resp}^{12} \quad \text{Eq. 3-13}$$

$$\frac{d\mathrm{Cr(OH)_{3(s)}}}{dt} = R_{ab}^{10} + R_{detox}^{11} + 2.66\, R_{resp}^{12} \quad \text{Eq. 3-14}$$

Arsenic: Eq. 3-6, 3-7 and additional equations

$$\frac{d\mathrm{HAsO_4^{2-}}}{dt} = -R_f^{15} + R_b^{16} - R_{detox}^{18} - 4\, R_{resp}^{19} \quad \text{Eq. 3-15}$$

$$\frac{d\mathrm{H_3AsO_3}}{dt} = -R_f^{21} + R_b^{22} + R_{detox}^{18} + 4\, R_{resp}^{19} - R_{methyl}^{24} \quad \text{Eq. 3-16}$$

$$\frac{d{\equiv}\mathrm{S_2HAsO_3}}{dt} = R_f^{21} - R_b^{22} - R_i^{23} \quad \text{Eq. 3-17}$$

$$\frac{d(\equiv \mathrm{S_2HAsO_3})_i}{dt} = R_i^{23} \quad \text{Eq. 3-18}$$

$$\frac{d{\equiv}\mathrm{S_2HAsO_3}}{dt} = R_{methyl}^{24} \quad \text{Eq. 3-19}$$

Antimony: Eq. 3-9, 3-10 and additional equations

$$\frac{d\mathrm{Sb(OH)_6^-}}{dt} = -\mathrm{R_f^{26}} + \mathrm{R_b^{27}} - 2\,\mathrm{R_{resp}^{30}} \quad \text{Eq. 3-20}$$

$$\frac{d(\equiv\mathrm{SO})_2\mathrm{Sb(OH)_4^-}}{dt} = \mathrm{R_f^{26}} - \mathrm{R_b^{27}} - \mathrm{R_i^{28}} - \mathrm{R_{detox}^{29}} \quad \text{Eq. 3-21}$$

$$\frac{d\mathrm{Sb_2O_{3(s)}}}{dt} = \mathrm{R_{detox}^{29}} + 2\,\mathrm{R_{resp}^{30}} \quad \text{Eq. 3-22}$$

A global sensitivity analysis was performed to ascertain how predictive model depends on parameters values via Fourier Amplitude Sensitivity Test (FAST) (Saltelli et al., 1999) by using an open source Python library SALib ("SALib – the open source Python library for sensitivity analysis https://github.com/SALib/SALib," n.d.) (see code on page 147). The sensitivity of the predicted aqueous concentrations to parameters values was analyzed by varying parameters one at a time ("First") and by accounting for the sum of the interaction effects ("Total"). The respective sensitivity indices were estimated by running the model with a distribution of parameters within a range spanning four orders of magnitude.

3.4 Results

3.4.1 Argillaceous Sample

Mineralogical composition of a Tégulines argillaceous sample (Table 3-5) was dominated by clay minerals (muscovite, smectite, kaolinite, biotite, chlorite, microcline) (56%), quartz (29%), calcite (12%) and contained minor amounts (< 2%) of gypsum, pyrite, and anatase. The sample was depleted in Fe-, Mn- and Al- oxide minerals (CDB extract), comprising less than 0.2% of argillaceous dry weight (d.w.) (Table 3-7). The major cations (Table 3-7) indicated typical clay composition: SiO_2 (56%), Al_2O_3 (14%), CaO (8%), Fe_2O_3 (5%), K_2O (2%), MgO (1%).

3.4.2 Redox Potential (E_H) and pH Conditions

Imposed redox oscillations resulted in reproducible fluctuations of E_H along cycles, which remained above +200 mV throughout the experiments (Figure 3-2). The E_H of the sterile control (Exp. I) oscillated between +368±8 and +338±10 mV under oxic and anoxic conditions, respectively. The E_H profiles were similar in Exp. II and Exp. III with anoxic and oxic variations from +345±5 to +338±10 mV, respectively. The E_H in Exp. IV ranged from +342±4 (oxic) to +245±15 (anoxic) mV. Overall, E_H values were lower with each new factor along the increasing complexity sequence depicted in Table 3-1. The pH remained stable at near-neutral values (pH 7±0.2) throughout all experiments (Figure 3-2).

3.4.3 Microbial Activity

ATP concentrations were either low or absent in Exp. I (Figure 3-2 (a)). When trace concentrations of ATP were detected (< 0.3 nM) on days 17 and 35, additional injections of inhibitors were performed. In Exp. II-IV, pre-equilibration of the experimental suspension for 7 days before oxyanion additions resulted in an ATP increase to 0.3±0.05 nM. It further increased and stabilized at 0.7 nM during the first 19 days of Exp. II, then decreased to 0.1 nM and remained at this level (Figure 3-2 (b)). In Exp. III, ATP remained at about 0.25 nM from the first ethanol addition to ~30 days, then gradually increased to reach 1.24 nM by the end of the experiment (Figure 3-2 (c)). In Exp. IV, the addition of soil inoculum resulted in the highest initial ATP concentration of 1.3 nM followed by a progressive increase over time (Figure 3-2 (d)). Interestingly, in Exp. IV, ATP concentration was the highest (5.0 nM) during anoxic periods and the lowest (2.0 nM) in the presence of O_2.

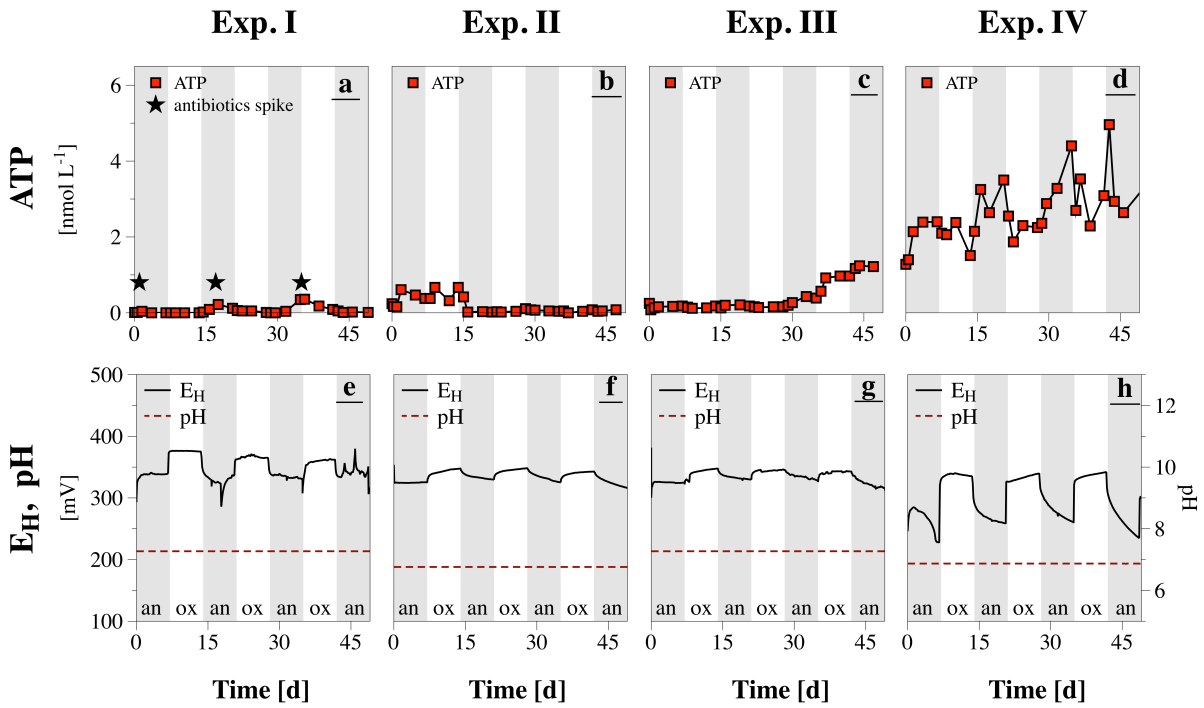

Figure 3-2. Time series of ATP concentrations (squares connected by lines), redox potential (E_H) (solid line), and pH (dashed line) values. Antibiotics spikes are indicated by stars, whereas shaded and white areas indicate anoxic (CO_2 + N_2) and oxic (O_2 + CO_2 + N_2) periods, respectively.

3.4.4 Dissolved Organic and Inorganic Carbon

During the pre-equilibration period 0.41±0.04 mM (0.1 mg g^{-1} solid) of DOC was released from the argillaceous sample to the solution in all experiments. The low absorbance (UVA_{254}=0.2, SUVA=0.04) of DOC suggests a primarily aliphatic structure. Further, DOC accumulated in solution to a level of 47.8 and 42.7 mM in Exp. I and Exp. II, respectively (Figure 3-3 (e-f)). During experiments with ethanol additions we observed a step-wise increase in total DOC concentration up to 54.3 mM (Exp. III) and 56.5 mM (Exp. IV), with C-acetate accounting for 10 and 15 mM, of final DOC concentrations, respectively. In Exp. IV, 3.6 mM C-acetate was initially present due to addition of the soil inoculum. It became depleted to 0.5 mM during first 15 days, i.e. during the first full anoxic-oxic cycle and accumulated in solution up to 14.5 mM during the rest of the experiment. The decrease in C-acetate concentration was coincident with the increase of DIC concentration from 4 to 7 mM by day 15. Concentration of DIC remained stable at the level of 4.05 ± 0.5 mM in all other experiments (Figure 3-3).

3.4.5 Bulk Water Chemistry and Contaminant Dynamics

Concentration of dissolved Ca increased from 3 to 6 mM in all experiments over 49 days (Figure 3-8 (d)) driven likely by calcite dissolution as supported by negative saturation index calculated using PHREEQC code with $pCO_2 = 10^{-2}$ atm ($SI_{calcite}$ = -0.33). Aqueous S was always present as 5.6 mM SO_4^{2-} in Exp. II, Exp. III, and Exp. IV (Figure 3-8 (b)). Sulfur concentrations higher than 5.6 mM in Exp. I were due to the addition of SO_4^{2-} as a counter anion in the antibiotics (streptomycin- and kanamycin-sulfate). Initial aqueous concentration of Mn was about 0.5 – 0.9 μM. This remained constant in Exp. I and Exp. II, and increased to 2.7 and 5.7 μM by the end of Exp. III and Exp.IV, respectively (Figure 3-8 (c)). Concentration of total Fe was generally ~3 μM, which is below the detection limit of the Fe(II) method (4 μM) (Figure 3-8 (a)). Finally, K^+ and Cl^- accumulated in solution at a constant rate (a linear regression of concentration *vs* time yields r = 0.99), indicative of electrode leakage (Figure 3-8 (f)).

In Exp. I, oscillating oxic and anoxic conditions did not affect the rates of oxyanion sequestration. Total [As] continuously decreased from 460 to 159 μM, [Sb] from 528 to 352 μM, and [Cr] from 560 to 235 μM (Figure 3-3 (a)). Over the course of the experiment, twice as much As and Cr was removed from the solution compared to Sb. [NO_3^-] remained at 488 ± 11 μM throughout the experiment. Speciation analyses indicate that aqueous As, Sb, and Cr remained in their initial oxidized states (Figure 3-10) and that NO_3^- was not reduced under anoxic conditions. Solid-phase As and Sb speciation suggests that both elements were sequestrated in their oxidized forms. In contrast, 90% of Cr was immobilized reduced Cr(III) (Figure 3-9).

In Exp. II, [As] steadily decreased from 460 to 105 μM during the first 30 days and increased only slightly afterwards to 135 μM (Figure 3-3 (b)). The decrease of [As] was coincident with removal of As(V) from solution and the appearance of As(III) (Figure 3-10). Targeted extractions suggest that 83% of sequestered As in the solid-phase was present as As(V) and 17% as As(III) by day 49 (Figure 3-9). Slightly more aqueous Sb was removed in Exp. II than in Exp. I. This is consistent with greater solid phase accumulation of Sb in Exp. II, of which 20% occurred as Sb(III). [Cr] decreased below the detection limit (0.05 μM) by day 49 with concurrent accumulation in the solid phase as Cr(III) (> 98%). Finally, $[NO_3^-]$ decreased during anoxic periods from 520 to 390 μM, yielding to 20 μM of $[NO_2^-]$ during the experiment (Figure 3-3 (b)), although the latter did not persist in solution.

In Exp. III, aqueous As, Sb, and Cr were sequestered as in Exp. II, although at an apparent faster rate. [As] decreased from 460 to 110 μM over 26 days (Figure 3-3 (c)), concomitant with complete reduction of As(V) to As(III) (Figure 3-10), and As(III) accumulation in the solid-phase (~15%) by the end of the experiment. [Sb], again, was sequestered to a lesser extent than other contaminants and remained in solution entirely as Sb(V), though with a solid-phase fraction of Sb(III) (~15%). [Cr] behaved as in Exp. II, but in Exp. III [Cr] depletion below 40 μM appeared to trigger $[NO_3^-]$ removal and subsequent $[NO_2^-]$ accumulation up to 395 μM.

It is in Exp. IV that the contaminants were sequestered to the greatest extent with the rates affected by oscillating oxic and anoxic conditions (Figure 3-3 (d)). Decreases in [As] were only observed under anoxic conditions, whereby all remaining aqueous As was under the form of As(III). Complete As(V) removal from solution appeared to trigger Sb(V) removal. After day 15 upon the depletion of As(V), [Sb] decreased at twice the initial rate. By the end of the experiment, only Sb(V) was detected in the aqueous phase, while both oxidized and reduced Sb species were measured, in a 4:1 ratio, in the solid-phase. [Cr] and $[NO_3^-]$ were both completely removed much earlier than in Exp. III, reaching undetectable concentrations during the 1st anoxic period.

Overall, solid-phase species of As(V), Sb(V), and Cr(III) comprised >75% of their total solid elements concentrations. Mass balance indicates that As, Sb and Cr were quantitatively accumulated (within a 10%) in the solid phase by the end of all experiments, with the exception of Sb in Exp. IV, for which 20% appears to be missing from the solid-phase.

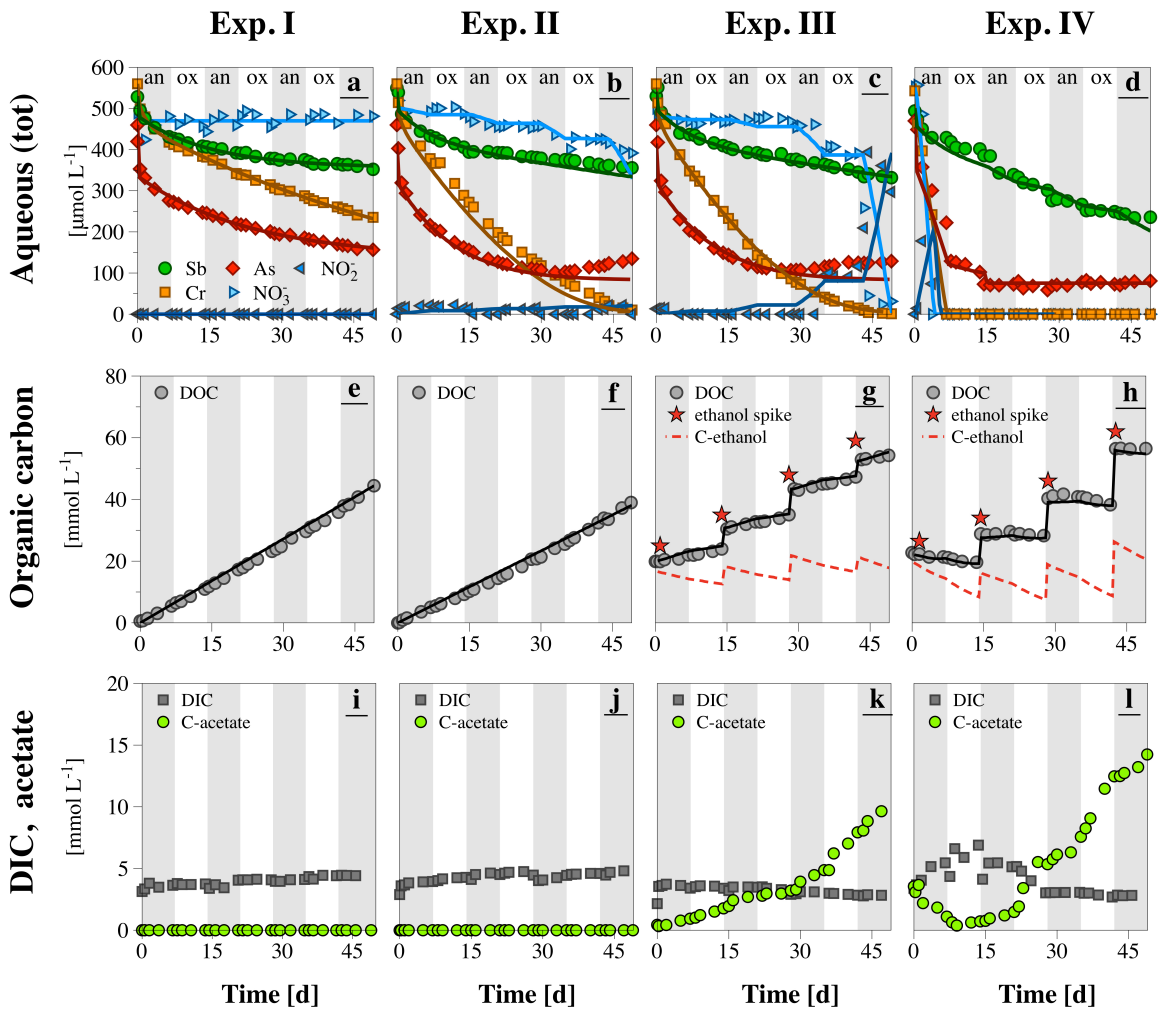

Figure 3-3. Time series of modelled (line) and measured [As] (diamonds), [Sb] (circle), [Cr] (square), [NO_3^-] (right-pointing triangle), [NO_2^-] (left-pointing triangle) (a-d); modelled (line) and measured (circle) DOC concentration along with the estimated ethanol concentration (dashed line) (e-h); and measured DIC (square) and acetate-C concentrations (circle) (i-l). Shaded and white areas indicate anoxic ($CO_2 + N_2$) and oxic ($O_2 + CO_2 + N_2$) periods, respectively.

3.5 Discussion

3.5.1 Experimental Artifacts

We observed leakages of K^+ and Cl^- from the pH and E_H electrodes as well as linear increase of DOC over time (Figure 3-3 (e-f)) in experiments where DOC was otherwise not manually added. Investigation revealed that the source of the increasing DOC was likely a leakage from the polymers in the electrodes, as has been previously observed (Wersin et al., 2011). Absorbance measurements indicated that leaked

DOC was aliphatic (UVA_{254}=0.01, SUVA=0.0002), consistent with glycerol (propane-1,2,3-triol) which is commonly used in Mettler-Toledo electrodes. The DOC leakage rate of 350±100 μM day^{-1} from a single electrode observed here is similar to the rate of 300 μM day^{-1} reported by De Cannière et al. (2011). Significant correlation between leaked DOC and Cl^- throughout Exp. I-II (Figure 3-8 (f)) suggests that the DOC was not labile, was not consumed or degraded.

3.5.2 Redox Conditions of the Argillaceous Suspension

Sparging of the solution with a mixture of oxic and anoxic gases resulted in reproducible E_H oscillations (Figure 3-2). In general, measured E_H of the argillaceous suspensions during anoxic periods appears to be higher than the Nernst equation predicts for the experimental conditions based on the redox couples: $CrO_4^{2-}/Cr(OH)_3$, $HAsO_4^{2-}/H_3AsO_3$, $Sb(OH)_6^-/Sb_2O_3$, and NO_3^-/NO_2^- (Table 3-3). Even though the activity ratios of the redox couples imply a range of redox conditions, from oxidizing (Exp. I) to reducing (Exp. II, III, IV), the measured E_H did not respond quantitatively to these conditions and remained above +200 mV throughout the experiments. Therefore, the measurement of E_H should not be taken as an indicator of Cr, As, Sb, and N redox processes. Overall, our results suggest that E_H measurements may not be particularly informative in environments depleted in electroactive redox couples (e.g., Fe couples), such as the argillaceous formations.

3.5.3 Abiotic Sequestration of As, Sb, and Cr

The ratio of the quantity of the contaminant adsorbed per unit mass of solid to the quantity of the contaminant remaining in solution at equilibrium can be characterized by calculation of the partition (distribution) coefficient (Kd):

$$K_d = \frac{C_0 - C_{eq}}{C_{eq}} \times \frac{V}{m} \qquad \text{Eq. 3-23}$$

where, C_0 – initial aqueous contaminant concentration (mol L^{-1}); C_{eq} – aqueous contaminant concentration in equilibrium with the sorbent (mol L^{-1}); m – mass of the sorbent (kg); V – solution volume (L).

Even though thermodynamic equilibrium was not achieved within the experimental time scale (49 days), we used the model to estimate concentrations at equilibrium and thus Kd values in abiotic Exp. I. Results suggest that equilibrium would be reached after 72 days for Sb(V) (Kd = 9.78 L kg^{-1}) after 113 days for As(V) (Kd = 46.72 L kg^{-1}), and after 400 days for Cr(VI) (Kd = 11108 L kg^{-1}) (Table 3-2). As expected, derived Kd values of As and Sb are lower than those for the pure clay phases reported in the literature likely due to the lower content of pure clay phases in the heterogeneous argillaceous matrix. At

near-neutral pH, the Kd values of Sb(V) in kaolinite suspension are estimated to vary from 73 to 115 L kg^{-1} according to the experimental data of Rakshit et al. (2015). This Kd range is comparable with the Kd value (9.78 L kg^{-1}) calculated for Sb(V) in the present subsoil suspension, considering ten times lower kaolinite fraction in the argillaceous sample (11% d.w.). The Kd value (46.72 L kg^{-1}) of As(V) falls in the range of sorption capacity of muscovite (15% d.w.) from 282 to 416 L kg^{-1} at neutral pH, as estimated from the experiments with pure muscovite (Chakraborty et al., 2007). The Kd value of Cr is higher than that of As and Sb driven by reductive precipitation and complete removal of Cr from the solution. Oscillating oxic and anoxic conditions did not affect the sequestration behavior of any contaminant.

Table 3-2. Partition (or distribution) coefficient (Kd), equilibrium constant (log K), forward (k_f), backward (k_b), and irreversible (k_i) rate constants for As(V), As(III), Sb(V), and Cr(VI) sorption obtained by fitting experimental data to the multi-reaction model.

Sorbate	Kd (L kg^{-1})	Log K	k_f (h^{-1})	k_b (h^{-1})	k_i (h^{-1})	RMSE
As(V)	47	-0.542	3.0×10^{-3}	5.8×10^{-3}	2.3×10^{-3}	1.55
As(III)	-	-0.381	1.7×10^{-5}	4.8×10^{-2}	2.7×10^{-3}	-
Sb(V)	10	-1.075	1.1×10^{-3}	4.2×10^{-3}	6.7×10^{-4}	3.01
Cr(VI)	11 110	-1.027	4.0×10^{-3}	3.8×10^{-2}	0.0	6.54

Arsenic abiotic sequestration. Similar to As(V) sequestration by pure mineral phases (Couture et al., 2013a) and natural soils (Zhang and Selim, 2005), a two-phase sorption with an initial rapid uptake followed by a slow kinetic immobilization is modelled in Exp. I (Figure 3-4 (a)). Instantaneous removal of 30% aqueous As(V), likely via the formation of outer-sphere complexes, corresponds to equilibrium sorption with log K = -0.542 (Table 3-2). Whereas, a slow reversible uptake, presumably through the formation of inner-sphere complexes, is represented by adsorption (k_f) and desorption (k_b) rate constants. Derived k_f and k_b for As(V) in the argillaceous suspension in this study are up to 3 orders of magnitude lower than those estimated for As(V) sorption on Fe-bearing minerals (2-line ferrihydrite, goethite, amorphous mackinawite, pyrite) (Couture et al., 2013a) and natural soils containing 5.7±2 mg g^{-1} of amorphous Fe (Oliver loam, Sharkey clay, Windsor sand) (Zhang and Selim, 2005).

Clays offer a variety of sites suitable for As(V) sorption, which can occur onto: (1) broken clay edges via surface ligand exchange (Charlet et al., 2012; Lin and Puls, 2000; Wilson et al., 2010), (2) negatively charged clay surfaces (e.g., kaolinite) at neutral pH via cation (e.g., Ca^{2+}) bridging (Sharma and Kappler, 2011), and (3) a hydroxide interlayer in the clay structure of chlorite (Lin and Puls, 2000). These mechanisms are likely given the presence of kaolinite (11% d.w.) and chlorite (3.9% d.w.), the pH of 7.3

and high [Ca] concentrations (4 mM). Sorption onto calcite (12% d.w.) would occur at similar carbon dioxide pressure ($pCO_2=10^{-3.5}$ atm) but would require a higher pH (>8.3) (Sø et al., 2008).

Finally, we estimate slow As(V) removal via irreversible kinetic uptake representing intra- or interparticle diffusion (Zhang and Stanforth, 2005) or the formation of surface precipitates (Gallegos et al., 2007). For example, As is known to form Ca-arsenate precipitates (Raposo et al., 2004). The experimental solution was oversaturated with respect to several Ca-phases: $CaNaAsO_4$ (SI = 0.2), $CaHAsO_4$ (SI = 3.0), $Ca_3(AsO_4)_2(H_2O)_4$ (SI = 6.1), $Mg_3(AsO_4)_2$ (SI = 6.2) and $Ca_3(AsO_4)_2$ (SI = 6.3), suggesting that such reactions were thermodynamically favourable based on initial [As] concentration.

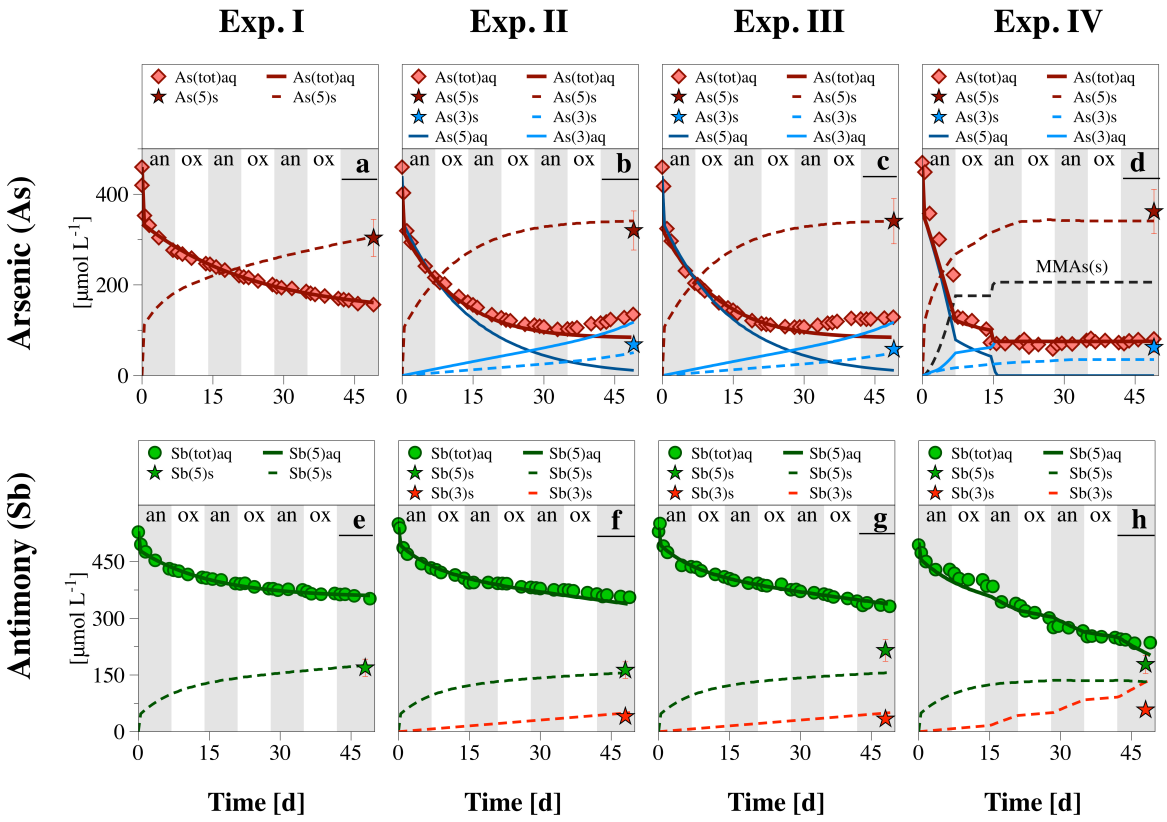

Figure 3-4. Time series of measured (symbols) and modelled aqueous (solid lines) and solid (dashed lines) speciation of As (a-d) and Sb (e-h). Kinetic and equilibrium formulations and parameters use in the model are presented in Table 3-2 and Table 3-4. Shaded and white areas indicate anoxic ($CO_2 + N_2$) and oxic ($O_2 + CO_2 + N_2$) periods, respectively.

Antimony abiotic sequestration. In contrast to As(V), sequestration of Sb(V) was mainly kinetically-controlled with equilibrium uptake accounting for only 5% of total Sb sequestration (log K = -1.075) (Table 3-2). This is consistent with recent results suggesting low Sb(V) sorption on clay minerals

(i.e., kaolinite) at neutral pH (Rakshit et al., 2015). Although estimated rate constants of Sb(V) adsorption and desorption are lower, they are still on the same order of magnitude as those of As(V). The fact that the Sb(V) desorption rate constant (k_b) is higher than that of sorption (k_f) by low irreversible sequestration (k_i) indicates that Sb(V) uptake is overall reversible, as previously observed (Haggard et al., 2006; Xi et al., 2010). Further, $Ca[Sb(OH)_6]_2$ precipitation (Johnson et al., 2005) was thermodynamically possible (SI = 3.33) in our experiments, although it might be kinetically limited given the high SI values. Antimonate removal thus possibly occurred via kinetic sorption on clay (Figure 3-4 (e)).

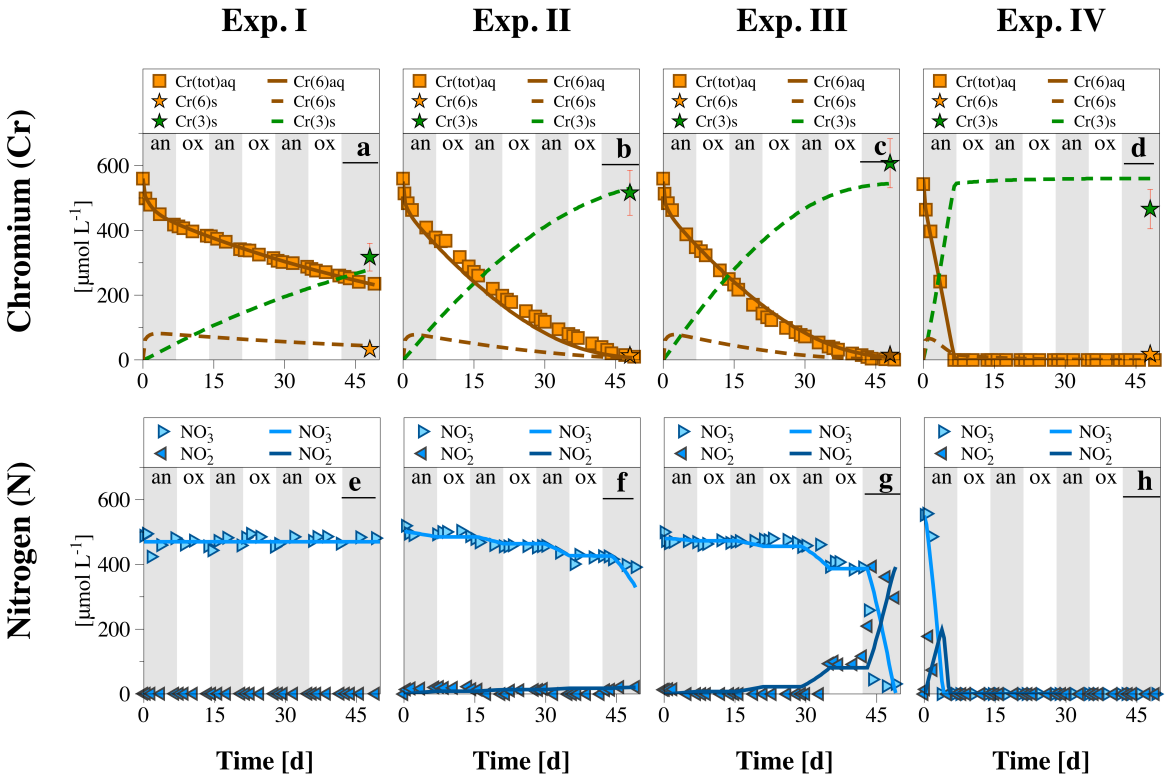

Figure 3-5. Time series of measured (symbols) and modelled aqueous (solid lines) and solid (dashed lines) Cr and N speciation. Kinetic and equilibrium formulations and parameters use in the model are presented in Table 3-2 and Table 3-4. Shaded and white areas indicate anoxic (CO_2 + N_2) and oxic (O_2 + CO_2 + N_2) periods, respectively.

Chromium abiotic sequestration. Results of the multi-reaction model suggests weak Cr(VI) sorption on the argillaceous matrix as reported previously. For instance, Lan et al. (2008) pointed to weak chromate adsorption on kaolinite, montmorillonite, and illite. Consistent with these reports, the model predicts that most of the Cr(VI) immobilization (~90%) occurred via its reductive precipitation as

$Cr(OH)_3$, consistent with SI = 1.18, the rest (~10%) being removed via sorption. This is contrast to As and Sb, which remained oxidized under abiotic conditions. Cr(VI) is a strong oxidant that can be reduced at surface sites of Fe(II)-bearing clay minerals and pyrite (Chon et al., 2006) to form $Cr(OH)_{3(am)}$, $Cr(OH)_3{\cdot}H_2O_{(cr)}$, Cr_2O_3, or $(Cr,Fe)(OH)_3$ (Nriagu et al., 1993) even in the presence of O_2 (Rai et al., 1989). The fact that abiotic Cr reduction is not inhibited by O_2 corroborates our observations of a continuous decrease of [Cr] concentration during oxic and anoxic periods (Figure 3-5 (a)). Moreover, Cr can also be reduced by DOC (Jamieson-Hanes et al., 2012b) released from the argillaceous matrix itself, which can provide 2.6 mM electron equivalents, enough to reduce 0.5 mM dissolved Cr(VI) as it requires 1.5 mM electron equivalents.

Speciation of solid-phase Cr was used to constrain the multi-reaction model capturing the two-step Cr uptake: weak sorption of Cr(VI) followed by its abiotic reduction leading to Cr sequestration as Cr(III) hydroxide (Figure 3-5 (a)). This mechanism is consistent with the XANES results of Jamieson-Hanes et al. (2012) indicating that Cr reduction occurs on the particulate phase rather than in solution. Therefore, we introduce a first-order kinetic reduction of surface-bound Cr(VI) (Table 3-4, R^{10}). Our estimated rate constant (Table 3-12) is close to that reported for soil (6.9×10^{-3} h^{-1}) (Matern and Mansfeldt, 2016) and clay (0.2×10^{-3} h^{-1}) (Lan et al., 2008).

3.5.4 Microbial Effect on the Mobility of As, Sb, Cr, and N

The effect of microbial activity and functionality on contaminant (As, Sb, and Cr) and nutrient (N) behavior was evaluated first by letting the natural community in the argillaceous sample develop without sterilization (Exp. II), then with addition of ethanol (Exp. III), or both ethanol and microbial soil inoculum (Exp. IV). From the ATP measurements we assume that microorganisms were present and active in the bioreactor without inoculation (Figure 3-2 (b-c)). Using an average ATP-per-biovolume concentration of 1.75×10^{-10} nmol $cell^{-1}$ ATP (Hammes et al., 2010) and the mean ATP concentration (1 nM) observed in Exp. II and Exp. III, we estimate biomass $\approx 5\times10^8$ cells g^{-1} under our experimental conditions. Ethanol fermentation to acetate occurred, but did not appear to stimulate a biomass increase.

Arsenic. The occurrence of As(V) reduction in Exp. II-III, which did not occur in Exp. I, suggests microbial control of the reaction. Reduction rates were similar regardless of the addition of ethanol, suggesting that this carbon source was not used as a primary electron donor for As reduction. Microbial As reduction can either proceed via enzymatic (respiration and detoxification) or non-enzymatic (oxidation of microbially produced glutathione) pathways (Scott et al., 1993). Given that our experimental [As] values exceed the threshold of 100 μM As for expression of detoxification genes by bacteria

Shewanella sp. (Saltikov et al., 2005) by 4-fold, reduction by detoxification is a plausible pathway.

The ability to detoxify As is widespread among aerobic and anaerobic bacteria (Saltikov et al., 2005) as well as by algae and fungi (Cervantes et al., 1994; Zhang and Selim, 2008). The fact that the As reduction rate was not increased by ethanol additions supports detoxification over respiration as an As-reducing mechanism. In the absence of a suitable external electron donor, possible electron donors of detoxification are endogenous reservoirs (DNA and proteins), mediated by intracellular reductants (e.g., NADH, NADPH, ascorbate, glutaredoxin, glutathione) (Silver and Phung, 2005). The detoxification mechanism is also supported by the lack of ATP increase throughout Exp. II and Exp. III, confirming that As reduction was not an energy gaining process (Lloyd and Oremland, 2006; Oremland et al., 2009; Plant et al., 2005). In agreement with the observations of Saltikov et al. (2005) who reported aerobic As(V) detoxification by *Shewanella sp*. ANA-3, As reduction was not inhibited by the presence of O_2 in our study (Figure 3-3 (b)). Moreover, other TEAs of higher redox potential, such as chromate and nitrate (Table 3-3) did not interfere with the formation of As(III), which occurred simultaneously with Cr(VI) and NO_3^- reduction. The often-hypothesized cascade of thermodynamically favorable TEAs reduction, thus, was not observed.

To account for both microbial and mineralogical controls on As sequestration in Exp. II-III, we introduce Monod type kinetics. We assume that the rate limiting half-saturation term is independent on ethanol concentration and not inhibited by O_2 (Table 3-4, R^{18}). Further, calibration of the model parameters against solid As speciation on the last day of Exp. II and Exp. III allowed us to estimate kinetic-equilibrium constants of As(III) sorption. Persistence of As(III) in solution is consistent with its low sorption affinity to clay minerals, relative to As(V) (Lin and Puls, 2000), and the under-saturation of the solution with respect to $CaHAsO_3$ (SI = -0.38). The model fails to capture the observed slight increase of As between day ~30 and the end of Exp. II-III (Figure 3-4 (b-c)). Late As remobilization could reflect reduction of surface-bound As(V) (Ghorbanzadeh et al., 2015), followed by the release of As(III) in the solution (Burnol et al., 2007).

In Exp. IV, the microbial inoculation resulted in the inhibition of As(V) reduction by O_2 during oxic periods (Figure 3-3 (d)). As(V) reduction was associated with a 1:1 conversion of C-acetate to DIC (Figure 3-3 (l)), suggesting acetate oxidation to bicarbonate. Because acetate may provide electrons for microbial As reduction (Lloyd and Oremland, 2006; Oremland et al., 2009), it can enable As respiration (Gorny et al., 2015). An increase in ATP concentration, indicative of favourable respiratory process (Oremland, 2005), was also observed (Figure 3-2 (d)).

In the model, As respiration is simulated by kinetics rate expression including an inhibiting thermodynamic term (i.e., inhibition by O_2) and following a 2nd-order reaction, which is now coupled to acetate concentration (Table 3-4, R^{19}). This led, however, to the overestimation of [As] due to higher yield of As(III) which persists in the solution, and to underestimation of As(V) accumulated in the solid phase. One of the plausible mechanisms of enhanced immobilization of total aqueous As could be As(III) biosorption (Prasad et al., 2013; Sibi, 2014), $As(OH)_3°$ hydrophobic sorption on neutral siloxane surfaces or its aqueous complexation with microbially produced organics (Redman et al., 2002). However, this would not explain imbalance of As speciation in the solid phase, suggesting that an As(V) sink was missing in the model.

A potential mechanism, not accounted for in the initial model as we lacked supporting data, is the sorption of non-volatile mono-methyl As(V) formed via oxidative biomethylation of As(III) (Mestrot et al., 2013). Such species are produced by soil bacteria (Thayer, 2002) in the absence of oxygen (Frohne et al., 2011) and are known to sorb on Fe and Al minerals (Lafferty and Loeppert, 2005). Further, the process may be inhibited in the presence of Sb(III) (Andrewes et al., 2000) and this interplay was observed in Exp. IV. We thus tested this reaction in the model (Table 3-4, R^{24}), an exercise reveals that > 60% of As(III) could be immobilized via sorption of freshly formed methylated As(V) species (Figure 3-4 (d)). The overall aqueous As(V) concentration predicted by the model is more sensitive to the rates of abiotic adsorption ($k_f^{HAsO_4^{2-}}$) and microbial respiration ($k_{resp}^{HAsO_4^{2-}}$) (Figure 3-11) suggesting that both sorption and reduction mechanisms play significant roles in As(V) sequestration.

Antimony. Similar to As, Sb(V) reduction is consistent with detoxification occurring in Exp. II-III (Figure 3-4 (f-g)). Based on the saturation index calculations, the model suggests precipitation of Sb(III) in the form of $Sb_2O_{3(s)}$ (Abin and Hollibaugh, 2014). Fast reductive precipitation of Sb is consistent with the absence of aqueous Sb(III) and co-existence of Sb(V) with As(III) (Casiot et al., 2007; Fawcett et al., 2015; Mitsunobu et al., 2006). Fit to the experimental data required that a fraction of surface-bound Sb(V) be available for detoxification to Sb(III) (Table 3-4, R^{29}), although to our knowledge such a mechanism has not been described in the literature.

In Exp. IV, after complete As(V) removal by day 15, the removal rate of Sb increased, but only during anoxic periods (Figure 3-3 (d)). Compared to As, little is known on the ability of microorganisms to respire or gain energy from Sb reduction. However, since Sb(V) reduction was recently found to be inhibited by As(V) in natural sediments (Kulp et al., 2014) and to cause an increase of bacterial cell density (*Bacillus sp*. MLFW-2) under anaerobic conditions (Abin and Hollibaugh, 2014), it is plausible that Sb underwent microbial reductive respiration coupled to incomplete oxidation of ethanol to acetate

(Figure 3-3 (l)). As(V) is known to suppress Sb(V) reduction (Fawcett et al., 2015; Kulp et al., 2014; Mitsunobu et al., 2006), consistent with the sequence observed in Exp. IV. Thermodynamic calculations of redox potentials relevant to the experimental conditions of Exp. IV (Table 3-3) suggest that the observed sequence holds only for Sb(V) reduction to $Sb_2O_{3(s)}$ and not to $Sb(OH)_3$, supporting the reductive precipitation mechanism controlling Sb mobility.

Table 3-3. Thermodynamic sequence based on the redox potentials (E_H) of half reduction reactions at the experimental pH (6.9), temperature (25 °C), and concentrations of reduced and oxidized species at the beginning of Exp. IV. Thermodynamic order of As and Sb reductions differs depending on pH ($E_H°'$ and $E_H°$) and products of Sb reduction. The observed experimental sequence of Sb reduction followed by As reduction, suggests Sb reduction to $Sb_2O_{3(s)}$, rather than to $Sb(OH)_3$. Calculations are based on the thermodynamic values given in Bard et al. (1985); Filella and May (2003); Nordstrom et al. (2014); Tratnyek and Macalady (2000); Zotov et al. (2003).

Reduction reactions	E_H [mV] pH 6.9	$E_H°'$ [mV] pH 7	$E_H°$ [mV] pH 0
$O_2 + 4\ H^+ + 4\ e \rightarrow 2\ H_2O$	816	816	1230
$CrO_4^{2-} + 5\ H^+ + 3\ e \rightarrow Cr(OH)_3 + H_2O$	524	579	1270
$NO_3^- + 2\ H^+ + 2\ e \rightarrow NO_2^- + H_2O$	316	426	840
$Sb(OH)_6^- + 3\ H^+ + 2\ e \rightarrow Sb(OH)_3 + 3\ H_2O$	188	91	712
$HAsO_4^{2-} + 4\ H^+ + 2\ e \rightarrow H_3AsO_3 + H_2O$	160	18	846
$2\ Sb(OH)_6^- + 6\ H^+ + 4\ e \rightarrow Sb_2O_{3(s)} + 9\ H_2O$	130	218	839
$CO_2 + 12\ H^+ + 12\ e \rightarrow C_2H_5OH$ (ethanol) $+ 3\ H_2O$	-795	-356	90

Inclusion of Sb(V) reduction via a respiration mechanism inhibited by O_2 and aqueous As(V) to the model (Table 3-4, R^{30}), allows to reproduce features of the Sb time-series observed in Exp. IV (Figure 3-4 (h)). Sensitivity analyses identified the rate of adsorption ($k_f^{Sb(OH)_6^-}$) as the most critical parameter controlling aqueous Sb(V) concentration (Figure 3-11). Finally, the mismatch between Sb loss from solution and that accumulated in the solid-phase highlighted by mass balance calculations (Figure 3-7) is attributed to Sb loss via volatilization of methylated Sb species (Bentley and Chasteen, 2002; Wilson et al., 2010), which is known to be enhanced in the presence of As (Filella et al., 2007).

Table 3-4. The reaction network and kinetic formulations used in the biogeochemical models.

Description	Reaction	Kinetic or equilibrium formulation	R#
Electrode leak		$R_1 = r_{leak}^{DOC}$	1
Fermentation of ethanol	$C_2H_5OH + H_2O \rightarrow CH_3COO^- + 5\ H^+ + 4\ \bar{e}$	$R_2 = k^{C_2H_5OH} \cdot [C_2H_5OH] \cdot \left(\frac{K_{in}^{O_2}}{K_{in}^{O_2} + [O_2]} \right)$	2
Fermentation of acetate	$CH_3COO^- + 4\ H_2O \rightarrow 2\ HCO_3^- + 9\ H^+ + 8\ \bar{e}$	$R_3 = k^{CH_3COO^-} \cdot [CH_3COO^-] \cdot \left(\frac{K_{in}^{O_2}}{K_{in}^{O_2} + [O_2]} \right)$	3
Aerobic respiration of ethanol	$O_2 + C_2H_5OH \rightarrow CH_3COO^- + H_2O + H^+$	$R_4 = k_{eth}^{O_2} \cdot [C_2H_5OH] \cdot \left(\frac{[O_2]}{[O_2] + K_m^{O_2}} \right)$	4
Aerobic respiration of acetate	$2\ O_2 + CH_3COO^- + H^+ \rightarrow 2\ CO_2 + 2\ H_2O$	$R_5 = k_{ac}^{O_2} \cdot [CH_3COO^-] \cdot \left(\frac{[O_2]}{[O_2] + K_m^{O_2}} \right)$	5
Chromium			
Equilibrium sorption of Cr(VI)	$CrO_4^{2-} + \equiv SOH + H^+ \rightleftarrows \equiv SOH_2^+ CrO_4^{2-}$	$\log K_{sorp}^{CrO_4^{2-}}$	6
Kinetic sorption of Cr(VI)	$CrO_4^{2-} + \equiv SOH + H^+ \rightleftarrows \equiv SOH_2^+ CrO_4^{2-}$	$R_f^7 = k_f^{CrO_4^{2-}} \cdot [CrO_4^{2-}]$	7
		$R_b^8 = k_b^{CrO_4^{2-}} \cdot \equiv SOH_2^+ CrO_4^{2-}$	8
		$R_i^9 = k_i^{CrO_4^{2-}} \cdot \equiv SOH_2^+ CrO_4^{2-}$	9
Abiotic reduction of surface-bound Cr(VI)	$\equiv SOH_2^+ CrO_4^{2-} + 5\ H^+ + 3\ \bar{e} \rightarrow Cr(OH)_{3(s)} + H_2O$	$R_{ab}^{10} = k_{ab}^{CrO_4^{2-}} \cdot \equiv SOH_2^+ CrO_4^{2-}$	10

Description	Reaction	Kinetic or equilibrium formulation	R#
Detoxification of aqueous Cr(VI)	$CrO_4^{2-} + 5\ H^+ + 3\ \bar{e} \rightarrow Cr(OH)_{3(s)} + H_2O$	$R_{detox}^{11} = r_{max}^{CrO_4^{2-}} \cdot \left(\frac{[CrO_4^{2-}]}{K_{m\ (detox)}^{CrO_4^{2-}} + [CrO_4^{2-}]} \right)$	11
Respiration of aqueous Cr(VI)	$8\ CrO_4^{2-} + 3\ CH_3COO^- + 13\ H^+ + 4\ H_2O \rightarrow 8\ Cr(OH)_3 + 6\ HCO_3^-$	$R_{resp}^{12} = k_{resp}^{CrO_4^{2-}} \cdot [CH_3COO^-] \cdot \left(\frac{[CrO_4^{2-}]}{K_{m\ (resp)}^{CrO_4^{2-}} + [CrO_4^{2-}]} \right) \left(\frac{K_{in}^{O_2}}{K_{in}^{O_2} + [O_2]} \right)$	12
Precipitation of Cr(III)	$Cr(OH)_3\,(s) + H+ \rightleftarrows Cr(OH)_2^+ + H_2O$	$\log K_{sp}^{Cr(OH)_3}$	13
Arsenic			
Equilibrium sorption of As(V)	$HAsO_4^{2-} + 2 \equiv SOH \rightleftarrows \equiv SOHAsO_4 + H_2O$	$\log K_{sorp}^{HAsO_4^{2-}}$	14
		$R_f^{15} = k_f^{HAsO_4^{2-}} \cdot [HAsO_4^{2-}]$	15
Kinetic sorption of As(V)	$HAsO_4^{2-} + 2 \equiv SOH \rightleftarrows \equiv SOHAsO_4 + H_2O$	$R_b^{16} = k_b^{HAsO_4^{2-}} \cdot \equiv SOHAsO_4$	16
		$R_i^{17} = k_i^{HAsO_4^{2-}} \cdot \equiv SOHAsO_4$	17
Detoxification of aqueous As(V)	$HAsO_4^{2-} + 4\ H^+ + 2\ \bar{e} \rightarrow H_3AsO_3 + H_2O$	$R_{detox}^{18} = r_{max}^{HAsO_4^{2-}} \cdot \left(\frac{[HAsO_4^{2-}]}{K_{m\ (detox)}^{HAsO_4^{2-}} + [HAsO_4^{2-}]} \right)$	18

Description	Reaction	Kinetic or equilibrium formulation	R#
Respiration of aqueous As(V)	$4\ HAsO_4^{2-} + C_2H_4O_2 + 6\ H^+ \rightarrow 4\ H_3AsO_3 + 2\ HCO_3^-$	$R_{resp}^{19} = k_{resp}^{HAsO_4^{2-}} \cdot [CH_3COO^-] \cdot \left(\frac{[HAsO_4^{2-}]}{K_{m\ (resp)}^{HAsO_4^{2-}} + [HAsO_4^{2-}]}\right)\left(\frac{K_{in}^{O_2}}{K_{in}^{O_2} + [O_2]}\right)$	19
Equilibrium sorption of As(III)	$H_3AsO_3 + 2{\equiv}SOH \rightleftarrows {\equiv}S_2HAsO_3 + 2\ H_2O$	$\log K_{sorp}^{H_3AsO_3}$	20
Kinetic sorption of As(III)	$H_3AsO_3 + 2{\equiv}SOH \rightleftarrows {\equiv}S_2HAsO_3 + 2\ H_2O$	$R_f^{21} = k_f^{H_3AsO_3} \cdot [H_3AsO_3]$	21
		$R_b^{22} = k_b^{H_3AsO_3} \cdot {\equiv}S_2HAsO_3$	22
		$R_i^{23} = k_i^{H_3AsO_3} \cdot {\equiv}S_2HAsO_3$	23
Oxidative biomethylation of As(III)	$CH_4 + H_3AsO_3 \rightarrow CH_3As^VO(OH)_2 + 2\ H^+ + 2\ \bar{e}$	$R_{methyl}^{24} = k^{H_3AsO_3} \cdot \left(\frac{[H_3AsO_3]}{K_m^{H_3AsO_3} + [H_3AsO_3]}\right)\left(\frac{K_{in}^{O_2}}{K_{in}^{O_2} + [O_2]}\right)$	24
Antimony			
Equilibrium sorption of Sb(V)	$Sb(OH)_6^- + 2{\equiv}SOH \rightleftarrows ({\equiv}SO)_2Sb(OH)_4^- + 2\ H_2O$	$\log K_{sorp}^{Sb(OH)_6^-}$	25
Kinetic sorption of Sb(V)	$Sb(OH)_6^- + 2{\equiv}SOH \rightleftarrows ({\equiv}SO)_2Sb(OH)_4^- + 2\ H_2O$	$R_f^{26} = k_f^{Sb(OH)_6^-} \cdot [Sb(OH)_6^-]$	26
		$R_b^{27} = k_b^{Sb(OH)_6^-} \cdot ({\equiv}SO)_2Sb(OH)_4^-$	27
		$R_i^{28} = k_i^{Sb(OH)_6^-} \cdot ({\equiv}SO)_2Sb(OH)_4^-$	28
Detoxification of surface-bound Sb	$({\equiv}SO)_2Sb(OH)_4^- + 3\ H^+ + 2\ \bar{e} \rightarrow Sb(OH)_3 + 3\ H_2O$	$R_{detox}^{29} = r_{max}^{Sb(OH)_6^-} \cdot \left(\frac{({\equiv}SO)_2Sb(OH)_4^-}{K_{m\ (detox)}^{Sb(OH)_6^-} + ({\equiv}SO)_2Sb(OH)_4^-}\right)$	29

Description	Reaction	Kinetic or equilibrium formulation	R#
Respiration of aqueous Sb(V)	$2\ Sb(OH)_6^- + C_2H_5OH + H^+ \rightarrow$ $2\ Sb(OH)_3 + CH_3COO^- + 5\ H_2O$	$R_{resp}^{30} = k_{resp}^{Sb(OH)_6^-} \cdot [C_2H_5OH] \cdot \left(\frac{[Sb(OH)_6^-]}{K_{m\ (resp)}^{Sb(OH)_6^-} + [Sb(OH)_6^-]}\right)\left(\frac{K_{in}^{O_2}}{K_{in}^{O_2} + [O_2]}\right) \cdot \left(\frac{K_{in}^{HAsO_4^{2-}}}{K_{in}^{HAsO_4^{2-}} + [HAsO_4^{-2}]}\right)$	30
Precipitation of Sb(III)	$Sb_2O_3\ (c) + 3\ H_2O \ \rightleftarrows\ 2\ Sb(OH)_3\ (aq)$	$\log K_{sp}^{Sb_2O_3}$	31
Nitrogen			
Respiration of N(V)	$2\ NO_3^- + CH_2O \rightarrow$ $2\ NO_2^- + CO_2 + H_2O$	$R_{resp}^{32} = k^{NO_3^-} \cdot [CH_2O] \cdot \left(\frac{[NO_3^-]}{K_m^{NO_3^-} + [NO_3^-]}\right)\left(\frac{K_{in}^{O_2}}{K_{in}^{O_2} + [O_2]}\right)\left(\frac{K_{in}^{CrO_4^{2-}}}{K_{in}^{CrO_4^{2-}} + [CrO_4^{2-}]}\right)$	32
Respiration of N(III)	$4\ NO_2^- + 3\ CH_2O + 4\ H^+ \rightarrow$ $2\ N_2 + 3\ CO_2 + 5\ H_2O$	$R_{resp}^{33} = k^{NO_2^-} \cdot [CH_2O] \cdot \left(\frac{[NO_2^-]}{K_m^{NO_2^-} + [NO_2^-]}\right)\left(\frac{K_{in}^{O_2}}{K_{in}^{O_2} + [O_2]}\right)\left(\frac{K_{in}^{CrO_4^{2-}}}{K_{in}^{CrO_4^{2-}} + [CrO_4^{2-}]}\right)$	33

Comments:

- ≡SOH – a generic sorption entity, which can be protonated or non-protonated and may involve one, two or three surface oxygen
- CH_2O – argillaceous dissolved organic carbon
- Detoxification – microbial reduction of As, Sb and Cr which is not coupled to the oxidation of external electron donor
- Respiration – microbial reduction of As, Sb and Cr which is coupled to the oxidation of ethanol or acetate

Chromium. The immobilization of Cr in biotic Exp. II-III likely proceeded via reductive precipitation of Cr(III) with faster kinetics than in Exp. I (Figure 3-5 (b-c)). Similar to As and Sb, the presence of the native microorganisms could induce Cr reduction via the detoxification (Cheung and Gu, 2007). Reductive detoxification of both Cr and Sb may reflect a microbial strategy for metal sequestration via precipitation. Alternatively, Cr(VI) could be reduced via extracellular non-enzymatic processes. In this case bacteria could serve as electron donors after biosorption of chromate to the microbial cell wall (Viti et al., 2014). Accounting for a microbial control on Cr sequestration, we introduce a microbial pathway of Cr(VI) reduction (Table 3-4, R^{11}).

In Exp. IV, complete Cr removal during the first 3 days (Figure 3-5 (d)) likely responds to the addition of soil inoculum and Cr reduction via both detoxification and respiration (Viti et al., 2014). We, therefore, include Cr respiration (Chen and Hao, 1998) into the model (Table 3-4, R^{12}). Our estimate for the rate of Cr(VI) reduction falls within the range reported for Cr(VI) reduction by dissimilatory iron-reducing bacteria (0.8×10^{-4} – 3.1×10^{-4} h^{-1}) (Table 3-12) (Fendorf et al., 2000). Therefore, our modelling is consistent with previous studies indicating that several microbial processes responsible for Cr reduction progress at similar rates. Sensitive model parameters include the maximum rate of detoxification ($r_{max}^{CrO_4^{2-}}$), as well as, rate constants of abiotic reduction ($k_{ab}^{CrO_4^{2-}}$), sorption ($k_f^{CrO_4^{2-}}$), and desorption ($k_b^{CrO_4^{2-}}$) (Figure 3-11). Consistent with the experimental observations, the model of aqueous Cr(VI) concentration is relatively insensitive to the inhibition constant of O_2 ($K_{O_2}^{in}$).

Nitrogen. The overall reduction rate of [NO_3^-] (0.3 μM h^{-1}) was suppressed by the presence of [Cr] in Exp. II-III. However, the rate increased by an order of magnitude reaching 3.1 μM h^{-1} after the depletion of [Cr] by the end of Exp. III (Figure 3-5 (g)). Such a strong inhibitory effect by Cr, as well as simultaneous reduction of Cr(VI) and NO_3^-, are in agreement with previous reports (Kourtev et al., 2009; Middleton et al., 2003). The fact that NO_3^- reduction proceeded in the presence of Cr(VI) indirectly supports the detoxification as a non-respiratory Cr reduction mechanism in Exp. II-III as discussed above.

Being an essential nutrient, NO_3^- reduction is associated with energy production (Konhauser, 2007) and corresponding ATP increase was clearly observed in Exp. III (Figure 3-2 (c)). We find significant correlation ($p < 0.001$, $r = 0.99$) between ATP concentration and NO_3^- reduction rates in Exp. II-IV. Electron donor for nitrate reduction was likely present in the argillaceous matrix. Ethanol is an unlikely reductant, since NO_3^- reduction rate was not promoted by the ethanol additions during 1st, 2nd, and 3rd anoxic periods. We thus model the reduction as a heterotrophic denitrification pathway with complete

NO_3^- turnover via NO_2^- to $N_{2(g)}$ coupled to the oxidation of argillaceous DOC (Table 3-4, $R^{32,33}$) (Rivett et al., 2008). Thermodynamically, both organic carbon and pyrite constituents of the argillaceous sample may attenuate up to 12 μM g^{-1} and 417 μM g^{-1} of NO_3^-, respectively. Even though both process are widespread under biotic conditions (Bosch et al., 2012), the higher energy yield of NO_3^- reduction with organic matter should prioritize this reaction pathway over anaerobic pyrite oxidation (Appelo and Postma, 2005). Furthermore, we estimate that complete reduction of NO_3^- by pyrite would lead to an increase in SO_4^{2-} and Fe^{2+} aqueous concentration by 350 and 175 μM, respectively, which was not observed (Figure 3-8).

The most sensitive model parameters predicting NO_3^- concentration are the rate constant of NO_3^- reduction ($k^{NO_3^-}$) and the inhibition constant of Cr ($K_{in}^{CrO_4^{2-}}$) (Figure 3-11). Meanwhile, supplied ethanol was fermented to acetate, reflecting a defense mechanism of denitrifying bacteria under stress conditions (Jørgensen and Tiedje, 1993), e.g. in a contaminated suspension by potentially toxic chemicals.

3.5.5 Oxyanion Interplay

The experimental results present evidence that the fate of contaminant oxyanions (i.e., CrO_4^{2-}, $HAsO_4^{2-}$, $Sb(OH)_6^-$) added to an argillaceous suspension depends on the level of microbial activity (as inferred from ATP concentrations) and the microbial community structure (native versus inoculated consortiums). The results suggest two types of contaminant interplay revealing two strategies employed by the microorganisms to deal with contaminant mixtures (Figure 3-6).

The first strategy involves the simultaneous reduction of CrO_4^{2-}, $HAsO_4^{2-}$, $Sb(OH)_6^-$ under aerobic and denitrifying conditions. This is observed in the suspensions during Exp. II-III (Figure 3-3 (b-c)). It is consistent with the previously observed simultaneous reduction of SO_4^{2-} and As(V) (Macy et al., 2000) or Fe(III) and As(V) (Smeaton et al., 2012), when As was reduced via detoxification. Furthermore, the suggested mechanism may explain simultaneous bioreduction of other potentially toxic elements (i.e., U(VI)) under iron- or sulfate- reducing conditions observed in sediments (Finneran et al., 2002; Komlos et al., 2008).

The second strategy involves the respiratory reduction of the oxyanions that follows the thermodynamic sequence from highest to lowest reduction potentials (Table 3-3). The reduction sequence (O_2, CrO_4^{2-}, NO_3^-, $HAsO_4^{2-}$, $Sb(OH)_6^-$) is observed in the argillaceous suspension enriched with a soil inoculum (Exp. IV) (Figure 3-3 (d)).

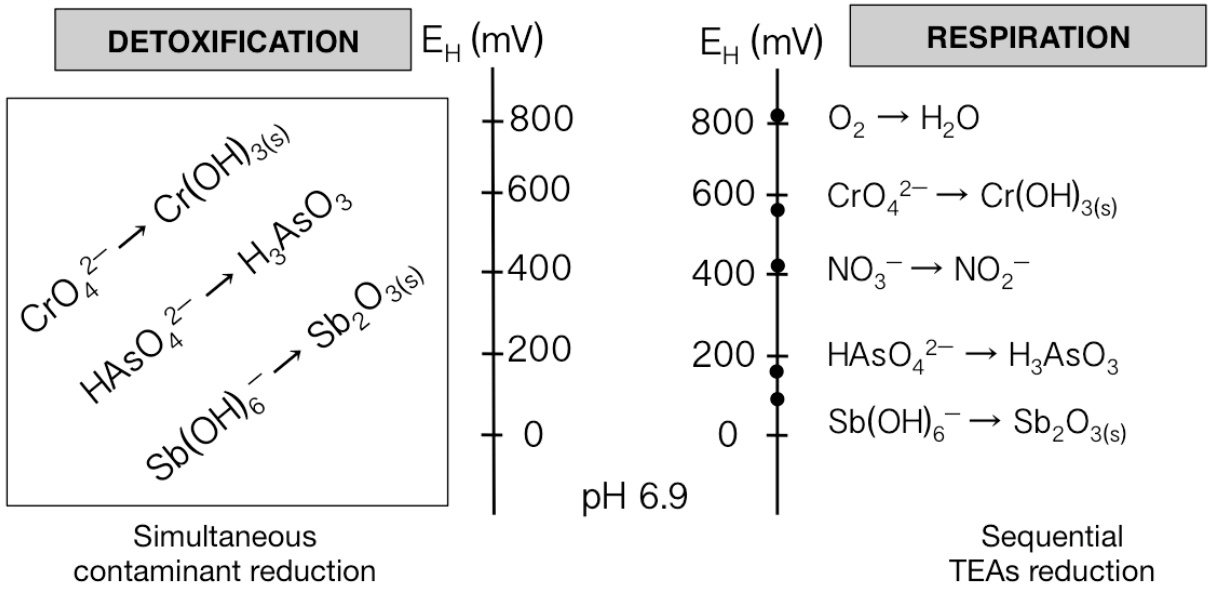

Figure 3-6. Redox scale showing the theoretical succession of redox potentials (E_H in mV) calculated for the initial experimental conditions (pH 6.9, activities of oxidized and reduced species) (Table 3-3). Potentially toxic CrO_4^{2-}, $HAsO_4^{2-}$, and $Sb(OH)_6^-$ can be reduced simultaneously likely via detoxification with no dependency on E_H (on the left) under aerobic and denitrifying conditions or successively as terminal electron acceptors (TEAs) via respiration following the thermodynamic order (i.e., E_H cascade) (on the right). An essential nutrient, NO_3^-, is exclusively reduced via the respiratory mechanism in the presence of microorganisms.

3.5.6 Stability of Reduced Species

We did not observe remobilization of contaminants under oscillating oxic/anoxic conditions, likely due to the absence of re-oxidation of As(III), Sb(III), Cr(III), and N(III) during oxic periods. Abiotic oxidation of the reduced forms of these elements by O_2 is thermodynamically possible (Campbell and Nordstrom, 2014) under the experimental conditions (Table 3-3). The stability of reduced species is in contrast with previous studies of contaminants dynamics in topsoil suspensions under the redox-oscillating conditions (e.g., Couture et al., 2015; Hockmann et al., 2014; Parsons et al., 2013), where re-oxidation was observed to various extents. We hypothesize that the lack of re-oxidation is due to kinetic limitation (Leuz and Johnson, 2005; Rai et al., 1989) in the argillaceous material lacking labile DOC, Fe- and Mn-oxyhydroxides (Table 3-7), and, possibly, oxidizing microorganisms. These factors have all been linked to catalyzed re-oxidation of contaminants in soils (Buschmann et al., 2005; Butler et al., 2015; Hug and Leupin, 2003) and are thus pre-requisite for contaminant redox cycling.

3.6 Conclusions

Oxyanion mobility in a Tégulines suspension has been examined in a series of increasing complexity experiments and reproduced numerically providing a quantitative description of biogeochemical processes under oscillating oxic/anoxic conditions. The sensitivity analyses reveal that both abiotic sorption and microbial reduction reactions play equally significant roles in decreasing aqueous concentrations of As(V), Sb(V), and Cr(VI). Our result suggests that argillaceous formations may be suitable repositories that can withstand periodical oxidative perturbations without releasing contaminants to the aqueous phase, at least at the experimental time-scale of days investigated here.

3.7 Supporting Information

3.7.1 Characterization of Argillaceous Matrix

Table 3-5. Powder XRD mineralogy of argillaceous sample with the limit of detection (LOD) of 2%.

Mineral	Formula	Weight %
Quartz	SiO_2	29.21
Muscovite	$KAl_2(AlSi_3O_{10})(F,OH)_2$	15.25
Smectite (Montmorillonite)	$(Na, Ca)_{0,3}(Al, Mg)_2Si_4O_{10}(OH)_2 \cdot nH_2O$	14.2
Calcite	$CaCO_3$	12.18
Kaolinite	$Al_2Si_2O_5(OH)_4$	11.07
Biotite	$K(Mg, Fe)_3A(AlSi_3O_{10})\ (F,OH)_2$	7.07
Chlorite (Clinochlore)	$(Mg_5Al)(AlSi_3)O_{10}(OH)_8$	3.89
Microcline	$KAlSi_3O_8$	3.75
Gypsum	$CaSO_4 \cdot 2H_2O$	< LOD
Pyrite	FeS_2	< LOD
Anatase	TiO_2	< LOD

Table 3-6. Synthetic pore-water composition.

Compounds	mmol L^{-1}
$CaCO_3$	0.06
$SrCO_3$	0.25
$MgCl_2$, $6H_2O$	0.53
$MgSO_4$, $7H_2O$	1.41
$CaSO_4$, $2H_2O$	3.03
$NaHCO_3$	2.85

Table 3-7. ICP-OES elemental analysis of the initial argillaceous sample before experiments with the limit of detection (LOD) for As and Sb of 0.01 mg g^{-1}.

Element	Concentration (mg g^{-1})	
	Acidic digestion	CBD extraction
Fe	35.51	1.60±0.16
Mn	0.25	0.041±0.005
Al	74.57	0.243±0.01
Si	264.42	
Ca	57.88	
K	18.75	
Mg	6.85	
S	6.68	
Ti	4.46	
Na	1.27	
P	0.59	
As	< LOD	
Cr	0.15	
Sb	< LOD	

Table 3-8. Water content and particle size distribution of argillaceous sample.

Measurement	Value
Water Content [%]*	6.7
Total volatiles [%]**	10.9
Clay particles (<2 μm) :	
766 nm [%]	77.4
235 nm [%]	22.6
Zeta potential [mV]	-23
pH***	7.25

* Water content by loss on ignition (L.O.I.) after 24h 110°C

** Total volatiles (H_2O^+, H_2O^-, CO_2, S, F and Cl) by L.O.I. after 1h 1000°C.

** pH of argillaceous suspension in MQ H_2O (50 g L^{-1})

Table 3-9. Actual initial aqueous concentrations (μM) of contaminants and nitrate in suspensions.

Elements	Exp. I	Exp. II	Exp. III	Exp. IV
As(V)	460	461	460	461
Sb(V)	528	550	530	501
Cr(VI)	560	561	560	561
N(V)	488	520	501	553

Table 3-10. Elemental composition following the complete acidic digestion of the solid samples measured before and after batch experiments (SD±0.01 mg g^{-1} of triplicates) with the limit of detection (LOD) of 0.01 mg g^{-1}.

Element	Total concentration (mg g^{-1})				
	Before Exp-s	After Exp. I	After Exp. II	After Exp. III	After Exp. IV
As	<LOD	0.43	0.55	0.61	0.63
Cr	0.15	0.35	0.68	0.77	0.63
Sb	<LOD	0.38	0.47	0.58	0.55

Table 3-11. Solubility products of co-precipitation reactions.

Reaction	Log K_{sp}	Reference
$CaHAsO_3$ (s) + 2 H^+ ⇄ Ca^{2+} + H_3AsO_3	-8.229	(Román-Ross et al., 2006)
$Mg_3(AsO_4)_{2(s)}$ ⇄ $2AsO_4^{3-}$ + $3Mg^{2+}$	-22.32	(Raposo et al., 2004)
$Ca_3(AsO_4)_{2(s)} \cdot 4H_2O$ ⇄ $2AsO_4^{3-}$ + $3Ca^{2+}$ + $4H_2O$	-21.00	(Bothe and Brown, 1999)
$CaHAsO_{4(s)}$ ⇄ AsO_4^{3-} + Ca^{2+} + H^+	-16.34	(Bothe and Brown, 1999)
$Ca_3(AsO_4)_2$ ⇄ 2 AsO_4^{3-} + 3 Ca^{2+}	-21.21	(Raposo et al., 2004)
$CaNaAsO_4$ ⇄ AsO_4^{3-} + Ca^{2+} + Na^+	-9.08	(Raposo et al., 2004)
$NaSb(OH)_6$(mopungite) ⇄ $Sb(OH)_{6\,(aq)}^-$ + Na^+	-4.996	(Blandamer et al., 1974)
$Ca[Sb(OH)_6]_2$ ⇄ $2Sb(OH)_{6\,(aq)}^-$ + Ca^{2+}	-12.55	(Haggard et al., 2006)

Table 3-12. Kinetic and equilibrium parameters used in model formulations (Table 3-4).

Description	Parameter	Value				Units	Source	Range	Ref.
		Exp. I	Exp. II	Exp. III	Exp. IV				
Organic carbon									
Rate of electrode leak	r_{leak}^{DOC}	907	778	518	518	$\mu M\ day^{-1}$	C	100 – 600	[1]
Rate constant of ethanol fermentation	$k^{C_2H_5OH}$	-	-	20×10^{-3}	20×10^{-3}	day^{-1}	M	10×10^{-3} – 691×10^{-3}	[2]
Rate constant of acetate oxidation	$k^{CH_3COO^-}$	-	-	2×10^{-3}	440×10^{-3}	day^{-1}	M	10×10^{-3} – 691×10^{-3}	[2]
Rate constant of oxygen reduction by ethanol	$k_{eth}^{O_2}$	-	-	20×10^{-3}	80×10^{-3}	day^{-1}	M	10×10^{-3} – 691×10^{-3}	[2]
Rate constant of oxygen reduction by acetate	$k_{ac}^{O_2}$	-	-	2×10^{-3}	80×10^{-3}	day^{-1}	M	10×10^{-3} – 691×10^{-3}	[2]
Half-saturation of O_2 respiration	$K_m^{O_2}$	-	-	1	1	μM	L	1 – 8	[3], [4], [5]
Inhibition constant of O_2	$K_{O_2}^{in}$	-	-	1	1	μM	L	3.2×10^{-3} – 1	[3], [4]
Chromium									
Equilibrium constant of Cr(III) precipitation	$\log K_{sp}^{Cr(OH)_3}$	1.335	1.335	1.335	1.335	-	L		[8]
Rate constant of abiotic Cr(VI) reduction	$k_{ab}^{CrO_4^{2-}}$	3.9×10^{-3}	3.9×10^{-3}	3.9×10^{-3}	3.9×10^{-3}	h^{-1}	M	0.2×10^{-3} – 6.9×10^{-3}	[9], [10]
Maximum rate of Cr(VI) detoxification	$r_{max}^{CrO_4^{2-}}$	-	6.4×10^{-7}	6.4×10^{-7}	6.4×10^{-7}	$\mu M\ h^{-1}$	M		

Description	Parameter	Value				Units	Source	Range	Ref.
		Exp. I	Exp. II	Exp. III	Exp. IV				
Half-saturation of Cr(VI) detoxification	$K_{m\ (detox)}^{CrO_4^{2-}}$	-	72	72	72	μM	M	40	[11]
Rate constant of Cr(VI) respiration	$k_{resp}^{CrO_4^{2-}}$	-	-	-	2.5×10^{-4}	h^{-1}	M	0.8×10^{-4} – 3.1×10^{-4}	[12]
Half-saturation of Cr(VI) respiration	$K_{m\ (resp)}^{CrO_4^{2-}}$	-	-	-	12	μM	M	13	[13]
Arsenic									
Maximum rate of As(V) detoxification	$r_{max}^{HAsO_4^{2-}}$	-	1.8×10^{-7}	1.8×10^{-7}	1.8×10^{-7}	μM h^{-1}	M		
Half-saturation of As(V) detoxification	$K_{m\ (detox)}^{HAsO_4^{2-}}$	-	47	47	47	μM	M		
Rate constant of As(V) respiration	$k_{resp}^{HAsO_4^{2-}}$	-	-	-	1.1×10^{-4}	h^{-1}	M		
Half-saturation of As(V) respiration	$K_{m\ (resp)}^{HAsO_4^{2-}}$	-	-	-	4.2	μM	M	6.0	[6]
Rate constant of As(III) oxidative biomethylation	$k^{H_3AsO_3}$	-	-	-	3.2×10^{-4}	h^{-1}	M		
Half-saturation of As(III) oxidative biomethylation	$K_m^{H_3AsO_3}$	-	-	-	4.0	μM	M		
Antimony									
Equilibrium constant of Sb(III) precipitation	$\log K_{sp}^{Sb_2O_3}$	-	-4.98	-4.98	-4.98	-	L		[7]
Maximum rate of Sb(V) detox	$r_{max}^{Sb(OH)_6^-}$	-	4.3×10^{-8}	4.3×10^{-8}	4.3×10^{-8}	μM h^{-1}	M		

Description	Parameter	Value				Units	Source	Range	Ref.
		Exp. I	Exp. II	Exp. III	Exp. IV				
Half-saturation of Sb(V) detoxification	$K_{m\,(detox)}^{Sb(OH)_6^-}$	-	4.5×10^{-6}	4.5×10^{-6}	4.5×10^{-6}	μM	M		
Rate constant of Sb(V) respiration	$k_{resp}^{Sb(OH)_6^-}$	-	-	-	1.1×10^{-5}	h^{-1}	M		
Half-saturation of Sb(V) respiration	$K_{m\,(resp)}^{Sb(OH)_6^-}$	-	-	-	4.2	μM	M		
Inhibition constant of As(V)	$K_{in}^{HAsO_4^{2-}}$	-	-	-	5.0	μM	M		
Nitrogen									
Rate constant of N(V) respiration	$k^{NO_3^-}$	-	5.0×10^{-4}	5.0×10^{-4}	3.6×10^{-3}	h^{-1}	M		
Half-saturation of N(V) respiration	$K_m^{NO_3^-}$	-	10	10	10	μM	L	10 – 2000	[14], [15]
Inhibition constant of Cr(VI)	$K_{in}^{CrO_4^{2-}}$	-	3	3	40	μM	C	3 – 12	[16]
Rate constant of N(III) respiration	$k^{NO_2^-}$	-	1.1×10^{-4}	1.1×10^{-4}	2.9×10^{-3}	h^{-1}	M		
Half-saturation of N(III) respiration	$K_m^{NO_2^-}$	-	10	10	10	μM	M		

References: [1] (De Cannière et al., 2011); [2] (Couture et al., 2015); [3] (Couture et al., 2010); [4] (Canavan et al., 2006); [5] (Van Cappellen and Wang, 1995); [6] (Zhou et al., 2004); [7] (Zotov et al., 2003); [8] (Parkhurst and Appelo, 2013); [9] (Lan et al., 2008); [10] (Matern and Mansfeldt, 2016); [11] (Ishibashi et al., 1990); [12] (Fendorf et al., 2000); [13] (Chen and Hao, 1998); [14] (Laverman et al., 2006); [15] (André et al., 2011); [16] (Mazierski, 1994).

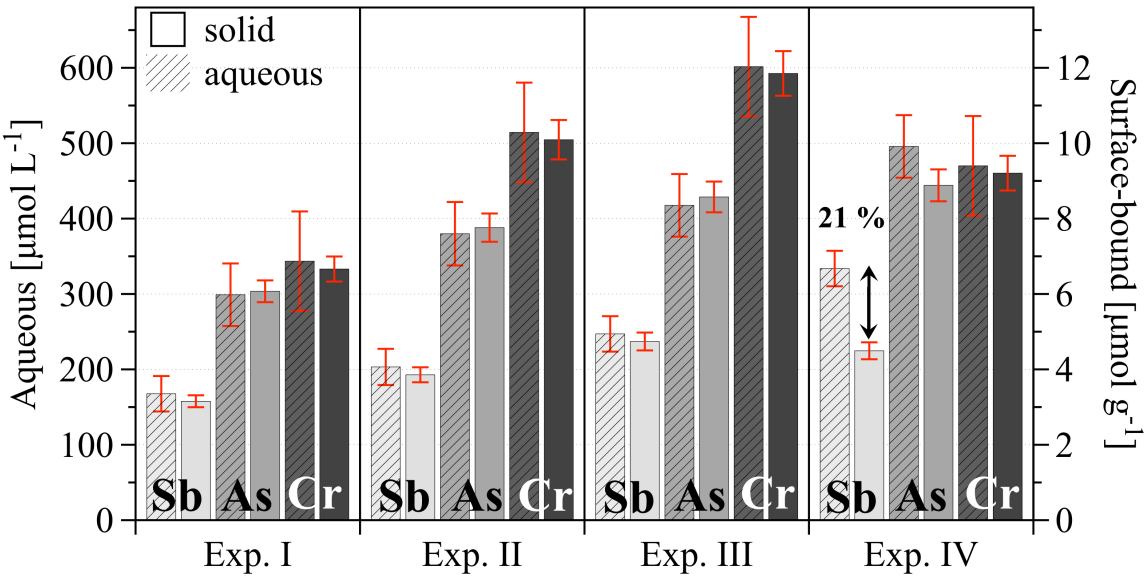

Figure 3-7. Comparison of contaminant removal from the aqueous phase (box with oblique line) with its accumulation in the solid phase (empty box) by the end of experiments (Table 3-10). Double arrow indicates loss of 21% Sb in Exp.IV.

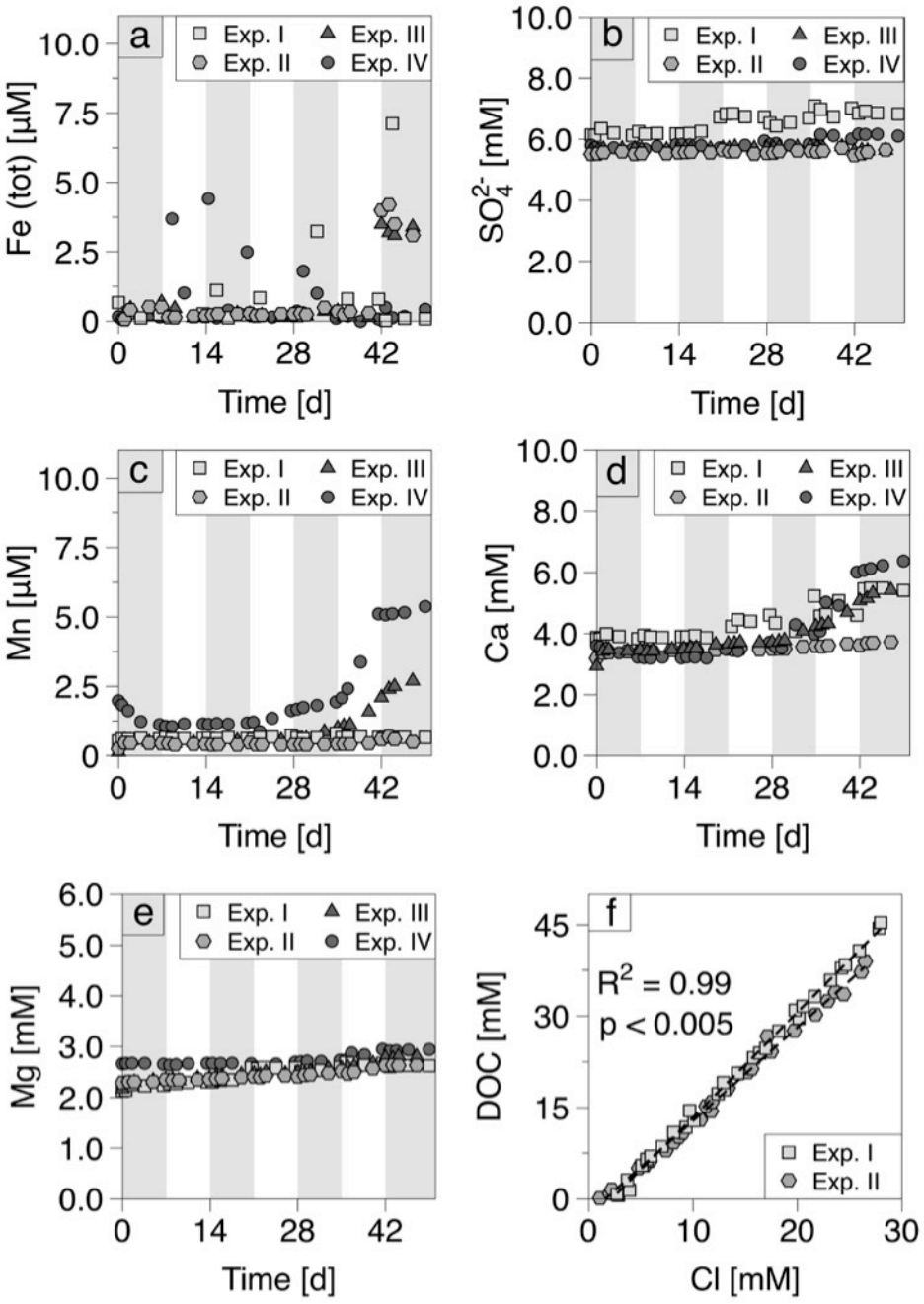

Figure 3-8. Bulk wet chemistry time-series of aqueous Fe (a), SO_4^{2-} (b), Mn (c), Ca (d), Mg (e). Dissolved organic carbon (DOC) concentration leached from the pH and E_H electrodes as a function of Cl in Exp. I (squares) and Exp. II (hexagons) (f). Dashed lines represent linear function fit with significant ($p<0.005$) correlation coefficient of 0.99 for both experiments. Shaded areas indicate anoxic periods and white areas – oxic periods.

3.7.2 Preparation and Injection of Soil Inoculum

The microbial effect on the contaminant fate of As, Sb and Sb was evaluated by enrichment of indigenous argillaceous microbial community with soil inoculum in Exp. IV. The soil inoculum was prepared from water-extractable microbial community of natural fresh top 5 cm soil. The soil was sampled from the redox fluctuation zone of Saone aquifer (France) (Couture et al., 2015), (Parsons et al., 2013a) presuming the presence of mixed cultures of aerobes and anaerobes. Fresh soil was sieved through 1mm, dispersed in Saone river water at density of 250 g L^{-1} and placed on the shaker at 100 rpm at room temperature for one-week equilibration. To stimulate mutual coexistence of soil and clay microorganisms during the main experimental time, 30 g L^{-1} of argillaceous substrate was added to the soil suspension. Further, 0.1 mM mixture of contaminants (As(V), Cr(VI), Sb(V) and N(V)) along with 20 mM ethanol dissolved in synthetic pore water was added to activate redox reactions. After one month of incubation mixed soil-clay suspension was let sediment during 2 min and 70 ml from the top of the supernatant was extracted and amended into 930 ml of pre-equilibrated experimental suspension, making 1 L of working solution.

3.7.3 Contaminant Speciation

Solid-phase concentration of oxidized species was determined analytically by ICP-OES after hot extraction with 0.1 M Na_2CO_3 solution (Panichev et al., 2005) for the samples collected on the last day of each experiment. Indirect quantification of the corresponding reduced species was done by subtracting concentration of the oxidized species from the total concentration of the elements measured after acidic dissolution of the solid material.

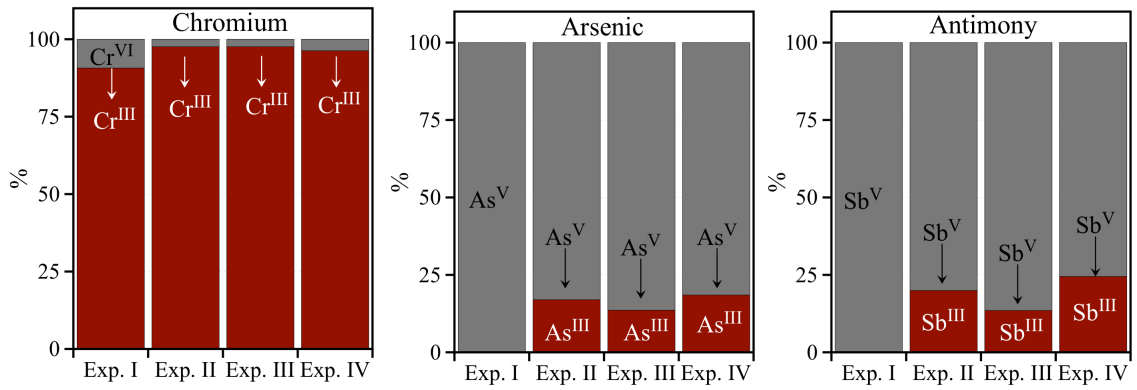

Figure 3-9. Estimated distribution of solid speciation of Cr, As and Sb by the end of the experiments.

Aqueous Cr speciation was identified based on the typical spectrum of Cr(VI) with maximal sensitivities around 272 and 373 nm (Zydorczak et al., 2012) of untreated samples. Absorption spectrum of aqueous samples of Exp. II and of Cr(VI) standards (0.5 mM and 0.25 mM) prepared freshly from dissolution of K_2CrO_4 (≥99%, SIGMA-ALDRICH) in 18Ω MQ H_2O have the same shapes and appearance time of the peaks. Spectrum of Cr(III) is different with the main peaks around 230 nm, 425 nm and 590 nm as confirmed by the absorption spectrum of Cr(III) standards prepared freshly from dissolution of $CrCl_3 \cdot 6H_2O$ (≥98%, SIGMA-ALDRICH) in 6 M NaOH. This method has been applied in the other studies showing similar absorption spectrums for Cr(VI) (Burke et al., 1972; Weckhuysen et al., 1997, 1994) and Cr(III) (Mytych et al., 2001).

Speciation of Sb was analysed by HPLC (high pressure liquid chromatography) coupled to ICP-OES according to (Lintschinger et al., 1998). Briefly, Hamilton column (PRP-X100, 4.1 9 150 mm, 10 lm) was used with mobile phase of 20 mM EDTA (Fluka), 2 mM KHP (Sigma-Aldrich) (pH 4.3) with a flow rate of 1.5 ml min^{-1} for separation of Sb(V) and Sb(III) peaks. Aqueous speciation of As(V) and As(III) was performed using the same column and mobile phase of KH_2PO_4 : K_2HPO_4 (Merk) a pH 6.25 prior to detection on ICP-OES (Roig-Navarro et al., 2001).

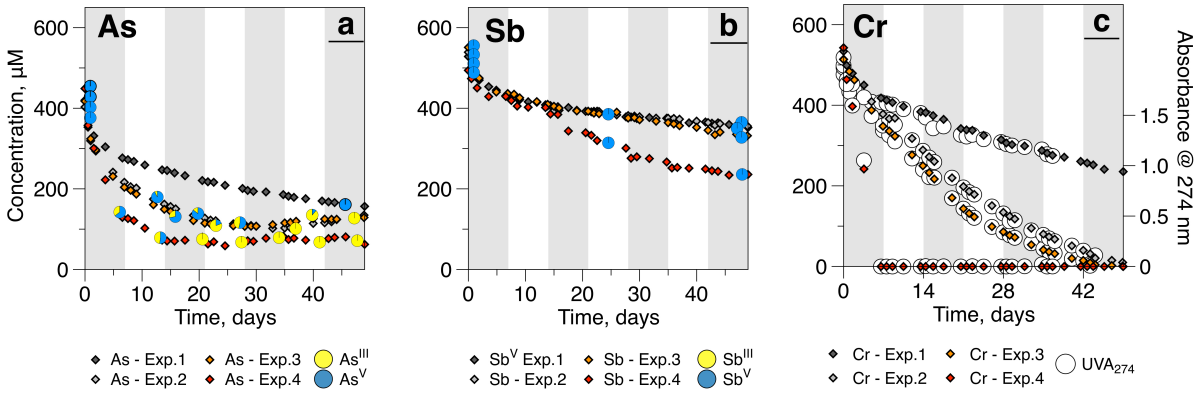

Figure 3-10. Time-series of aqueous contaminant speciation. Arsenic speciation was measured by the end of each half-cycle, Sb speciation on day 1, 24, 49, and Cr speciation on every sampling point.

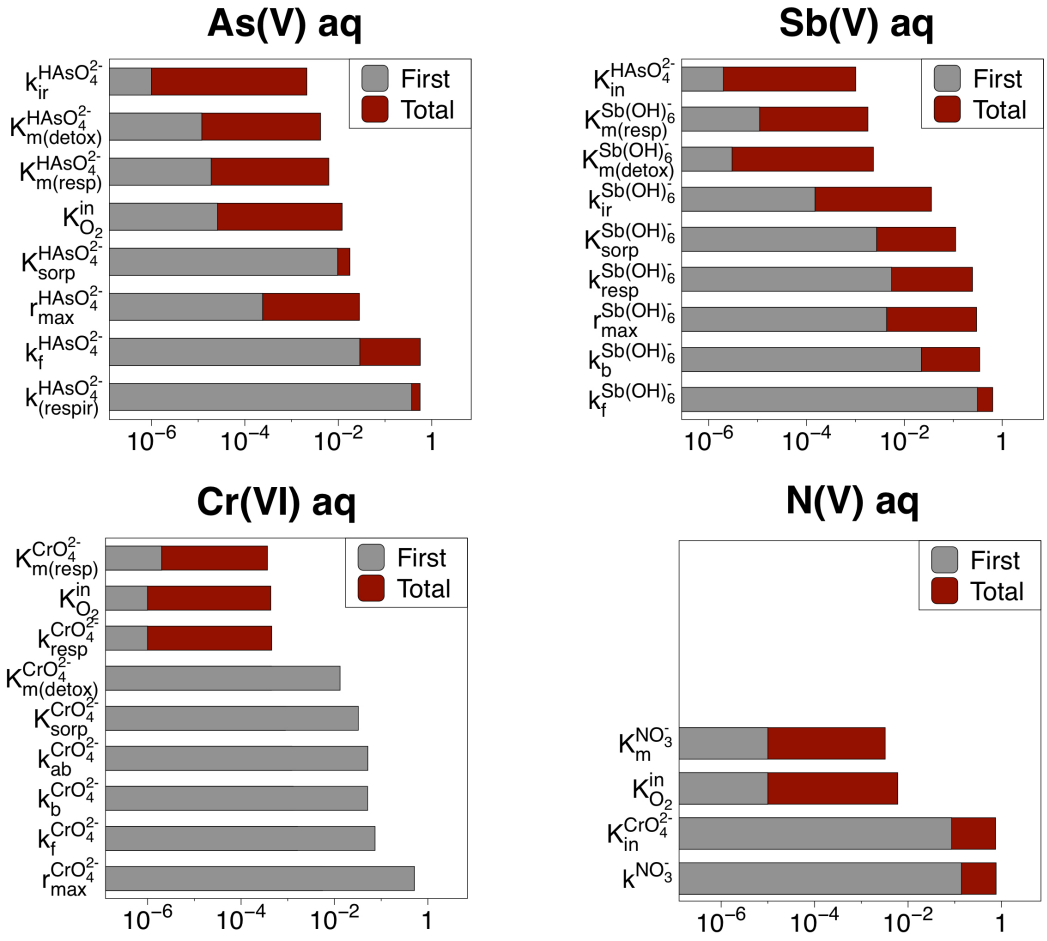

Figure 3-11. Sensitivity analyses testing one at a time ("First") input parameters and by accounting for the sum of the interaction effects ("Total") controlling aqueous contaminant concentration. Parameter abbreviations are explained in Table 3-4.

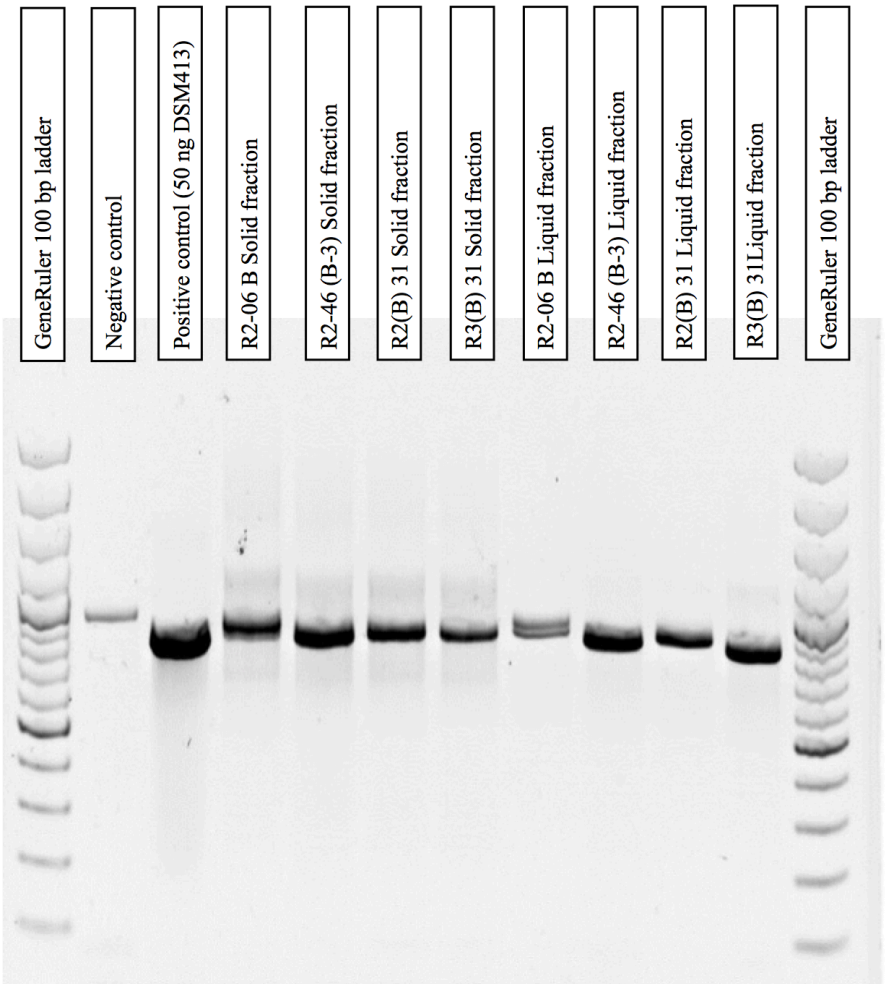

Figure 3-12. Polymerase chain reaction (PCR) of samples from Exp. III and IV indicating the presence of amplifiable DNA for prospective phylogenetic analyses.

Chapter 4

Contrasting contaminant mobility

in topsoil and subsoil:

Role of Fe- and Mn- oxyhydroxide minerals

4.1 Summary

The mobility of potentially toxic arsenic (As), antimony (Sb), and chromium (Cr) is affected by environmental conditions (e.g., redox state, microbial activity, and mineralogical composition), which vary with depth in soil profiles. As a result, the mechanisms controlling the fate of contaminants may substantially differ between the near-surface topsoil and the deeper subsoil horizons. In this chapter, I compare experimental data from two topsoil (-0.15 m) and two subsoil (-22.5 m) experiments previously described in Chapter 3 and in a published paper given in Annex-I. Although these experiments were designed as stand-alone studies there is an added value in comparing them. To facilitate the comparison, an additional modelling exercise is performed applying the multi-reaction model to describe contaminant sorption to the topsoil and subsoil mineral matrices. The key difference between two systems is the higher content of readily reducible Fe- and Mn- oxyhydroxide minerals in the topsoil suspension, which was subjected to redox oscillations between +500 mV and -300 mV. The subsoil sample has a lower content of reactive Fe and Mn minerals, while it is rich in clay (phyllosilicate) minerals. In contrast to the topsoil suspension, the subsoil suspension was less susceptible to the imposed redox oscillations, with minor E_H fluctuations between +350 mV and +250 mV conditions. The results of this comparison suggest that the contaminant mobility was largely affected by the presence of Fe- and Mn- oxyhydroxide minerals, acting not only as major sorbents, but also promoting contaminant oxidation. It led to reversible mobility of As and Sb following cycles of oxic and anoxic oscillations in the topsoil suspension, where As mobility was enhanced during anoxic phases and Sb mobility was enhanced during oxic phases. Conversely, in the absence of reactive Fe and Mn in the subsoil suspension, Sb underwent irreversible immobilization likely via microbial reductive precipitation of Sb(III), whereas reduced As(III) persisted in aqueous phase. As a strong oxidant, Cr(VI) was irreversibly removed from both experimental solutions via a combination of biotic and abiotic reductive precipitation of solid-solutions, such as $(Cr,Fe)(OH)_3$. This comparative study suggests the key biogeochemical mechanisms driving contaminant mobility in complete soil profile from oxide-rich to clay-rich mineral matrices and adds the value for safety risk assessments of environments exposed to periodic changes in redox conditions. Overall, argillaceous formation stands out as a suitable environment for contaminant retention, as it can withstand periodical redox oscillation without releasing contaminants back to the aqueous phase.

4.2 Background

The soil profile is host to a strong redox gradient from generally oxic near-surface (topsoil) to anoxic deep subsurface (subsoil) zones. Penetration of atmospheric air through the soil profile can vary with seasonal or diurnal dynamics in the temperature and water regime (e.g., precipitation, snow melt, water table fluctuations) and modulate the depth and frequency of anoxia. As a result, periodically flooded soils (e.g., floodplain soils, rice fields, wetlands) are often reported to experience natural oscillations in redox conditions (Fiedler, 2000).

Redox conditions depend, in addition to the aeration conditions, on the soil biogeochemical properties, which vary as a function of depth in the soil profile. Common to the topsoil zone (e.g., 0 to 15 cm), redox-sensitive labile organic carbon and Fe-, Mn- oxyhydroxide minerals are able to act as electron donors and acceptors (Borch et al., 2010) creating highly reactive zones of redox transformations. Such zones support diverse microbial communities capable of using redox gradients for sustaining diverse biogeochemical functions (Malkin and Meysman, 2014). Soil organic carbon content generally gets depleted within the first 10 m of profile, depending on the active rooting zone (e.g., 2.5 m in grassland, 5 m in forests, 7 m in shrubland) (O'Rourke et al., 2015). The content of readily reducible Fe and Mn minerals also decreases giving way for mineralogical domination of aluminosilicate minerals (feldspars and clays).

Soils can act as sinks for metalloids (e.g., As, Sb) and trace metals (e.g., Cr). Soil sequestration capacity for contaminants varies with soil geochemical characteristics, depth, and redox gradient. Contaminated soil is an international problem, as contaminants are often found to co-exist in the topsoil of industrially polluted areas (e.g., mining, coal combustion, smelting) (Cornelis et al., 2008; Lindsay et al., 2011; Resongles et al., 2014). Further, contaminants may be introduced into the subsoil being a part of waste disposal. In this thesis, I focus on such activities, in particular the disposal of low-level long-lived (LL-LL) radioactive waste. The disposal of LL-LL waste is being designed for shallow subsurface at a depth varying from 15 to 200 m in low permeable argillaceous formations (Andra, 2009). Although, engineered barriers are designed to protect the environment from contamination, in the worst-case scenario, the failure to do so may liberate potentially toxic chemicals in the subsurface.

The mobility and chemical reactivity of the contaminant present in the soil are governed by the contaminant concentration and speciation, which may vary as a function of temperature, pH, redox state, microbial activity, and mineralogical composition (Borch et al., 2010; Campbell and Nordstrom, 2014). In the presence of atmospheric oxygen and near-neutral pH, oxidized As, Sb, and Cr are present as oxyanions

(i.e., CrO_4^{2-}, $HAsO_4^{2-}$, $Sb(OH)_6^-$) and have generally high sorption affinities to Fe-, Mn-, and Al-oxyhydroxide minerals (Mitsunobu et al., 2006). The point of zero charge (pH_{zpc}) for Fe- and Al- oxides varies from 7 to 10 (Alloway, 1995) generating positively charged adsorbent surface attracting anions. Whereas, point of zero charge below pH 4 for silica and clay minerals (Sposito, 1998) imposes less affinity for surface complexation between negatively charged aluminosilicate minerals and oxyanions. With high solubility of minerals containing oxidized metalloids (Blowes et al., 2000), subsoil is generally considered as less efficient contaminant sink, as compared to the topsoil. Under anoxic conditions, abiotic reductive co-precipitation of contaminants with elemental Fe (Blowes et al., 2000) or biologically mediated reductive co-precipitation with sulfides (Lindsay et al., 2011) can effectively decrease oxyanion mobility across the soil profile.

Spatial heterogeneity of biogeochemical properties with depth implies that the assessment of contaminant mobility must consider the complete soil profile with oxides-rich versus clay-rich mineral matrices under dynamic oxic and anoxic conditions. Given that the deeper subsoil matrices have been less rigorously evaluated for oxyanions sequestration, a mechanistic understanding of the key processes can be better understood from the comparative examination of topsoil to subsoil systems. A comparative analysis can be drawn from existing data of two relevant stand-alone studies presented in the Thesis. Namely, here in Chapter 4, the fate of As, Sb, and Cr in subsoil argillaceous matrix under redox-oscillating conditions, which was demonstrated in Chapter 3, is compared to that in a topsoil matrix from the study given in Annex.

Admittedly, a direct association of two experimental approaches, which were not designed for a critical comparison, is not optimal. Nevertheless, as shown below, there is a significant added value in interpreting two studies together to identify the key biogeochemical drivers of contaminant mobility in saturated environments. Specifically, I hypothesized the key role of Fe- and Mn- oxyhydroxide minerals abundant in the topsoil and depleted in the subsoil in reversibility of contaminant sequestration under oxic/anoxic-oscillating conditions.

Disparities between experimental conditions (e.g., contaminant concentrations, solid to liquid ratios) limiting the power of comparative conclusions are established. To facilitate the comparison of oxyanion immobilization in topsoil and subsoil matrices, an additional modelling exercise is performed applying multi-reaction sorption model to describe both systems. The acquired knowledge of the contaminant behavior in complete soil profile can contribute to the safety assessment of natural barriers aimed to prevent contaminant migration from the radioactive waste storage sites.

4.3 Materials and Methods

4.3.1 Compiled Experimental Dataset

In this chapter, I provide a comparative study using experiments that were initially designed as stand-alone studies. Therefore, the direct comparison of experimental results on contaminant mobility is challenged by disparities between experimental conditions, which are summarized below. To systematize this comparative study, I compiled a dataset based on as many as possible similarities between the two experiments.

Out of 12 bioreactor experiments performed to examine mobility of Cr(VI), As(V), and Sb(V) in homogeneous suspensions, I selected per 2 experiments representative for subsoil and topsoil environments. Experiments with subsoil suspensions are reproduced from Chapter 3 ("Exp. I" and "Exp. IV", hereafter referred to as "Subsoil-abiotic" and "Subsoil-biotic", respectively). Experiments with subsoil suspensions comprise one out of nine published experiments given in Annex ("50-Sb+As+Cr", hereafter "Topsoil-dynamic") and an additional unpublished experiment under static oxic conditions ("Topsoil-static"). Below, I critically compare experimental conditions of subsoil and topsoil systems discussed in this chapter.

4.3.2 Similarities and discrepancies between the two experiments.

There are essential similarities between the experiments facilitating the comparative study, such as that contaminant that were examined as mixtures of oxidized oxyanions rather than individually. The contaminants were prepared by dissolving high purity analytical compounds of $Na_2HAsO_4 \cdot 7H_2O$ (≥98%, SIGMA), $KSb(OH)_6$ (≥99%, Fluka), K_2CrO_4 (≥99%, SIGMA-ALDRICH) and were injected into the experimental suspensions in the beginning of the experiments. Moreover, the same organic compound (ethanol) was imposed as a source of carbon and electrons (Wu et al., 2007). A concentration of ~5 mM and 10 mM ethanol (C_2H_5OH≥99.8%, Sigma-Aldrich) (Table 4-1) was added to the "Subsoil-biotic" and "Topsoil-dynamic" experiments at the beginning of each of the anoxic periods.

All batch experiments discussed in this chapter were performed using the same bioreactor system described on page 44 (Chapter 3, section *Materials and Methods*). Redox oscillations were induced by the alternate sparging of the suspensions with oxic (O_2 + N_2 + CO_2) and anoxic (N_2 + CO_2) gases. Gas composition differed between the topsoil and subsoil experiments by carbon dioxide content with regard to near-surface and subsurface natural conditions, and accounted for 0.03% and 1% CO_2, respectively (Table 4-3). Meanwhile, pCO_2 was kept constant between oxic and anoxic periods within each experiment

to maintain stable pH and carbonate chemistry. Each of the redox-oscillating suspensions was subjected to at least three full 14-day cycles of oxic (7 days) and anoxic (7 days) periods. The E_H and pH data were recorded in situ within the reactor vessel every 2 minutes using solid polymer open junction pH and redox electrodes (Mettler-Toledo Xerolyt Solid).

Table 4-1. The key similarities in experimental conditions of topsoil and subsoil suspensions.

	Similarities between experimental conditions	
	Topsoil suspension	**Subsoil suspension**
Contaminant mixture	Cr(VI)+As(V)+Sb(V)	Cr(VI)+As(V)+Sb(V)
Added organic carbon	C_2H_5OH (ethanol)	C_2H_5OH (ethanol)
Suspension pH	7.8±0.2	7.1±0.1
Oxic gas phase	$O_2 + N_2 + CO_2$	$O_2 + N_2 + CO_2$
Anoxic gas phase	$N_2 + CO_2$	$N_2 + CO_2$
Oxic/anoxic periods	7 days	7 days

A difference relevant for the comparison is that samples of topsoil and subsoil matrices were taken at different depths and locations. The top horizon (0-15 cm) of a Mollic Fluvisol was sampled from the first flood stage of the Saône River close to the town of Trévoux (eastern France). The subsoil sample was collected at 22.5 m depth of the Gault formation (north-eastern France). Experimental performance using a system of bioreactors required samples sieving through a 1 mm screen to remove large sand grains and organic debris. Homogenized samples were dispersed at different solid to liquid ratios: 100 g of the topsoil sample in 1 L of Saone river water and 50 g of the subsoil sample in 1 L of synthetic argillaceous pore water. Both aqueous matrices contained alternative to oxidized contaminants electron acceptors, such as sulfate and nitrate (Table 4-2). The ionic strength of experimental suspensions differed by an order of magnitude with higher strength of the electric field of the subsoil (0.05 M) than the topsoil (0.005 M) suspensions.

Nevertheless, several other disparities in experimental conditions between topsoil and subsoil batch experiments potentially limit the power of conclusions drawn. The key parameters that were different between the experiments are summarized in Table 4-3. They include, for example, different contaminant concentrations, solid to liquid ratios, and ionic strengths.

Table 4-2. Cationic and anionic composition of Saone river water and synthetic pore water.

Cations and anions	Saone river water [mM]	Synthetic pore water [mM]
SO_4^{2-}	0.5	4.44
NO_3^-	0.8	0.5
HCO_3^-	2.8	2.85
CO_3^{2-}	no data	0.31
Ca^{2+}	no data	3.09
Mg^{2+}	no data	1.94
NH_4^+	no data	0.5
Sr^{2+}	no data	0.25

Table 4-3. The key disparities in experimental conditions of topsoil and subsoil suspensions.

	Disparities between experimental conditions	
	Topsoil suspension	Subsoil suspension
Density of suspension	100 g L^{-1}	50 g L^{-1}
Experimental matrix	Saone river water	Synthetic pore water
Contaminant concentrations	50 μM	500 μM
Ionic strength	0.005 M	0.05 M
Zeta potential	-18 mV	-28 mV
Experimental temperature	30 °C	25 °C
Gas phase pCO_2	0.03% = $10^{-3.5}$ atm	1.0% = 10^{-2} atm

4.3.3 Solid, Microbial, and Aqueous Analyses

Subsoil and topsoil samples were characterized prior to bioreactor experiments for their mineralogical (powder XRD) and elemental (ICP-OES following complete acidic dissolution) (Table 4-5) compositions. Fraction of reactive Fe and Mn particles was assessed following the selective extration of amorphous readily reducible phases by citrate-bicarbonate-dithionite solution (Jackson et al., 1986) (Table 4-5). Total organic matter fraction was quantified by loss on ignition at 110 °C (Table 4-5). Topsoil samples were analyzed for phylogenetic and functional analyses of the microbial community (Parsons et al., 2013a). Subsoil samples were not characterised for the microbial community with certainty, though, preliminary PCR analysis indicates that the samples contain amplifiable DNA (see Figure 3-12).

Sampling for aqueous analyses was performed with the same frequency four times per oxic/anoxic period using gas-tight sterile syringes in both systems. Samples were subsampled and preserved under an O_2-free atmosphere in a glove box (Jacomex BS 531, EP20Ra-nm purification, 100% N_2, < 1 ppm O_2) during anoxic periods. The suspension was immediately centrifuged (4000 rpm) and filtered to 0.2 μm (cellulose hydrophilic membrane, Chromafil RC, ROTH). Aliquots for total aqueous concentrations were acidified by HNO_3 to pH < 3 and stored at 4 °C. The filtered supernatant was flash frozen with liquid nitrogen and stored at -80 °C prior to aqueous speciation analysis.

Anion speciation (NO_3^-, SO_4^{2-}, Cl^-) was analyzed by ion chromatography (Metrohm 761 Compact IC). Total aqueous concentrations of As, Sb, Cr, Fe, and Mn were measured by inductively coupled plasma optical emission spectrometry ICP-OES (Varian 720 ES). Matrix-matched standards were prepared with 18 MΩ cm^{-1} water (Millipore) and analytical grade chemicals. Dissolved organic carbon (DOC) concentrations were determined on a carbon analyzer (Shimadzu TOC-Vcsn). Speciation measurements of As, Sb, and Cr were performed on selected Subsoil-abiotic and Subsoil-biotic samples. Aqueous speciation of Cr was assessed using UV-Vis spectrophotometry at 272 and 373 nm (Rai et al., 2007; Zydorczak et al., 2012). Speciation of aqueous As (Roig-Navarro et al., 2001) and Sb (Lintschinger et al., 1997) was measured by high performance liquid chromatography (HPLC) coupled to ICP-OES using a Hamilton anion exchange column (PRP-X100, 4.1 9 150 mm, 10 mm). Solid-phase fraction of Cr(VI) was determined by ICP-OES after leaching with 0.1 M Na_2CO_3 solution (Panichev et al., 2005).

4.3.4 Biogeochemical Modelling

Aqueous concentrations of Cr, As, and Sb in Subsoil-abiotic and Topsoil-static experiments were modelled applying a multi-reaction sorption scheme (Figure 3-1 (A), Chapter 3) (Zhang and Selim, 2005). This model accounts for reversible and irreversible sorption reactions between dissolved contaminants and a generic surface (topsoil or subsoil). Derived equilibrium constants and rate constants of adsorption, desorption, and irreversible complexation (Table 4-7) incorporate competitive interactions between contaminants and other dissolved species present in suspensions (Selim and Zhang, 2013). The reaction scheme was implemented in PHREEQC v.3.1.7 (Parkhurst and Appelo, 2013) and parameters were calibrated in Python (see code in Annex-II, page 146) to minimize the root-mean-square error (RMSE) between the multi-reaction model and experimental data. Although it is not optimal to compare contaminant behavior with parameter values that are specific to experimental conditions (Table 4-1),

application of the same model allowed relative comparison of Cr, As, and Sb sorption in systems with high degree of mineralogical heterogeneity and, likely, different densities of sorption sites.

Partition coefficients (Kd), as a measure of contaminant distribution between solid and aqueous phases, were calculated for Cr, As, and Sb in the Subsoil-abiotic and Topsoil-static experiments following Equation 3-23 (Table 4-6). There is a practical advantage of calculating Kd values normalized per suspension density, as they can be used in formulating the retardation factors in contaminant transport codes. However, there is a considerable uncertainty in Kd values that are specific to experimental conditions (e.g., pH, temperature, ligands) and it is important to account for this in assessment applications. The assumptions of the use of Kd values include a thermodynamic equilibrium, reversibility of sequestration reactions, and linear relationship between sorbed and non-sorbed species of the element.

The fate of contaminants in the Subsoil-biotic and Topsoil-dynamic experiments was reproduced in PHREEQC v.3.1.7 and v.3.1.2, respectively (Parkhurst and Appelo, 2013). The WATEQ4F database augmented with the additional constants selected from literature (Table 3-11 and Table 6-6) was used in both models. Cycles of oxic and anoxic conditions were implemented by alternating the equilibrium headspace composition using the PHREEQC keyword (hereafter capitalized words) GAS_PHASE and input parameters of $O_2(g)$ = 0.2 atm (oxic), $CO_2(g)$ = 0.0003 atm (topsoil anoxic), and $CO_2(g)$ = 0.01 atm (subsoil anoxic). The pH of solutions was set by equilibrium with pCO_2 and calcite buffering introduced via EQUILIBRIUM_PHASES. Mineralogical composition in equilibrium with the solution was reproduced in a block EQUILIBRIUM_PHASES. The keyword SURFACE was used to define the surface complexation properties of the topsoil (ferrihydrite with weak and strong site proportion) and subsoil (generic surface) matrices. Sorption of CO_3^{2-}, Fe^{2+}, AsO_4^{3-}, AsO_3^{3-}, $Sb(OH)_6^-$, and $Sb(OH)_3$ on ferrihydrite in the Topsoil-dynamic suspension was modeled using diffuse double layer complexation with user-defined equilibrium constants selected from the literature (Table 6-6). Microbially driven reductions of oxidized species were represented by second-order reactions with respect to organic carbon and contaminant concentrations.

4.4 Results and Discussion

4.4.1 Redox Oscillations in Topsoil and Oxic/Anoxic Oscillations in Subsoil

Sparging with oxic and anoxic gas mixtures resulted in reproducible E_H fluctuations that differed substantially between the topsoil and subsoil suspensions. In the Topsoil-dynamic suspension, as expected, a change to anoxia led to the reversible E_H decrease from +500 to -300 mV, representing redox-

oscillating conditions over 800 mV (Figure 4-2). Such range of E_H fluctuations is frequently observed in natural topsoils, for example, in response to daily precipitation (Figure 4-1), and is likely induced via both abiotic and microbial forcing. Observed experimental E_H oscillations were negatively correlated with pH in the range from pH 7.5 to 8.0 ($r = -0.32$, $p < 0.005$). This pH range is consistent with calcite buffering via its precipitation in response to reduction reactions consuming protons and its dissolution during oxidation reactions releasing protons suggesting a variety of redox transformations, thus, redox-oscillating conditions. According to thermodynamics, E_H down to -300 mV is favorable for the reduction reactions of the oxidized species present in the media: including CrO_4^{2-}, $MnOOH_{(s)}$, $Sb(OH)_6^-$, $HAsO_4^{2-}$, and α-$FeOOH_{(s)}$ (Table 4-4). Redox scale showing the theoretical succession of equilibrium redox potentials at pH 7 for dominant aqueous species of O, Cr, Mn, N, Sb, As, and Fe is demonstrated in Figure 4-3. Thus, over the experimental range, E_H could be controlled by transformations in inorganic redox couples. Alternatively, considering that topsoil matrix comprised 33.4 mg g^{-1} organic fraction (Table 4-5), measured E_H oscillations could be controlled by a variety of organic redox couples typically found in soil humic substances (Brezonik and Arnold, 2011; Klüpfel et al., 2014)

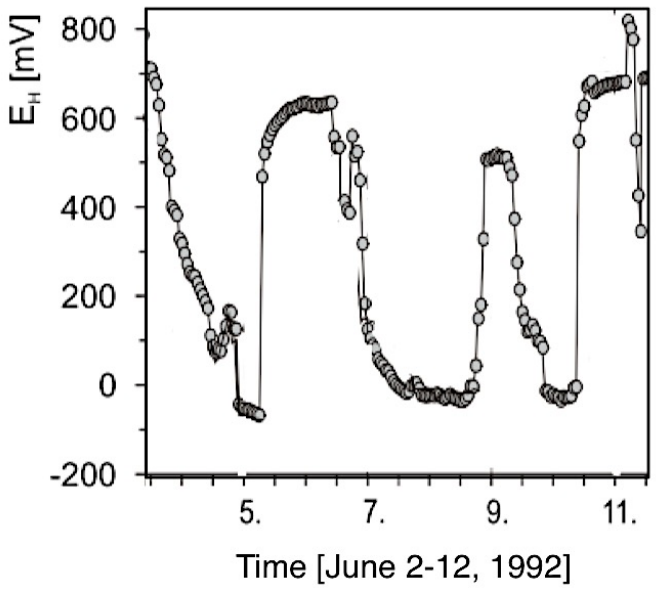

Figure 4-1. Measured E_H of the Aeric Humaquept topsoil (Germany) in response to precipitation during the period from June 2 to June 12 (1992). Reprinted with modifications from Schuring et al. (1999).

In the subsoil suspensions, alternating oxygenated and anoxic headspace resulted in minor E_H fluctuations. The measured E_H values corresponded to suboxic conditions (Sposito, 1989), which were previously reported for argillaceous suspensions (Parsons, 2011). In Subsoil-abiotic suspension, measured

E_H varied by less than 20 mV (from +368 to +338 mV) between oxic and anoxic periods, likely due to inhibited microbial activity and the lack of redox transformations. Such small E_H fluctuations, thus, were controlled by dissolved oxygen saturation demonstrating oxic/anoxic, rather than redox oscillating conditions. The E_H in Subsoil-biotic experiment fluctuated over a greater range of 100 mV (from +350 mV to +250 mV), possibly induced by microbial activity (Hunting and Kampfraath, 2013; Oktyabrskii and Smirnova, 2012). In contrast to the Topsoil-dynamic experiment, pH was stable over Subsoil-abiotic (pH = 7.2) and Subsoil-biotic (pH = 6.9) experiments and did not fluctuate with the changing E_H values. The pH remained near-neutral being buffered by calcite, HCO_3^- in synthetic pore water and by pCO_2 in the gas phase, as confirmed by PHREEQC calculations ($pH_{PHREEQC}$ = 7.2).

The reduction reactions of As(V) and Sb(V) at near-neutral pH are theoretically favorable when the standard redox potentials are lower than +200 mV (Table 4-4). Here, despite the E_H remained above +250 mV, both As and Sb underwent reduction reactions (for details see Chapter 3, section *Results*). Meanwhile, thermodynamically favorable oxidation reactions of Cr, As, and Sb above +200 mV were kinetically limited in the subsoil suspension on the experimental time scale (7 days oxic cycles). These results demonstrate that attempts to relate measured E_H to the activities of As, Sb, and Cr should be avoided.

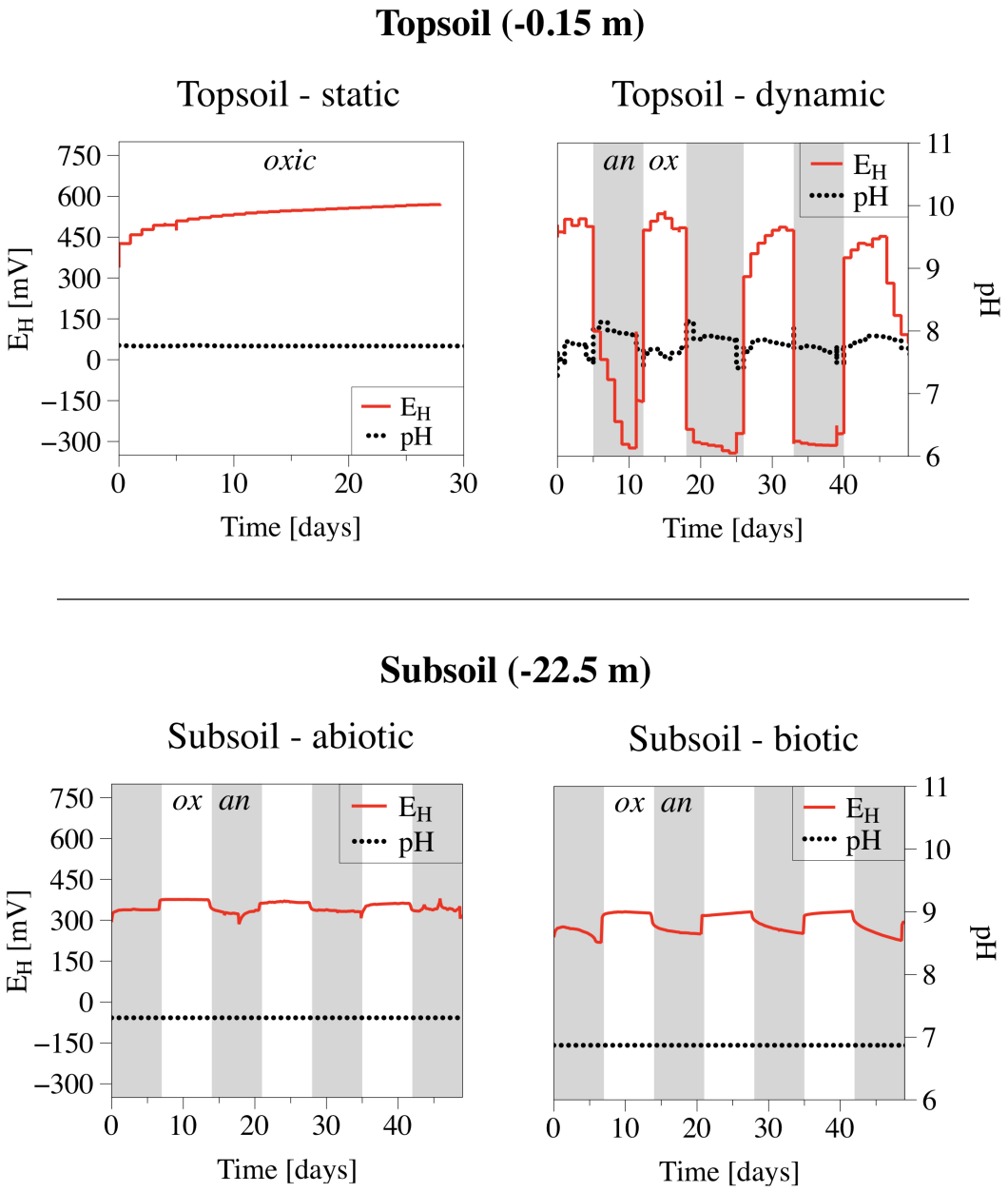

Figure 4-2. Time series of pH (dash line) and redox potential (solid line) with regard to the standard hydrogen electrode (E_H, SHE) measured in the experimental suspensions. The Topsoil-dynamic, Subsoil-abiotic, and Subsoil-biotic suspensions were exposed to oscillating oxic ($O_2/N_2/CO_2$) and anoxic (N_2/CO_2) conditions. The Topsoil-static suspension was maintained under constant oxic conditions.

Table 4-4: Thermodynamic sequence based on the standard redox potential of half reduction reactions at pH 0 ($E_H°$) and pH 7 ($E_H°'$). Thermodynamic order of As and Sb reductions differs depending on pH and activities of redox species (E_H). Calculations are based on the thermodynamic values given in Bard et al. (1985); Filella and May (2003); Nordstrom et al. (2014); Tratnyek and Macalady (2000); Zotov et al. (2003), experimental pH (6.9) and concentrations of Cr, As, and Sb in the Subsoil-biotic experiment. Experiments depleted in Mn oxides (e.g., manganite, $MnOOH_{(s)}$) and Fe oxides (e.g., goethite, α-$FeOOH_{(s)}$) are indicated.

Reduction reactions	E_H [mV] pH 6.9	$E_H°'$ [mV] pH 7	$E_H°$ [mV] pH 0
$O_2 + 4\ H^+ + 4\ e \rightarrow 2\ H_2O$	816	816	1230
$CrO_4^{2-} + 5\ H^+ + 3\ e \rightarrow Cr(OH)_3 + H_2O$	524	579	1270
$MnOOH_{(s)} + 3\ H^+ + e \rightarrow Mn^{2+}_{(aq)} + 2\ H_2O$	depleted	490	1500
$NO_3^- + 2\ H^+ + 2\ e \rightarrow NO_2^- + H_2O$	316	426	840
$HAsO_4^{2-} + 4\ H^+ + 2\ e \rightarrow H_3AsO_3 + H_2O$	160	18	846
$2\ Sb(OH)_6^- + 6\ H^+ + 4\ e \rightarrow Sb_2O_3 + 9\ H_2O$	130	218	839
$Sb(OH)_6^- + 3\ H^+ + 2\ e \rightarrow Sb(OH)_3 + 3\ H_2O$	188	91	712
α-$FeOOH_{(s)} + 3\ H^+ + e \rightarrow Fe^{2+}_{(aq)} + 2\ H_2O$	depleted	-571	769
$CO_2 + 12\ H^+ + 12\ e \rightarrow C_2H_5OH$ (ethanol) $+ 3\ H_2O$	-795	-356	90

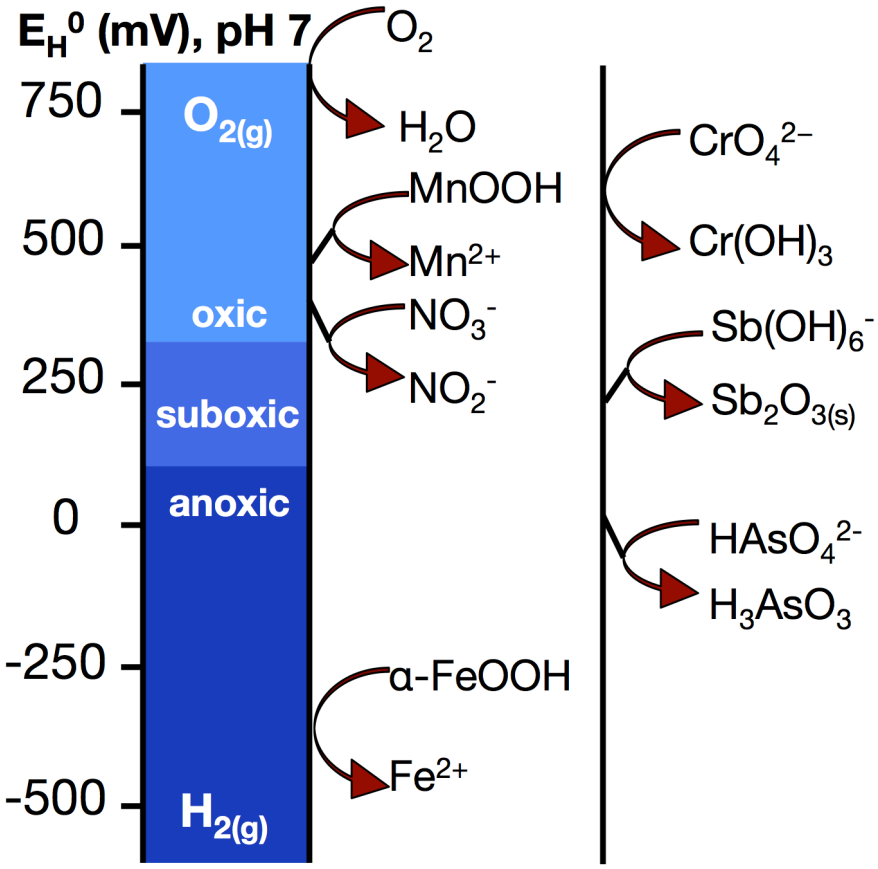

Figure 4-3. Redox scale showing the theoretical succession of equilibrium redox potentials ($E_H°$ in mV) at pH 7 for dominant species of major nutrients (O, Mn, N, Fe) and contaminants (Cr, Sb, As). Oxidized Mn and Fe are demonstrated as manganite ($MnOOH_{(s)}$) and goethite (α-$FeOOH_{(s)}$), respectively. Calculations based on the thermodynamic values given in (Bard et al., 1985; Filella and May, 2003; Nordstrom et al., 2014; Zotov et al., 2003) and are summarized in Table 4-4.

4.4.2 Reactivity of Fe and Mn in Topsoil and Subsoil Suspensions

Powder XRD and ^{57}Fe Mössbauer spectroscopy of topsoil sample prior to bioreactor experiments revealed relatively high content of total Fe comprising Fe(III)-oxyhydroxides (goethite), amorphous Fe, and Fe-rich clay minerals (illite and chlorite), described elsewhere (Parsons et al., 2013a). In contrast, the subsoil was dominated by clay minerals containing little Fe (muscovite, smectite, and kaolinite), depleted in Fe(III)-oxyhydroxides, and reducible Fe (Table 4-5).

The dispersion of the topsoil sample in river water under oxic conditions (Topsoil-static) did not release any Fe and Mn ions into the solution, which remained below detection limit (0.05 μM) over 35 days (Figure 4-4). Conversely, both metals were found in the aqueous phase of Topsoil-dynamic suspension during each of anoxic phases (up to 40 μM of Fe and 80 μM of Mn). The oscillation between oxic and anoxic conditions, thus, led to a reversible mobilization of Fe and Mn likely via microbially induced reductive dissolution and chemical re-oxidation of minerals. In contrast to the reactive mineral fraction of the topsoil sample, the lack of readily reducible amorphous minerals in the subsoil sample was supported by the low concentrations (~4 μM) of dissolved metals, which remained non-reactive during the redox oscillations.

Table 4-5. Composition of the topsoil and subsoil matrices after total acidic dissolution and citrate-bicarbonate-dithionite (CBD) extractions (selected data). Concentrations of As and Sb were lower than the limit of detection (LOD) (0.01 mg g^{-1}).

Parameter	Topsoil [mg g^{-1}]	Subsoil [mg g^{-1}]
Organic matter	33.4	1.8
Fe tot	92.4	35.51
Fe (CBD)	9.04	1.60
Mn tot	2.9	0.25
Mn (CBD)	0.42	0.04
Al tot	no data	74.57
Al (CBD)	0.93	0.24
Si	652.5	264.42
Ca	197.8	57.88
K	47.8	18.75
Ti	11.6	4.46
As	0.029	<LOD
Cr	0.065	0.15
Sb	no data	<LOD
U	0.003	no data

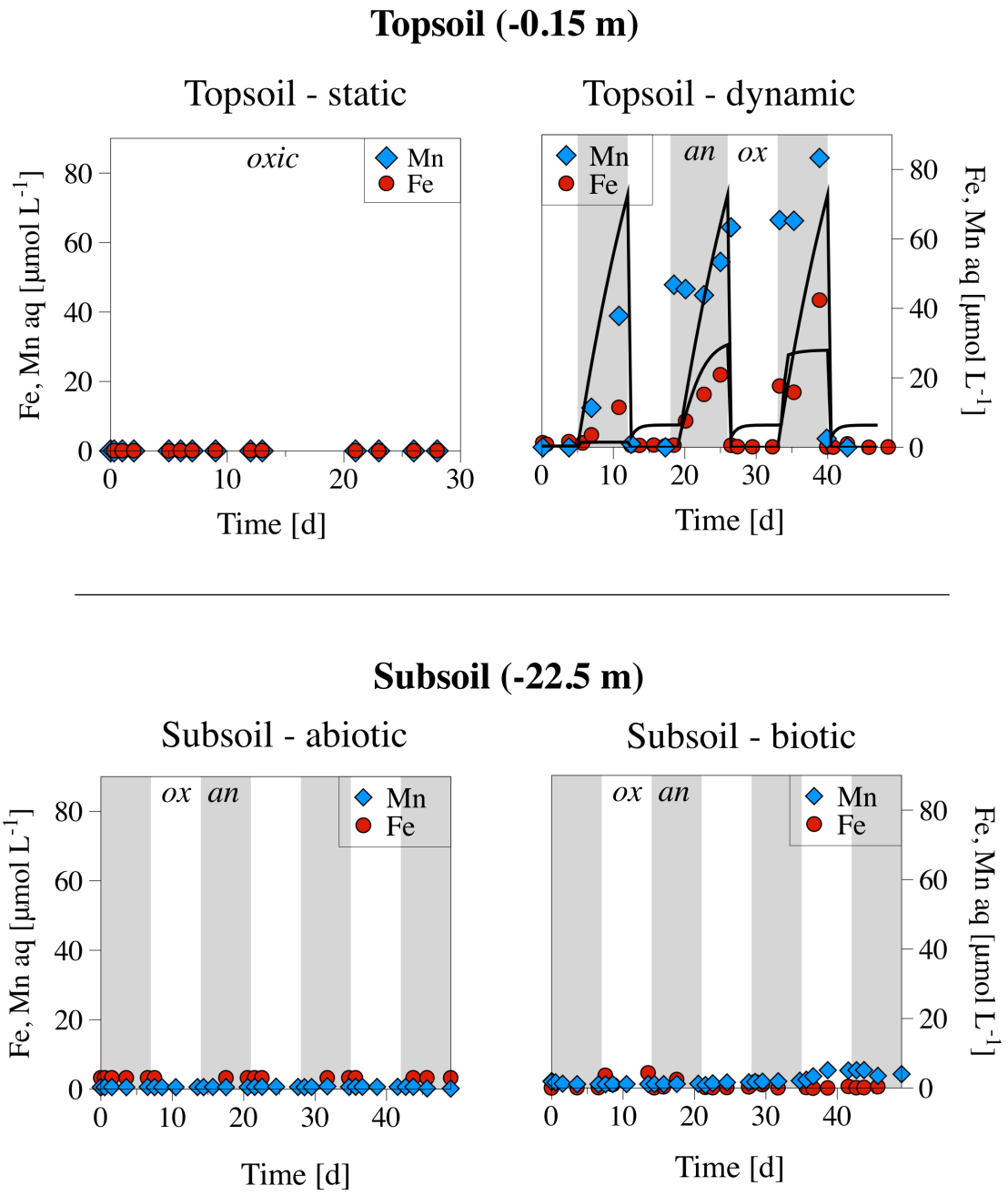

Figure 4-4. Time series of measured (symbols) and modeled (lines) dissolved Fe (circle) and Mn (rhombus) in the topsoil and subsoil suspensions. The results indicate the readily reducible mineral fraction in the topsoil matrix and the lack of redox reactive minerals in the subsoil matrix.

4.4.3 Contaminant Sequestration by Topsoil and Subsoil Matrices

Steady-state conditions between aqueous and solid fractionation of Cr, As, and Sb in the topsoil suspension were achieved by the end of the Topsoil-static experiment (Figure 4-5). Therefore, the Kd values were calculated based on the difference between the initial and remaining aqueous contaminant concentrations by day 35 (Table 4-6). In contrast, contaminant concentrations in Subsoil-abiotic suspension were continuously changing even after 49 days of reaction time. Therefore, Kd calculations for the subsoil experiment included equilibrium contaminant concentrations predicted by the predictive model for As on day 113 (137 μM), Sb on day 72 (356 μM), and Cr on day 400 (1 μM). Oscillating oxic and anoxic conditions in the subsoil suspension did not affect contaminant sequestration under abiotic conditions and the Kd values of Cr sequestration compares well with the Kd values reported for Callovo-Oxfordian clay suspensions (Parsons, 2011). Overall, comparison of Kd values suggest that the topsoil matrix was a better sorbent for the As(V), Sb(V), and Cr(VI) oxyanions than the subsoil likely due to (1) higher content of Fe-, Mn-, and Al- fractions, (2) higher zeta potential of the suspension, and (3) lower ionic strength of the bulk solution, as compared to the subsoil suspension (Table 4-3 and Table 4-5).

Table 4-6. Partition coefficients (Kd) for sequestration of oxidized Cr, As, and Sb by topsoil and subsoil suspensions. For details on experimental conditions (e.g., pH, ionic strength) see Table 4-1 and Table 4-3.

Experiment	Sorbate	Kd (L kg^{-1})
Topsoil - static	As(V)	169
	Sb(V)	33
	Cr(VI)	12 500
Subsoil - abiotic	As(V)	47
	Sb(V)	10
	Cr(VI)	11 110

4.4.3.1 Instantaneous uptake of As in topsoil and kinetically controlled As uptake in subsoil

Considerable As(V) sequestration was observed in the Topsoil-static experiment, with decreasing initial contaminant concentration by > 90% by day 1. In contrast, less than 30% As(V) sequestration occurred in the Subsoil-abiotic suspension within the same time interval (Figure 4-5). Multi-reaction sorption model suggests that As sequestration followed a two-step process in both experimental suspensions: fast sorption described by an equilibrium constant (log $K_{topsoil}$ = 0.811 and log $K_{subsoil}$ = -0.542) and slow kinetic uptake

represented by reversible adsorption (k_f) and desorption (k_b) and irreversible sorption (k_i) rate constants (Table 4-7).

Table 4-7. Multi-reaction sorption parameters of As(V), Sb(V), and Cr(VI) fitted to the time series of aqueous contaminant concentrations: equilibrium constant (log K), forward (k_f), backward (k_b), and irreversible (k_i) rate constants. Kinetically controlled reactions follow 1st-order rate equations.

Experiment	Sorbate	log K	k_f (h^{-1})	k_b (h^{-1})	k_i (h^{-1})	RMSE
Topsoil - static	As(V)	0.811	2.3×10^{-1}	2.3×10^{-2}	6.1×10^{-2}	0.1
	Sb(V)	-24.7	9.0×10^{-3}	3.4×10^{-3}	1.7×10	1.65
	Cr(VI)	0.362	5.8×10^{-3}	2.3×10^{-4}	8.1×10	0.60
Subsoil - abiotic	As(V)	-0.542	3.0×10^{-3}	5.8×10^{-3}	2.3×10^{-3}	1.55
	Sb(V)	-1.075	1.1×10^{-3}	4.2×10^{-3}	6.7×10^{-4}	3.01
	Cr(VI)	-1.027	4.0×10^{-3}	3.8×10^{-2}	0.0	6.54

Equilibrium As sequestration may involve a non-specific adsorption via the formation of outer-sphere complexes at constant surface charge sites of minerals (Charlet et al., 2011). This mechanism of sorption is generally affected by ionic strength with a decrease of sorption at increasing ionic strength (Lützenkirchen, 1997). Considering an order of magnitude difference in ionic strengths of the experimental suspensions (Table 4-1), lower As sequestration in the subsoil experiment might be partly due to a decrease in As activity at the solid-solution interface. Another rapid surface complexation mechanism could be the formation of a monodentate inner-sphere complex through a ligand exchange mechanism, whereas, the rate-limiting As uptake could involve conversion of monodentate to bidentate inner-sphere complexes (Grossl et al., 1997). Relatively low desorption rate constant ($k_{b(topsoil)} = 2.3\times10^{-2}$ h^{-1}) may suggest that a high activation energy of dissociation is required, which is consistent with the discussion of Farrel & Chaudhary (2013) on As(V) release from uncharged bidentate complexes with ferric hydroxides (Farrell and Chaudhary, 2013).

The most effective As retaining minerals are poorly crystalline oxyhydroxides (Fe, Mn, Al) forming monodentate and bidentate binuclear and mononuclear complexes (Charlet et al., 2011; Couture et al., 2013a; Wilson et al., 2010). In fact, the CDB extractable fraction of these minerals was eleven times higher in the topsoil suspension (1039 mg L^{-1}) than in the subsoil (94 mg L^{-1}) suggesting its major control on As mobility in the topsoil suspension. The correlation between As sorption and content of oxyhydroxide minerals has been widely reported by other researches, where As adsorption behavior in

natural soils was well comparable with that on pure ferric oxides (B. A. Manning and Goldberg, 1997; Zhang and Selim, 2005). Similarly, we observe a good agreement between As(V) sorption in the topsoil suspension examined in this study (Table 4-7) and As(V) sorption on a synthetic 2-lines ferrihydrite (2l-Fh) (log K = 1.0, $k_f = 0.6\ h^{-1}$, $k_b = 0.6\ h^{-1}$, $k_{ir} = 0.002\ h^{-1}$), reported by Couture et al. (2013).

In the subsoil suspension, clay minerals (muscovite, smectite, kaolinite, biotite, and chlorite) may offer reactive surface functional groups and a large specific surface area typical of small-sized particles for As complexation. However, at neutral experimental pH (7.2), the surface functional groups are expected to be mainly deprotonated (e.g., pH_{zpc} of kaolinite = 3.5) (Xi et al., 2010) resulting in electrostatic repulsion with negatively charged As(V). Lower sorption affinity of As oxyanion to the subsoil matrix than to the topsoil matrix is consistent with more negative zeta potential of the subsoil suspension increasing electrostatic repulsion (Table 4-1). That is, a continuous decrease of aqueous As(V) concentration in the subsoil suspension over experimental time could be favored by non-specific sorption on (1) positively charged broken clay edges (Lin and Puls, 2000; Wilson et al., 2010), (2) negatively charged clay surfaces (e.g. kaolinite) at neutral pH via a cation (e.g., Ca^{2+}) bridging (Sharma and Kappler, 2011), or (3) a hydroxide interlayer in the clay structure of chlorite (Lin and Puls, 2000). Finally, the presence of competing ligands in pore water (Table 4-2), such as sulfate (SO_4^{2-}) and bicarbonate (HCO_3^-) may compete for sorption sites and increase As mobility in the subsoil solution (Appelo et al., 2002).

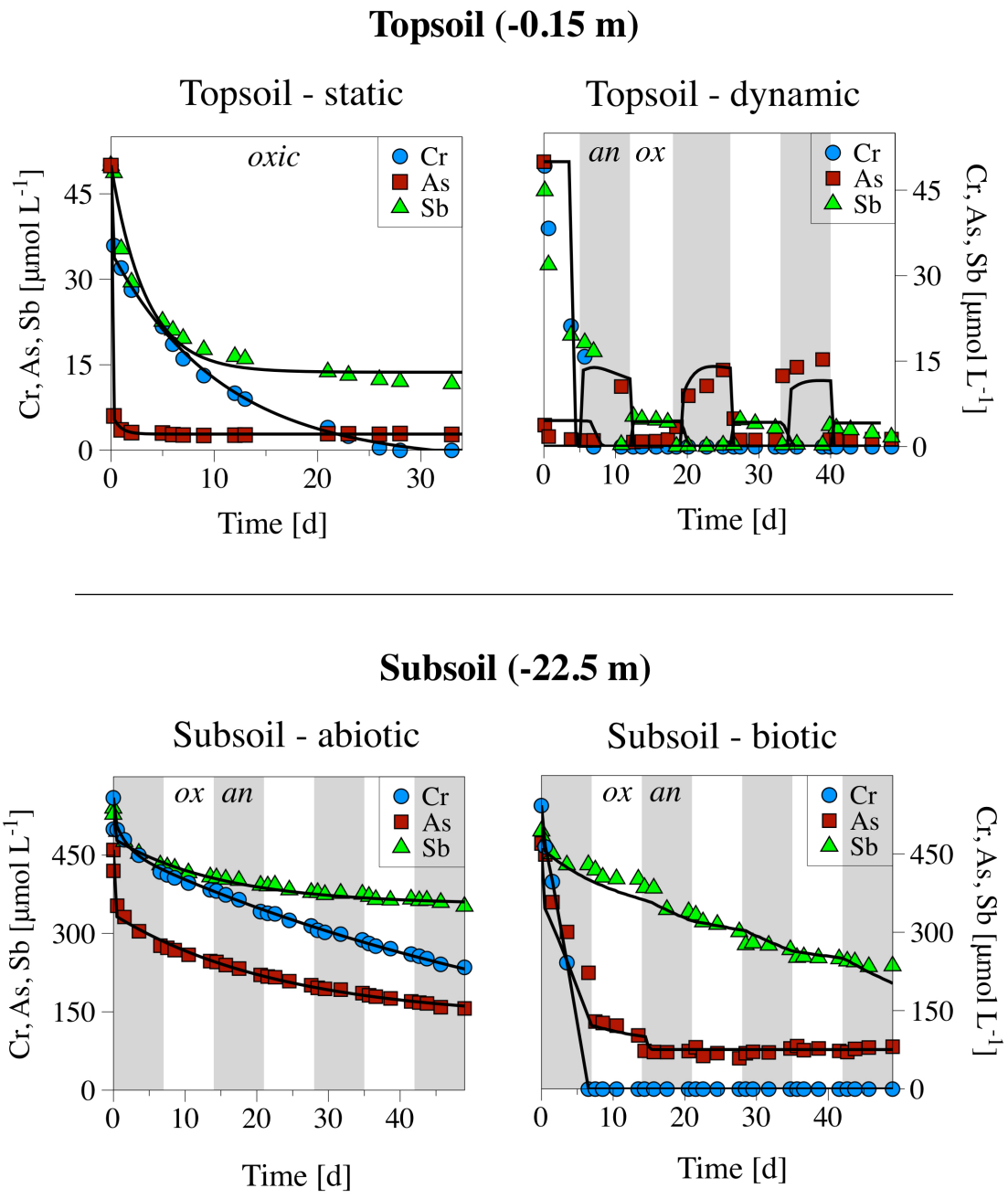

Figure 4-5. Time series of measured (symbols) and modeled (solid line) total aqueous concentrations of As (square), Sb (triangle), and Cr (circle) in topsoil and subsoil suspensions. Contaminant sequestration is reversible following oxic/anoxic cycles in the Topsoil-dynamic experiment and irreversible in the Subsoil-abiotic and Subsoil-biotic experiments.

4.4.3.2 Low sorption affinity of Sb to topsoil and subsoil matrices

Similar to aqueous As, immobilization behavior of Sb in natural soil systems and synthetic solutions has been reported to correlate with the abundancy of Fe-, Mn-, and Al- oxyhydroxides, acting as effective host phases for Sb complexation (Casiot et al., 2007; Crecelius et al., 1975; Ilgen and Trainor, 2012; A. Leuz et al., 2006; Mitsunobu et al., 2006). Nevertheless, Sb(V) uptake by topsoil matrix in the Topsoil-static experiment was less than that of As(V), as also reported by Casiot et al. (2007). Relatively low desorption and high irreversible sorption constants ($k_{b(subsoil)}$ = 3.4×10^{-3} h^{-1} and $k_{ir(subsoil)}$ = 17 h^{-1}) suggests that Sb(V) sorbs strongly to the topsoil mineral matrix. At neutral pH, a strong inner-sphere Sb complexation with Fe minerals was previously reported (Ilgen and Trainor, 2012; A. Leuz et al., 2006; Vithanage et al., 2013). Overall, modelling results suggest a slow kinetically-controlled reaction of Sb uptake in both topsoil and subsoil systems ($k_{f(topsoil)}$ = 9.0×10^{-3} h^{-1} and $k_{f(subsoil)}$ = 1.1×10^{-3} h^{-1}).

Among clay minerals, solid-solution interactions of Sb have been studied more intensively in kaolinite systems than on any other clay mineral (Ilgen and Trainor, 2012; Xi et al., 2016, 2013). In the subsoil suspension, the relatively high backward and low irreversible rate constants estimated by the model suggest that Sb(V) uptake is reversible, which is in agreement with Sb(V) sorption/desorption on kaolinite at similar experimental conditions (I = 0.02 M, pH = 7-8, 25 °C) (Xi et al., 2010). Moreover, at near-neutral pH, the Kd values of Sb(V) in kaolinite suspension are estimated to be from 73 to 115 L kg^{-1} according to the experimental data of Rakshit et al. (2015). This Kd range is consistent with the Kd value (9.78 L kg^{-1}) calculated for the subsoil suspension, considering ten times lower kaolinite fraction in the argillaceous sample as compared to pure kaolinite in Rakshit et al. (2015) experiments.

4.4.3.3 Sorption and abiotic reductive precipitation of Cr

In contrast to As(V) and Sb(V) sequestration, aqueous Cr(VI) concentration was continuously decreasing in Topsoil-static and Subsoil-abiotic experiments (Figure 4-5). In Topsoil-static suspension, Cr concentration decreased below detection limit (0.05 μM) by day 28 with an average rate 0.08 μM h^{-1}. In the subsoil suspension with the higher level of Cr contamination (500 μM compared to 50 μM), the average rate of Cr sequestration was respectively higher, 0.22 μM h^{-1}.

In natural environments, minerals exhibit the strongest Cr complexation in the order: Fe_2O_3 > $Fe_2O_3{\cdot}H_2O_{(am)}$ > α-FeOOH > Al_2O_3 > Na-Kaolinite > Na-Montmorillonite (Nriagu et al., 1993). The sorption of Cr(VI) is influenced by the solution composition such as pH, ionic strength, and the presence of other ions, particularly carbonate. That is, under our high carbonates experimental conditions (pH 7-8,

0.005 – 0.05 M, 2.8 mM HCO_3^-), a negligible Cr uptake would be expected even in the presence of available Fe oxyhydroxides in the topsoil suspension. Therefore, high Cr sequestration observed in this study suggests an additional Cr removal mechanism, such as reductive precipitation of $Cr(OH)_{3(am)}$, $Cr(OH)_3 \cdot H_2O_{(cr)}$, Cr_2O_3, or $(Cr,Fe)(OH)_3$ (Nriagu et al., 1993; Rai et al., 1989). Given the low solubility of $(Cr,Fe)(OH)_3$ solid-solutions, which may form during Cr(VI) reduction by Fe(II) even under oxic conditions (Rai et al., 1989), this sequestration mechanism was likely involved in Cr removal from experimental suspensions.

Reductive precipitation mechanism is supported by Cr solid speciation measurements in Subsoil-abiotic suspension, where 90% of surface-bound Cr was present in its reduced state. Our model for Subsoil-abiotic experiment decouples Cr(VI) sorption from its reductive precipitation as a 2-step process: weak sorption (10%) followed by its abiotic reductive precipitation (90%). The details on model parameters can be found in Table 3-4 (Chapter 3).

4.4.4 Contaminant Mobility under Oscillating Oxic/anoxic Conditions

4.4.4.1 Anoxic conditions in topsoil suspension: coupled As mobility with Fe/Mn release, immobilization of Cr and Sb

In the topsoil suspension, the mobilityof As was drastically altered when the conditions changed from oxic to anoxic. Up to 30% of previously sorbed As was released into solution likely via coupled reductive dissolution of As-bearing Fe- and Mn- minerals, as inferred from a strong correlation between aqueous As and Fe ($r = 0.85$, $p<0.005$) or As and Mn ($r = 0.90$, $p<0.005$) concentrations along to the redox-oscillating conditions. The synchronous on-off mobilization of As with the appearance of dissolved Fe and Mn coupled to DOC availability is well captured by the model (Figure 4-5).

Although As speciation was not analyzed in this experiment, following findings of Casiot et al. (2007) and Burnol et al. (2007) under anoxic non-sterile conditions we assume the release of As in its reduced state. Our model implies that microbially produced As(III) (reaction 1) sorbs strongly to the remaining sorbent under anoxic conditions, which is supported by higher Kd for As(III) than As(V) sorption on ferrihydrite and goethite at pH 7.5 (Inskeep et al., 2004). The modelling results suggest that the total mobility of As is increased due to desorption of As(III) from the diminished surface sites in the presence of competing ligands (e.g., carbonate ions).

Microbially-mediated contaminant reduction:

(1) $6\ HAsO_4^{2-} + C_2H_5OH + 10\ H^+ \rightarrow\ 6\ H_3AsO_3 + 2\ HCO_3^- + H_2O$

(2) $6\ Sb(OH)_6^- + C_2H_5OH + 4\ H^+ \rightarrow 3\ Sb_2O_{3(s)} + 2\ HCO_3^- + 22\ H_2O$

(3) $4\ CrO_4^{2-} + C_2H_5OH + H_2O + 6\ H^+ \rightarrow 4\ Cr(OH)_{3(s)} + 2\ HCO_3^-$

Mobility of As was inverse to that of Sb, with Sb higher sequestration under anoxic conditions. The modelling exercise suggest that Sb(V) was reduced to Sb(III) (reaction 2) affecting total aqueous Sb concentration. Although reduced As(III) and Sb(III) form uncharged pyramidal acids ($As(OH)_3$ and $Sb(OH)_3$) of similar structure (Porquet and Filella, 2007), solubility of As(III) species differ substantially from that of Sb(III) species. As(III) species are soluble, while reduced Sb(III) species (e.g., Sb_2O_3) (Abin and Hollibaugh, 2014) are less so.

Aqueous Cr completely disappeared from the topsoil solution presumably via microbially-induced reductive precipitation of $Cr(OH)_3$ or (Cr,Fe)OOH (reaction 3) (Charlet and Manceau, 1992; Pratt et al., 1997). These observations suggest that common remediation strategies (e.g., reductive precipitation via biomineralization) could be effective for sequestration of Sb and Cr. At the low level of contamination (50 μM), reduction reactions of As, Cr, and Sb did not interfere with each other, enabling independent oxyanion behavior in the topsoil suspension.

4.4.4.2 Oxic conditions in topsoil suspension: increased Sb and decreased As mobility coupled to cycling of Fe and Mn, irreversible Cr sequestration

During oxic periods, only Sb(V) was consistently appearing in the aqueous phase of the topsoil suspension. Mobility of Sb was inverse to that of As and was negatively correlated with redox cycling of Fe ($r = -0.42$, $p<0.005$) and Mn ($r = -0.26$, $p<0.005$). The square-wave behavior of total Sb under oscillating oxic and anoxic conditions observed in Topsoil-dynamic experiment is consistent with reports that the oxidation of Sb is fast and readily reversible in the presence of Fe and Mn minerals (Belzile et al., 2001).

Although abiotic oxidation of Sb, As, and Cr by atmospheric oxygen are kinetically controlled (Leuz and Johnson, 2005; Rai et al., 1989), contaminants can be rapidly oxidized by various direct and indirect mechanisms coupled to the reduction of matrix components. Direct contaminant oxidation by oxide minerals (e.g., birnessite, manganite) has been demonstrated for Sb(III) (e.g., Wang et al., 2012), As(III) (e.g., Tournassat et al., 2002), and Cr(III) (e.g., Silvester et al., 1995). The mechanism frequently involves a stepwise oxidation controlled by an ion diffusion in mineral cavities, a geometry change, and an electron transfer (Silvester et al., 1995).

Indirect oxidation mechanisms are based on the catalytic effect of reactive species produced during (1) aerobic oxidation of Fe oxides (Hug and Leupin, 2003; Ilgen et al., 2012; Nriagu et al., 1993) and Mn oxides (Butler et al., 2015; Katsoyiannis et al., 2004; Oze et al., 2007) generating Fe(IV) and reactive oxygen species (HO_2•/•O_2^-, H_2O_2, •OH) (reactions 5-8), (2) aerobic oxidation of natural organic matter (NOM) under sunlight, but also in the dark, yielding excited triplet states of NOM and/or phenoxyl radicals (Buschmann et al., 2005), or (3) solar photolysis of NO_3^- and NO_2^- producing hydroxyl radical (•OH) (Kim et al., 2014).

Abiotic contaminant oxidation by reactive oxygen species produced during Fe(II) oxidation:

(4) $Fe^{2+} + O_2$/or $H_2O_2 \rightarrow Fe^{3+} +$ •O_2^-/or •OH + [products] (Hug and Leupin, 2003)

(5) As^{3+} + •OH $\rightarrow As^{4+} + O_2 \rightarrow As^{5+}$ + [products] (Hug and Leupin, 2003)

(6) Sb^{3+} + •OH $\rightarrow Sb^{4+} + O_2 \rightarrow Sb^{5+}$ + [products] (A. K. Leuz et al., 2006)

(7) Cr^{3+} + •OH/or HO_2• $\rightarrow Cr^{6+}$ + [products] (Nriagu et al., 1993)

Thus, in the presence of reactive Fe and Mn minerals, oxidation of Sb in the topsoil suspension has lead to Sb re-mobilization, while oxidation of As has lead to its immobilization as indicated by a reversible sharp decrease of aqueous As concentration to ~1 μM at the beginning of every oxic period. This is consistent with the formation of As(V), which strongly associates with poorly crystalline Fe oxyhydroxides and As-rich ferric oxides (Parsons et al., 2013a; Roberts et al., 2010) or co-precipitates with Mn^{2+} as $MnHAsO_4$ (Tournassat et al., 2002).

In contrast to changes in the mobility of As and Sb, under oxic conditions Cr remained below detection limit in Topsoil-dynamic suspension. Freshly reduced Cr(III) most likely was re-oxidized by reactive Mn minerals (Silvester et al., 1995), however, immediately re-reduced by microorganisms present in the topsoil. Thus, the interplay between microbial Cr reduction and chemical Cr oxidation may have lead to an overall irreversible Cr sequestration even in the presence of reactive Mn minerals, as was recently demonstrated by Butler et al. (2015).

4.4.4.3 Stability of reduced As, Sb, and Cr under oxic conditions in the absence of reactive Fe and Mn

In the subsoil suspension (Subsoil-biotic), reduced As(III), Sb(III), and Cr(III) were not remobilized under oscillating oxic/anoxic conditions. Behavior of As and Sb, thus, was strikingly different from that in the topsoil system, where contaminants were periodically reduced and re-oxidized on the same experimental time scale. In the subsoil suspension, residual aqueous As concentrations were found to occur entirely as As(III), which persisted in solution at the level of 75 μM for the remainder of the experiment. Meanwhile,

Sb sequestration, likely via reductive precipitation of Sb in form of Sb_2O_3, is consistent with the absence of aqueous Sb(III) and abundance of Sb(V), demonstrating the co-existence of Sb(V) with As(III) in the solution as previously reported (Casiot et al., 2007; Fawcett et al., 2015; Mitsunobu et al., 2006). Reductive precipitation of Cr was likely responsible for complete Cr removal from the solution and its accumulation in the solid phase mainly as Cr(III) (97%). Relatively slow Cr oxidation by oxygen (Rai et al., 1989) was insignificant on the experimental time scale. Therefore, it can be suggested that the low content of reactive Fe and Mn minerals in the subsoil matrix constrained the oxidation of contaminants, thus, favored immobilization of Sb and Cr, however, implied a potential mobility of As. Alternatively, stability of reduced contaminants under oxic conditions could invoke the lack of microorganisms capable to contaminant oxidation. This needs to be assessed via a combination of proteomic and genomic analyses.

4.5 Environmental Significance

Contrasting contaminant mobility in the topsoil and subsoil environments indicates the role of reactive Fe- and Mn- oxyhydroxides, microbial activity, and co-contamination in biogeochemical behavior of As and Sb, as inferred from this comparative study. Being a strong oxidant, Cr is inevitably sequestered via reductive precipitation reactions under oxic/anoxic and biotic/abiotic conditions in Fe/Mn- rich or depleted systems. In the absence of reactive Fe and Mn minerals capable for direct and indirect contaminant oxidation, Sb and Cr were irreversibly sequestered from the subsoil suspension on the experimental time scale (7 days half-cycle) due to slow oxidation by oxygen at neutral pH. Irreversible reduction of As resulted in As(III) persistence in the solution.

Despite the fact that Fe- and Mn- oxyhydroxides play a significant role in scavenging contaminants via surface complexation and oxidative co-precipitation reactions (Charlet et al., 2011; Inskeep et al., 2004), they do not decrease dissolved contaminant concentrations below drinking water limit (e.g., 75 $\mu g\ L^{-1}$ As) and even contribute to magnification of Sb contamination as demonstrated in this study. This suggests that when As and Sb coexist in the subsurface environment exposed to changes in redox regime, their sequestration can be mutually exclusive hindering remediation approaches for multi-elemental contamination.

One of the common sequestration mechanisms could be the precipitation of metal-sulfides (e.g., Sb_2S_3, As_2S_3, AsS) (Wilson et al., 2010) or co-precipitation of As and Sb with secondary sulfides (e.g., mackinawite, pyrite, sphalerite). These reactions are favorable in the presence of sulfate-reducing bacteria under strictly anaerobic conditions, although the geochemistry of trace elements under sulfidic conditions is still uncertain (Lindsay et al., 2011; Planer-Friedrich and Scheinost, 2011; Planer-Friedrich and Wilson,

2012). In the current study, sulfate was present in both topsoil and subsoil suspensions, however, remained constant over experimental time suggesting that sulfate-reducing conditions were not reached.

The models were able to capture the main features of the observed time-series of major elements (C, Fe, and Mn) and contaminants (As, Sb, and Cr). The modeling results suggest that in two different environments microbial activity favors immobilization of Sb and Cr via reductive precipitation of solid-solutions. At low level of contamination, Sb reduction is independent of the presence of As and Cr in the topsoil suspension. Conversely, at high level of contamination, Sb reduction is inhibited until the As(V) becomes depleted from the subsoil solution. Contrasting contaminant mobility in the topsoil and subsoil environments indicates the role of Fe and Mn minerals, microbial activity, and co-contamination in biogeochemical behavior of As and Sb. Although the current models do not include transport control on contaminant mobility, the biogeochemical kinetic and equilibrium parameters can be coupled to other codes via several interfaces for PHREEQC and enable safety risk assessments for environments exposed to periodic changes in redox conditions.

Finally, even though it was reported that the E_H measured by Pt electrode is an important factor controlling the mobility of As and Sb (Frohne et al., 2011), our results suggest that these measurements may not be particularly informative in environments depleted in reactive Fe- and Mn- oxyhydroxides, such as the subsoil rich in clays (argillaceous formations). Despite constantly high E_H values (+350±50 mV), which were not largely affected by induced oscillations of oxic and anoxic gaseous mixtures in the subsoil suspension, oxidized As(V), Sb(V), and Cr(VI) were microbially reduced resulting in lower mobility of barely soluble Sb(III) and Cr(III) solid-solutions.

Chapter 5

Conclusions

5.1 Novel Scientific Contributions

Research presented in this thesis contributes to the field of redox (bio)geochemistry of systems involving mixtures of major elements (C, N, Fe, Mn) and environmentally important contaminants (As, Sb, Cr). The primary aim of this thesis was to investigate synthetic biogeochemical systems under controlled, redox-oscillating conditions, in order to provide new quantitative and qualitative insights into contaminant mobility in natural redox-dynamic geosystems (e.g., aquatic sediments, flooded soils). This goal was met by developing systematic experimental and modelling approaches of increasing complexity. I first reassessed the interpretation of conventional redox potential measurements with Pt electrodes. Then, I performed comprehensive experimental and modelling investigations of contaminant mobility using soil samples from two contrasting near-surface and subsurface environments. Below, I detail how my research has improved our understanding of redox potential measurements and contaminant mobility in response to changes in redox conditions, mineralogy, and microbial activity.

5.1.1 Interpretation of Redox Potential Measurements

Chapter 2, and to a lesser extent Chapter 3, of this thesis present a systematic attempt to elucidate the factors affecting redox potential measurements made with a conventional Pt electrode. The key findings are as follows.

(1) Under oxic and suboxic conditions, physicochemical influences (stirring rate, dissolved O_2 saturation, and anionic physisorption), and the presence and activity of a model bacterium (*S. oneidensis*) shape the measured E_H time-series records.

(2) Under anoxic conditions, the α-$FeOOH_{(s)}/Fe^{2+}_{(aq)}$ couple is electroactive and acts as a redox buffer. In that case, the measured E_H is correctly predicted by the Nernst equation. However, for the redox buffer to be active, a fraction of $Fe^{2+}_{(aq)}$ must accumulate in solution. That is, in saturated sediments and soils, when Fe(II) is adsorbed or co-precipitated, E_H measurements cannot be a reliable indicator of Fe(III) reduction reactions.

(3) Under anoxic conditions, but in the absence of a dominant electroactive redox couple, the presence of bacteria strongly influences the E_H measurements, both under favorable (i.e., abundant TEA) and stressed (i.e., TEA starvation) conditions. Possibly, the microbial effects are largely the result of the extracellular release of organic compounds that interact with the electrode.

(4) The redox couples O_2/H_2O, $NO_3^-/NO_2^-/NH_4^+$, $CrO_4^{2-}/Cr(OH)_3$, $HAsO_4^{2-}/H_3AsO_3$, and $Sb(OH)_6^-/Sb_2O_3$ are not electroactive and do not directly control measured E_H values. Therefore, the assessment of contaminant fate based on the measurements of E_H is not recommended.

(5) Abrupt changes in continuous E_H time-series records (so-called "E_H knees") may identify transitions in the microbial utilization of a TEA with higher redox potential to one with lower redox potential. In the experiments I carried out, such an E_H knee was observed for the transition from nitrite to goethite reduction.

5.1.2 Microbial Role in Redox Interplay Between As, Sb, and Cr

Chapter 3 presents evidence that the fate of contaminant oxyanions (i.e., As, Sb, and Cr) added to an argillaceous (subsoil) suspension depends on the microbial activity (as inferred from ATP and nitrate concentrations) and the microbial community structure. The latter was investigated by comparing results of experiments where only the native microbial population was present with those where the argillaceous suspension was inoculated with microflora extracted from a topsoil. The results are consistent with two distinct strategies employed by the microorganisms when faced with the contaminant mixtures. The first strategy involves the simultaneous reduction of CrO_4^{2-}, $HAsO_4^{2-}$, and $Sb(OH)_6^-$ under aerobic and denitrifying conditions. This is observed in the non-inoculated subsoil suspensions (Exp. II and Exp. III). The concurrent reduction of the three contaminants is interpreted as either a detoxification mechanism or non-enzymatic microbial reductive catalysis. The second strategy involves the respiratory reduction of the oxyanions and follows the thermodynamic order from highest to lowest redox potentials. In other words, the reduction of available terminal electron acceptors proceeds in the following order: O_2, CrO_4^{2-}, NO_3^-, $HAsO_4^{2-}$, $Sb(OH)_6^-$. This reduction sequence is observed in the argillaceous subsoil suspension enriched with topsoil inoculum (Exp. IV). Overall, microbial presence resulted in irreversible contaminant sequestration on the experimental time scale (days).

5.1.3 Contrasting Mineralogical Controls on Mobility of As, Sb, and Cr Mobility in Fe/Mn-rich and Clay-rich Matrices

Chapter 3 and Chapter 4 of the thesis compare the mineralogical controls on contaminant mobility in the topsoil and subsoil matrices. The focus of this part of the work is to investigate the mechanisms controlling the reversibility of contaminant sequestration under redox-oscillating conditions. The main caveat in comparing the experiments with the topsoil and subsoil samples are differences in experimental design, conditions, and diagnostic tools. Although these disparities limit the power of conclusions drawn,

the comparison of two systems contribute to better understanding of mechanisms controlling contaminant mobility.

(1) Higher As uptake by the topsoil is due to the higher content of reactive Fe- and Mn-oxyhydroxides (operationally defined as the citrate-bicarbonate-dithionite-extractable Fe and Mn), which are considered the major sorbents in the topsoil matrix. In contrast, As sequestration in the subsoil argillaceous matrix is limited by the low abundance of Fe- and Mn- oxyhydroxides and is likely controlled by complexation to muscovite.

(2) The overall higher Sb mobility in solution in both systems, as compared to that of As, is interpreted as kinetically-controlled complexation of Sb to oxyhydroxides in the topsoil and weak sorption of Sb to kaolinite in the subsoil suspensions.

(3) The observed decrease of aqueous Cr concentration is suggested to follow a two-step kinetic process: reversible sorption of Cr(VI) followed by abiotic reductive precipitation of Cr(III) driven by structural Fe(II) in clay minerals (e.g., biotite) or pyrite present in both topsoil and subsoil matrices.

The results indicate that the reversibility of contaminant sequestration is controlled by the presence of reactive Fe- and Mn- oxyhydroxides under experimental conditions of this study. Under anoxic conditions, reductive dissolution of minerals strongly correlates with As release and Sb removal from the aqueous phase. Opposite As and Sb mobility responds to weak sorption affinity of As(III) in the presence of competing ligands and low solubility of Sb(III). Under oxic conditions, oxidation of As(III) to As(V) and Sb(III) to Sb(V) is likely promoted by the oxidation of Fe and Mn, which are known to produce reactive species catalyzing oxidation reactions. Co-precipitation and/or adsorption of As(V) on the mineral host phases decreases total As aqueous concentration. Overall, contaminant sequestration was reversible when controlled by Fe- and Mn- oxyhydroxides.

5.1.4 Overall Contaminant Mobility under Redox-Oscillating Conditions

In Chapter 3, Chapter 4, and as a co-author in the publication given in Annex-I, I demonstrated that the sequestration of As and Sb can be either reversible or irreversible when oscillating oxic-anoxic conditions are imposed. The mobility of As and Sb is found to be mainly controlled by microbial activity during anoxic periods and by chemical reactivity of Fe- and Mn- oxyhydroxides during oxic periods. Thus, in topsoil suspensions rich in Fe- and Mn- oxyhydroxides, reductive microbial activity and oxidative catalytic activity of minerals has lead to the cycling of aqueous As and Sb concentrations. Whereas, in the

argillaceous subsoil suspensions lacking reactive Fe- and Mn- oxyhydroxides and, likely, oxidative bacteria, microbially reduced As and Sb were insensitive to oxygen intrusion and were irreversibly sequestrated on the experimental time scale (days). Considering that slow contaminant oxidation kinetics by atmospheric oxygen can be overcome in the presence of reactive Fe- and Mn- oxyhydroxides, argillaceous matrix, in contrast to the topsoil matrix, is shown to provide a more suitable environment for contaminant sequestration. Argillaceous matrix demonstrated ability to withstand periodical oxic-anoxic oscillations without releasing contaminants back to the aqueous phase, at least at the time scale of the experiments.

5.1.5 Biogeochemical Modelling of As, Sb, and Cr Mobility in Argillaceous Systems

The models created in Chapter 3 provide diagnostic and prognostic tools for the quantitative simulation of biogeochemical processes driving mobility of Cr, As, and Sb in argillaceous systems. The increasing complexity modelling has been demonstrated to describe the experimental observations (kinetic and equilibrium sorption, microbial reduction via detoxification and respiration, reductive precipitation) s. The set of parameters obtained for less complex systems was fixed and applied unchanged in the models of more complex system, in order to derive reaction parameters robust to experimental changes. The models are flexible in the way that rate formulations and parameter values, associated with abiotic and biotic processes, could be assigned separately. The implementation of the multi-reaction model (Zhang and Selim, 2005) in PHREEQC provides a flexible modelling tool on time scales exceeding that of the experiments, as shown in Chapter 3.

5.2 Practical Recommendations and Avenue for Future Research

The results presented in this thesis demonstrate that valuable information can be extracted from continuous E_H measurements. For example, the identification of break points may be used to diagnose key redox transitions. Therefore, continuous in-situ monitoring of E_H, rather than single measurements, are recommended for the application of redox electrode measurements in complex environmental systems. During field measurements, the observation of E_H "knees" in suggest taking a new set of samples to fully characterize new predominant redox reaction, whereas, in the laboratory, it suggest an appropriate time to replenish limiting substrate to the system.

In line with previous work in this field, measured E_H distributions cannot be related to the activities of the non-electroactive couples O_2/H_2O, $NO_3^-/NO_2^-/NH_4^+$, $CrO_4^{2-}/Cr(OH)_3$, $HAsO_4^{2-}/H_3AsO_3$, and $Sb(OH)_6^-/Sb_2O_3$. This finding suggests that measured E_H values have limited usefulness in

argillaceous formations that are depleted in electroactive redox couples (such as ferrous/ferric iron). Alternatively, the redox state of such systems could be quantified by chemical titrations with strong oxidants (e.g., H_2O_2, $KMnO_4$) and reductants (e.g., I_2), or qualitatively assessed by measuring pH_2.

The contrasting results of measured E_H in the topsoil and subsoil suspensions under successive oxic and anoxic conditions reveal that the common assumption that "oxic" and "anoxic" equates with "reducing" and "oxidizing" is simplistic. Instead, it is more appropriate to use "oxic/anoxic" conditions when referring to the presence of dissolved oxygen, which can be detected by the Pt electrode, and "redox" conditions when referring to the presence of reduced and oxidized species, which may or may not be electroactive towards the Pt electrode.

Although my research demonstrates the capacity of a natural barrier (here, the argillaceous matrix) to withstand oxic conditions without releasing contaminants back to the aqueous phase, my work does not address the additional effects the presence of an engineered barrier (i.e., steel canisters used in waste storage) would have. Such barrier might be reactive, for instance due to the catalytic activity of aqueous and mineral Fe(II) produced during zero-valent Fe corrosion. Therefore, future research on the sequestration capacity of an argillaceous matrix could include the effect of in-situ formation of secondary minerals produced during Fe corrosion (e.g., magnetite, siderite). Furthermore, we have not tested the behavior of radiotoxic elements relevant for subsurface disposal (e.g., U, Mo, Tc, Np). The present work on As, Sb, and Cr can serve as a useful basis for future studies given the similarities in the redox properties of radionuclides and potentially toxic elements. For radionuclides, redox-oscillating experiments should be performed in contact with both natural and engineered barriers, and in multi-contaminant environments.

The results in this thesis highlight the important role that subsurface microorganisms play in the overall contaminant immobilization in the argillaceous suspensions. The systematic approach presented in the thesis should be used in future investigations to decouple microbial from abiotic processes for long-term safety assessment. Challenges of keeping natural heterogeneous matrices sterile using microbial inhibitors (e.g., antibiotics) could be solved using gamma radiation. Sterilization by radiation has the advantage that it does not introduce cations and anions into the system that can alter sorption and reduction processes. Furthermore, future research should make use of the rapidly developing -omics techniques, including proteomics and genomics, to identify the type of microorganisms, their biogeochemical functionalities and their activities in the geochemical system.

Chapter 6

Annex-I: *On-off mobilization of contaminants in soils during redox oscillations*

Reprinted with permission from: Couture, R-M., Charlet, L., Markelova, E., Madé, B., Parsons, C.T. 2015. On–Off Mobilization of Contaminants in Soils during Redox Oscillations. Environ. Sci. Technol. 49 (5), 3015–3023. DOI: 10.1021/es5061879.

6.1 Summary

Near-surface biogeochemical systems can oscillate between oxic and anoxic conditions. Under such periodic changes many redox-sensitive inorganic contaminants undergo speciation, mobility and toxicity changes. We investigated the changes to chromium (Cr), arsenic (As), selenium (Se), antimony (Sb) and uranium (U) mobility during a series of laboratory experiments where argillaceous substrates were subjected to successive cycles of oxidizing and reducing conditions. The E_H oscillated between -320 and +470 mV, induced via both abiotic and microbial forcings. Chemically induced cycles of oxidation and reduction were achieved via a combination of gas (N_2:CO_2 vs. compressed air) and carbon (ethanol) addition, to stimulate the metabolism of a natively present microbial community. The contaminants were added either alone or as contaminant mixtures. Results show clear on-off switch mobility behavior for both major elements such as carbon (C), iron (Fe) and manganese (Mn) and for contaminants. Mn, Fe, and As were mobilized under anoxic conditions, whereas Sb, Se, and U were mobilized under oxic conditions. While As, Sb and U were reversibly sorbed, Se and Cr were irreversibly sequestered via reductive precipitation. When present in aqueous solutions at high concentrations, Cr^{VI} prevented the reduction of Mn and Fe, and inhibited the mobilization of elements with lower E_H^o. To improve remediation strategies for multiple contaminants in redox-dynamic environments, we propose a mixed kinetic-equilibrium biogeochemical model that can be forced by oscillating boundary conditions and that uses literature rates and constants to capture the key processes responsible for the mobilization of contaminants in soils.

6.2 Background

Floodplain soils are often subjected to a high loading of toxic metals and metalloids, transported with the river water and suspended sediments from various anthropogenic or geogenic sources within the river basin. Wetlands and flood plain soils can act as sinks for metals (e.g. Cr, Cu, Pb), actinides (e.g. U), metalloids (e.g. As, Sb) and non-metals (e.g. Se). These trace elements accumulate in such soils, sediments and wetlands up to a few thousand mg g^{-1}, as a result of historical mining activities, dam tailing failure, and long term weathering (Barth et al., 2009; Mandaliev et al., 2014; Parsons et al., 2013b). Natural wetlands have proven so successful at removing nutrients and contaminants from wastewater that, in the last decades, engineered systems such as constructed wetlands (Maine et al., 2006) have been introduced as barriers between natural aquatic ecosystems and industrialized zones. This is a promising strategy to limit contaminant fluxes to the aquatic environment and control pollution (GARCÍA et al., 2010). However, sediments that act as sinks for inorganic contaminants may also release them under varying hydraulic regimes (Y. Wang et al., 2013). The efficiency of wetlands, as well as the capacity of periodically flooded soils to sequester trace elements, depends on climatic factors such as flooding and drought; such factors are predicted to become more severe under climate change (Barth et al., 2009).

During dry periods, when oxic conditions prevail in the top soil, uranium (U), chromium (Cr) and selenium (Se) released into the environment in their oxidized forms predominantly persist as uranyl $[U^{VI}]_{(aq)}$, chromate $[Cr^{VI}]_{(aq)}$ (Richard and Bourg, 1991) and selenate $[Se^{VI}]_{(aq)}$ anionic species or as complexes such as the $UO_2(CO_3)_3^{4-}{}_{(aq)}$ species formed with the uranyl ion (Guillaumont, 2003). These species are rather mobile, although their mobility can be restricted by association with mineral phases such as ferrihydrite (Stewart et al., 2009). Upon water saturation of near surface substrates, conditions change from aerobic to anaerobic, due to the decreased oxygen diffusion from the atmosphere and the fast consumption of residual oxygen by aerobic heterotrophic bacteria gaining energy from the mineralization of organic matter (OM). Subsequently, other microbial processes further influence the speciation of trace elements and major redox sensitive elements such as manganese (Mn), iron (Fe), and sulfur (S). The microbial reduction of the contaminants themselves (Watts and Lloyd, 2012), or of major mineral phases such as Fe^{III} oxyhydroxides producing $Fe^{II}{}_{(aq)}$ and lowering the ambient redox potential, leads to the reductive precipitation of rather insoluble U_3O_8 or UO_2 (Guillaumont, 2003), a-(Fe,Cr)OOH, $Cr(OH)_{3(s)am}$, or Cr_2O_3 (Charlet and Manceau, 1992) and Fe(S,Se) or Se° solid solutions (Nolang et al., 2005). Because of the low solubility of these phases under reducing conditions at near-neutral pH, their formation as a result of (bio)reduction is considered an efficient strategy for their immobilization (Bishop et al., 2014) as

long as reducing conditions are maintained. A similar reductive immobilization process is sought in constructed wetland systems.

In contrast, the reduction of arsenate [As^{V}] to arsenite [As^{III}] generally increases its solubility, rendering it more mobile and bioavailable (Filella et al., 2002; Hering et al., 2011). Similarly, the formation of mobile monomeric U^{IV}-organic soluble species has been shown to mobilize U under reducing conditions (Bargar et al., 2013; Y. Wang et al., 2013). A large body of literature considers the impact of changing redox conditions on speciation, mobility and toxicity of inorganic contaminants (e.g. (Borch et al., 2010) and references therein). However, few studies have considered the impact of the temporal variability of redox conditions, despite its ubiquity in near surface natural environments (Frohne et al., 2014, 2011; Parsons et al., 2013a; Weigand et al., 2010).

Activities such as coal combustion (Querol et al., 1996), chromate copper-arsenate (CCA) wood treatment (Khan et al., 2006), nuclear fuel storage and enrichments (Duro et al., 2014; Stucker et al., 2014, 2013), and disposal of residual-treated soils (Basta et al., 2005) can lead to high levels of contaminants in soils. A recent study revealed that a biostimulation treatment aimed at immobilizing one element (e.g., U) can mobilize another (e.g., As) (Stucker et al., 2014), due to the contrasting reactivity of these elements. During remediation processes, redox conditions evolve with the depletion of electron donors (Parsons et al., 2013a) and acceptors (Bethke et al., 2011) and with progressive changes to the mineral assemblages present. In particular, it has been suggested that successive redox oscillations increase the crystallinity in Fe^{III}-oxyhydroxides (Thompson et al., 2006), modify the structure of clays (Stucki, 2011) and result in the passivation of mineral surfaces (Ehlert et al., 2014).

The objective of this research was to assess the influence of successive redox oscillations on the microbially mediated mobilization–sequestration behavior of Cr, As, Se, Sb, U in a complex natural soil system. The redox changes associated with natural cycles are mimicked by seven days of oxic conditions followed by a carbon pulse (OM input) and seven days of anoxia. We postulated that consecutive Fe redox cycles, defined here to comprise the transition from Fe^{III} to Fe^{II} and back to Fe^{III}, would result in a long-term behavior differing from that observed in a single cycle reducing or oxidizing event, and that, depending on their concentration, the mobility of redox-sensitive inorganic contaminants would be controlled either by the bulk chemistry of the soil or by the other trace contaminants present within the matrix. Specifically, we hypothesized that: i) redox oscillations would cause a different behavior of contaminants for experiments with individual trace contaminants compared to experiments with complex contaminant mixtures and ii) this interaction among contaminants would be of increasing importance as

their total concentration increased and thus become comparable to that of dominant natural terminal electron acceptors (TEAs), namely Fe and Mn. The approach was to force systematic redox oscillations on stirred soil suspensions while applying a comprehensive geochemical sampling protocol and coupled kinetic and thermodynamic (bio)geochemical modelling. This approach has not been applied previously to the study of redox sensitive contaminant cycling.

6.3 Materials and Methods

6.3.1 Soil Sampling and Characterization

Samples were taken following established sampling protocols (USEPA, 2000) in the top-horizon (0-15 cm) of a mollic Fluvisol (FAO, 2014), located on the lower terrace of a small vegetated island on the Saône River (45.9327N, 4.7555E). The soil was characterized prior to bioreactor experiments; whereby elemental composition was determined by Inductively Coupled Plasma Mass Spectrometry (ICP-MS, Agilent Technologies 7500ce,) following microwave assisted digestions (USEPA, 1996). The particle size distribution was analyzed by laser granulometry (Malvern instruments Mastersizer 2000). The powder XRD and Mössbauer spectroscopy-derived soil mineralogical composition, described elsewhere (Parsons et al., 2013a), revealed Fe^{III}-oxyhydroxides and Fe-rich clays.

6.3.2 Experimental Design and Redox Oscillation Sequence

A custom Pyrex glass bioreactor system (Parsons et al., 2013a) was filled with 1 L of soil suspension with a 1:10 soil:water ratio. The suspension was prepared using the < 600 µm soil fraction and equilibrated with surface water for 5 days prior to the start of experiments. Further details of the reactor setup and suspension preparation are provided in the Supporting Information (SI). At t=0 an aliquot of sodium chromate, sodium arsenate, sodium selenite, potassium antimonate or uranyl nitrate contaminant solution, or mixtures of these, was added to the suspension. The resulting contaminant concentrations were either 50 µM, or, 500 µM to simulate different levels of contamination. The suspension was then subjected to three 14 day cycles of reduction and oxidation. Redox potential (E_H) variation was induced by alternating between the sparging of N_2:CO_2 (7 days) and O_2:N_2:CO_2 (7 days) under constant p_{CO2} ($10^{-3.5}$ atm) and temperature (30°C) (DeAngelis et al., 2010; Parsons et al., 2013a; Thompson et al., 2006). On days -0.5, 1, 2 and 5 of each half-cycle, the soil suspension was sampled with a 20 ml syringe, introduced to a N_2-filled anaerobic chamber ($O_{2(g)}$ < 1 µL L^{-1}), centrifuged at 4000 rpm and filtered (0.45 µm nylon membrane). To avoid the depletion of the electron donor, a concentration of ~200 mg L^{-1} ethanol (8.7 mM

C) was imposed at the beginning of each of the reducing cycles. Target ethanol concentrations were achieved by spiking the suspension with a quantity of ethanol determined based on measured DOC immediately before the spike and on the remaining suspension volume at that time.

Nine 49-days experiments were conducted. A control experiment in which the soil suspension was subjected to redox oscillations in the absence of contaminant additions is hereafter referred to as "0-Soil". Three experiments were carried out with low (50 μM) concentrations of contaminants: Sb ("50-Sb"), Sb and As ("50-Sb+As"), and Sb, As and Cr ("50-Sb+As+Cr"). Five experiments were carried out with high (500 μM) concentrations of contaminants: As ("500-As"),Se ("500-Se"), Cr ("500-Cr"), U ("500-U"), and Cr, U and Se ("500-Cr+U+Se").

6.3.3 Aqueous Chemistry Analyses

Standards and reagents were prepared with 18 MΩ cm^{-1} water (Millipore) and analytical grade chemicals. Analysis of total concentrations of Na, K, Ca, Mn, Fe and of contaminants (Cr, As, Sb, Se, U) in the aqueous phase was performed in triplicate with an ICP-OES (Varian 720ES). Matrix-matched standards were used for all calibrations and NIST certified reference materials (CRMs) were used as controls. Precision was <5% relative standard deviation (RSD) and accuracy was within 10% with respect to the CRM. DOC concentrations were determined on a Shimadzu TOC-5000 analyzer. Nitrate and sulfate concentrations were measured by ion chromatography (Dionex IC 5000). The E_H and pH were recorded in-situ every 30 s within the reactors using solid polymer open-junction electrodes (Mettler-Toledo Xerolyt Solid) resistant to drift (Parsons et al., 2013a).

6.3.4 Biogeochemical Modelling

A mixed kinetic-equilibrium model was implemented in PHREEQC v.3.1.2 (Parkhurst and Appelo, 2013). Each half-cycle was imposed by alternating the head-space composition between $N_{2(g)}$ and $O_{2(g)}$, while carrying over the solution chemistry, exchanger, adsorbent composition, and solid-phase assemblage using the PHREEQC keywords SAVE and USE (Parsons et al., 2013a). Kinetic reactions were written in kinetic blocks while equilibrium reactions were those provided in the WATEQ4F database, augmented with the constants described in the SI (Table 6-6). The model simulated multiple cycles of abiotic oxidation and biologically mediated reduction in a batch reactor soil system containing OM and a simple soil mineral assemblage (ferrihydrite, birnessite, and clay exchanger).

The aim of the modelling exercise was to identify geochemical processes, by capturing key features of the observed time-series (E_H, DOC, Fe, Mn, Cr, As, Se, Sb, U) observed either at low (50 μM)

or high (500 μM) concentrations of contaminants. Model parameters were taken from the literature when possible and not fitted to the data, increasing the confidence that a process is correctly identified when the model reproduces both the trends and magnitude of changes in the observations. Fitted parameters were the initial mass of reactive solids, the lability of DOC and those for which no literature values were available. The reduction of contaminants was represented by 2nd-order reactions with respect to DOC and to the contaminant concentration, which are inhibited by the presence of more thermodynamically favorable TEAs (e.g., Figure 6-1). TEA consumption was implemented via Monod kinetic formulation (Canavan et al., 2006) and the degradation of DOC using the 1G model (Van Cappellen and Wang, 1996). Adsorption of contaminants was described by the diffuse double layer surface complexation model (DDLM) (Dzombak and Morel, 1990) with constants taken from the literature (Table 6-6). Internal consistency of the model was insured by checking the electron balance between ethanol input and Fe and Mn reduction in early reducing conditions. In order to capture the complexity of multiple TEA contaminants, the adopted modelling approach was to proceed in two steps, by modifying initial contaminant concentrations.

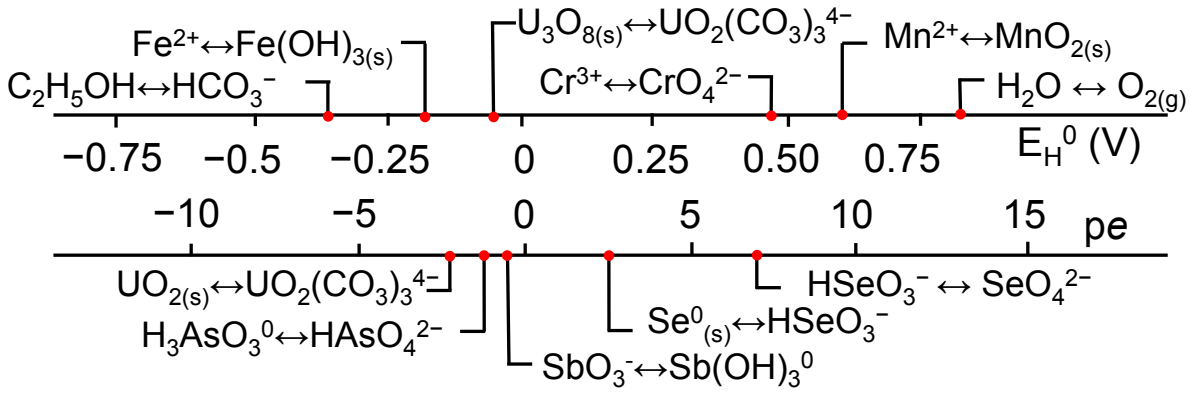

Figure 6-1. Redox scale showing the theoretical succession of equilibrium redox potentials (E_H^o in V) and corresponding p*e* values calculated at pH 7.5 for dominant aqueous species of Cr, Mn, U, Se, Sb, As, Fe and C. Concentrations of dissolved contaminants are set to 5×10^{-4} M and those of Fe^{2+}, Mn^{2+}, and CO_3^{2-} to 1, 1 and 3 mM, respectively.

Firstly, the data from the 50 μM low concentration contaminants was fitted, as at such low concentrations contaminants have little influence on the soil suspension bulk physical-chemical data, and as little difference was observed between single- and multiple-contaminant experiments at low concentrations. Secondly, the high concentration contaminant data were modeled, as single contaminants were found to impact the behavior of others. For each simulation, pH was fixed as the measured value.

The sensitivity of the predicted aqueous concentrations of contaminants to parameter values was analyzed using an extended Fourier amplitude sensitivity test (Extended FAST) (Saltelli et al., 1999) implemented in Matlab (Saloranta, 2006; Starrfelt and Kaste, 2014) and coupled to the batch version of PHREEQC. The FAST method reveals the parameter's main effect, and the sum of the effects due to high-order interactions amongst parameters. The performance of the model was assessed using the Pearson's correlation coefficient (r), root-mean-square error (RMSE), and the RMSE:observation standard deviation ratio (RSR). The r coefficient describes the degree of collinearity between simulated and measured data, RMSE indicates the error in concentration units (μM), and RMR is a normalized error index statistic (Moriasi et al., 2007).

6.4 Results and Discussion

Results of the control experiment are shown in Figure 6-4, and those of the experiments carried out with 50 or 500 μM of contaminants are summarized in Figures 2 and 3, respectively. The complete dataset including E_H, pH, DOC, NO_3^-, SO_4^{2-}, Fe and Mn for all experiments is shown in the SI (Figure 6-4, Figure 6-5, and Figure 6-6).

The pH remained relatively constant throughout the experiments at values between 7.5 and 8.2, consistent with calcite buffering (Parsons et al., 2013a). NO_3^- was quickly depleted during anoxic conditions, while SO_4^{2-} levels remained constant, suggesting that sulfate reducing conditions were not reached. Both TEAs were therefore excluded from the model. Below, we detail the mobility of major and trace elements along redox-oscillations during single and multiple contaminant experiments.

6.4.1 Electron Balance

The C addition represents ~35 mM electrons (4 *e*- per mole of ethanol assuming its oxidation to HCO_3^-) available at the beginning of each reducing cycle, of which about 8−12 mM are rapidly consumed during the first time-steps of the reducing half-cycles. At the onset of the oxidizing phase, DOC concentration decreased rapidly to ~1 mM, as modeled using a rate constant for microbial oxidation of DOC via oxic respiration of 6×10^{-8} mol s^{-1} L^{-1}. During reducing cycles, the maximum measured $Mn^{II}_{(aq)}$ (83 μM) and $Fe^{II}_{(aq)}$ (45 μM) concentrations represent a DOC consumption of at most 211 μM *e*- equivalents, which is negligible in the *e*− balance. However, the model predicts that, at the end of the last reducing cycle in the Cr-U-Se experiment (Figure 6-3), most of the Fe^{II} produced during that cycle is either adsorbed on the remaining Fe^{III} oxyhydroxides (~400 μM) or exchanged on clays[34] (~12 mM). Accounting for this additional Fe^{II} allows to balance *e*-.

6.4.2 Fe^{II} and Mn^{II} Cycling in Solution

Cycling of both Fe and Mn is closely replicated in several experiments (0-soil, 500-As, 500-Se and 500-U), showing a release to solution in anoxic conditions. Fe and Mn release and immobilization are not impacted by As, Se or U during the anoxic/oxic cycles. For U^{VI}, previous studies have shown that its additions to > 50 µM of stimulated the reduction of Fe^{III}-oxyhydroxides (Nevin and Lovley, 2000) or of structural Fe^{III} in clay (Zhang et al., 2009), but this was not observed here (Figure 6-3 and Figure 6-6), possibly because more abundant electron donors were present. The amount of Fe^{II} released was not limited by the total amount of Fe^{III} oxyhydroxides, always present in excess, but likely by DOC depletion and by reabsorption and exchange reactions of Fe^{2+}. The model predicts that most of the Fe^{2+} produced is exchanged to clay edges, coupled to the release of one or two protons (Géhin et al., 2007; Klein et al., 2010). However, this process should be limited by high ionic strength and the elevated concentration of Ca^{2+} ions, which compete with Fe^{2+} ions for sorption in the clay interlayer (Klein et al., 2010). The proportion of exchanged Fe^{2+} may be overestimated by the model, and the low observed $Fe^{II}_{(aq)}$ could instead be due to its adsorption onto Fe^{III}-oxyhydroxides. At pH 7.5−8, Fe^{2+} has a strong affinity for ferrihydrite and hematite (Liger et al., 1999). In systems with freshly precipitated Fe^{III} oxyhydroxides, the total =FeOH° site concentration at the oxyhydroxides surface might be higher than what was assumed by the DDLM model. Burnol (Burnol et al., 2007) used a batch-reaction geochemical model to access the solubility of ferrihydrite, forcing the model with the concentration of Fe^{II} , pH and pK for Fe^{2+} sorption, and concluded that the oxyhydroxides had a particle size of 5 nm (Burnol et al., 2007), with very high surface site density. However, we have not implemented this approach here, because our model including Fe^{2+} exchange on clays and sorption sites as a limiting factor adequately reproduced both Fe^{II} and the behavior of oxyanions as they co-adsorbed with Fe^{II} and other competing anions such as carbonates. Other Fe^{II} minerals such as siderite ($FeCO_3$) and magnetite (Fe_2O_3) were excluded from the model based on previous evidence that these minerals were not forming as the soil underwent redox oscillation (Parsons et al., 2013a).

XRD analysis was not conclusive as to the nature of the Mn present in the solid-phase, which likely consists of Mn^{II} and $Mn^{III/IV}$- containing minerals. We assume the presence of birnessite ($Mn^{II}O_2$), as it is the initial product of Mn^{II} oxidation in soils (Post, 1999), with an initial concentration of 1 mmol L^{-1} , because the solid-phase Mn is 30-fold lower than the solid-phase Fe present (Parsons et al., 2013a). U, Se and As are not assumed to interact with birnessite in their reduced forms; UO_2(s), Se°(s), and $As(OH)_3$°, respectively. Of these three species, only As^{III} has been shown to absorb onto Mn oxides (Manning et al.,

2002) and, at much higher As concentration, to lead to $Mn^{II}O_2$ reductive dissolution (Tournassat et al., 2002). However, these reactions were not required in the model to capture Mn and As behavior, consistent with recent evidence suggesting that Mn^{II} oxides become rapidly passivated towards As^{III} oxidation in microbially active soils containing both Fe and Mn oxides (Ehlert et al., 2014).

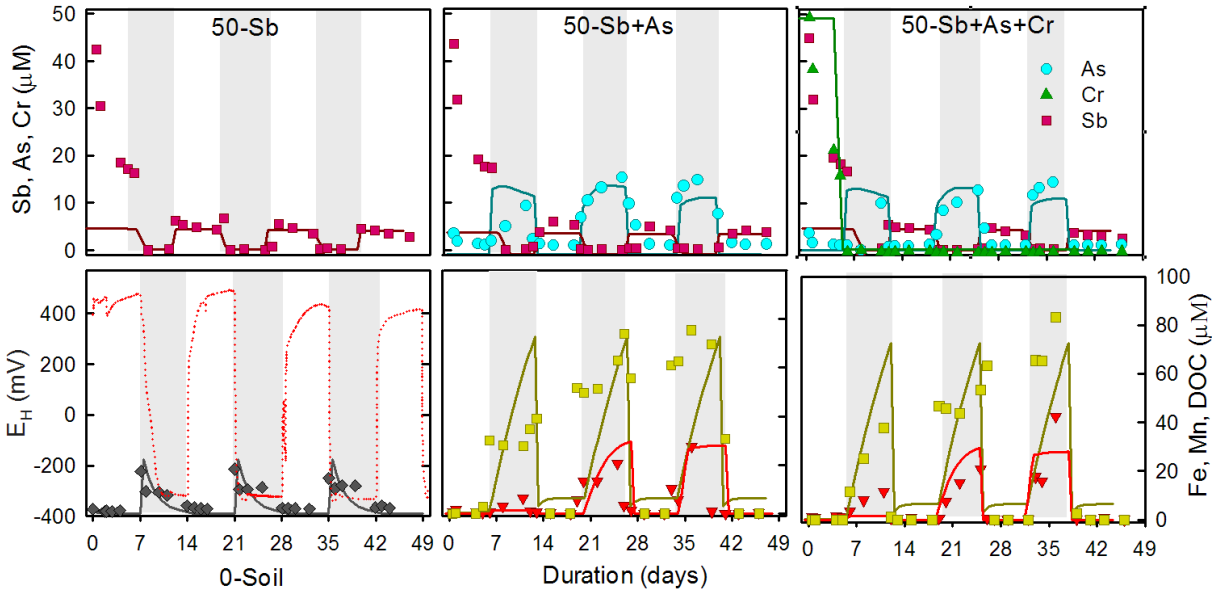

Figure 6-2. Measured (symbols) and modelled (solid lines) time-series of Sb (dark squares), As (circles), Cr (upward triangles), Mn (light squares), Fe (downward triangles), and DOC (diamonds) during 7 consecutive experimental half-cycles spanning 49 days. Measured E_H is indicated by a dotted line and shaded areas indicate half-cycles during which an anoxic headspace was imposed.

Aqueous Mn is quickly removed with the return of oxygen (Figure 6-2 and Figure 6-3). Although the homogenous abiotic oxidation of Mn^{2+} by O_2 is slow, the presence of mineral surfaces such as MnO_2 and ferrihydrite catalyze oxidation and increases its rate by 2 orders of magnitude (Morgan, 2005). Microbially-mediated Mn^{II} oxidation is likewise several orders of magnitude faster than homogenous abiotic oxidation alone, suggesting that surface-catalyzed and microbially-mediated oxidation are both likely pathways controlling Mn removal. The square-wave appearance of $Mn^{2+}_{(aq)}$ in solution (Figure 6-2), only during the anoxic periods in the experiments Soil-0, 500-As, 500-Se and 500-U can be simulated by: (i) microbial MnO_2 reduction (R3 in Table 6-4) (Kersten and Kulik, 2005) or (ii) Fe^{II}-driven reductive dissolution of MnO_2, according to: $R_{Fe\_Mnox} = 6.98([Fe^{2+}])\ (m/m_o)(1-\Omega_{MnO2})$, where m and m_o are the current and initial moles of MnO_2, and Ω_{MnO2} the saturation index of the solution with respect to this solid phase (Postma and Appelo, 2000). Using the microbial pathway leads to the modeled concentrations

shown on Figure 6-2 and Figure 6-3, while using the Fe^{II} pathway resulted in a three order of magnitude overestimation of Mn^{2+} concentration in solution, even accounting for adsorption of Mn^{2+} on Fe oxyhydroxides (Tessier et al., 1996).

6.4.3 Mn^{II} and Fe^{II} Cycling in Solution in the Rresence of Contaminants

In the low concentration experiments (50-Sb, 50-Sb+As, 50-Sb+As+Cr), Mn and Fe are increasingly released in solution (Figure 6-2 and Figure 6-5), from one reducing cycle to the other. On the contrary, in the 500-Cr and 500-Cr+U+Se experiments (Figure 6-3 and Figure 6-6), no mobilization of Fe is observed during the reducing half-cycles when Cr is present in solution. Similarly, in the 500-Cr and 500-Cr+U+Se experiments, almost no Mn appears in solution during the anoxic phase. We hypothesize that the blocking of Fe and Mn release is due to the scavenging of *e-* by Cr, and that therefore no reduction of Fe-oxyhydroxides or birnessite occurs in the presence of $Cr^{VI}_{(aq)}$. The same reasoning can explain the slow Fe and Mn release during the first reducing cycle of the 50-Sb+As+Cr experiments (Figure 6-2). Alternative pathways of Fe and Mn sequestration cannot be discounted, such as co-precipitation of an α–(Fe,Cr)OOH solid phase (Charlet and Manceau, 1992). At equilibrium with this phase (Rai et al., 1987), about 10µM of Fe^{II} are scavenged by 400 µM Cr^{VI}. Mn scavenging could likewise be interpreted as the reaction of Cr^{VI} with birnessite, which can stabilize its structure together with Mn^{III} and thus limit Mn^{II} release (Charlet and Manceau, 1992).

6.4.4 Chromium

Cr, the contaminant with the highest $E_H°$ value (Figure 6-1), can be immobilized in Fe-rich soils via three main mechanisms: adsorption under oxic conditions, reductive (co)precipitation during anoxic conditions, or by exchange of Cr^{III} on the interlayer and external surfaces of clays (Bishop et al., 2014) following the reduction of Cr^{IV} by Fe^{II}. A two-step Cr removal is observed in Figure 6-3, with 10% of the added chromate being removed during the first oxic half-cycle. In the following oxic half-cycles, neither additional sorption nor oxidative remobilization is observed, suggesting that Cr^{VI} sorbs weakly onto mineral surfaces. In Figure 6-3, oxyanion concentrations plateau during the oxic half-cycles suggesting the following apparent order of surface affinity: $SeO_4^{3-} > UO_2(CO_3)_2^{2-} > CrO_4^{2-}$. Furthermore, the solubility of Cr^{III} hydroxides and of mixed $Fe_xCr^{III}_{1-x}OOH$ phases are low and $O_{2(aq)}$ is known to be a very slow Cr^{III} oxidant in the absence of light (Wang et al., 2008). As discussed above, Fe and Mn release is inhibited by the presence of Cr, presumably while the redox potential is controlled by the $CrO_4^{2-}/Cr_2O_3(s)$ or CrO_4^{2-} /(Fe,Cr)OOH redox couples. Subsequently, E_H values drop from -100 to -400 mV from one reducing cycle

to the next (Figure 6-3) and upon the release of Fe^{II}. The reductive immobilization of chromate can occur during the anoxic half-cycles via microbial reduction or abiotic reduction by DOC (Jamieson-Hanes et al., 2012b). Cr removal was described in the model by a 2^{st}-order kinetic reaction where the rate is a function of the fraction of Cr available for reduction (Table 6-4) and of DOC (i.e. ethanol) concentrations. The combination of a fast rate constant and an excess of DOC causes the removal of Cr to be quasi linear and follows apparent 0^{th}-order kinetics, as was previously observed (Jamieson-Hanes et al., 2012a).

6.4.5 Selenium

Little sorption of selenite was observed during the first oxidizing half-cycle (Figure 6-3); the model results suggest that this is due to competition for binding sites with other anions such as bicarbonate (Appelo et al., 2002). During the subsequent reducing half-cycle, aqueous Se is kinetically transformed to solidSe^0, FeSe or $FeSe_2$, which are the endpoints for Se during its microbially mediated reduction (Gibson et al., 2012; Lenz et al., 2008). In the following oxidative half-cycles, we observed remobilization of Se, which we ascribe to oxidative dissolution, as observed in previous studies (Dowdle and Oremland, 1998). Both Se^0 precipitation and oxidative dissolution processes were implemented in the model as slow apparent 0^{th}-order kinetics, which allows the features of the observed of Se cycling time-series to be captured. However, the rate of Se^0 formation constrained by the model (Table 6-6) is likely underestimated because biogenic Se^0 readily forms colloids, especially in the presence of organic ligands (Buchs et al., 2013). Here, these colloidal species were included with analysis of the dissolved fraction (< 0.45 μm).

6.4.6 Antimony

Antimonate ($Sb(OH)_{6\,(aq)}^-$) sorbs strongly to Fe oxyhydroxides, as complexation constants for Sb^V adsorption are several orders of magnitude larger than those for Se^{IV}, leading to >60% removal of Sb during the first oxic half-cycle (Figure 6-2). However, the sorption appears to be kinetically controlled during the first oxic half-cycle, a process that is not captured by the model (Figure 6-2). During the following reducing cycles, the formation of $Sb(OH)_3°$ and precipitation of $HSbO_2$ lowers the $Sb^{III}_{(aq)}$ concentrations (Filella et al., 2002). The square-wave behavior of total $Sb_{(aq)}$ is synchronous to the O_2 square-wave, consistent with reports that the reduction of Sb^V to Sb^{III} is fast and readily reversible if Fe and Mn mineral surfaces are present to catalyze the reaction (Belzile et al., 2001). This reversible thermodynamic behavior is captured by the model (Figure 6-2).

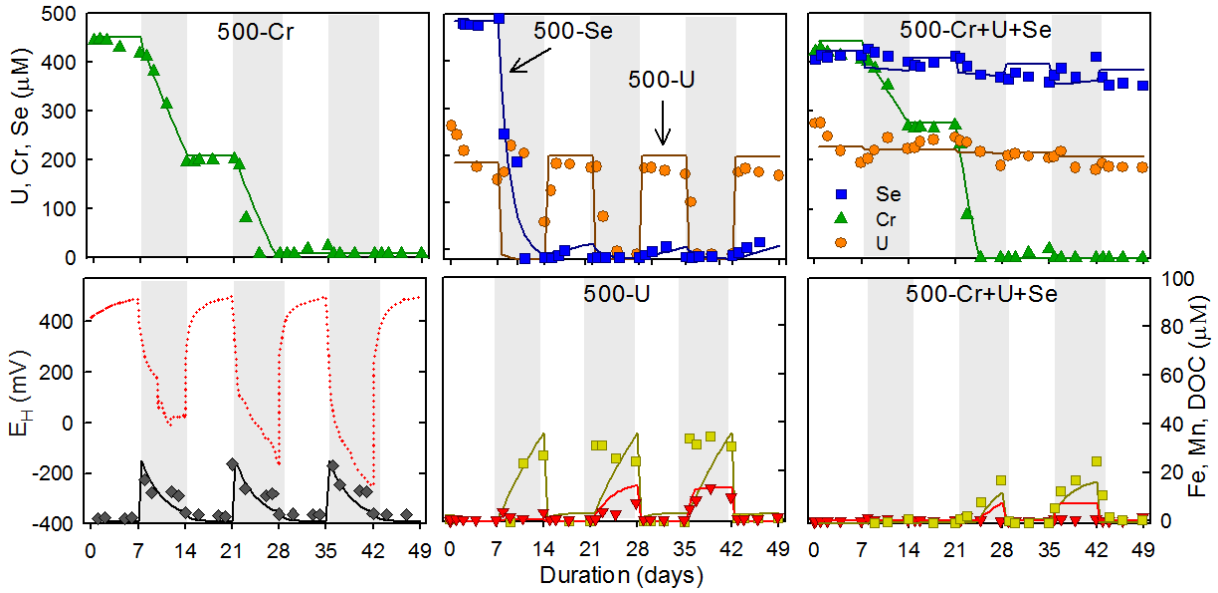

Figure 6-3. Measured (symbols) and modelled (solid lines) time-series of Cr (upward triangles), U (circles), Se (dark squares), Mn (light squares), Fe (downward triangles), and DOC (diamonds) during 7 consecutive experimental half-cycles spanning 49 days. Measured E_H is indicated by a dotted line and shaded areas indicate half-cycles during which an anoxic headspace was imposed.

6.4.7 Uranium

U behavior is similar to Sb behavior in the experiment, that is, U is more mobile under oxic conditions, as expected (Stewart et al., 2009). During the first half-cycle, a fast initial adsorption step removes 50% of U^{VI}, followed by a kinetically controlled process which removes another 20% from solution (Figure 3). At the onset of the reductive phase, a peak of soluble U is observed. Sorbed uranyl may be displaced under the effect of: (i) competition with Fe^{2+} for sorption sites, and (ii) complexation by carbonates formed as by-products of Fe and Mn oxyhydroxides respiration. The reduction of U^{VI} to U^{V} by Fe^{II} at the surface of ferrihydrite (Neiss et al., 2007) or to mixed $U^{IV}/^{VI}$ solids at the surface of clays (Chakraborty et al., 2010) can both lead to the fast removal of uranyl from solution. The reduction of uranyl to colloidal U^{IV} solids is fast and reversible in the presence of high Fe^{II} concentrations (Stewart et al., 2009). This behavior may explain our observations (Figure 6-3) that U cycling is synchronous to the O_2 square-wave. Under low Fe^{II} and high HCO_3^- conditions, U^{VI} co-adsorbed with Fe^{II} and carbonate undergoes a 1 *e*- transfer leading to a $Fe^{III}_{1-x}U^{V}_{0.6x}OOH$ solid solution (similar to the $Fe^{III}_{x}Cr^{III}_{1-x}OOH$ solid solution) which would lower the availability of U for re-oxidation during the next oxic half-cycle (Liger et al., 1999). The presence of large

amounts of colloidal Fe^{II} (Stewart et al., 2009) or monomeric U^{IV} species, however, is thought to enhance the reversible oxidation of uranium (Y. Wang et al., 2013).

6.4.8 Arsenic

When oxic conditions prevail, i.e. during initial flooding and particle deposition, As in floodplain soils is predominantly present as As^{V} and is strongly associated with poorly crystalline Fe oxyhydroxides and As-rich ferric oxides (Parsons et al., 2013a; Roberts et al., 2010). Here, sorption processes remove >95% of $As^{V}_{(aq)}$ within the first day of the oxic half-cycle (Figure 6-2). As^{V} adsorption onto natural particles during the oxidation half-cycle is highly sensitive to pH (Charlet et al., 2011), as pH 7−8 encompasses the edge for As^{V} sorption on various minerals such as Fe oxyhydroxides (Dixit and Hering, 2003). Upon the transition to anoxia following the addition of DOC, the associated reduction of Fe oxides, and the concomitant drop in E_H, the microbial reduction of As-bearing Fe^{III} phases and of As^{V} to $As^{III}(OH)_3°$ raise As solubility (Hering et al., 2011). Although increased As mobility under reducing conditions is often ascribed to weaker binding of As^{III} (Burnol et al., 2007; Roberts et al., 2010), differing evidence from laboratory experiments suggest that both As^{V} and As^{III} sorb strongly to the oxide's surface (Couture et al., 2013a; Dixit and Hering, 2003). Here, modelling results suggest that As^{III} sorbs strongly to the remaining sorbent during the reductive dissolution of As-bearing Fe oxyhydroxides phases, and that it is the diminution of surface sites and the competition with other oxyanions that ultimately increases As mobility. Thus, in the model, the kinetically controlled reduction of ferrihydrite leads to the release of As^{V} and the production of Fe^{II} and HCO_3^{2-} in solution, while the As^{V} to As^{III} transformation strictly follows thermodynamics (Burnol et al., 2007). Finally, we do not observe the attenuation of dissolved As across cycles noted in previous redox-oscillating experiments (Parsons et al., 2013a): instead we observe that As is replenished every cycle. This behavior is likely controlled by dissolution of Fe oxides, which required an excess of DOC to occur to its full extent. In previous experiments (Parsons et al., 2013a), DOC was slowly depleted, while here DOC was replenished every cycle.

6.4.9 Behavior of Multiple Contaminants and the On-off Switch Mechanism

Because of their diversity, the microbial communities native in soil are thought to be more resistant to contaminants than pure cultures (Roane et al., 2001). As a result, soil has the widespread capability to utilize the oxidized forms of contaminants as TEAs, such that 500 µM of contaminant oxyanions is unlikely to inhibit the microbial community (Chen and Hao, 1998; Fellowes et al., 2013; Kulp et al., 2013; Tapia-Rodríguez et al., 2012). However, contaminant mixtures can induce toxic effects leading

microorganisms to reduce contaminants via a detoxification mechanisms not linked to energy gain (Kulp et al., 2013).

In the 500-Cr+U+Se experiments, Cr impacted not only the redox cycling of Fe and Mn, as discussed above, but also inhibited the cycling of both Se and U under reducing conditions (Figure 6-3). It outcompete the redox couples with lower $E_H°$, such as U^{VI}/U^{IV} for the consumption of *e-* provided by ethanol, consistent with thermodynamic predictions (Figure 6-1). Therefore Se and U concentrations in the 500-Cr+U+Se experiment stay nearly constant regardless of the oxygenation conditions, with U concentrations remaining identical to those observed under oxic conditions in the 500-U experiment. In contrast, no effect of Cr on other elements is noticeable in the 50-Sb+As+Cr experiments (Figure 6-2), likely due to the excess of carbon and of surface sorption sites, enabling independent oxyanion behavior.

In the absence of high Cr concentrations, alternating oxygen imposed on-off switch behavior on contaminant mixtures (Figure 6-2 and Figure 6-3). In particular, for the 50-Sb+As and 50-Sb+As+Cr experiments, the model suggests that during each reducing half-cycle, Sb^V was reduced to the less soluble Sb^{III}, while As^V was reduced to As^{III}, concurrent with a decrease of available sorption sites on the ferrihydrite surface. This suggests that, in periodically flooded soils, the sequestration of As and Sb can be mutually exclusive, hindering remediation approaches when both contaminants are of priority. Under persistent reducing conditions, during which dissolved sulfides may accumulate, both As and Sb can then undergo complexation and precipitation with sulfides (Couture and Van Cappellen, 2011; Helz et al., 2002; Helz and Tossell, 2008; Planer-Friedrich and Scheinost, 2011). Under these conditions, their fates might then converge, although the geochemistry of metalloids under sulfidic conditions is still uncertain.

As seen in Figure 6-2 and Figure 6-3, the model captures the dominant features of the time series of C, Fe and Mn, as well as those of the contaminants. There is a good pattern agreement between observations and model predictions. Moreover, the performance metrics generally indicate good model performance ($r = 0.61-0.99$, RMSE =0.02−8.6 and RSR=0.11−0.94), although the performance is better at high concentrations (i.e., 500 mM) than at low concentrations (i.e., 50 mM) of contaminants. The lower performance at low contaminant concentrations is mostly explained by mismatches during the first oxic half-cycle: the RMSE values for the 50-Sb and 50-Cr experiments decrease by 5-fold if this cycle is omitted from the calculations (Table 6-7). FAST analysis shows that As, Sb, and U concentrations are most sensitive to the initial concentrations of Fe^{III} oxyhydroxides. Cr and to a lesser extent, Se are sensitive to the rate of OM degradation and to the ancillary parameters that modulate it. pH values affect primarily As and U, while the constants controlling Mn and Cr microbial reduction affect Se and U.

Detailed results of this analysis are presented in the SI (Figure 6-8 and Figure 6-9). Although the model is a simplification of real-world processes, in particular of transport, which is not included, it can be coupled to sophisticated codes via several interfaces for PHREEQC (Charlton and Parkhurst, 2011) and enable the prediction of the risk posed by soils affected by multiple legacy contaminants once they undergo periodic changes in redox regime.

The return time of extreme hydrologic events is changing as a result of climate change (Milly et al., 2008). Recent extreme floods such as those of the Elbe River (Germany), Chao Phraya River (Thailand) and Indus River (Pakistan) in the year 2013 have been widely discussed with respect to their impact and costs to infrastructure, and are being evaluated closely by insurance companies who include them in the natural hazards covered by their contracts (Jongman et al., 2014). However, the mobilization of legacy contaminant mixtures is seldom mentioned, although the phenomena is amplified by: i) the flooding of lignite mine lakes, as in the case of the Elbe River bringing more contaminants to the riparian flood system (Krüger et al., 2005), and ii) the overflow of combined sewage overflows (CSO) and water treatment plants, leading to the injection of new organic matter and contaminants into these dynamic systems. The risk created by oscillating redox conditions, e.g. during extreme drought events, must also be taken into account in engineered systems where anoxia is planned to insure the immobilization of contaminants and the absence of gas emissions (H_2S, Rn), such as in constructed wetlands (Maine et al., 2006) and, as was recently observed (Duro et al., 2014), in low-level long-lived nuclear waste (LL-LLW) sites. LL-LLW sites contain a variety of contaminants, including Cr, As, Se, Sb and U, which may be subjected to redox oscillations when stored in shallow clay-rich repositories (Duro et al., 2014).

Adding to previous evidence showing that oscillating redox conditions may alter the properties of clay material due to the illitization of smectite clays (Stucki, 2011), we showed that mobility predictions performed for a single contaminant may be irrelevant when a variety of contaminants are present. At low concentrations, opposing on-off switch behavior is observed both for As and Sb, whether alone or in the presence of a strong electron acceptor such as Cr. In contrast, U and Se behave differently when present, at high concentration, either alone or together with Cr. As single contaminants, they precipitate as rather insoluble solid species during anoxic events, and while some U was remobilized during oxic events, Se was not. In contrast, when they are present together with Cr, they become insensitive to anoxia, the concentration reached after one day in oxidizing conditions only slowly decreased with time regardless of the availability of dissolved oxygen.

6.5 Supporting Information

6.5.1 Details on the Redox-Oscillating Reactor (ROR) Setup

A custom two part Pyrex® glass redox stat reactor system was used, previously described in (Parsons et al., 2013a). The E_H and pH electrode signals were connected to FET instrumentation amplifiers with high input impedance. The signal was then passed to an Agilent acquisition/switching unit (34970a) connected to a PC running Agilent BenchLink Data Logger 3 software. E_H and pH data were recorded every 5 minutes and the sparging gas was modulated between N_2:CO_2 (392 ppmv) and compressed air via the Agilent switching unit, a relay board and a system of solenoid valves.

The lower part of the reactor (Ace-Glass Inc, NJ, USA) contained a working volume of 1 L and used a water jacket to allow for precise temperature control. Ethylene glycol was added to the temperature regulating circuit to avoid fungal and bacterial growth. The upper part of the reactor contained a headspace volume of approximately 300 mL and used ace-glass threaded connections for sampling, electrodes and mechanical agitation (seals secure up to 2.4 bar of internal/external pressure difference). The agitation shaft and blades were Teflon coated and prior to the introduction of soil suspensions the reactor and all glass and plastic parts were washed with 5% HNO3 then rinsed thoroughly in 18.2 MΩ cm^{-1} water.

Solid polymer open junction Xerolyt electrodes (Mettler-Toledo, France) were selected for their long-term stability and low electrolyte leak rates. A five point calibration was performed for the pH electrodes at the start and end of the experiment showing that electrode response had not shifted more than 0.02 pH units during the experiments. Measured E_H readings were converted to a redox potential with respect to the Standard Hydrogen Electrode (SHE) by normalization using ZoBell's solution. The calculated difference at the start of experiments was equal to the electrode manufacturer specification of 207 mV. The E_H electrode was found to drift by 4 mV during the experiments.

6.5.2 Soil Characterization and Preparation

Table 6-1. ICP-MS elemental analysis on initial soil after acid-digestion

Element	Total concentration (mg kg^{-1})
Cr	65.8
Mn	2900
Fe	92400
As	29
Se	0.1 < x < 1
Cd	0.415
U	3.12
Sb	ND

Table 6-2. Water content, pH, carbon and particle size analysis sieving and sedimentation and after decarbonisation

Measurement	Value	Units
Water Content	19.22	%
pH	8.3	
Organic Carbon	12.1	g kg^{-1}
$CaCO_3$ total	100	g kg^{-1}
Clay (<2 µm)	94	g kg^{-1}
Fine Silt (2−32 µm)	120	g kg^{-1}
Coarse Silt (32−63 µm)	136	g kg^{-1}
Fine Sand (63−500 µm)	400	g kg^{-1}
Coarse Sand (500−2000 µm)	150	g kg^{-1}

Soil preparation: The field moist soil was removed from polyethylene sampling bags and suspended in river water to provide a background electrolyte mix and avoid osmotic shock to the microbial community. The concentration of the suspension was approximately 150 g L^{-1} (dry-weight equivalent). The suspension was shaken for 5 minutes in a polyethylene bottle and then passed through a <600 m sieve to remove larger rock fragments and large solid organic material. This procedure was repeated until a homogeneous

suspension was achieved. The dry weight was then re-determined, and the 150 g L^{-1} solution was diluted with MQ water to a precise final concentration of 100 g L^{-1}. The resulting suspension was agitated on a shaker and left to equilibrate for 5 days prior to reactor experiments.

6.5.3 Complete Dataset for all Experiments

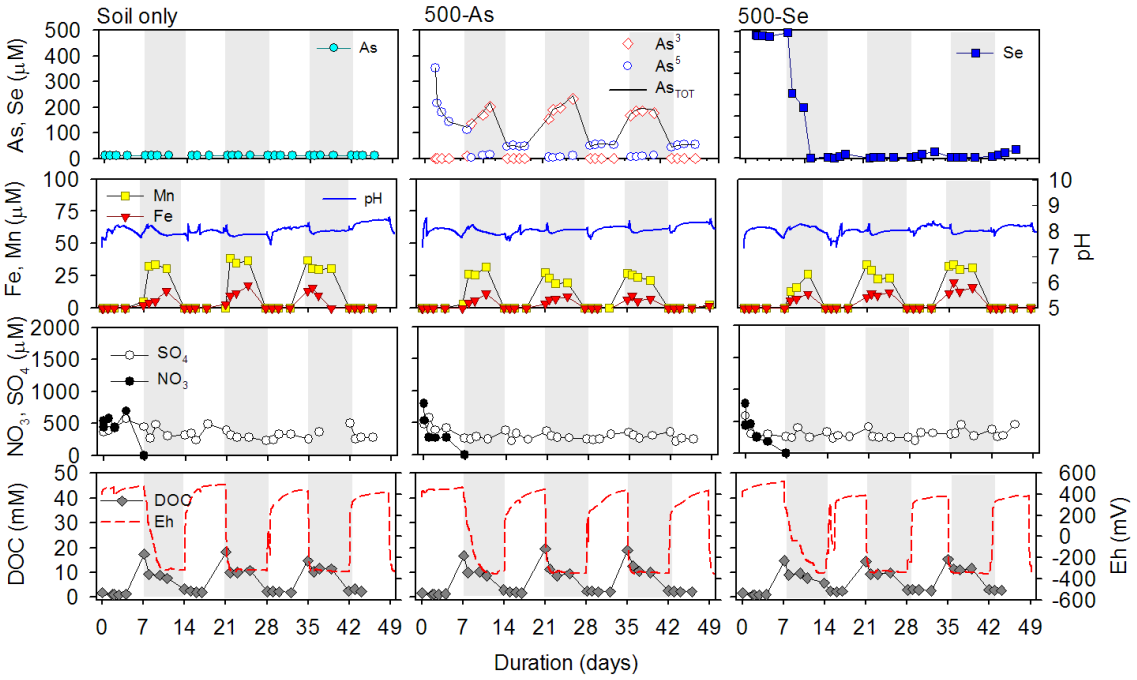

Figure 6-4. Measured time-series of As^{V} (open squares), As^{III} (open diamonds), Se (dark squares), Mn (light squares), Fe (downward triangles), NO_3^- (solid circles), SO_4^{2-} (open circles), DOC (dark squares), and E_H (line) during 7 consecutive experimental half-cycles for experiments 0-Soil, 500-As and 500-Se. Shaded areas indicate half-cycles during which an anoxic headspace was imposed. Only As was measured during the "Soil only" experiment, with concentrations consistently < 1 µM.

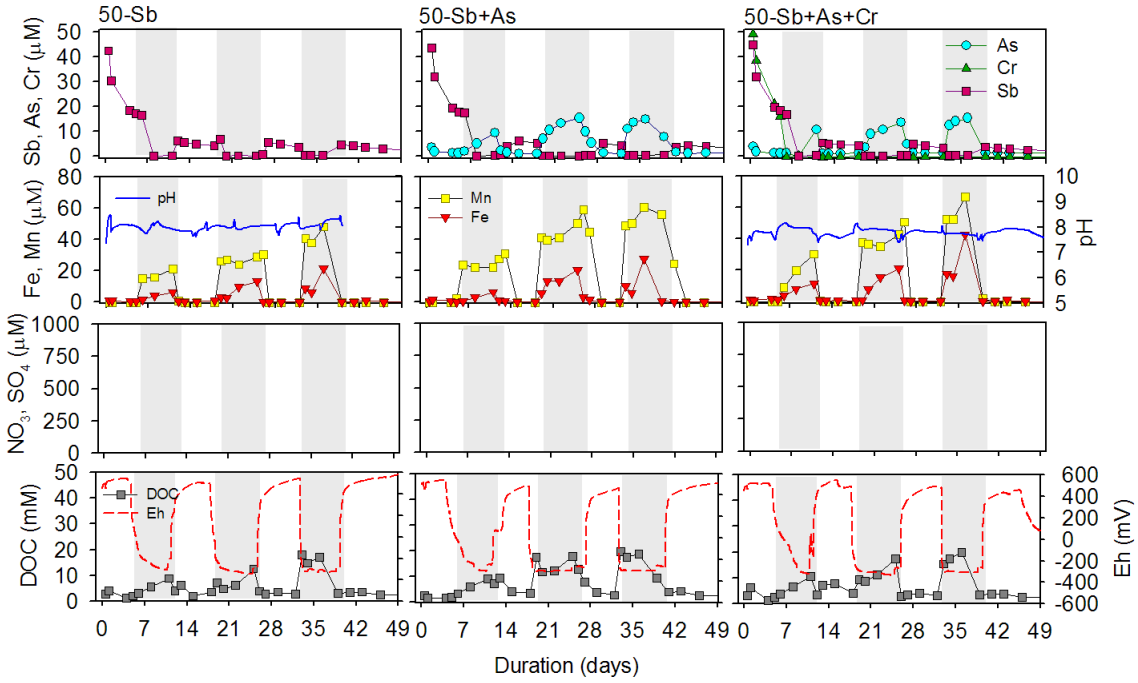

Figure 6-5. Measured time-series of Sb (solid diamonds), As (light circles), Cr (upward triangles), Mn (light squares), Fe (downward triangles), DOC (dark squares), and E_H (line) during 7 consecutive experimental half-cycles for experiments 50-Sb, 50-Sb+As and 50-Sb+As+Cr. Shaded areas indicate half-cycles during which an anoxic headspace was imposed. Samples for NO_3^- and SO_4^{2-} could not analyze for these experiments due to instrument downtime.

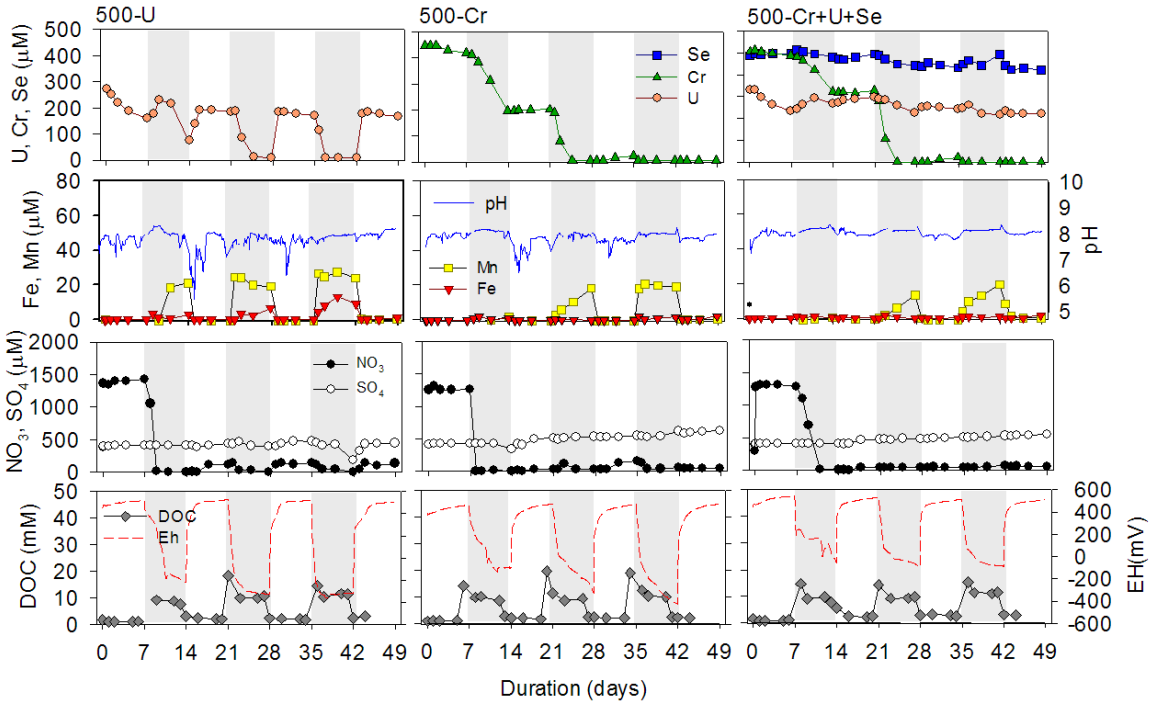

Figure 6-6. Measured time-series of U (circles), Cr (upward triangles), Se (blue squares), Mn (light squares), Fe (downward triangles), NO_3^- (solid circles), SO_4^{2-} (open circles), DOC (dark squares), and E_H (line) during 7 consecutive experimental half-cycles for experiments 500-U, 500-Cr and 500-Cr+Se+U. Shaded areas indicate half-cycles during which an anoxic headspace was imposed.

6.5.4 Supporting Information on Model Rates and Constants

Table 6-3. Redox reactions, their theoretical equilibrium redox potentials (E_H^0, in volts relative to the standard hydrogen electrode) and corresponding p*e* for dominant species at standard state and at pH 7.5. For the calculations at pH 7.5, concentrations of 5×10^{-4} M are set for Cr, Mn, U, Se, Sb, As, Fe and C. Fe and Mn are in equilibrium with ferrihydrite and birnessite, respectively, and the aqueous concentrations for Fe^{II} and Mn^{II} were set to 1×10^{-6} M.

Reaction	E_H^0 pH = 7.5	p$e^{7.5}$	E_H^0 pH = 0	pe^0	Log K	R
$O_2 + 4H^+ + 4e^- = 2H_2O$	0.77	13.11	1.22	20.78	83.12	2
$MnO_{2(s)} + 4H^+ + 2e^- = Mn^{2+} + 2H_2O$	0.55	9.44	1.22	20.8	41.60	2
$CrO_4^{2-} + 8H^+ + 3e^- = Cr^{3+} + 4H_2O$	0.43	7.39	1.51	25.66	77.00	2
$SeO_4^{2-} + 2e^- + 3H^+ = HSeO_3^- + H_2O$	0.40	6.85	1.07	18.16	36.32	2
$HSeO_3^- + 5H^+ + 4e^- = Se^0_{(s)} + 3H_2O$	0.16	2.74	0.77	14.8	59.2	2
$SbO_3^- + 3H^+ + 2e^- = Sb(OH)_3^0$	-0.03	-0.45	0.76	11.3	24.31	2
$UO_2^{2+} + 2e^- = UO_{2(s)}$	-0.06	-1.14	0.19	-3.3	16.22	3
$AsO_4^{3-} + 2H^+ + 2e^- = AsO_3^{3-} + H_2O$	-0.06	-1.15	0.15	2.64	5.29	2
$Fe(OH)_{3(s)} + 3H^+ + e^- = Fe^{2+} + 3H_2O$	-0.17	-2.97	0.67	11.31	17.1	2
$2CO_2 + 12H^+ + 12e^- = C_2H_5OH + 3H_2O$	-0.35	-5.99	0.09	1.52	33.93	5

References: 2 - Brezonik and Arnold (2011); 3 - Chappaz et al. (2010); 5 - Canfield et al. (2005).

Table 6-4. Kinetic formulations used in the model.

Description	Reaction	Kinetic formulation	Rxn ID
Aerobic respiration	$CH_2O + O_2 \rightarrow CO_2 + H_2O$	Roxy = k_om×[CH_2O]×f_O_2	1
Cr(VI) bioreduction	$3CH_2O + 4CrO_4^{2-} + 16H+ \rightarrow 4Cr(OH)^{2+} + 3CO_2 + 9H_2O$	Rcr = k_om×[CH_2O]×f_Cr	2
Mn(IV) oxide bioreduction	$CH_2O + 4MnO_2 \rightarrow 4Mn^{3+} + CO_2 + H_2O$	Rmnox = k_om×[CH_2O]×f_Mnox	3
Fe(III) oxide bioreduction	$CH_2O + 4Fe(OH)_3 + 8H^+ \rightarrow 4Fe^{2+} + CO_2 + 11H_2O$	Rhfo = k_om×[CH_2O]×f_hfo	4
Oxidation of Fe(II)	$Fe^{2+} + 0.25O_2 + H^+ \rightarrow Fe^{3+} + 0.5H_2O$	Rfeox = k_feox×[O_2]×[Fe^{+2}]	5
Se(IV) bioreduction	$HSeO_3^- + 5H^+ + 4e^- \rightarrow Se^0_{(s)} + 3H_2O$	Rse = k_se_zero × [$HSeO_3$-]	6
Se(0) oxidation	$Se^0_{(s)} + 3H_2O \rightarrow HSeO_3^- + 5H+ + 4e^-$	R_se = k_seox × [O_2]	7

Where:

f_O_2 = [O_2]/([O_2]+Km_O_2)

f_Cr = ([CrO_4^{-2}]/([

CrO_4^{-2}]+Km_Cr)) · (Kin_O_2/(Kin_O_2+[O_2]))

f_Mnox = ([MnO_2]/([MnO_2]+Km_Mn)) · (Kin_O_2/(Kin_O_2+[O_2])) · (Kin_Cr/(Kin_Cr+[CrO_4^{-2}]))

f_hfo = ([hfo]/([hfo]+Km_Fe)) · (Kin_O_2/(Kin_O_2+[O_2])) · (Kin_Cr/(Kin_Cr+[CrO_4^{-2}])) ·

(Kin_Mnox/(Kin_Mnox+[MnO_2]))

Table 6-5. Reaction parameters constrained by the model, which correspond to reactions #1-7 given in Table 6-4 and to reaction #28 in Table 6-6.

Parameter	Abbrev.	Value	Unit	Source	Range	Ref.
OM oxidation rate constant	k_om	20	yr^{-1}	M	1-400	6
Half-saturation value for oxic respiration	Km_o2	5	μmole L^{-1}	L	4–8	7, 8
Inhibition of TEAs by O_2	Kin_o2	1	μmole L^{-1}	L	3.2×10^{-3}–1	7, 8
Half-saturation for Cr reduction	Km_cr	1	μmole L^{-1}	L	0–1	9
Inhibion of TEAs by Cr	Kin_cr	3	μmole L^{-1}	M		
Half-saturation for Mn reduction	Km_mn	15	μmole L^{-1}	L	16	10
Inhibition of TEAs by Mn	Kin_mn	500	μmole L^{-1}	M		
Half-saturation for Fe reduction	Km_fe	1	μmole L^{-1}	L	0.2–200	7, 8
Rate constant for Fe oxidation by O_2	k_feox	4	L μmole $^{-1}$ s^{-1}	L	3.5–40	7, 8
Equilibrium constant for Fe exange on cays	k_fe_exch	-2.5		L	-2–-3	11
Rate constant for Se^0 precipitation	k_se_zero	7×10^{-6}	s^{-1}	M		
Rate constant for Se^0 oxidation by O_2	k_seox	1.5	L μM^{-1} s^{-1}	L	1–3000 s^{-1}	12

M = model fit, L = literature value

References: 6 - Paraska et al. (2014); 7 - Canavan et al. (2006); 8 - Couture et al. (2010); 9 - Jamieson-Hanes et al. (2012a); 10 - Van Cappellen and Wang (1996); 11 - Appelo and Postma (2005); 12 - Dowdle and Oremland (1998).

Table 6-6. Reactions for the formation of the various oxyanion species and their corresponding equilibrium constants added to the WATEQ4F database in PHREEQC. Solid phases allowed to form in the model are also listed.

Reaction	Log K	Ref.	Rxn ID
Surface complexation reactions			
$Hfo\_wOH + CO_3^{-2} + H^+ = Hfo\_wOCO_2^- + H_2O$	12.78	[13]	8
$Hfo\_wH + CO_3^{-2} + 2H^+ = Hfo\_wOCO_2H + H_2O$	20.37	[13]	9
$Hfo\_sOH + Fe^{+2} = Hfo\_sOFe^+ + H^+$	−0.95	[13]	10
$Hfo\_wOH + Fe^{+2} = Hfo\_wOFe^+ + H^+$	−2.98	[14]	11
$Hfo\_wOH + Fe^{+2} + H_2O = Hfo\_wOFeOH + 2H^+$	−11.55	[14]	12
$Hfo\_OH + AsO_4^{-3} + 2H^+ = Hfo\_HAsO_4^- + H_2O$	24.4	[15]	13
$Hfo\_OH + AsO_4^{-3} + H^+ = Hfo\_AsO_4^{-2} + H_2O$	18.1	[15]	14
$Hfo\_OH + AsO_3^{-3} + 3H^+ = Hfo\_H_2AsO_4^{-2} + H_2O$	38.8	[15]	15
$Hfo\_OH + AsO_3^{-3} + 2H^+ = Hfo\_HAsO_4^{-2} + H_2O$	31.9	[15]	16
$2Hfo\_sOH + Sb(OH)_6^- = (Hfo\_sO)_2Sb(OH)_4^- + 2H_2O$	13	[16]	17
$2Hfo\_sOH + Sb(OH)_3 = (Hfo\_sO)_2Sb(OH) + 2H_2O$	15	[16]	18
$2Hfo\_wOH + Sb(OH)_6^- = (Hfo\_wO)_2Sb(OH)_4^- + 2H_2O$	5	[16]	19
$2Hfo\_wOH + Sb(OH)_3 = (Hfo\_wO)_2Sb(OH) + 2H_2O$	6	[16]	20
$Hfo\_sOH + UO_2^{+2} = Hfo\_sOUO_2^+ + H^+$	1.74	[17]	21
$Hfo\_wOH + UO_2^{+2} = Hfo\_wOUO_2^+ + H^+$	1.54	[17]	22
Solid phases			
$Cr(OH)_3$	1.34	[18]	24
$Sb(OH)_{3(aq)} = Sb(OH)_{3(s)}$	−7.11	[18]	25
$U^{4+} + 2H_2O = UO_{2(s)} + 4H^+$	−4.67	[18]	26
Cation exchange			
$X^- + H^+ = XH$	3	[11]	27
$Fe^{+2} + XH = FeX^+ + H^+$	−2.5	[11]	28

References: 11 - Appelo and Postma (2005); 13 - Appelo et al. (2002); 14 - Liger et al. (1999); 15 - Dixit and Hering (2003); 16 - Vithanage et al. (2013); 17 - Mahoney et al. (2009); 18 - Parkhurst and Appelo (2013).

6.5.5 Model Code

The model code is available online at https://github.com/biogeochemistry/ROR-phreeqc. To gain access to the repository please email your GitHub username to rmc@niva.no.The structure of the code is sumarized on Figure 6-7.

```
### SIMULATION 1 ###

SOLUTION_MASTER_SPECIES
SURFACE_SPECIES
SOLUTION_SPECIES
PHASES
EXCHANGE_MASTER_SPECIES
EXCHANGE_SPECIES
SOLUTION 0
EQUILIBRIUM_PHASES 0
EXCHANGE 0
SAVE SOLUTION 0;SAVE EXCHANGE 0; SAVE EQUILIBRIUM_PHASES 0;
END

# KINETIC MODEL PARAMETER #

RATES
[...]

# OUTPUT CONFIGURATION #
USER_GRAPH
INCREMENTAL_REACTIONS true ;

# REDOX CYCLING  #

### SIMULATION 2 ###
TITLE 0.5 CYCLE OXIC
USE SOLUTION 0 ; USE EXCHANGE 0; USE EQUILIBRIUM_PHASES 0;
GAS_PHASE;
KINETICS 0
SURFACE 0
SAVE SOLUTION 0;SAVE EXCHANGE 0; SAVE EQUILIBRIUM_PHASES 0; SAVE  SURFACE 0
END

### SIMULATION 3 ###
TITLE MIXING A DOC SPIKE WITH THE RESULT OF SIMULATION 0
SOLUTION 1
MIX 1;
SAVE SOLUTION 0

### SIMULATION 4 ###
TITLE 1.0 CYCLE ANOXIC
USE SOLUTION 0 ; USE EXCHANGE 0; USE EQUILIBRIUM_PHASES 0; USE  SURFACE 0;
GAS_PHASE;
KINETICS 1
SAVE SOLUTION 0;SAVE EXCHANGE 0; SAVE EQUILIBRIUM_PHASES 0; SAVE  SURFACE 0
END

[...]
```

Figure 6-7. Sequence of the PHREEQC v3 section headings and keywords used to simulate element behavior during redox oscillations and produce Figure 6-2 and Figure 6-3 of the main text.

6.5.6 Model Sensitivity Analysis and Performance Metrics

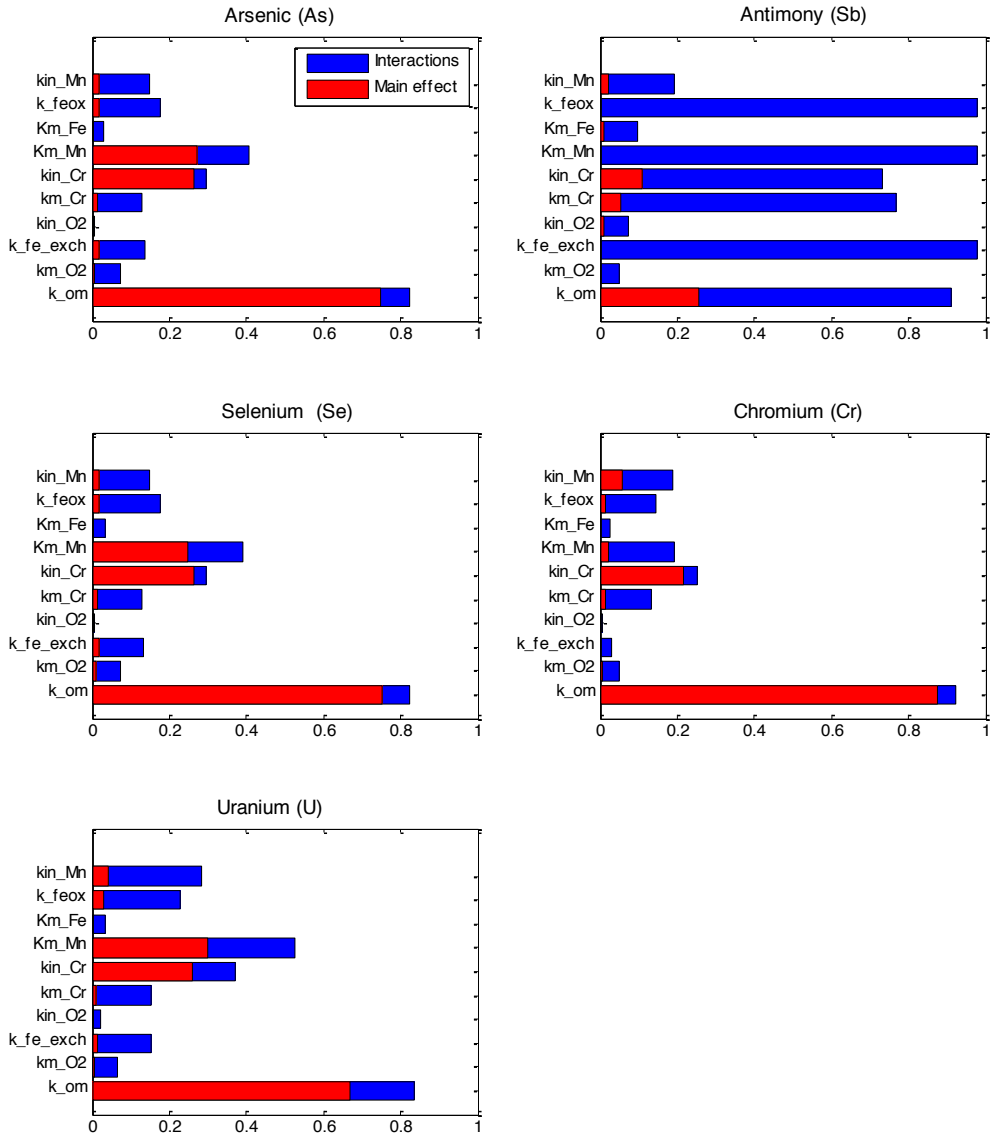

Figure 6-8. Proportion of total variance in modeled aqueous concentrations of As, Sb, Se, Cr and U explained by 10 parameters analyzed by the Extended Fourier amplitude sensitivity test (Extended FAST) sensitivity analysis method. "Main effect" denotes the part of total variance explained by a single parameter and "Interactions" the part explained by interactions with all other parameters. Parameter abbreviations are explained in Table 6-4.

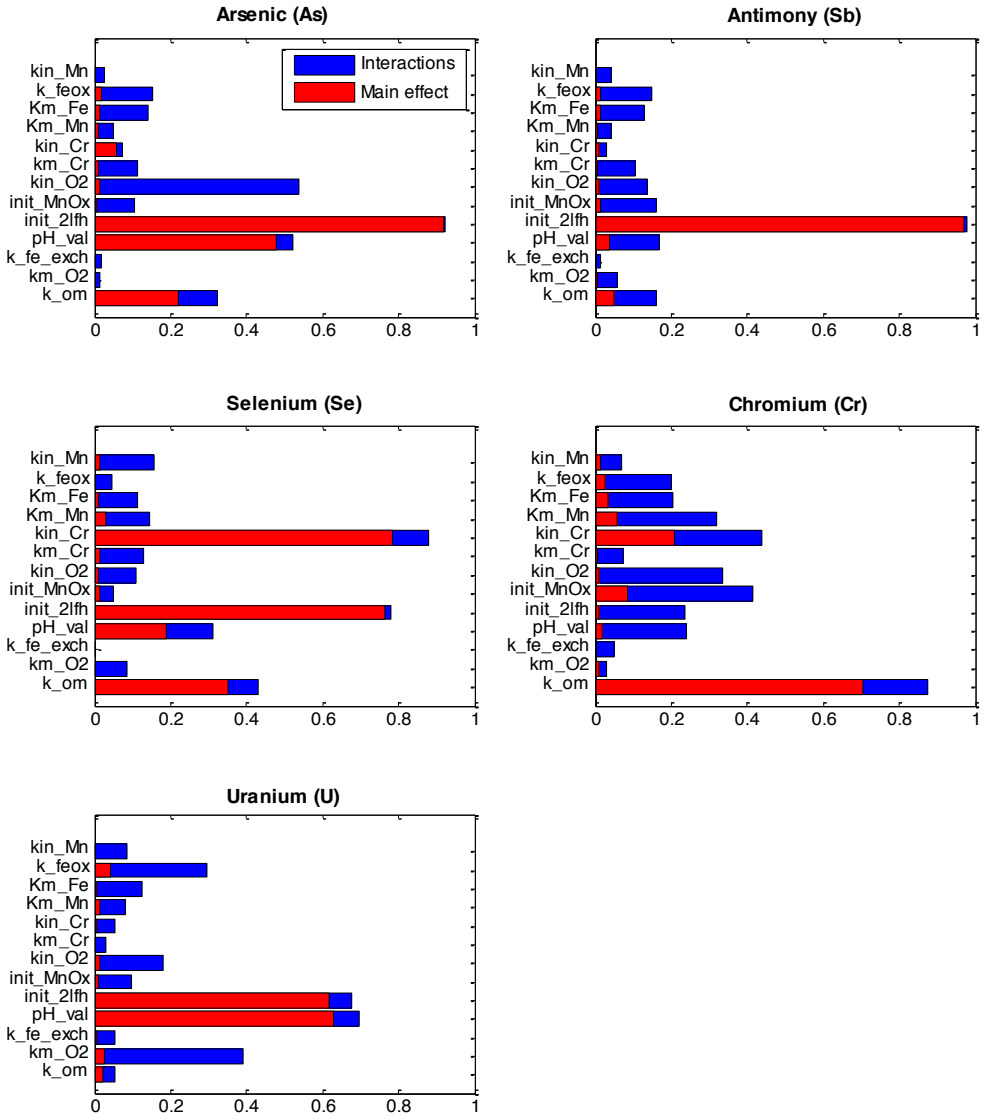

Figure 6-9. Proportion of total variance in modeled aqueous concentrations of As, Sb, Se, Cr and U explained by 13 parameters analyzed by the Extended Fourier amplitude sensitivity test (Extended FAST) sensitivity analysis method. "Main effect" denotes the part of total variance explained by a single parameter and "Interactions" the part explained by interactions with all other parameters. Parameter abbreviations are explained in Table 6-4.

Table 6-7. Pearson's correlation coefficient (r), root-mean-square error (RMSE), observation standard deviation (σ_{obs}) and RMSE:σ_{obs} ratio (RSR) calculated using modeled and measured contaminant concentrations time-series.

Element (50 μM)	**Sb**	**As**	**Cr**	**Mn**	**Fe**	**C**
r	0.61	0.89	0.91	0.92	0.65	0.89
RMSE	6.9**	2.9	8.5*	11.1	7.5	3.3
σ	7.7	5.2	12.6	28.1	8.5	5.3
RSR	0.89	0.56	0.67	0.40	0.88	0.61

Element (500- μM)	**Cr**	**Se**	**U**	**Mn**	**Fe**	**C**
r	0.99	0.99	0.75	0.81	0.81	0.90
RMSE	0.02	0.03	0.06	13.1	5.2	3.5
σ	0.18	0.23	0.07	9.4	2.5	6.8
RSR	0.11	0.14	0.94	1.40	2.07	0.52

*RMSE = 0.07 if the 1st oxic half-cycle is excluded
**RMSE = 2 if the 1st oxic half-cycle is excluded

Chapter 7

Annex-II: Geochemical codes for Chapter 3

7.1 Python Code for Calibration of PHREEQC Model (example for As model)

```
from __future__ import division  # normal division
import os
os.sys.path.append(os.path.dirname(os.path.abspath('..'))
import numpy as np
import math
from scipy.optimize import minimize
from scipy.interpolate import interp1d
import sys
from phreeqc_addon import *
import timeit

# Simple Python 3 compatiblity adjustment.
if sys.version_info[0] == 2:
    range = xrange

"""   %  tuple(x)
    # print string
    return string

def f(x0, dat=[], console=True):
    try:
        conc = simulate_with(phreqc_string(x0))
    except Exception as e:
        print e.args
        return 1e8
    else:
        r = rmsd(conc["As_five_aq(mol/kgw)"] * 1e6, y_interp)
        if console:
            print "".join(["%.5E, " for i in x0]) % tuple(x0)
            print '::::::: %.5E\n' % r
        return r

t_meas_30, y_meas_30 = np.loadtxt("../../../data/Katya exp/soil/As.txt", unpack=True, skiprows=1)
    # t_interp, y_interp = interpolate(t_meas_30, y_meas_30, 101)

    x0_inp = [-1.00381E+02, 7.38573E-07, 4.69315E-09, 1.33492E-05, 3.68692E-11, 4.66749E-05,
2.98233E-07, 2.56092E-09, 3.30171E-09, ]

    res_min = minimize(f, x0_inp, method='Nelder-Mead', options={'xtol': 1e-4, 'disp': True})

    res = simulate_with(phreqc_string(x0_inp))
```

7.2 Python Code for Sensitivity Analysis

```
from __future__ import division  # normal division
# from __future__ import print_function
import matplotlib.pyplot as plt
import numpy as np
import math
from scipy.optimize import minimize
from scipy.interpolate import interp1d
import sys
from SALib.sample import saltelli
from SALib.analyze import sobol
from SALib.test_functions import Ishigami
from phreeqc_addon import *
import os
import timeit
from SALib.analyze import dgsm
from SALib.sample import finite_diff
from SALib.sample import saltelli
from SALib.analyze import sobol
from SALib.analyze import fast
from SALib.sample import fast_sampler
from SALib.test_functions import Ishigami
# Simple Python 3 compatiblity adjustment.
if sys.version_info[0] == 2:
    range = xrange

MODE = 'dll'  # 'dll' or 'com'

if MODE == 'com':
    import phreeqpy.iphreeqc.phreeqc_com as phreeqc_mod
elif MODE == 'dll':
    import phreeqpy.iphreeqc.phreeqc_dll as phreeqc_mod
else:
    raise Exception('Mode "%s" is not defined use "com" or "dll".' % MODE)

def phreqc_string(x):
    new_x = []
    new_x.append( math.log10(x[0]) - 100 )
    new_x.append( math.log10(x[1]) - 100 )
    new_x.append( x[2] )
    new_x.append( x[3] )
    new_x.append( x[4] )
    new_x.append( x[5] )
    new_x.append( x[6] )
    new_x.append( x[7] )
    new_x.append( x[8] )
```

```
    new_x.append( x[9] )
    new_x.append( x[10] )
    new_x.append( x[11] )
    new_x.append( x[9] )
    new_x.append( x[12] )
    new_x.append( x[13] )
    new_x.append( x[14] )
    # print new_x
    x = [str(i) for i in new_x]
    # print x
    # print asd
    string = """

    ####Phreeqc txt file####

"""   %  tuple(x)
# print string
  return string

def f(x0, dat=[], console=True):
    try:
        conc = simulate_with(phreqc_string(x0))
    except Exception as e:
        print e.args
        return 1e8
    else:
        r = rmsd(conc[reference_concentration], y_init)
        if console:
            print "".join(["%.5E, " for i in x0]) % tuple(x0)
            print ':::::::: %.5E\n' % r
        return r

reference_concentration = 'm_As_five_aq(mol/kgw)'
x0_inp = [10**(-1.00542E+02 + 100), 10**(-1.00381E+02 + 100), 9.25315E-07, 1.11261E-07, 6.28567E-
07, 5.01E-11, 4.66749E-05, 3E-8, 4.17115E-06, 1e-6, 9E-8, 4E-06, 4.69315E-09, 1.33492E-05,
7.38573E-07]

conc_init = simulate_with(phreqc_string(x0_inp))
y_init = conc_init[reference_concentration]

    problem = {

        'num_vars': 15,

        'names': ['K_eq5', 'K_eq3', 'k_f5', 'k_b5', 'k_i5', 'k_As_five_aq_detox', 'Km_As_aq_detox',
'k_As_respir', 'Km_As_respir', 'K_in_O2', 'k_As_methyl', 'Km_As_methyl', 'k_f3', 'k_b3', 'k_i3'],

        'groups': None,
```

```
    'bounds': [[0.01 * 10*(-1.00542E+02 + 100), 100 * 10*(-1.00542E+02 + 100)],
               [0.01 * 10*(-1.00381E+02 + 100), 100 * 10*(-1.00381E+02 + 100)],
               [0.01 * 9.25315E-07, 100 * 9.25315E-07],
               [0.01 * 1.11261E-07, 100 * 1.11261E-07],
               [0.01 * 6.28567E-07, 100 * 6.28567E-07],
               [0.01 * 5.01E-11, 100 * 5.01E-11],
               [0.01 * 4.66749E-05, 100 * 4.66749E-05],
               [0.01 * 3E-8, 100 * 3E-8],
               [0.01 * 4.17115E-06, 100 * 4.17115E-06],
               [0.01 * 1e-6, 100 * 1e-6],
               [0.01 * 9E-8, 100 * 9E-8],
               [0.01 * 4E-06, 100 * 4E-06],
               [0.01 * 4.69315E-09, 100 * 4.69315E-09],
               [0.01 * 1.33492E-05, 100 * 1.33492E-05],
               [0.01 * 7.38573E-07, 100 * 7.38573E-07]]
  }
  param_values = fast_sampler.sample(problem, 300)
  Y = sensetivity_evaluate_f(f, param_values)
Si = fast.analyze(problem, Y, print_to_console=True)
```

7.3 PHREEQC Code for O, N, As, Sb, and Cr Fate in Exp. IV

```
DATABASE WATEQ4F.dat

SOLUTION_MASTER_SPECIES
 O           H2O       0.0   O   16.0
 O(0)        O2        0.0   O
 O(-2)       H2O       0.0   0.0

 N_five_aq    N_five_aq    0 N   14.0067
 N_tri_aq     N_tri_aq     0 N    14.0067
 N_gas        N_gas        0 N    28.00

 Ethanol    Ethanol        0.0    46.0684   46.0684
 # 2 mols of C in 1 mol of ethanol
 Acetat     Acetat-        0      59.045    59.045
 C_leak     C_leak         0 C    12

 As_five_aq       As_five_aq       0 As   74.9
 As_five_s_kin    As_five_s_kin    0 As   74.9
 As_five_s_irr    As_five_s_irr    0 As   74.9
 As_three_s_kin   As_three_s_kin   0 As   74.9
 As_three_aq      As_three_aq      0 As   74.9
 As_three_s_irr   As_three_s_irr   0 As   74.9
 As_three_methyl  As_three_methyl  0 As   74.9

 Cr_six_aq        Cr_six_aq        0 Cr   51.996
 Cr_three_solid   Cr_three_solid   0 Cr   51.996
 Cr_six_s_kin     Cr_six_s_kin     0 Cr   51.996
 Cr_six_s_irr     Cr_six_s_irr     0 Cr   51.996

 Sb_five_aq       Sb_five_aq       0 Sb   121.75
 Sb_five_s_kin    Sb_five_s_kin    0 Sb   121.75
 Sb_five_s_irr    Sb_five_s_irr    0 Sb   121.75
 Sb_three_s       Sb_three_s       0 Sb   121.75

SOLUTION_SPECIES
 H2O + 0.01e- = H2O-0.01;    log_k   -9.0
 # Redox buffer for numerical stability. Leave ON.
 2H2O = O2 + 4H+ + 4e-;      log_k   -86.08
 H2O = OH- + H+;             log_k   -14.0

 N_five_aq = N_five_aq;      log_k   0
 N_tri_aq = N_tri_aq;        log_k   0
 N_gas = N_gas;              log_k   0

 Ethanol = Ethanol;          log_k   0
```

```
  Acetat- = Acetat-;          log_k    0
  C_leak = C_leak;                  log_k 0

  As_five_aq = As_five_aq;            log_k 0
  As_five_s_kin = As_five_s_kin;      log_k 0
  As_five_s_irr = As_five_s_irr;      log_k 0
  As_three_s_kin = As_three_s_kin;    log_k 0
  As_three_aq = As_three_aq;          log_k 0
  As_three_s_irr = As_three_s_irr;    log_k 0
  As_three_methyl = As_three_methyl;  log_k 0

  Cr_six_aq = Cr_six_aq;              log_k 0
  Cr_three_solid = Cr_three_solid;    log_k 0
  Cr_six_s_kin = Cr_six_s_kin;        log_k 0
  Cr_six_s_irr = Cr_six_s_irr;        log_k 0

  Sb_five_aq = Sb_five_aq;            log_k 0
  Sb_five_s_kin = Sb_five_s_kin;      log_k 0
  Sb_five_s_irr = Sb_five_s_irr;      log_k 0
  Sb_three_s = Sb_three_s;            log_k 0

SURFACE_MASTER_SPECIES
  As_five_surface   As_five_surface
  As_three_surface  As_three_surface
  Cr_six_surface    Cr_six_surface
  Sb_five_surface   Sb_five_surface

SURFACE_SPECIES
  As_five_surface = As_five_surface
  As_five_surface +  As_five_aq = As_five_surfaceAs_five_aq
#Keq = C(s) / C(aq) ; C(s) = Keq * C(aq)^1
    -log_k %s     #sens_As_aq_tot
  As_three_surface = As_three_surface
  As_three_surface +  As_three_aq = As_three_surfaceAs_three_aq
    -log_k %s     #sens_As_aq_tot

  Cr_six_surface = Cr_six_surface
  Cr_six_surface +  Cr_six_aq = Cr_six_surfaceCr_six_aq
    -log_k -1.01027E+02

  Sb_five_surface = Sb_five_surface
  Sb_five_surface +  Sb_five_aq = Sb_five_surfaceSb_five_aq
    -log_k -1.01075E+02

PHASES
Fix_pH; H+ = H+; log_k 0
```

```
CaHAsO3(s)
CaHAsO3 + 2H+ = Ca+2 + As_three_aq
  log_k -0.206    #Ka = 1.07*10^-7 (Vandercasteele et al., 2002)
  #log_k  -6.938    #Ka = 5.9*10^-9 (Roman-Ross et al., 2006)
  -no_check

CaHAsO4(H2O)(s)
CaHAsO4(H2O) = Ca+2 + H2O + As_five_aq
  log_k -4.79     #log K = -4.79 (Alexandratos et al., 2007: values summarized from different sources)
  -no_check

CaHAsO4(s)
CaHAsO4 = Ca+2 + As_five_aq + H+
  log_k -16.34    #log K = -16.34 (Couture et al., 2010: values summarized from different sources)
  -no_check

Ca3(AsO4)2(H2O)4(s)
Ca3(AsO4)2(H2O)4 = 3Ca+2 + 2As_five_aq + 4H2O
  log_k -21.00    #log K = -21.00 (Alexandratos et al., 2007: values summarized from different sources)
  -no_check

Ca4(OH)2(AsO4)2(H2O)4(s)
Ca4(OH)2(AsO4)2(H2O)44 = 4Ca+2 + 2As_five_aq + 4H2O + 2OH-
  log_k -29.20    #log K = -29.20 (Alexandratos et al., 2007: values summarized from different sources)
  -no_check

Cr_tri(OH)3
Cr_tri(OH)3 + H+ = Cr_tri(OH)2+ + H2O
  log_k 1.3355

Sb(OH)3
Sb(OH)3 = Sb(OH)3
  log_k -7.1099

Sb2O3(s)     #senarmontite
Sb_three_s2O3 = Sb_three_s
  log_k -4.98        # Zotov, 2003
  -no_check

SOLUTION 0
-units mol/L
  pH  7.27  #pH measured in Exp. III
  #Alkalinity 4e-3  # as TIC = HCO3- makes pH = 7.05

  O(0)    1e-3
  Acetat  3e-3
```

```
 N_five_aq  550e-6
 As_five_aq 460e-6
 Cr_six_aq  0.560e-3
 Sb_five_aq 500e-6

 Cl      1.05e-3    #charge
 S       5.64e-3      # sulfur from ICP is 5.64 mM
 K       1.88e-3
 Na      1.84e-3    charge
 Ca      3.15e-3
 Mg      2.17e-3
 Sr      0.0801e-3

EQUILIBRIUM_PHASES 0
Calcite 0 1
#pH buffer, makes pH = 7.5
#Fix_pH -7.27 HCO3- 1
 # -force_equality true

#CaHAsO4(s) 0 1 precipitate_only
#Ca3(AsO4)2(H2O)4(s) 0 1 precipitate_only
#CaHAsO3(s) 0 1 precipitate_only

SAVE SOLUTION 0; SAVE EQUILIBRIUM_PHASES 0
#END

##############

RATES
doc_leak_electrode              #R1 Table 3-4
   -start
     6 k_doc_leak = 0.8e-8
#k_doc_leak = 0.9e-8 for Exp. II; 0.8e-8 for Exp. III;
     100 rate = k_doc_leak
     120 if rate <= 0 then rate = 0
     150 moles = rate * time
     200 save moles
   -end

Ethanol_fermentation_anoxic       #R2 Table 3-4
   -start
     5 if mol("Ethanol") < 1e-12 then goto 200
     6 k_ethanol_an = 4.06e-7
     7 K_in_O2 = 1e-6
     100 rate = k_ethanol_an * mol("Ethanol")*(K_in_O2/(mol("O2")+ K_in_O2))
     110 if rate <= 0 then rate = 0
     120 moles = rate * time
```

```
    130 if (m <= 0) then goto 200
    200 save moles
  -end

Oxygen respir_ethanol        #R3 Table 3-4
    -start
    5 if mol("Ethanol") < 1e-12 then goto 200
    40 k_O2 = 8.76e-7
    50 Km_O2 = 1e-6
    100 rate = k_O2 * mol("Ethanol") * (mol("O2")/(mol("O2")+ Km_O2))
    110 if rate <= 0 then rate = 0
    120 moles = rate * time
    130 if (m <= 0) then goto 200
    200 save moles
  -end

Cr_aq_solid_kin              #R7-8 Table 3-4
  -start
    5 if mol("Cr_six_aq") < 1e-12 then goto 200
    10 k_Cr_f = 1.10978E-06
    20 k_Cr_b = 1.06556E-05
    30 rate = k_Cr_f * mol("Cr_six_aq") - k_Cr_b * mol("Cr_six_s_kin")
    40 if rate <= 0 then rate = 0
    50 moles = rate * time
    200 save moles
  -end
Cr_k_irr                     #R9 Table 3-4
  -start
    5 if mol("Cr_six_s_kin") < 1e-12 then goto 200
    10 k_Cr_ir = 0
    30 rate = k_Cr_ir * mol("Cr_six_s_kin")
    40 if rate <= 0 then rate = 0
    50 moles = rate * time
    200 save moles
  -end

Cr_s_abiotic_reduction       #R10 Table 3-4
  -start
    5 if mol("Cr_six_s_kin") < 1e-12 then goto 200
    10 k_Cr_ab = 1.09070E-06
    20 Cr_s = mol("Cr_six_s_kin") + MOL("Cr_six_surfaceCr_six_aq")
    30 rate = k_Cr_ab * Cr_s
    40 if rate <= 0 then rate = 0
    50 moles = rate * time
    200 save moles
  -end
```

```
Cr_aq_detoxic               #R11 Table 3-4
   -start
     5 if mol("Cr_six_aq") < 1e-12 then goto 200
     10 k_Cr_detox = 1.78552E-10
     20 Km_Cr_detox = 7.17115E-05
     30 rate = k_Cr_detox * mol("Cr_six_aq")/(mol("Cr_six_aq")+ Km_Cr_detox)
     40 if rate <= 0 then rate = 0
     50 moles = rate * time
     200 save moles
   -end

Cr_respiration              #R12 Table 3-4
     -start
     5 if mol("Cr_six_aq") < 1e-12 then goto 200
     7 K_in_O2 = 1e-6
     10 k_Cr_respir = 7E-8
     20 Km_Cr_respir = 1.17115E-05
     25 Cr_tot = mol("Cr_six_aq") + mol("Cr_six_s_kin") + MOL("Cr_six_surfaceCr_six_aq")
     30 rate = k_Cr_respir * mol("Acetat-") * Cr_tot /(Cr_tot + Km_Cr_respir)*(K_in_O2/(mol("O2")+
K_in_O2))
     #30 rate = k_Cr_respir * mol("Acetat-") * mol("Cr_six_aq")/(mol("Cr_six_aq")+Km)
     40 if rate <= 0 then rate = 0
     50 moles = rate * time
     200 save moles
   -end

Nitrate_respiration          #R32 Table 3-4
     -start
     4 k_N_five  = 1e-6
     5 Km_nitrate = 1e-5
#half saturation constant of NO3 = 0.01 mM=1e-5 from Roden, 2008 (simulated, not experimental by
Roden) or 0.25 mM = 25e-5 (Lawerman, 2006
     6 K_in_O2 = 1e-6
#Inhibition constant for higher TEAs,  1e-6
     7 K_in_Cr = 4e-5
#lower Kin -> higher inhibition
     8 Organic_carbon = mol("Ethanol")
     9  if mol("Ethanol") < 1e-12 then goto 200
     20 f_nitrate =  (mol("N_five_aq") / (mol("N_five_aq") + Km_nitrate))*(K_in_O2/(mol("O2")+
K_in_O2))*(K_in_Cr/(mol("Cr_six_aq")+ K_in_Cr))
     30 rate = f_nitrate * k_N_five * Organic_carbon
     40 if rate <= 0 then rate = 0
     60 moles = rate * time
     200 save moles
   -end

Nitrite_respiration        #R33 Table 3-4
```

```
    -start
    4 k_N_three = 8e-7
#1st order rate of ethanol cons. in R2-2014 (1st phase=1e-05) (2d and 3d phase =6e-6)
    5 Km_nitrite = 1e-5
    6 K_in_O2 = 1e-6
    7 K_in_Cr = 4e-5
    8 Organic_carbon = mol("Ethanol")
    9  if mol("Ethanol") < 1e-12 then goto 200
    20 f_Nitrite = (mol("N_tri_aq")/(mol("N_tri_aq") + Km_nitrite))*(K_in_O2/(mol("O2")+
K_in_O2))*(K_in_Cr/(mol("Cr_six_aq")+ K_in_Cr))
    30 rate = f_Nitrite * k_N_three * Organic_carbon
    40 if rate <= 0 then rate = 0
    60 moles = rate * time
    200 save moles
   -end

As_five_aq_solid_kin       #R15-16 Table 3-4
   -start
    5 if mol("As_five_aq") < 1e-12 then goto 200
    10 k_As_five_f = %s    #sens_As_aq_tot
    20 k_As_five_b = %s    #sens_As_aq_tot
    30 rate = k_As_five_f * mol("As_five_aq") - k_As_five_b * mol("As_five_s_kin")
    40 if rate <= 0 then rate = 0
    50 moles = rate * time
    200 save moles
   -end

As_five_k_irr              #R17 Table 3-4
   -start
    5 if mol("As_five_s_kin") < 1e-12 then goto 200
    10 k_As_five_ir = %s   #sens_As_aq_tot
    30 rate = k_As_five_ir * mol("As_five_s_kin")
    40 if rate <= 0 then rate = 0
    50 moles = rate * time
    200 save moles
   -end

As_five_aq_detox          #R18 Table 3-4
   -start
    5 if mol("As_five_aq") < 1e-12 then goto 200
    22 k_As_five_aq_detox = %s      #sens_As_aq_tot
    23 Km_As_aq_detox = %s   #sens_As_aq_tot
    30 rate = k_As_five_aq_detox * mol("As_five_aq")/(mol("As_five_aq")+ Km_As_aq_detox)
    40 if rate <= 0 then rate = 0
    50 moles = rate * time
    200 save moles
   -end
```

```
As_respiration                #R19 Table 3-4
     -start
     5 if mol("As_five_aq") < 1e-12 then goto 200
     10 k_As_respir = %s       #sens_As_aq_tot
     20 Km_As_respir = %s      #sens_As_aq_tot
#higher Km -> slower reaction
     21 K_in_O2 = %s     #sens_As_aq_tot
     22 K_in_Cr = 9e-4
     23 K_in_NO3 = 9e-4
     24 Organic_carbon = mol("Acetat-")
     25 As_tot = mol("As_five_aq")# + mol("As_five_s_kin") + MOL("As_five_surfaceAs_five_aq")
     30 rate = k_As_respir * mol("Acetat-") * As_tot /(As_tot + Km_As_respir) * (K_in_O2/(mol("O2")+
K_in_O2))*(K_in_Cr/(mol("Cr_six_aq")+ K_in_Cr))* (K_in_NO3/(mol("N_five_aq")+ K_in_NO3))
     40 if rate <= 0 then rate = 0
     50 moles = rate * time
     200 save moles
   -end

As_three_methylation              #R24 Table 3-4
     -start
     # 5 if mol("As_five_aq") < 1e-5 then goto 200     #limited by the presence of As(5) 1e-5
     5 if mol("Sb_three_s") > 16.5e-6 then goto 200
     10 k_As_methyl = %s       #sens_As_aq_tot         #9e-8 makes 200 uM MeAs
     20 Km_As_methyl = %s     #sens_As_aq_tot
     21 K_in_O2 = %s    #sens_As_aq_tot
     25 As_tot = mol("As_three_aq")# + mol("As_five_s_kin") + MOL("As_five_surfaceAs_five_aq")
     30 rate = k_As_methyl * mol("Acetat-") * As_tot /(As_tot + Km_As_methyl) *
(K_in_O2/(mol("O2")+ K_in_O2))
     40 if rate <= 0 then rate = 0
     50 moles = rate * time
     200 save moles
   -end

As_three_aq_solid_kin          #R21-22 Table 3-4
   -start
     5 if mol("As_three_aq") < 1e-12 then goto 200
     10 k_As_three_f =  %s    #sens_As_aq_tot
     20 k_As_three_b = %s   #sens_As_aq_tot
     30 rate = k_As_three_f * mol("As_three_aq") - k_As_three_b * mol("As_three_s_kin")
     40 if rate <= 0 then rate = 0
     50 moles = rate * time
     200 save moles
   -end

As_three_k_irr              #R23 Table 3-4
   -start
```

```
    5 if mol("As_three_s_kin") < 1e-12 then goto 200
    10 k_As_three_irr = %s   #sens_As_aq_tot
    30 rate = k_As_three_irr * mol("As_three_s_kin")
    40 if rate <= 0 then rate = 0
    50 moles = rate * time
    200 save moles
  -end

Sb_aq_solid_kin             #R26-27 Table 3-4
  -start
    5 if mol("Sb_five_aq") < 1e-12 then goto 200
    10 k_Sb_f = 3.18435E-07
    20 k_Sb_b = 1.16488E-06
    30 rate = k_Sb_f * mol("Sb_five_aq") - k_Sb_b * mol("Sb_five_s_kin")
    40 if rate <= 0 then rate = 0
    50 moles = rate * time
    200 save moles
  -end

Sb_k_irr                    #R28 Table 3-4
  -start
    5 if mol("Sb_five_s_kin") < 1e-12 then goto 200
    10 k_Sb_ir = 1.85301E-07
    30 rate = k_Sb_ir * mol("Sb_five_s_kin")
    40 if rate <= 0 then rate = 0
    50 moles = rate * time
    200 save moles
  -end

Sb_five_s_detox          #R29 Table 3-4
  -start
    5 if mol("Sb_five_s_kin") < 1e-12 then goto 200
    22 k_Sb_s_detox = 1.19e-11
    23 Km_Sb_s_detox = 4.53093E-12
    24 Sb_s = mol("Sb_five_s_kin") + mol("Sb_five_surfaceSb_five_aq")
    30 rate = k_Sb_s_detox * Sb_s/(Sb_s + Km_Sb_s_detox)
    40 if rate <= 0 then rate = 0
    50 moles = rate * time
    200 save moles
  -end

Sb_respiration              #R30 Table 3-4
    -start
    5 if mol("Sb_five_aq") < 1e-12 then goto 200
    10 k_Sb_respir = 3E-9
    20 Km_Sb_respir = 4.17115E-06
    21 K_in_O2 = 1e-6
```

```
    # 22 K_in_Cr = 9e-4
    # 23 K_in_NO3 = 9e-4
    22 K_in_As = 5e-6
    23 Organic_carbon = mol("Ethanol")
    30 rate = k_Sb_respir * Organic_carbon * mol("Sb_five_aq") /(mol("Sb_five_aq") + Km_Sb_respir) *
(K_in_O2/(mol("O2")+ K_in_O2)) * (K_in_As/(mol("As_five_aq")+
K_in_As))#*(K_in_Cr/(mol("Cr_six_aq")+ K_in_Cr))* (K_in_NO3/(mol("N_five_aq")+ K_in_NO3))
    40 if rate <= 0 then rate = 0
    50 moles = rate * time
    200 save moles
  -end

USER_GRAPH 0
-headings  x
-chart_title "Exp. IV"
-axis_titles "Time / days" "Concentration"
-axis_scale x_axis 0 15
#-axis_scale y_axis -1 10
-initial_solutions true
#-plot_tsv_file NO3_exp4.txt
#-plot_tsv_file Cr_exp4.txt
#-plot_tsv_file As_exp4.txt
#-plot_tsv_file As_exp4_speciation_aq.txt
-start
10 graph_x total_time /3600/24
#20 graph_y MOL("N_five_aq")*1e6
#40 graph_y MOL("N_tri_aq")*1e6
#50 graph_y mol("O2")*1e6
#60 graph_y mol("Ethanol")*2*1e3
# ethanol * 2 = Carbon in ethanol

#80 graph_y MOL("Cr_six_aq")*1e6
#30 graph_y MOL("Cr_three_solid")*1e6
#40 graph_y MOL("Cr_six_s_kin")*1e6 + MOL("Cr_six_surfaceCr_six_aq")*1e6

#90 graph_y mol("C_leak")*1e3
#100 graph_y mol("Ethanol")*2*1e3 + mol("C_leak")*1e3      #tot DOC
#110 graph_y mol("Acetat-")*2*1e3
#120 graph_y mol("Ethanol")*2*1e3

#120 graph_y MOL("As_three_aq")*1e6 + MOL("As_five_aq")*1e6
#130 graph_y MOL("As_three_aq")*1e6
 140 graph_y MOL("As_five_aq")*1e6
#150 graph_y MOL("As_three_methyl")*1e6

#160 graph_y MOL("As_three_s_kin")*1e6 + MOL("As_three_s_irr")*1e6 +
MOL("As_three_surfaceAs_three_aq")*1e6
```

```
#170 graph_y MOL("As_five_s_kin")*1e6 + MOL("As_five_s_irr")*1e6 +
MOL("As_five_surfaceAs_five_aq")*1e6 #+ MOL("As_three_methyl")*1e6

#160 graph_y MOL("As_three_s_kin")*1e6
#170 graph_y MOL("As_three_s_irr")*1e6
#180 graph_y MOL("As_three_surfaceAs_three_aq")*1e6

#160 graph_y MOL("As_five_s_kin")*1e6
#170 graph_y MOL("As_five_s_irr")*1e6
#180 graph_y MOL("As_five_surfaceAs_five_aq")*1e6


#140 graph_y MOL("Sb_five_s_kin")*1e6 + MOL("Sb_five_surfaceSb_five_aq")*1e6+
MOL("Sb_five_s_irr")*1e6
#150 graph_y MOL("Sb_three_s")*1e6

#130 graph_y MOL("Sb_five_aq")*1e6
#140 graph_y MOL("Sb_three_s")*1e6
#150 graph_y MOL("Sb_five_s_kin")*1e6 + MOL("Sb_five_s_irr")*1e6 +
MOL("Sb_five_surfaceSb_five_aq")*1e6
-end

INCREMENTAL_REACTIONS true

KINETICS 1
 doc_leak_electrode
  -formula C_leak +1

 Ethanol_fermentation_anoxic
  -formula Ethanol -1 Acetat- +1

 Oxygen respir_ethanol
 # 3O2 + ethanol = acetate + H2O + H+
 # 3O2 + ethanol = 2HCO3- + H2O + 2H+
   -formula O2 -3 Ethanol -1 Acetat- +1 H2O +1

 Cr_aq_solid_kin
  -formula Cr_six_aq -1 Cr_six_s_kin +1
 Cr_s_abiotic_reduction
  -formula Cr_six_s_kin -1 Cr_three_solid +1
 Cr_k_irr
  -formula Cr_six_s_irr 1 Cr_six_s_kin -1
 Cr_aq_detoxic
  -formula Cr_six_aq -1 Cr_three_solid +1
 Cr_respiration
  -formula Cr_six_aq -2.66 Acetat- -1  Cr_three_solid +2.66   HCO3- +2  #2.66 Cr
```

```
 Nitrate_respiration
   -formula N_five_aq -2 Ethanol -1 N_tri_aq +2 Acetat- +1 H2O +1

 Nitrite_respiration
 # 0.66 NO2- + ethanol + 1/3 H+ = 0.66 NH4+ + acetate + 0.33 H2O
 # 2 NO2- + ethanol + H2O + 2H+ = 2 NH4+ + 2 HCO3-
 ###or
 # 4 NO2- + ethanol + 2H+ = 2 N2 + 2 HCO3- + 3 H2O
 # 1.66 NO2- + ethanol + 1.66 H+ = 0.83 N2 + acetate + 14/6 H2O
   -formula  N_tri_aq -1.66 Ethanol -1 N_gas +0.83 Acetat- +1 H2O +2.33

 As_five_aq_solid_kin
   -formula As_five_aq -1 As_five_s_kin 1
 As_five_k_irr
   -formula As_five_s_irr 1 As_five_s_kin -1
 As_three_aq_solid_kin
   -formula As_three_aq -1 As_three_s_kin 1
 As_three_k_irr
   -formula As_three_s_irr 1 As_three_s_kin -1
 As_five_aq_detox
   -formula As_five_aq -1 As_three_aq 1
 As_respiration
    -formula As_five_aq -4 Acetat- -1  As_three_aq +4   HCO3- +2
 As_three_methylation
   -formula As_three_aq -1 As_three_methyl +1

 Sb_aq_solid_kin
   -formula Sb_five_aq -1 Sb_five_s_kin +1
 Sb_k_irr
   -formula Sb_five_s_irr 1 Sb_five_s_kin -1
 Sb_five_s_detox
   -formula Sb_five_s_kin -1 Sb_five_surfaceSb_five_aq -1   Sb_three_s 1
 Sb_respiration
   -formula Sb_five_aq -2 Sb_three_s 2 Ethanol -1 Acetat- +1

 -tol 1e-8
 -steps 604800 sec in 15 steps   #4233600 sec

SURFACE 0
 #unlimited surface as an example in Phreeqc Manual

    Cr_six_surface    1e100   1   1

 As_three_surface  1e100   1   1
 As_five_surface   1e100   1   1
 Sb_five_surface   1e100   1   1
```

```
USER_PUNCH 1
   -headings As(tot)
   -start
   20 punch MOL("As_three_aq")*1e6 + MOL("As_five_aq")*1e6
   -end

SELECTED_OUTPUT 1
  -file Exp4.txt
  -molalities As_five_aq

TITLE 1 - ANOXIC CYCLE

USE SOLUTION 0; USE EQUILIBRIUM_PHASES 0; use kinetics 1; USE SURFACE 0
GAS_PHASE
  CO2(g)  0.01              #atm

REACTION 1
Ethanol
11.2e-3 in 1 step
#moles of ethanol => x*2 = moles of carbon 10e-3 for ethanol; or 11.2e-3 for tot

SAVE SOLUTION 0; SAVE EQUILIBRIUM_PHASES 0; SAVE SURFACE 0
END

TITLE 2 - OXIC CYCLE

USE SOLUTION 0; USE EQUILIBRIUM_PHASES 0; USE KINETICS 1; USE SURFACE 0
GAS_PHASE
  CO2(g)  0.01
  O2(g)   0.22      # 0.22 atm in the AIR

SAVE SOLUTION 0; SAVE EQUILIBRIUM_PHASES 0; SAVE SURFACE 0
END

TITLE 3 - ANOXIC CYCLE

USE SOLUTION 0; USE EQUILIBRIUM_PHASES 0; USE KINETICS 1; USE SURFACE 0
GAS_PHASE
  CO2(g)  0.01

REACTION 2
Ethanol
4.2e-3 in 1 step    #moles of ethanol => 2.5e-3*2 = moles of carbon

SAVE SOLUTION 0; SAVE EQUILIBRIUM_PHASES 0; SAVE SURFACE 0
END
```

TITLE 4 - OXIC CYCLE

USE SOLUTION 0; USE EQUILIBRIUM_PHASES 0; USE KINETICS 1; USE SURFACE 0
GAS_PHASE
 CO2(g) 0.01
 O2(g) 0.22 # 0.22 atm in the AIR

SAVE SOLUTION 0; SAVE EQUILIBRIUM_PHASES 0; SAVE SURFACE 0
END

TITLE 5 - ANOXIC CYCLE

USE SOLUTION 0; USE EQUILIBRIUM_PHASES 0; USE KINETICS 1; USE SURFACE 0
GAS_PHASE
 CO2(g) 0.01

REACTION 3
Ethanol
6e-3 in 1 step #3.9e-3

SAVE SOLUTION 0; SAVE EQUILIBRIUM_PHASES 0; SAVE SURFACE 0
END

TITLE 6 - OXIC CYCLE

USE SOLUTION 0; USE EQUILIBRIUM_PHASES 0; USE KINETICS 1; USE SURFACE 0
GAS_PHASE
 CO2(g) 0.01
 O2(g) 0.22 # 0.22 atm in the AIR

SAVE SOLUTION 0; SAVE EQUILIBRIUM_PHASES 0; SAVE SURFACE 0
END

TITLE 7 - ANOXIC CYCLE

USE SOLUTION 0; USE EQUILIBRIUM_PHASES 0; USE KINETICS 1; USE SURFACE 0
GAS_PHASE
 CO2(g) 0.01

REACTION 4
Ethanol
9.1e-3 in 1 step

SAVE SOLUTION 0; SAVE EQUILIBRIUM_PHASES 0; SAVE SURFACE 0
END

Bibliography

Abin, C.A., Hollibaugh, J.T., 2014. Dissimilatory Antimonate Reduction and Production of Antimony Trioxide Microcrystals by a Novel Microorganism. Environ. Sci. Technol. 48, 681–688. doi:10.1021/es404098z

Aeschbacher, M., Sander, M., Schwarzenbach, R.P., 2010. Novel electrochemical approach to assess the redox properties of humic substances. Environ. Sci. Technol. 44, 87–93. doi:10.1021/es902627p

Al-Ghusain, I., Hao, O.J., 1995. Use of pH as Control Parameter for Aerobic/Anoxic Sludge Digestion. J. Environ. Eng. 121, 225–235. doi:10.1061/(ASCE)0733-9372(1995)121:3(225)

Aldous, L., Compton, R.G., 2011. The mechanism of hydrazine electro-oxidation revealed by platinum microelectrodes: role of residual oxides. Phys. Chem. Chem. Phys. 13, 5279. doi:10.1039/c0cp02261f

Alloway, B.J., 1995. Heavy metals in soils: Trace Metals and Metalloids in Soils and their Bioavailability. Chapman and Hall, London, UK.

Altmaier, M., Xavier, G., David, F., Gunnar, B., 2011. Intercomparison of Redox Determination Methods on Designed and Near-Natural Aqueous Systems. Volume 7572 of KIT scientific reports, Karlsruher Institut für Technologie.

Altmann, S., 2008. “Geo”chemical research: A key building block for nuclear waste disposal safety cases. J. Contam. Hydrol. 102, 174–179. doi:10.1016/j.jconhyd.2008.09.012

Amend, J.P., Saltikov, C., Lu, G.-S., Hernandez, J., 2014. Microbial Arsenic Metabolism and Reaction Energetics. Rev. Mineral. Geochemistry 79, 391–433. doi:10.2138/rmg.2014.79.7

Andra, 2009. French National Plan for the Management of Radioactive Materials and Waste (PNGMDR).

André, L., Pauwels, H., Dictor, M.-C., Parmentier, M., Azaroual, M., 2011. Experiments and numerical modelling of microbially-catalysed denitrification reactions. Chem. Geol. 287, 171–181. doi:10.1016/j.chemgeo.2011.06.008

Andrewes, P., Cullen, W.R., Polishchuk, E., 2000. Arsenic and Antimony Biomethylation by Scopulariopsis brevicaulis : Interaction of Arsenic and Antimony Compounds. Environ. Sci. Technol. 34, 2249–2253. doi:10.1021/es991269p

Appelo, C.A.., Postma, D., 2005. Geochemistry, Groundwater and Pollution. CRC Press LLC.

Appelo, C.A.J., Van Der Weiden, M.J.J., Tournassat, C., Charlet, L., 2002. Surface Complexation of Ferrous Iron and Carbonate on Ferrihydrite and the Mobilization of Arsenic. Environ. Sci. Technol.

36, 3096–3103. doi:10.1021/es010130n

Auqué, L., Gimeno, M.J., Gómez, J., Nilsson, A.-C., 2008. Potentiometrically measured Eh in groundwaters from the Scandinavian Shield. Appl. Geochemistry 23, 1820–1833. doi:10.1016/j.apgeochem.2008.02.016

Awad, M.I., Saleh, M.M., Ohsaka, T., 2011. Impact of SO2 poisoning of platinum nanoparticles modified glassy carbon electrode on oxygen reduction. J. Power Sources 196, 3722–3728. doi:10.1016/j.jpowsour.2010.12.080

Barcelona, M.J., Holm, T.R., Schock, M.R., George, G.K., 1989. Spatial and temporal gradients in aquifer oxidation-reduction conditions. Water Resour. Res. 25, 991–1003. doi:10.1029/WR025i005p00991

Bard, J.A., Parsons, R., Jordan, J., 1985. Standard Potentials in Aqueous Solution. Marcel Dekker, Inc.

Bargar, J.R., Williams, K.H., Campbell, K.M., Long, P.E., Stubbs, J.E., Suvorova, E.I., Lezama-Pacheco, J.S., Alessi, D.S., Stylo, M., Webb, S.M., Davis, J. a, Giammar, D.E., Blue, L.Y., Bernier-Latmani, R., 2013. Uranium redox transition pathways in acetate-amended sediments. Proc. Natl. Acad. Sci. 110, 4506–4511. doi:10.1073/pnas.1219198110

Barth, J.A.C., Grathwohl, P., Fowler, H.J., Bellin, A., Gerzabek, M.H., Lair, G.J., Barceló, D., Petrovic, M., Navarro, A., Négrel, P., Petelet-Giraud, E., Darmendrail, D., Rijnaarts, H., Langenhoff, A., de Weert, J., Slob, A., van der Zaan, B.M., Gerritse, J., Frank, E., Gutierrez, A., Kretzschmar, R., Gocht, T., Steidle, D., Garrido, F., Jones, K.C., Meijer, S., Moeckel, C., Marsman, A., Klaver, G., Vogel, T., Bürger, C., Kolditz, O., Broers, H.P., Baran, N., Joziasse, J., Von Tümpling, W., Van Gaans, P., Merly, C., Chapman, A., Brouyère, S., Aguilar, J.B., Orban, P., Tas, N., Smidt, H., 2009. Mobility, Turnover and Storage of Pollutants in Soils, Sediments and Waters: Achievements and Results of the EU Project AquaTerra - A Review, in: Sustainable Agriculture. Springer Netherlands, Dordrecht, pp. 857–871. doi:10.1007/978-90-481-2666-8_52

Bartlett, R.J., 1991. Chromium cycling in soils and water: links, gaps, and methods. Environ. Health Perspect. 92, 17–24. doi:10.1289/ehp.919217

Basta, N.T., Ryan, J.A., Chaney, R.L., 2005. Trace Element Chemistry in Residual-Treated Soil. J. Environ. Qual. 34, 49. doi:10.2134/jeq2005.0049dup

Becking, L.G.M.B., Kaplan, I.R., Moore, D., 1960. Limits of the Natural Environment in Terms of pH and

Oxidation-Reduction Potentials. J. Geol. 68, 243–284. doi:10.1086/626659

Beliaev, A.S., Klingeman, D.M., Klappenbach, J.A., Wu, L., Romine, F., Tiedje, J.M., Nealson, K.H., Fredrickson, J.K., Zhou, J., Romine, M.F., 2005. Global Transcriptome Analysis of Shewanella oneidensis MR-1 Exposed to Different Terminal Electron Acceptors. J. Bacteriol. 187, 7138–7145. doi:10.1128/JB.187.20.7138

Belzile, N., Chen, Y., Wang, Z., 2001. Oxidation of antimony (III) by amorphous iron and manganese oxyhydroxides. Chem. Geol. 174, 379–387. doi:10.1016/S0009-2541(00)00287-4

Bentley, R., Chasteen, T.G., 2002. Microbial Methylation of Metalloids: Arsenic, Antimony, and Bismuth. Microbiol. Mol. Biol. Rev. 66, 250–271. doi:10.1128/MMBR.66.2.250-271.2002

Bergmann, J., Friedel, P., Kleeberg, R., 1998. BGMN - a new fundamental parameters based Rietveld program for laboratory X-ray sources, it's use in quantitative analysis and structure investigations. Comm. Powder Diffraction, Int. Union Crystallogr. CPD Newsl. No. 20, 5–8.

Berner, R.A., 1963. Electrode studies of hydrogen sulfide in marine sediments. Geochim. Cosmochim. Acta 27, 563–575. doi:10.1016/0016-7037(63)90013-9

Bertron, A., Jacquemet, N., Erable, B., Sablayrolles, C., Escadeillas, G., Albrecht, A., 2014. Reactivity of nitrate and organic acids at the concrete–bitumen interface of a nuclear waste repository cell. Nucl. Eng. Des. 268, 51–57. doi:10.1016/j.nucengdes.2013.11.085

Bethke, C.M., Sanford, R. a., Kirk, M.F., Jin, Q., Flynn, T.M., 2011. The thermodynamic ladder in geomicrobiology. Am. J. Sci. 311, 183–210. doi:10.2475/03.2011.01

Bildstein, O., Pozo, C., Jullien, M., Trotignon, L., 2005. Modelling oxidising perturbations in argillaceous material, in: Clays in Natural and Engineered Barriers for Radioactive Waste Confinement Meeting. 14-18/ 03, Tours, France.

Bishop, M.E., Glasser, P., Dong, H., Arey, B., Kovarik, L., 2014. Reduction and immobilization of hexavalent chromium by microbially reduced Fe-bearing clay minerals. Geochim. Cosmochim. Acta 133, 186–203. doi:10.1016/j.gca.2014.02.040

Blandamer, M.J., Burgess, J., Peacock, R.D., 1974. Solubility of sodium hexahydroxoantimonate in water and in mixed aqueous solvents. J. Chem. Soc. Dalt. Trans. 1084. doi:10.1039/dt9740001084

Blowes, D.W., Ptacek, C.J., Benner, S.G., McRae, C.W.., Bennett, T.A., Puls, R.W., 2000. Treatment of

inorganic contaminants using permeable reactive barriers. J. Contam. Hydrol. 45, 123–137. doi:10.1016/S0169-7722(00)00122-4

Bolleter, W.T., Bushman, C.J., Tidwell, P.W., 1961. Spectrophotometric Determination of Ammonia as Indophenol. Anal. Chem. 33, 592–594. doi:10.1021/ac60172a034

Borch, T., Kretzschmar, R., Kappler, A., Cappellen, P. Van, Ginder-Vogel, M., Voegelin, A., Campbell, K., 2010. Biogeochemical Redox Processes and their Impact on Contaminant Dynamics. Environ. Sci. Technol. 44, 15–23. doi:10.1021/es9026248

Bosch, J., Lee, K.-Y., Jordan, G., Kim, K.-W., Meckenstock, R.U., 2012. Anaerobic, Nitrate-Dependent Oxidation of Pyrite Nanoparticles by Thiobacillus denitrificans. Environ. Sci. Technol. 46, 2095–2101. doi:10.1021/es2022329

Bothe, J. V., Brown, P.W., 1999. The stabilities of calcium arsenates at 23±1°C. J. Hazard. Mater. 69, 197–207. doi:10.1016/S0304-3894(99)00105-3

Brezonik, P.L., Arnold, W.A., 2011. Water Chemistry: An Introduction to the Chemistry of Natural and Engineered Aquatic Systems. Oxford University Press, New York.

Buchs, B., Evangelou, M.W.H., Winkel, L.H.E., Lenz, M., 2013. Colloidal Properties of Nanoparticular Biogenic Selenium Govern Environmental Fate and Bioremediation Effectiveness. Environ. Sci. Technol. 47, 2401–2407. doi:10.1021/es304940s

Burke, R.W., Deardorff, E.R., Menis, O., 1972. Liquid absorbance standards. J. Res. Natl. Bur. Stand. Sect. A Phys. Chem. 76A, 469. doi:10.6028/jres.076A.041

Burnol, A., Garrido, F., Baranger, P., Joulian, C., Dictor, M.-C., Bodénan, F., Morin, G., Charlet, L., 2007. Decoupling of arsenic and iron release from ferrihydrite suspension under reducing conditions: a biogeochemical model. Geochem. Trans. 8, 12. doi:10.1186/1467-4866-8-12

Burrows, W., 1941. Oxidation-Reduction Potentials in Salmonella Cultures: III. The Relation between Characteristic Potential and Antigenic Structure. J. Infect. Dis. 69, 141–147.

Buschmann, J., Canonica, S., Sigg, L., 2005. Photoinduced Oxidation of Antimony(III) in the Presence of Humic Acid. Environ. Sci. Technol. 39, 5335–5341. doi:10.1021/es050269o

Butler, E.C., Chen, L., Hansel, C.M., Krumholz, L.R., Elwood Madden, A.S., Lan, Y., 2015. Biological versus mineralogical chromium reduction: potential for reoxidation by manganese oxide. Environ.

Sci. Process. Impacts 17, 1930–1940. doi:10.1039/C5EM00286A

Campbell, K.M., Nordstrom, D.K., 2014. Arsenic Speciation and Sorption in Natural Environments. Rev. Mineral. Geochemistry 79, 185–216. doi:10.2138/rmg.2014.79.3

Canavan, R.W., Slomp, C.P., Jourabchi, P., Van Cappellen, P., Laverman, A.M., van den Berg, G. a., 2006. Organic matter mineralization in sediment of a coastal freshwater lake and response to salinization. Geochim. Cosmochim. Acta 70, 2836–2855. doi:10.1016/j.gca.2006.03.012

Canfield, D., Thamdrup, B., Kristensen, E., 2005. Aquatic Geomicrobiology. Advances in Marine Biology (Appendix), Aquatic Geomicrobiology. Advances in Marine Biology. Academic, New York.

Casiot, C., Ujevic, M., Munoz, M., Seidel, J.L., Elbaz-Poulichet, F., 2007. Antimony and arsenic mobility in a creek draining an antimony mine abandoned 85 years ago (upper Orb basin, France). Appl. Geochemistry 22, 788–798. doi:10.1016/j.apgeochem.2006.11.007

Cervantes, C., Guangyong, J., Ramirez, J., Silver, S., 1994. Resistance to arsenic compounds in microorganisms. FEMS Microbiol. Rev. 15, 355–367. doi:10.1016/0168-6445(94)90069-8

Chakraborty, S., Favre, F., Banerjee, D., Scheinost, A.C., Mullet, M., Ehrhardt, J.-J., Brendle, J., Vidal, L., Charlet, L., 2010. U(VI) Sorption and Reduction by Fe(II) Sorbed on Montmorillonite. Environ. Sci. Technol. 44, 3779–3785. doi:10.1021/es903493n

Chakraborty, S., Wolthers, M., Chatterjee, D., Charlet, L., 2007. Adsorption of arsenite and arsenate onto muscovite and biotite mica. J. Colloid Interface Sci. 309, 392–401. doi:10.1016/j.jcis.2006.10.014

Chappaz, A., Gobeil, C., Tessier, A., 2010. Controls on uranium distribution in lake sediments. Geochim. Cosmochim. Acta 74, 203–214. doi:10.1016/j.gca.2009.09.026

Charlet, L., Bardelli, F., Parsons, C.T., He, J., Chakraborty, S., Gailer, J., 2012. Arsenic binding onto phyllosilicates and glutathione: soil immobilisation and human excretion mechanisms, in: Ng, Noller, Naidu, Bundschuh, Bhattacharya (Eds.), Understanding the Geological and Medical Interface of Arsenic. Taylor & Francis Group, London, pp. 59–62.

Charlet, L., Manceau, A.A., 1992. X-ray absorption spectroscopic study of the sorption of Cr(III) at the oxide-water interface: II. Adsorption, coprecipitation, and surface precipitation on hydrous ferric oxide. J. Colloid Interface Sci. 148, 443–458. doi:10.1016/0021-9797(92)90182-L

Charlet, L., Morin, G., Rose, J., Wang, Y., Auffan, M., Burnol, A., Fernandez-Martinez, A., 2011.

Reactivity at (nano)particle-water interfaces, redox processes, and arsenic transport in the environment. Comptes Rendus Geosci. 343, 123–139. doi:10.1016/j.crte.2010.11.005

Charlton, S.R., Parkhurst, D.L., 2011. Modules based on the geochemical model PHREEQC for use in scripting and programming languages. Comput. Geosci. 37, 1653–1663. doi:10.1016/j.cageo.2011.02.005

Chen, J.M., Hao, O.J., 1998. Microbial Chromium (VI) Reduction. Crit. Rev. Environ. Sci. Technol. 28, 219–251. doi:10.1080/10643389891254214

Cheung, K.H., Gu, J., 2007. Mechanism of hexavalent chromium detoxification by microorganisms and bioremediation application potential: A review. Int. Biodeterior. Biodegradation 59, 8–15. doi:10.1016/j.ibiod.2006.05.002

Chon, C.-M., Kim, J.G., Moon, H.-S., 2006. Kinetics of chromate reduction by pyrite and biotite under acidic conditions. Appl. Geochemistry 21, 1469–1481. doi:10.1016/j.apgeochem.2006.06.012

Christensen, T.H., Bjerg, P.L., Banwart, S. a, Jakobsen, R., Heron, G., Albrechtsen, H.-J., 2000. Characterization of redox conditions in groundwater contaminant plumes. J. Contam. Hydrol. 45, 165–241. doi:10.1016/S0169-7722(00)00109-1

Claret, F., Lerouge, C., Laurioux, T., Bizi, M., Conte, T., Ghestem, J.P., Wille, G., Sato, T., Gaucher, E.C., Giffaut, E., Tournassat, C., 2010. Natural iodine in a clay formation: Implications for iodine fate in geological disposals. Geochim. Cosmochim. Acta 74, 16–29. doi:DOI 10.1016/j.gca.2009.09.030

Cornelis, G., Johnson, C.A., Gerven, T. Van, Vandecasteele, C., 2008. Leaching mechanisms of oxyanionic metalloid and metal species in alkaline solid wastes: A review. Appl. Geochemistry 23, 955–976. doi:10.1016/j.apgeochem.2008.02.001

Cornell, R.M., Schwertmann, U., 2003. The Iron Oxides: Structure, Properties, Reactions, Occurences and Uses. Wiley_VCH Verlag GmbH & Co. KGaA, Weinheim.

Cory, R.M., McKnight, D.M., 2005. Fluorescence Spectroscopy Reveals Ubiquitous Presence of Oxidized and Reduced Quinones in Dissolved Organic Matter. Environ. Sci. Technol. 39, 8142–8149. doi:10.1021/es0506962

Cotten, J., Le Dez, A., Bau, M., Caroff, M., Maury, R.C., Dulski, P., Fourcade, S., Bohn, M., Brousse, R.,

1995. Origin of anomalous rare-earth element and yttrium enrichments in subaerially exposed basalts: Evidence from French Polynesia. Chem. Geol. 119, 115–138. doi:10.1016/0009-2541(94)00102-E

Couture, R.-M., Charlet, L., Markelova, E., Madé, B., Parsons, C.T., 2015. On–Off Mobilization of Contaminants in Soils during Redox Oscillations. Environ. Sci. Technol. 49, 3015–3023. doi:10.1021/es5061879

Couture, R.-M., Rose, J., Kumar, N., Mitchell, K., Wallschläger, D., Van Cappellen, P., 2013a. Sorption of Arsenite, Arsenate, and Thioarsenates to Iron Oxides and Iron Sulfides: A Kinetic and Spectroscopic Investigation. Environ. Sci. Technol. 47, 5652–5659. doi:10.1021/es3049724

Couture, R.-M., Shafei, B., Van Cappellen, P., Tessier, A., Gobeil, C., 2010. Non-Steady State Modeling of Arsenic Diagenesis in Lake Sediments. Environ. Sci. Technol. 44, 197–203. doi:10.1021/es902077q

Couture, R.-M., Van Cappellen, P., 2011. Reassessing the role of sulfur geochemistry on arsenic speciation in reducing environments. J. Hazard. Mater. 189, 647–652. doi:10.1016/j.jhazmat.2011.02.029

Couture, R.-M., Wallschläger, D., Rose, J., Van Cappellen, P., 2013b. SI: Arsenic binding to organic and inorganic sulfur species during microbial sulfate reduction: a sediment flow-through reactor experiment. Environ. Chem. 10, 285.

Crecelius, E.A., Bothner, M.H., Carpenter, R., 1975. Geochemistries of arsenic, antimony, mercury, and related elements in sediments of Puget Sound. Environ. Sci. Technol. 9, 325–333. doi:10.1021/es60102a007

Cruz-García, C., Murray, A.E., Klappenbach, J. a, Stewart, V., Tiedje, J.M., 2007. Respiratory nitrate ammonification by Shewanella oneidensis MR-1. J. Bacteriol. 189, 656–62. doi:10.1128/JB.01194-06

Cubas, S.A., Foresti, E., Rodrigues, J.A.D., Ratusznei, S.M., Zaiat, M., 2007. Effects of solid-phase mass transfer on the performance of a stirred anaerobic sequencing batch reactor containing immobilized biomass. Bioresour. Technol. 98, 1411–1417. doi:10.1016/j.biortech.2006.05.045

Daniels, W.R.., Wolfsberg, K., Rundberg, K., Ogard, A.E., Kerrisk, J.F., Duffy, C.J., Newton, T.W.,

Thompson, J.L., Bayhurst, B.P., Bish, D.L., Blacic, J.D., Crowe, B.M., Erdal, B.R., Griffith, J.F., Knight, S.D., Lawrence, F.O., Rundberg, V.L., Skyes, M.L., Thompson, G.M., Travis, B.J., Treher, E.N., Vidale, R.J., Walter, G.R., Aguilar, R.D., Ciseneros, M.R., Maestas, S., Mitchell, A.J., Oliver, P.Q., Raybold, N.A., Wanek, P.L., 1982. Summary report on the geochemistry of Yucca Mountain and environs.

Das, A., Sligar, S.G., 2009. Modulation of the Cytochrome P450 Reductase Redox Potential by the Phospholipid Bilayer. Biochemistry 48, 12104–12112. doi:10.1021/bi9011435

De Cannière, P., Moors, H., Lolivier, P., De Preter, P., Put, M., 1996. Laboratory and in situ migration experiments in the Boom Clay.

De Cannière, P., Schwarzbauer, J., Höhener, P., Lorenz, G., Salah, S., Leupin, O.X., Wersin, P., 2011. Biogeochemical processes in a clay formation in situ experiment: Part C – Organic contamination and leaching data. Appl. Geochemistry 26, 967–979. doi:10.1016/j.apgeochem.2011.03.006

de Combarieu, G., Barboux, P., Minet, Y., 2007. Iron corrosion in Callovo–Oxfordian argilite: From experiments to thermodynamic/kinetic modelling. Phys. Chem. Earth, Parts A/B/C 32, 346–358. doi:10.1016/j.pce.2006.04.019

DeAngelis, K.M., Silver, W.L., Thompson, A.W., Firestone, M.K., 2010. Microbial communities acclimate to recurring changes in soil redox potential status. Environ. Microbiol. 12, 3137–3149. doi:10.1111/j.1462-2920.2010.02286.x

DiChristina, T.J., 1992. Effects of nitrate and nitrite on dissimilatory iron reduction by Shewanella putrefaciens 200. J. Bacteriol. 174, 1891–6.

DiChristina, T.J., Fredrickson, J.K., Zachara, J.M., 2005. Enzymology of Electron Transport: Energy Generation With Geochemical Consequences. Rev. Mineral. Geochemistry 59, 27–52. doi:10.2138/rmg.2005.59.3

Dixit, S., Hering, J.G., 2003. Comparison of Arsenic(V) and Arsenic(III) Sorption onto Iron Oxide Minerals: Implications for Arsenic Mobility. Environ. Sci. Technol. 37, 4182–4189. doi:10.1021/es030309t

Dos Santos Afonso, M., Stumm, W., 1992. Reductive dissolution of iron(III) (hydr)oxides by hydrogen sulfide. Langmuir 8, 1671–1675. doi:10.1021/la00042a030

Dowdle, P.R., Oremland, R.S., 1998. Microbial Oxidation of Elemental Selenium in Soil Slurries and Bacterial Cultures. Environ. Sci. Technol. 32, 3749–3755. doi:10.1021/es970940s

Duro, L., Domènech, C., Grivé, M., Roman-Ross, G., Bruno, J., Källström, K., 2014. Assessment of the evolution of the redox conditions in a low and intermediate level nuclear waste repository (SFR1, Sweden). Appl. Geochemistry 49, 192–205. doi:10.1016/j.apgeochem.2014.04.015

Duro, L., Montoya, V., Colàs, E., García, D., 2010. Groundwater equilibration and radionuclide solubility calculations.

Dzombak, D.A., Morel, F.M., 1990. Surface complexation modeling: hydrous ferric oxide. Wiley: New York.

Ehlert, K., Mikutta, C., Kretzschmar, R., 2014. Impact of Birnessite on Arsenic and Iron Speciation during Microbial Reduction of Arsenic-Bearing Ferrihydrite. Environ. Sci. Technol. 48, 11320–11329. doi:10.1021/es5031323

El Mendili, Y., Abdelouas, A., Ait Chaou, A., Bardeau, J.F., Schlegel, M.L., 2014. Carbon steel corrosion in clay-rich environment. Corros. Sci. 88, 56–65. doi:10.1016/j.corsci.2014.07.020

Enright, A.M.L., Ferris, F.G., 2016. Bacterial Fe(II) oxidation distinguished by long-range correlation in redox potential. J. Geophys. Res. Biogeosciences 121, 1249–1257. doi:10.1002/2015JG003306

Essington, M.E., 2004. Delete! Soil and Water Chemistry: An Integrative Approach. CRC Press LLC.

Ewing, R.C., Whittleston, R.A., Yardley, B.W.D., 2016. Geological Disposal of Nuclear Waste: a Primer. Elements 12, 233–237. doi:10.2113/gselements.12.4.233

Fagerbakke, K., Heldal, M., Norland, S., 1996. Content of carbon, nitrogen, oxygen, sulfur and phosphorus in native aquatic and cultured bacteria. Aquat. Microb. Ecol. 10, 15–27. doi:10.3354/ame010015

FAO, 2014. World Reference Base for Soil Resources 2014. International Soil Classification System for Naming Soils and Creating Legends for Soil Maps, Experimental Agriculture. doi:10.1017/S0014479706394902

Farrell, J., Chaudhary, B.K., 2013. Understanding Arsenate Reaction Kinetics with Ferric Hydroxides. Environ. Sci. Technol. 73, 130710154344009. doi:10.1021/es4013382

Fawcett, S.E., Jamieson, H.E., Nordstrom, D.K., McCleskey, R.B., 2015. Arsenic and antimony geochemistry of mine wastes, associated waters and sediments at the Giant Mine, Yellowknife, Northwest Territories, Canada. Appl. Geochemistry 62, 3–17. doi:10.1016/j.apgeochem.2014.12.012

Fellowes, J.W., Pattrick, R. a. D., Boothman, C., Al Lawati, W.M.M., van Dongen, B.E., Charnock, J.M., Lloyd, J.R., Pearce, C.I., 2013. Microbial selenium transformations in seleniferous soils. Eur. J. Soil Sci. 64, 629–638. doi:10.1111/ejss.12051

Fendorf, S., Wielinga, B.W., Hansel, C.M., 2000. Chromium Transformations in Natural Environments: The Role of Biological and Abiological Processes in Chromium(VI) Reduction. Int. Geol. Rev. 42, 691–701. doi:10.1080/00206810009465107

Fiedler, S., 2000. In Situ Long-Term-Measurement of Redox Potential in Redoximorphic Soils, in: Schuring, J. (Ed.), Redox-Fundamentals, Processes and Measuring Techniques. Springer-Verlag, New York, pp. 81–94.

Fiedler, S., Sommer, M., 2004. Water and Redox Conditions in Wetland Soils — Their Influence on Pedogenic Oxides and Morphology. Soil Sci. Soc. Am. J. 68, 326–335.

Filella, M., Belzile, N., Chen, Y., 2002. Antimony in the environment : a review focused on natural waters II. Relevant solution chemistry. Earth-Science Rev. 59, 265–285.

Filella, M., Belzile, N., Lett, M.-C., 2007. Antimony in the environment: A review focused on natural waters. III. Microbiota relevant interactions. Earth-Science Rev. 80, 195–217. doi:10.1016/j.earscirev.2006.09.003

Filella, M., May, P.M., 2003. Computer simulation of the low-molecular-weight inorganic species distribution of antimony(III) and antimony(V) in natural waters. Geochim. Cosmochim. Acta 67, 4013–4031. doi:10.1016/S0016-7037(03)00095-4

Finneran, K.T., Housewright, M.E., Lovley, D.R., 2002. Multiple influences of nitrate on uranium solubility during bioremediation of uranium-contaminated subsurface sediments. Environ. Microbiol. 4, 510–516. doi:10.1046/j.1462-2920.2002.00317.x

Frevert, T., 1984. Can the redox conditions in natural waters be predicted by a single parameter? Schweizerische Zeitschrift für Hydrol. 46, 269–290. doi:10.1007/BF02538066

Frohne, T., Diaz-Bone, R. a., Du Laing, G., Rinklebe, J., 2015. Impact of systematic change of redox

potential on the leaching of Ba, Cr, Sr, and V from a riverine soil into water. J. Soils Sediments 15, 623–633. doi:10.1007/s11368-014-1036-8

Frohne, T., Rinklebe, J., Diaz-Bone, R.A., 2014. Contamination of Floodplain Soils along the Wupper River, Germany, with As, Co, Cu, Ni, Sb, and Zn and the Impact of Pre-definite Redox Variations on the Mobility of These Elements. Soil Sediment Contam. An Int. J. 23, 779–799. doi:10.1080/15320383.2014.872597

Frohne, T., Rinklebe, J., Diaz-Bone, R. a., Du Laing, G., 2011. Controlled variation of redox conditions in a floodplain soil: Impact on metal mobilization and biomethylation of arsenic and antimony. Geoderma 160, 414–424. doi:10.1016/j.geoderma.2010.10.012

Fukuda, A., Hagiwara, H., Ishimura, T., Kouduka, M., Ioka, S., Amano, Y., Tsunogai, U., Suzuki, Y., Mizuno, T., 2010. Geomicrobiological Properties of Ultra-Deep Granitic Groundwater from the Mizunami Underground Research Laboratory (MIU), Central Japan. Microb. Ecol. 60, 214–225. doi:10.1007/s00248-010-9683-9

Gallegos, T.J., Hyun, S.P., Hayes, K.F., 2007. Spectroscopic Investigation of the Uptake of Arsenite from Solution by Synthetic Mackinawite. Environ. Sci. Technol. 41, 7781–7786. doi:10.1021/es070613c

Gao, S., Tanji, K.K., Scardaci, S.C., Chow, A.T., 2002. Comparison of Redox Indicators in a Paddy Soil during Rice-Growing Season. Soil Sci. Soc. Am. J. 66, 805. doi:10.2136/sssaj2002.0805

GARCÍA, J., ROUSSEAU, D.P.L., MORATÓ, J., LESAGE, E., MATAMOROS, V., BAYONA, J.M., 2010. Contaminant Removal Processes in Subsurface-Flow Constructed Wetlands: A Review. Crit. Rev. Environ. Sci. Technol. 40, 561–661. doi:10.1080/10643380802471076

Garske, E.E., Schock, M.R., 1986. An Inexpensive Flow-Through Cell and Measurement System for Monitoring Selected Chemical Parameters in Ground Water. Ground Water Monit. Remediat. 6, 79–84. doi:10.1111/j.1745-6592.1986.tb00953.x

Gascoyne, M., 2004. Hydrogeochemistry, groundwater ages and sources of salts in a granitic batholith on the Canadian Shield, southeastern Manitoba, Applied Geochemistry. doi:10.1016/S0883-2927(03)00155-0

Gascoyne, M., 1997. Evolution of Redox Conditions and Groundwater Composition in Recharge-Discharge Environments on the Canadian Shield. Hydrogeol. J. 5, 4–18.

doi:10.1007/s100400050253

Gascoyne, M., 1989. High levels of uranium and radium in groundwaters at Canada's Underground Research Laboratory, Lac du Bonnet, Manitoba, Canada. Appl. Geochemistry 4, 577–591. doi:10.1016/0883-2927(89)90068-1

Gaucher, E.C., Tournassat, C., Pearson, F.J., Blanc, P., Crouzet, C., Lerouge, C., Altmann, S., 2009. A robust model for pore-water chemistry of clayrock. Geochim. Cosmochim. Acta 73, 6470–6487. doi:10.1016/j.gca.2009.07.021

Géhin, A., Grenèche, J.-M., Tournassat, C., Brendlé, J., Rancourt, D.G., Charlet, L., 2007. Reversible surface-sorption-induced electron-transfer oxidation of Fe(II) at reactive sites on a synthetic clay mineral. Geochim. Cosmochim. Acta 71, 863–876. doi:10.1016/j.gca.2006.10.019

Gezahegne, W.A., Planer-Friedrich, B., Merkel, B.J., 2007. Obtaining stable redox potential readings in gneiss groundwater and mine water: difficulties, meaningfulness, and potential improvement. Hydrogeol. J. 15, 1221–1229. doi:10.1007/s10040-007-0174-0

Ghorbanzadeh, N., Lakzian, A., Halajnia, A., Kabra, A.N., Kurade, M.B., Lee, D.S., Jeon, B.-H., 2015. Influence of clay minerals on sorption and bioreduction of arsenic under anoxic conditions. Environ. Geochem. Health 37, 997–1005. doi:10.1007/s10653-015-9708-x

Gibson, B.D., Blowes, D.W., Lindsay, M.B.J., Ptacek, C.J., 2012. Mechanistic investigations of Se(VI) treatment in anoxic groundwater using granular iron and organic carbon: An EXAFS study. J. Hazard. Mater. 241–242, 92–100. doi:10.1016/j.jhazmat.2012.09.015

Gillespie, L.J., 1920. Reduction potentials of bacterial cultures and of water-logged soils. Soil Sci. 9, 199–216.

Gimeno, M.J., Auque, L., Gomez, J., Acero, P., Laaksoharju, M., 2009. General characterisation of the redox systems in the Swedish candidate sites for deep disposal of nuclear waste, in: 1st Annual Workshop Proceedings of the Collaborative Project "'Redox Phenomena Controlling Systems'" (7th EC FP CP RECOSY) Forschungszentrum Karlsruhe in Der Helmholtz-Gemeinschaft Wissenschaftliche Berichte FZKA 7466. Forschungszentrum Karlsruhe, pp. 111–120.

Godgul, G., Sahu, K.C., 1995. Chromium contamination from chromite mine. Environ. Geol. 25, 251–257. doi:10.1007/BF00766754

Good, N.E., Winget, G.D., Winter, W., Connolly, T.N., Izawa, S., Singh, R.M.M., 1966. Hydrogen Ion Buffers for Biological Research. Biochemistry 5, 467–477. doi:10.1021/bi00866a011

Gorny, J., Billon, G., Lesven, L., Dumoulin, D., Madé, B., Noiriel, C., 2015. Arsenic behavior in river sediments under redox gradient: A review. Sci. Total Environ. 505, 423–434. doi:10.1016/j.scitotenv.2014.10.011

Grambow, B., 2016. Geological Disposal of Radioactive Waste in Clay. Elements 12, 239–245. doi:10.2113/gselements.12.4.239

Grambow, B., 2008. Mobile fission and activation products in nuclear waste disposal. J. Contam. Hydrol. 102, 180–186. doi:10.1016/j.jconhyd.2008.10.006

Grenthe, I., Stumm, W., Laaksuharju, M., Nilsson, A.C., Wikberg, P., 1992. Redox potentials and redox reactions in deep groundwater systems. Chem. Geol. 98, 131–150. doi:10.1016/0009-2541(92)90095-M

Grossl, P.R., Eick, M., Sparks, D.L., Goldberg, S., Ainsworth, C.C., 1997. Arsenate and Chromate Retention Mechanisms on Goethite. 2. Kinetic Evaluation Using a Pressure-Jump Relaxation Technique. Environ. Sci. Technol. 31, 321–326. doi:10.1021/es9506541

Grundl, T.J., Macalady, D.L., 1989. Electrode measurement of redox potential in anaerobic ferric/ferrous chloride systems. J. Contam. Hydrol. 5, 97–117. doi:10.1016/0169-7722(89)90008-9

Guillaumont, R., 2003. Update on the chemical thermodynamics of uranium, neptunium, plutonium, americium and technetium. North Holland Elsevier Science Publishers B.V.: Amsterdam.

Guo, J., Yang, Q., Peng, Y., Yang, A., Wang, S., 2007. Biological nitrogen removal with real-time control using step-feed SBR technology. Enzyme Microb. Technol. 40, 1564–1569. doi:10.1016/j.enzmictec.2006.11.001

Haggard, B.E., Galloway, J.M., Green, W.R., Meyer, M.T., 2006. Pharmaceuticals and Other Organic Chemicals in Selected North-Central and Northwestern Arkansas Streams. J. Environ. Qual. 35, 1078. doi:10.2134/jeq2005.0248

Hallbeck, L., Pedersen, K., 2012. Culture-dependent comparison of microbial diversity in deep granitic groundwater from two sites considered for a Swedish final repository of spent nuclear fuel. FEMS Microbiol. Ecol. 81, 66–77. doi:10.1111/j.1574-6941.2011.01281.x

Hammes, F., Goldschmidt, F., Vital, M., Wang, Y., Egli, T., 2010. Measurement and interpretation of microbial adenosine tri-phosphate (ATP) in aquatic environments. Water Res. 44, 3915–3923. doi:10.1016/j.watres.2010.04.015

Hartshorne, R.S., Jepson, B.N., Clarke, T.A., Field, S.J., Fredrickson, J., Zachara, J., Shi, L., Butt, J.N., Richardson, D.J., 2007. Characterization of Shewanella oneidensis MtrC: a cell-surface decaheme cytochrome involved in respiratory electron transport to extracellular electron acceptors. J. Biol. Inorg. Chem. 12, 1083–94. doi:10.1007/s00775-007-0278-y

Hauch, A., Georg, A., 2001. Diffusion in the electrolyte and charge-transfer reaction at the platinum electrode in dye-sensitized solar cells. Electrochim. Acta 46, 3457–3466. doi:10.1016/S0013-4686(01)00540-0

Hedin, A., Olsson, O., 2016. Crystalline Rock as a Repository for Swedish Spent Nuclear Fuel 247–252. doi:10.2113/gselements.12.4.247

Helm, I., Jalukse, L., Leito, I., 2010. Measurement Uncertainty Estimation in Amperometric Sensors: A Tutorial Review. Sensors 10, 4430–4455. doi:10.3390/s100504430

Helz, G.R., Tossell, J.A., 2008. Thermodynamic model for arsenic speciation in sulfidic waters: A novel use of ab initio computations. Geochim. Cosmochim. Acta 72, 4457–4468. doi:10.1016/j.gca.2008.06.018

Helz, G.R., Valerio, M.S., Capps, N.E., 2002. Antimony Speciation in Alkaline Sulfide Solutions: Role of Zerovalent Sulfur. Environ. Sci. Technol. 36, 943–948. doi:10.1021/es011227c

Hering, J.G., Hug, S.J., Farnsworth, C., O'Day, P.A., 2011. Role of Coupled Redox Transformations in the Mobilization and Sequestration of Arsenic, in: ACS Symposium Series. pp. 463–476. doi:10.1021/bk-2011-1071.ch021

Hewitt, L.F., 1950. Oxidation-reduction potentials in bacteriology and biochemistry. Baltimore, Williams and Wilkins.

Hindersmann, I., Mansfeldt, T., 2014. Trace Element Solubility in a Multimetal-Contaminated Soil as Affected by Redox Conditions. Water, Air, Soil Pollut. 225, 2158. doi:10.1007/s11270-014-2158-8

Hobbie, J.E., Daley, R.J., Jasper, S., 1977. Use of Nuclepore Filters for Counting Bacteria by Fluorescence Microscopy. Appl. Environ. Microbiol. 33, 1225–1228.

Hockmann, K., Lenz, M., Tandy, S., Nachtegaal, M., Janousch, M., Schulin, R., 2014. Release of antimony from contaminated soil induced by redox changes. J. Hazard. Mater. 275, 215–221. doi:10.1016/j.jhazmat.2014.04.065

Holm, T.R., Curtiss, C.D., 1989. A comparison of oxidation-reduction potentials calculated from the As(V)/As(III) and Fe(III)/Fe(II) couples with measured platinum-electrode potentials in groundwater. J. Contam. Hydrol. 5, 67–81. doi:10.1016/0169-7722(89)90006-5

Holm, T.R., George, G.K., Barcelona, M.J., 1987. Fluorometric determination of hydrogen peroxide in groundwater. Anal. Chem. 59, 582–586. doi:10.1021/ac00131a010

Hostettler, J.D., 1984. Electrode electrons, aqueous electrons, and redox potentials in natural waters. Am. J. Sci. 284, 734–759. doi:10.2475/ajs.284.6.734

Hug, S.J., Leupin, O., 2003. Iron-Catalyzed Oxidation of Arsenic(III) by Oxygen and by Hydrogen Peroxide: pH-Dependent Formation of Oxidants in the Fenton Reaction. Environ. Sci. Technol. 37, 2734–2742. doi:10.1021/es026208x

Hunting, E.R., Kampfraath, A.A., 2013. Contribution of bacteria to redox potential (E h) measurements in sediments. Int. J. Environ. Sci. Technol. 10, 55–62. doi:10.1007/s13762-012-0080-4

Husson, O., 2013. Redox potential (Eh) and pH as drivers of soil/plant/microorganism systems: a transdisciplinary overview pointing to integrative opportunities for agronomy. Plant Soil 362, 389–417. doi:10.1007/s11104-012-1429-7

Ilgen, A.G., Foster, A.L., Trainor, T.P., 2012. Role of structural Fe in nontronite NAu-1 and dissolved Fe(II) in redox transformations of arsenic and antimony. Geochim. Cosmochim. Acta 94, 128–145. doi:10.1016/j.gca.2012.07.007

Ilgen, A.G., Majs, F., Barker, A.J., Douglas, T.A., Trainor, T.P., 2014. Oxidation and mobilization of metallic antimony in aqueous systems with simulated groundwater. Geochim. Cosmochim. Acta 132, 16–30. doi:10.1016/j.gca.2014.01.019

Ilgen, A.G., Trainor, T.P., 2012. Sb(III) and Sb(V) sorption onto al-rich phases: Hydrous al oxide and the clay minerals kaolinite KGa-1b and oxidized and reduced nontronite NAu-1. Environ. Sci. Technol. 46, 843–851. doi:10.1021/es203027v

Inskeep, W.P., Macur, R.E., Harrison, G., Bostick, B.C., Fendorf, S., 2004. Biomineralization of As(V)-

hydrous ferric oxyhydroxide in microbial mats of an acid-sulfate-chloride geothermal spring, Yellowstone National Park. Geochim. Cosmochim. Acta 68, 3141–3155. doi:10.1016/j.gca.2003.09.020

Ioka, S., Sakai, T., Igarashi, T., Ishijima, Y., 2011. Determination of redox potential of sulfidic groundwater in unconsolidated sediments by long-term continuous in situ potentiometric measurements. Environ. Monit. Assess. 178, 171–178. doi:10.1007/s10661-010-1680-4

Ishibashi, Y., Cervantes, C., Silver, S., 1990. Chromium reduction in Pseudomonas putida. Appl. Environ. Microbiol. 56, 2268–2270.

Ishizaki, A., Shibau, H., Hirose, Y., 1974. Basic Aspects of Electrode Potencial Change in Submerged Fermentation. Agric. Biol. Chem. 38, 2399–2406. doi:10.1080/00021369.1974.10861537

Islam, F.S., Gault, A.G., Boothman, C., Polya, D. a, Charnock, J.M., Chatterjee, D., Lloyd, J.R., 2004. Role of metal-reducing bacteria in arsenic release from Bengal delta sediments. Nature 430, 68–71. doi:10.1038/nature02638

Iwatsuki, T., Furue, R., Mie, H., Ioka, S., Mizuno, T., 2005. Hydrochemical baseline condition of groundwater at the Mizunami underground research laboratory (MIU). Appl. Geochemistry 20, 2283–2302. doi:10.1016/j.apgeochem.2005.09.002

Jackson, M.L., Lim, C.H., Zelazny, L.W., 1986. Oxides, hydroxides, and aluminosilicates., in: Klute, A. (Ed.), Methods of Soil Analysis Part 1. pp. 101–150.

Jamieson-Hanes, J.H., Amos, R.T., Blowes, D.W., 2012a. Reactive Transport Modeling of Chromium Isotope Fractionation during Cr(VI) Reduction. Environ. Sci. Technol. 46, 13311–13316. doi:10.1021/es3046235

Jamieson-Hanes, J.H., Gibson, B.D., Lindsay, M.B.J., Kim, Y., Ptacek, C.J., Blowes, D.W., 2012b. Chromium Isotope Fractionation During Reduction of Cr(VI) Under Saturated Flow Conditions. Environ. Sci. Technol. 46, 6783–6789. doi:10.1021/es2042383

Johnson, C.A., Moench, H., Wersin, P., Kugler, P., Wenger, C., 2005. Solubility of antimony and other elements in samples taken from shooting ranges. J. Environ. Qual. 34, 248–254.

Jones, E., Oliphant, T., Peterson, P., 2001. SciPy: Open source scientific tools for Python.

Jongman, B., Hochrainer-Stigler, S., Feyen, L., Aerts, J.C.J.H., Mechler, R., Botzen, W.J.W., Bouwer,

L.M., Pflug, G., Rojas, R., Ward, P.J., 2014. Increasing stress on disaster-risk finance due to large floods. Nat. Clim. Chang. 4, 264–268. doi:10.1038/nclimate2124

Jørgensen, K., Tiedje, J., 1993. Survival of denitrifiers in nitrate-free, anaerobic environments. Appl. Environ. Microbiol. 59, 3297–3305.

Karl, D.M., 1980. Cellular nucleotide measurements and applications in microbial ecology. Microbiol. Rev. 44, 739–796. doi:0146-0749/80/04-0739/58

Katsoyiannis, I. a, Zouboulis, A.I., Jekel, M., 2004. Kinetics of bacterial As(III) oxidation and subsequent As(V) removal by sorption onto biogenic manganese oxides during groundwater treatment. Ind. Eng. Chem. Res. 43, 486–493. doi:10.1021/ie030525a

Kersten, M., Kulik, D., 2005. Competitive Scavenging of Trace Metals by HFO and HMO during Redox-driven Early Diagenesis of Ferromanganese Nodules (11 pp). J. Soils Sediments 5, 37–47. doi:10.1065/jss2005.02.130

Khan, B.I., Jambeck, J., Solo-Gabriele, H.M., Townsend, T.G., Cai, Y., 2006. Release of Arsenic to the Environment from CCA-Treated Wood. 2. Leaching and Speciation during Disposal. Environ. Sci. Technol. 40, 994–999. doi:10.1021/es051471u

Kim, D., Lee, J., Ryu, J., Kim, K., Choi, W., 2014. Arsenite Oxidation Initiated by the UV Photolysis of Nitrite and Nitrate. Environ. Sci. Technol. 48, 4030–4037. doi:10.1021/es500001q

Kjaergaard, L., 1977. The redox potential: Its use and control in biotechnology, in: Advances in Biochemical Engineering, Volume 7. Springer-Verlag, Berlin/Heidelberg, pp. 131–150. doi:10.1007/BFb0048444

Klein, A.R., Baldwin, D.S., Singh, B., Silvester, E.J., 2010. Salinity-induced acidification in a wetland sediment through the displacement of clay-bound iron(II). Environ. Chem. 7, 413. doi:10.1071/EN10057

Klüpfel, L., Piepenbrock, A., Kappler, A., Sander, M., 2014. Humic substances as fully regenerable electron acceptors in recurrently anoxic environments. Nat. Geosci. 7, 195–200. doi:10.1038/ngeo2084

Koch, F.A., Oldham, W.K., 1985. Oxidation-reduction potential - A tool for monitoring, control and optimization of biological nutrient removal systems. Water Sci. Technol. 17, 259–281.

Komlos, J., Moon, H.S., Jaffé, P.R., 2008. Effect of Sulfate on the Simultaneous Bioreduction of Iron and Uranium. J. Environ. Qual. 37, 2058. doi:10.2134/jeq2007.0665

Konhauser, K.O., 2007. Introduction to Geomicrobiology. Blackwell Science.

Kourtev, P.S., Nakatsu, C.H., Konopka, A., 2009. Inhibition of Nitrate Reduction by Chromium(VI) in Anaerobic Soil Microcosms. Appl. Environ. Microbiol. 75, 6249–6257. doi:10.1128/AEM.00347-09

Krause, B., Nealson, K.H., 1997. Physiology and enzymology involved in denitrification by Shewanella putrefaciens. Appl. Environ. Microbiol. 63, 2613–8.

Krüger, F., Meissner, R., Gröngröft, A., Grunewald, K., 2005. Flood Induced Heavy Metal and Arsenic Contamination of Elbe River Floodplain Soils. Acta Hydrochim. Hydrobiol. 33, 455–465. doi:10.1002/aheh.200400591

Kulp, T.R., Miller, L.G., Braiotta, F., Webb, M., Kocar, B.D., Blum, J.S., Oremland, R.S., 2013. Microbiological reduction of Sb (V) in anoxic freshwater sediments. Environ. Sci. Technol.

Kulp, T.R., Miller, L.G., Braiotta, F., Webb, S.M., Kocar, B.D., Blum, J.S., Oremland, R.S., 2014. Microbiological Reduction of Sb(V) in Anoxic Freshwater Sediments. Environ. Sci. Technol. 48, 218–226. doi:10.1021/es403312j

Kumar, A.R., Riyazuddin, P., 2012. Seasonal variation of redox species and redox potentials in shallow groundwater: A comparison of measured and calculated redox potentials. J. Hydrol. 444–445, 187–198. doi:10.1016/j.jhydrol.2012.04.018

Laaksoharju, M., Gurban, I., Skaarman, C., 1998. Summary of hydrochemical conditions at Aberg, Beberg and Ceberg.

Laaksoharju, M., Smellie, J., Tullborg, E.-L., Gimeno, M., Molinero, J., Gurban, I., Hallbeck, L., 2008. Hydrogeochemical evaluation and modelling performed within the Swedish site investigation programme. Appl. Geochemistry 23, 1761–1795. doi:10.1016/j.apgeochem.2008.02.015

Lafferty, B.J., Loeppert, R.H., 2005. Methyl arsenic adsorption and desorption behavior on iron oxides. Environ. Sci. Technol. 34, 3131–3136. doi:10.1021/es048701+

Lan, Y., Li, C., Mao, J., Sun, J., 2008. Influence of clay minerals on the reduction of Cr6+ by citric acid. Chemosphere 71, 781–787. doi:10.1016/j.chemosphere.2007.10.010

Langmuir, D., 1990. Aqueous Environmental Geochemistry. Washington, DC: Am. Chem. Soc.

Laverman, A.M., Van Cappellen, P., Van Rotterdam-Los, D., Pallud, C., Abell, J., 2006. Potential rates and pathways of microbial nitrate reduction in coastal sediments. FEMS Microbiol. Ecol. 58, 179–192. doi:10.1111/j.1574-6941.2006.00155.x

Lechler, P.J., Desilets, M.O., 1987. A review of the use of loss on ignition as a measurement of total volatiles in whole-rock analysis. Chem. Geol. 63, 341–344. doi:10.1016/0009-2541(87)90171-9

Lenz, M., Hullebusch, E.D. van, Farges, F., Nikitenko, S., Borca, C.N., Grolimund, D., Lens, P.N.L., 2008. Selenium Speciation Assessed by X-Ray Absorption Spectroscopy of Sequentially Extracted Anaerobic Biofilms. Environ. Sci. Technol. 42, 7587–7593. doi:10.1021/es800811q

Leuz, A.-K., Johnson, C.A., 2005. Oxidation of Sb(III) to Sb(V) by O2 and H2O2 in aqueous solutions. Geochim. Cosmochim. Acta 69, 1165–1172. doi:10.1016/j.gca.2004.08.019

Leuz, A., Mönch, H., Johnson, C.A., 2006. Sorption of Sb(III) and Sb(V) to Goethite: Influence on Sb(III) Oxidation and Mobilization †. Environ. Sci. Technol. 40, 7277–7282. doi:10.1021/es061284b

Leuz, A.K., Hug, S.J., Wehrli, B., Johnson, C.A., 2006. Iron-mediated oxidation of antimony(III) by oxygen and hydrogen peroxide compared to arsenic(III) oxidation. Environ. Sci. Technol. 40, 2565–2571. doi:10.1021/es052059h

Liger, E., Charlet, L., Van Cappellen, P., 1999. Surface catalysis of uranium(VI) reduction by iron(II). Geochim. Cosmochim. Acta 63, 2939–2955. doi:10.1016/S0016-7037(99)00265-3

Lin, Z., Puls, R.W., 2000. Adsorption, desorption and oxidation of arsenic affected by clay minerals and aging process. Environ. Geol. 39, 753–759. doi:10.1007/s002540050490

Lindberg, R.D., Runnells, D.D., 1984. Ground water redox reactions: an analysis of equilibrium state applied to eh measurements and geochemical modeling. Science 225, 925–7. doi:10.1126/science.225.4665.925

Lindsay, M.B.J., Blowes, D.W., Condon, P.D., Ptacek, C.J., 2011. Organic carbon amendments for passive in situ treatment of mine drainage: Field experiments. Appl. Geochemistry 26, 1169–1183. doi:10.1016/j.apgeochem.2011.04.006

Lintschinger, J., Koch, I., Serves, S., Feldmann, J., Cullen, W.R., 1997. Determination of antimony species with high-performance liquid chromatography using element specific detection. Fresenius. J.

Anal. Chem. 359, 484–491. doi:10.1007/s002160050618

Lintschinger, J., Schramel, O., Kettrup, a., 1998. The analysis of antimony species by using ESI-MS and HPLC-ICP-MS. Fresenius. J. Anal. Chem. 361, 96–102. doi:10.1007/s002160050841

Liu, X., Huang, Y., Zhang, W., Fan, G., Fan, C., Li, G., 2005. Electrochemical investigation of redox thermodynamics of immobilized myoglobin: ionic and ligation effects. Langmuir 21, 375–8. doi:10.1021/la047928f

Lloyd, J.R., Oremland, R.S., 2006. Microbial Transformations of Arsenic in the Environment: From Soda Lakes to Aquifers. Elements 2, 85–90. doi:10.2113/gselements.2.2.85

Lovley, D.R., Phillips, E.J.P., 1986. Organic Matter Mineralization with Reduction of Ferric Iron in Anaerobic Sediments. Appl. Environ. Microbiol. 51, 683–689.

Lützenkirchen, J., 1997. Ionic Strength Effects on Cation Sorption to Oxides: Macroscopic Observations and Their Significance in Microscopic Interpretation. J. Colloid Interface Sci. 195, 149–155. doi:10.1006/jcis.1997.5160

Macalady, D.L., Langmuir, D., Grundl, T., Elzerman, A., 1990. Use of model-generated Fe3+ ion activities to compute Eh and ferric oxyhydroxide solubilities in anaerobic systems, in: Melchior, D.C., Bassett, R.L. (Eds.), Chemical Modelling of Aqueous Systems II.

Macy, J.M., Santini, J.M., Pauling, B. V, O'Neill, a H., Sly, L.I., 2000. Two new arsenate/sulfate-reducing bacteria: mechanisms of arsenate reduction. Arch. Microbiol. 173, 49–57. doi:10.1007/s002030050007

Mahoney, J.J., Cadle, S.A., Jakubowski, R.T., 2009. Uranyl Adsorption onto Hydrous Ferric Oxide—A Re-Evaluation for the Diffuse Layer Model Database. Environ. Sci. Technol. 43, 9260–9266. doi:10.1021/es901586w

Maine, M.A., Suñe, N., Hadad, H., Sánchez, G., Bonetto, C., 2006. Nutrient and metal removal in a constructed wetland for wastewater treatment from a metallurgic industry. Ecol. Eng. 26, 341–347. doi:10.1016/j.ecoleng.2005.12.004

Malkin, S.Y., Meysman, F.J.R., 2014. Rapid redox signal transmission by cable bacteria beneath a photosynthetic biofilm. Appl. Environ. Microbiol. 81, 948–956. doi:10.1128/AEM.02682-14

Mampuru, L. a., Panichev, N. a., Ngobeni, P., Mandiwana, K.L., Kalumba, M.M., 2015. Determination of

Leachable Vanadium (V) in Sediment. South African J. Chem. 57–60. doi:10.17159/0379-4350/2015/v68a9

Mandaliev, P.N., Mikutta, C., Barmettler, K., Kotsev, T., Kretzschmar, R., 2014. Arsenic Species Formed from Arsenopyrite Weathering along a Contamination Gradient in Circumneutral River Floodplain Soils. Environ. Sci. Technol. 48, 208–217. doi:10.1021/es403210y

Manning, B.A., Fendorf, S.E., Bostick, B., Suarez, D.L., 2002. Arsenic(III) Oxidation and Arsenic(V) Adsorption Reactions on Synthetic Birnessite. Environ. Sci. Technol. 36, 976–981. doi:10.1021/es0110170

Manning, B.A., Goldberg, S., 1997. ARSENIC(III) AND ARSENIC(V) ADSORPTION ON THREE CALIFORNIA SOILS. Soil Sci. 162, 886–895. doi:10.1097/00010694-199712000-00004

Manning, B., Goldberg, S., 1997. Adsorption and Stability of Arsenic(III) at the Clay Mineral−Water Interface. Environ. Sci. Technol. 31, 2005–2011. doi:10.1021/es9608104

Mansfeldt, T., 2003. In situ long-term redox potential measurements in a dyked marsh soil. J. Plant Nutr. Soil Sci. 166, 210–219. doi:10.1002/jpln.200390031

Marsili, E., Baron, D.B., Shikhare, I.D., Coursolle, D., Gralnick, J. a, Bond, D.R., 2008. Shewanella secretes flavins that mediate extracellular electron transfer. Proc. Natl. Acad. Sci. 105, 3968–3973. doi:10.1073/pnas.0710525105

Marty, N.C.M., Fritz, B., Clément, A., Michau, N., 2010. Modelling the long term alteration of the engineered bentonite barrier in an underground radioactive waste repository. Appl. Clay Sci. 47, 82–90. doi:10.1016/j.clay.2008.10.002

Matern, K., Mansfeldt, T., 2016. Chromium Release from a COPR-Contaminated Soil at Varying Water Content and Redox Conditions. J. Environ. Qual. 45, 1259. doi:10.2134/jeq2015.10.0506

Matia, L., Rauret, G., Rubio, R., 1991. Redox potential measurement in natural waters. Fresenius. J. Anal. Chem. 339, 455–462. doi:10.1007/BF00323797

Mazierski, J., 1994. Effect of chromium (CrVI) on the growth rate of denitrifying bacteria. Water Res. 28, 1981–1985. doi:10.1016/0043-1354(94)90173-2

Melton, E.D., Swanner, E.D., Behrens, S., Schmidt, C., Kappler, A., 2014. The interplay of microbially mediated and abiotic reactions in the biogeochemical Fe cycle. Nat. Rev. Microbiol. 12, 797–809.

doi:10.1038/nrmicro3347

Mesquita, M., 2013. Personal communication.

Mestrot, A., Planer-Friedrich, B., Feldmann, J., 2013. Biovolatilisation: a poorly studied pathway of the arsenic biogeochemical cycle. Environ. Sci. Process. Impacts 15, 1639. doi:10.1039/c3em00105a

Middleton, S.S., Latmani, R.B., Mackey, M.R., Ellisman, M.H., Tebo, B.M., Criddle, C.S., 2003. Cometabolism of Cr(VI) byShewanella oneidensis MR-1 produces cell-associated reduced chromium and inhibits growth. Biotechnol. Bioeng. 83, 627–637. doi:10.1002/bit.10725

Milly, P.C.D., Betancourt, J., Falkenmark, M., Hirsch, R.M., Kundzewicz, Z.W., Lettenmaier, D.P., Stouffer, R.J., 2008. Stationarity Is Dead: Whither Water Management? Science (80-.). 319, 573–574. doi:10.1126/science.1151915

Mitsunobu, S., Harada, T., Takahashi, Y., 2006. Comparison of Antimony Behavior with that of Arsenic under Various Soil Redox Conditions †. Environ. Sci. Technol. 40, 7270–7276. doi:10.1021/es060694x

Morgan, J.J., 2005. Kinetics of reaction between O2 and Mn(II) species in aqueous solutions. Geochim. Cosmochim. Acta 69, 35–48. doi:10.1016/j.gca.2004.06.013

Moriasi, Arnold, Van Liew, Bingner, Harmel, Veith, 2007. Model Evaluation Guidelines for Systematic Quantification of Accuracy in Watershed Simulations. Trans. ASABE 50, 885–900. doi:10.13031/2013.23153

Morris, J.C., Stumm, W., 1967. Redox equilibria and measurements of potentials in the aquatic environment, in: Stumm, W. (Ed.), Equilibrium Concepts in Natural Water Systems. American Chemical Society Advances in Chemistry Series 67, American Chemical Society, Washington, D.C., pp. 270–285. doi:10.1017/CBO9781107415324.004

Myers, M., Myers, L., Okey, R., 2006. The Use of Oxidation-Reduction Potential as a Means of Controlling Effluent Ammonia Concentration in an Extended Aeration Activated Sludge System. Water Environ. Fed. 5901–5926.

Mytych, P., Cieśla, P., Stasicka, Z., 2001. Photoredox reactions of environmental chromium. Int. J. Photoenergy. doi:10.1155/S1110662X0100023X

Nagra, 2002. Demonstration of disposal feasibility for spent fuel, vitrified high-level waste and long-lived

intermediate-level waste, NAGRA Technical Report NTB 02-05.

Neiss, J., Stewart, B.D., Nico, P.S., Fendorf, S., 2007. Speciation-Dependent Microbial Reduction of Uranium within Iron-Coated Sands. Environ. Sci. Technol. 41, 7343–7348. doi:10.1021/es0706697

Nevin, K.P., Lovley, D.R., 2000. Potential for Nonenzymatic Reduction of Fe(III) via Electron Shuttling in Subsurface Sediments. Environ. Sci. Technol. 34, 2472–2478. doi:10.1021/es991181b

Nolang, O.A., Ohman, B., Osadchii, L.O., Rosen, E., 2005. Chemical Thermodynamics of Selenium. Elsevier Science, Amsterdam.

Nordstrom, D.K., 2011. Hydrogeochemical processes governing the origin, transport and fate of major and trace elements from mine wastes and mineralized rock to surface waters. Appl. Geochemistry 26, 1777–1791. doi:10.1016/j.apgeochem.2011.06.002

Nordstrom, D.K., 2000. Aqueous Redox Chemistry and the Behaviour of Iron in Acid Mine Waters. Work. Monit. Oxidation-Reduction Process. Ground-Water Restoration, Dallas, Texas 43–47.

Nordstrom, D.K., Jenne, E.A., Ball, J.., 1979. Redox equilibria of iron in acid mine waters, in: Jenne, E.A. (Ed.), Chemical Modeling in Aqueous Systems: Speciation, Sorption, Solubility and Kinetics. Am. Chem. Soc. Symp. Ser. No 93, Washington, DC, pp. 51–80.

Nordstrom, D.K., Majzlan, J., Konigsberger, E., 2014. Thermodynamic Properties for Arsenic Minerals and Aqueous Species. Rev. Mineral. Geochemistry 79, 217–255. doi:10.2138/rmg.2014.79.4

Nriagu, J., Beaubien, S., Blowes, D., 1993. Chemistry of chromium in lakes. Environ. Rev. 1, 104–120. doi:10.1139/a93-009

Nriagu, J.O., Soon, Y.K., 1985. Distribution and isotopic composition of sulfur in lake sediments of northern Ontario. Geochim. Cosmochim. Acta 49, 823–834. doi:10.1016/0016-7037(85)90175-9

Nuclear Energy Agency, 1958. Clay Club [WWW Document]. URL https://www.oecd-nea.org (accessed 11.25.16).

O'Rourke, S.M., Angers, D.A., Holden, N.M., Mcbratney, A.B., 2015. Soil organic carbon across scales. Glob. Chang. Biol. 21, 3561–3574. doi:10.1111/gcb.12959

OECD, NEA, 2013. Underground Research Laboratories (URL) 1–52.

Oktyabrskii, O.N., Smirnova, G. V., 2012. Redox potential changes in bacterial cultures under stress

conditions. Microbiology 81, 131–142. doi:10.1134/S0026261712020099

Opel, O., Eggerichs, T., Otte, T., Ruck, W.K.L., 2014. Monitoring of microbially mediated corrosion and scaling processes using redox potential measurements. Bioelectrochemistry 97, 137–144. doi:10.1016/j.bioelechem.2013.11.004

Oremland, R.S., 2005. A Microbial Arsenic Cycle in a Salt-Saturated, Extreme Environment. Science (80-.). 308, 1305–1308. doi:10.1126/science.1110832

Oremland, R.S., Saltikov, C.W., Wolfe-Simon, F., Stolz, J.F., 2009. Arsenic in the Evolution of Earth and Extraterrestrial Ecosystems. Geomicrobiol. J. 26, 522–536. doi:10.1080/01490450903102525

Oze, C., Bird, D.K., Fendorf, S., 2007. Genesis of hexavalent chromium from natural sources in soil and groundwater. Proc. Natl. Acad. Sci. 104, 6544–6549. doi:10.1073/pnas.0701085104

Panichev, N., Mandiwana, K., Kataeva, M., Siebert, S., 2005. Determination of Cr(VI) in plants by electrothermal atomic absorption spectrometry after leaching with sodium carbonate. Spectrochim. Acta Part B At. Spectrosc. 60, 699–703. doi:10.1016/j.sab.2005.02.018

Paraska, D.W., Hipsey, M.R., Salmon, S.U., 2014. Sediment diagenesis models: Review of approaches, challenges and opportunities. Environ. Model. Softw. 61, 297–325. doi:10.1016/j.envsoft.2014.05.011

Park, D., Yun, Y., Park, J.M., 2005. Use of dead fungal biomass for the detoxification of hexavalent chromium: screening and kinetics. Process Biochem. 40, 2559–2565. doi:10.1016/j.procbio.2004.12.002

Parkhurst, D.L., Appelo, C.A.., 2013. Description of input and examples for PHREEQC version 3 – A computer program for speciation, batch-reaction, one-dimensional transport, and inverse geochemical calculations. U.S. Geol. Surv. Tech. Methods 6, 497.

Parsons, C.T., 2011. Distribution et mobilité de l ' arsenic dans les sols : Effets de cycles redox successifs. Université de Grenoble.

Parsons, C.T., Couture, R.-M., Omoregie, E.O., Bardelli, F., Greneche, J.-M., Roman-Ross, G., Charlet, L., 2013a. The impact of oscillating redox conditions: Arsenic immobilisation in contaminated calcareous floodplain soils. Environ. Pollut. 178, 254–263. doi:10.1016/j.envpol.2013.02.028

Parsons, C.T., Margui Grabulosa, E., Pili, E., Floor, G.H., Roman-Ross, G., Charlet, L., 2013b.

Quantification of trace arsenic in soils by field-portable X-ray fluorescence spectrometry: Considerations for sample preparation and measurement conditions. J. Hazard. Mater. 262, 1213–1222. doi:10.1016/j.jhazmat.2012.07.001

Pearson, F.J., Arcos, D., Bath, a, Gaucher, E., Gautschi, a, Griffault, L., Waber, H.N., Series, G., 2003. Mont Terri Project – Geochemistry of Water in the Opalinus Clay Formation Mont Terri Project – Geochemistry of Water in the Opalinus Clay Formation at the Mont Terri Rock Laboratory, Geology.

Pedersen, K., 2002. Chapter 10 Microbial processes in the disposal of high level radioactive waste 500 m underground in Fennoscandian Shield rocks, in: Interactions of Microorganisms with Radionuclides. pp. 279–311. doi:10.1016/S1569-4860(02)80039-0

Pedersen, K., 1996. Investigations of subterranean bacteria in deep crystalline bedrock and their importance for the disposal of nuclear waste. Can. J. Microbiol. 42, 382–391. doi:10.1139/m96-054

Peiffer, S., Klemm, O., Pecher, K., Hollerung, R., 1992. Redox measurements in aqueous solutions — A theoretical approach to data interpretation, based on electrode kinetics. J. Contam. Hydrol. 10, 1–18. doi:10.1016/0169-7722(92)90041-C

Perry, S.C., Denuault, G., 2015. Transient study of the oxygen reduction reaction on reduced Pt and Pt alloys microelectrodes: evidence for the reduction of pre-adsorbed oxygen species linked to dissolved oxygen. Phys. Chem. Chem. Phys. 17, 30005–30012. doi:10.1039/C5CP04667J

Pinchuk, G.E., Geydebrekht, O. V., Hill, E.A., Reed, J.L., Konopka, A.E., Beliaev, A.S., Fredrickson, J.K., 2011. Pyruvate and Lactate Metabolism by Shewanella oneidensis MR-1 under Fermentation, Oxygen Limitation, and Fumarate Respiration Conditions. Appl. Environ. Microbiol. 77, 8234–8240. doi:10.1128/AEM.05382-11

Planer-Friedrich, B., Scheinost, A.C., 2011. Formation and structural characterization of thioantimony species and their natural occurrence in geothermal waters. Environ. Sci. Technol. 45, 6855–63. doi:10.1021/es201003k

Planer-Friedrich, B., Wilson, N., 2012. The stability of tetrathioantimonate in the presence of oxygen, light, high temperature and arsenic. Chem. Geol. 322–323, 1–10. doi:10.1016/j.chemgeo.2012.06.010

Plant, J.A., Kinniburgh, D.G., Smedley, P.L., Fordyce, F.M., Klinck, B.A., 2005. Arsenic and Selenium, in: Lollar, B.S. (Ed.), Environmental Geochemistry. British Geological Survey, Keyworth, Nottingham, UK.

Porquet, A., Filella, M., 2007. Structural Evidence of the Similarity of Sb(OH) 3 and As(OH) 3 with Glycerol: Implications for Their Uptake. Chem. Res. Toxicol. 20, 1269–1276. doi:10.1021/tx700110m

Post, J.E., 1999. Manganese oxide minerals: Crystal structures and economic and environmental significance. Proc. Natl. Acad. Sci. 96, 3447–3454. doi:10.1073/pnas.96.7.3447

Postma, D., Appelo, C.A.J., 2000. Reduction of Mn-oxides by ferrous iron in a flow system: column experiment and reactive transport modeling. Geochim. Cosmochim. Acta 64, 1237–1247. doi:10.1016/S0016-7037(99)00356-7

Potter, A.M.C., 1911. Electrical Effects Accompanying the Decomposition of Organic Compounds. Proc. R. Soc. London. Ser. B, Contain. Pap. a Biol. Character 84, 260–276.

Prasad, K.S., Ramanathan, A.L., Paul, J., Subramanian, V., Prasad, R., 2013. Biosorption of arsenite (As +3) and arsenate (As +5) from aqueous solution by Arthrobacter sp. biomass. Environ. Technol. 34, 2701–2708. doi:10.1080/09593330.2013.786137

Pratt, A.R., Blowes, D.W., Ptacek, C.J., 1997. Products of Chromate Reduction on Proposed Subsurface Remediation Material. Environ. Sci. Technol. 31, 2492–2498. doi:10.1021/es9607897

Qi, Y., Luo, H., Zheng, S., Chen, C., Lv, Z., Xiong, M., 2014. Effect of temperature on the corrosion behavior of Carbon steel in Hydrogen sulphide environments. Int. J. Electrochem. Sci. 9, 2101–2112.

Querol, X., Juan, R., Lopez-Soler, A., Fernandez-Turiel, J., Ruiz, C.R., 1996. Mobility of trace elements from coal and combustion wastes. Fuel 75, 821–838. doi:10.1016/0016-2361(96)00027-0

Rabaey, K., Rodríguez, J., Blackall, L.L., Keller, J., Gross, P., Batstone, D., Verstraete, W., Nealson, K.H., 2007. Microbial ecology meets electrochemistry: electricity-driven and driving communities. ISME J. 1, 9–18. doi:10.1038/ismej.2007.4

Rai, D., Eary, L.E., Zachara, J.M., 1989. Environmental chemistry of chromium. Sci. Total Environ. 86, 15–23. doi:10.1016/0048-9697(89)90189-7

Rai, D., Moore, D. a., Hess, N.J., Rosso, K.M., Rao, L., Heald, S.M., 2007. Chromium(III) Hydroxide

Solubility in the Aqueous K+-H+-OH−-CO2-HCO 3 − -CO 3 2− -H2O System: A Thermodynamic Model. J. Solution Chem. 36, 1261–1285. doi:10.1007/s10953-007-9179-5

Rai, D., Sass, B.M., Moore, D. a, 1987. Chromium(III) hydrolysis constants and solubility of chromium(III) hydroxide. Inorg. Chem. 26, 345–349. doi:10.1021/ic00250a002

Rakshit, S., Sarkar, D., Datta, R., 2015. Surface complexation of antimony on kaolinite. Chemosphere 119, 349–354. doi:10.1016/j.chemosphere.2014.06.070

Raposo, J.C., Zuloaga, O., Olazabal, M.A., Madariaga, J.M., 2004. Study of the precipitation equilibria of arsenate anion with calcium and magnesium in sodium perchlorate at 25 °C. Appl. Geochemistry 19, 855–862. doi:10.1016/j.apgeochem.2003.10.012

Ratusznei, S.M., Rodrigues, J.A.D., Zaiat, M., 2003. Operating feasibility of anaerobic whey treatment in a stirred sequencing batch reactor containing immobilized biomass. Water Sci. Technol. 48, 179–186.

Redman, A.D., Macalady, D.L., Ahmann, D., 2002. Natural Organic Matter Affects Arsenic Speciation and Sorption onto Hematite. Environ. Sci. Technol. 36, 2889–2896. doi:10.1021/es0112801

Resongles, E., Casiot, C., Freydier, R., Dezileau, L., Viers, J., Elbaz-Poulichet, F., 2014. Persisting impact of historical mining activity to metal (Pb, Zn, Cd, Tl, Hg) and metalloid (As, Sb) enrichment in sediments of the Gardon River, Southern France. Sci. Total Environ. 481, 509–21. doi:10.1016/j.scitotenv.2014.02.078

Richard, F.C., Bourg, A.C.M., 1991. Aqueous geochemistry of chromium: A review. Water Res. 25, 807–816. doi:10.1016/0043-1354(91)90160-R

Rivett, M.O., Buss, S.R., Morgan, P., Smith, J.W.N., Bemment, C.D., 2008. Nitrate attenuation in groundwater: A review of biogeochemical controlling processes. Water Res. 42, 4215–4232. doi:10.1016/j.watres.2008.07.020

Roane, T.M., Josephson, K.L., Pepper, I.L., 2001. Dual-bioaugmentation strategy to enhance remediation of cocontaminated soil. Appl. Environ. Microbiol. 67, 3208–15. doi:10.1128/AEM.67.7.3208-3215.2001

Roberts, L.C., Hug, S.J., Dittmar, J., Voegelin, A., Kretzschmar, R., Wehrli, B., Cirpka, O. a., Saha, G.C., Ashraf Ali, M., Badruzzaman, a. B.M., 2010. Arsenic release from paddy soils during monsoon

flooding. Nat. Geosci. 3, 53–59. doi:10.1038/ngeo723

Rodwell, W., Norris, S., Cool, W., Cunado, M. et al., 2003. A thematic network on gas issues in safety assessment of deep repositories for radioactive waste (GASNET).

Roig-Navarro, A.., Martinez-Bravo, Y., López, F.., Hernández, F., 2001. Simultaneous determination of arsenic species and chromium(VI) by high-performance liquid chromatography–inductively coupled plasma-mass spectrometry. J. Chromatogr. A 912, 319–327. doi:10.1016/S0021-9673(01)00572-6

Román-Ross, G., Cuello, G.J., Turrillas, X., Fernández-Martínez, A., Charlet, L., 2006. Arsenite sorption and co-precipitation with calcite. Chem. Geol. 233, 328–336. doi:10.1016/j.chemgeo.2006.04.007

Sakamaki, K., Kataoka, M., Maeda, T., Iida, Y., Kamoshida, M., Yamaguchi, T., Tanaka, T., 2014. Experimental verification of models assessing Eh evolution induced by corrosion of carbon steel overpack. Corros. Eng. Sci. Technol. 49, 450–454. doi:10.1179/1743278214Y.0000000217

SALib – an open source Python library for sensitivity analysis https://github.com/SALib/SALib, n.d.

Saloranta, T.M., 2006. Highlighting the model code selection and application process in policy-relevant water quality modelling. Ecol. Modell. 194, 316–327. doi:10.1016/j.ecolmodel.2005.10.031

Saltelli, A., Tarantola, S., Chan, K.P.-S., 1999. A Quantitative Model-Independent Method for Global Sensitivity Analysis of Model Output. Technometrics 41, 39–56. doi:10.1080/00401706.1999.10485594

Saltikov, C.W., Wildman, R.A., Newman, D.K., 2005. Expression Dynamics of Arsenic Respiration and Detoxification in Shewanella sp. Strain ANA-3. J. Bacteriol. 187, 7390–7396. doi:10.1128/JB.187.21.7390-7396.2005

Sasamoto, H., Arthur, R.C., Hama, K., 2011. Interpretation of undisturbed hydrogeochemical conditions in Neogene sediments of the Horonobe area, Hokkaido, Japan. Appl. Geochemistry 26, 1464–1477. doi:10.1016/j.apgeochem.2011.05.020

Sato, M., 1960. Oxidation of sulfide ore bodies - 1. Geochemical environments in terms of Eh and pH. Econ. Geol. 55, 928–961. doi:10.2113/gsecongeo.55.5.928

Schuring, J., Schulz, H.D., Fischer, W.R., 1999. Redox: Fundamentals, Processes and Applications. Springer.

Schwertmann, U., 1991. Solubility and dissolution of iron oxides. Plant Soil 130, 1–25. doi:10.1007/BF00011851

Scott, N., Hatlelid, K.M., MacKenzie, N.E., Carter, D.E., 1993. Reactions of arsenic(III) and arsenic(V) species with glutathione. Chem. Res. Toxicol. 6, 102–106. doi:10.1021/tx00031a016

Selim, H.M., Zhang, H., 2013. Modeling Approaches of Competitive Sorption and Transport of Trace Metals and Metalloids in Soils: A Review. J. Environ. Qual. 42, 640. doi:10.2134/jeq2012.0323

Sharma, P., Kappler, A., 2011. Desorption of arsenic from clay and humic acid-coated clay by dissolved phosphate and silicate. J. Contam. Hydrol. 126, 216–225. doi:10.1016/j.jconhyd.2011.08.005

Sibi, G., 2014. Biosorption of Arsenic by Living and Dried Biomass of Fresh Water Microalgae - Potentials and Equilibrium Studies. J. Bioremediation Biodegrad. 5. doi:10.4172/2155-6199.1000249

Silver, S., Phung, L.T., 2005. Genes and Enzymes Involved in Bacterial Oxidation and Reduction of Inorganic Arsenic. Appl. Environ. Microbiol. 71, 599–608. doi:10.1128/AEM.71.2.599-608.2005

Silvester, E., Charlet, L., Manceau, A., 1995. Mechanism of chromium(III) oxidation by Na-buserite. J. Phys. Chem. 99, 16662–16669. doi:10.1021/j100045a028

Silvester, E., Charlet, L., Tournassat, C., Géhin, A., Grenèche, J.-M., Liger, E., 2005. Redox potential measurements and Mössbauer spectrometry of FeII adsorbed onto FeIII (oxyhydr)oxides. Geochim. Cosmochim. Acta 69, 4801–4815. doi:10.1016/j.gca.2005.06.013

Small, J., Nykyri, M., Helin, M., Hovi, U., Sarlin, T., Itävaara, M., 2008. Experimental and modelling investigations of the biogeochemistry of gas production from low and intermediate level radioactive waste. Appl. Geochemistry 23, 1383–1418. doi:10.1016/j.apgeochem.2007.11.020

Smeaton, C.M., Walshe, G.E., Smith, A.M.L., Hudson-Edwards, K. a., Dubbin, W.E., Wright, K., Beale, A.M., Fryer, B.J., Weisener, C.G., 2012. Simultaneous release of Fe and As during the reductive dissolution of Pb-As jarosite by Shewanella putrefaciens CN32. Environ. Sci. Technol. 46, 12823–12831. doi:10.1021/es3021809

Sø, H.U., Postma, D., Jakobsen, R., Larsen, F., 2008. Sorption and desorption of arsenate and arsenite on calcite. Geochim. Cosmochim. Acta 72, 5871–5884. doi:10.1016/j.gca.2008.09.023

Song, C., Zhang, J., 2008. Electrocatalytic oxygen reduction reaction, in: Zhang, J. (Ed.), PEM Fuel Cell

Electrocatalysts and Catalyst Layers: Fundamentals and Applications. Springer, pp. 89–134. doi:10.1007/978-1-84800-936-3_2

Sposito, G., 1998. On points of zero charge. Environ. Sci. Technol. 32, 2815–2819. doi:10.1021/es9802347

Sposito, G., 1989. The chemistry of soils. Oxford University Press, New York.

Starrfelt, J., Kaste, Ø., 2014. Bayesian uncertainty assessment of a semi-distributed integrated catchment model of phosphorus transport. Environ. Sci. Process. Impacts 16, 1578. doi:10.1039/c3em00619k

Stewart, B.D., Nico, P.S., Fendorf, S., 2009. Stability of Uranium Incorporated into Fe (Hydr)oxides under Fluctuating Redox Conditions. Environ. Sci. Technol. 43, 4922–4927. doi:10.1021/es803317w

Stookey, L.L., 1970. Ferrozine -A new spectrophotometric reagent for iron. Anal. Chem. 42, 779–781. doi:10.1021/ac60289a016

Stroes-Gascoyne, S., Hamon, C.J., Vilks, P., Gierszewski, P., 2002. Microbial, redox and organic characteristics of compacted clay-based buffer after 6.5 years of burial at AECL's Underground Research Laboratory. Appl. Geochemistry 17, 1287–1303. doi:10.1016/S0883-2927(02)00020-3

Stucker, V.K., Silverman, D.R., Williams, K.H., Sharp, J.O., Ranville, J.F., 2014. Thioarsenic Species Associated with Increased Arsenic Release during Biostimulated Subsurface Sulfate Reduction. Environ. Sci. Technol. 48, 13367–13375. doi:10.1021/es5035206

Stucker, V.K., Williams, K.H., Robbins, M.J., Ranville, J.F., 2013. Arsenic geochemistry in a biostimulated aquifer: An aqueous speciation study. Environ. Toxicol. Chem. 32, 1216–1223. doi:10.1002/etc.2155

Stucki, J.W., 2011. A review of the effects of iron redox cycles on smectite properties. Comptes Rendus Geosci. 343, 199–209. doi:10.1016/j.crte.2010.10.008

Stumm, W., Morgan, J., 1996. Aquatic Chemistry: Chemical Equilibria and Rates in Natural Waters, 3d ed. New York : Wiley.

Stumm, W., Morgan, J., 1981. Aquatic chemistry. John Wiley & Sons, New York.

Swift, P.N., Bonano, E.J., 2016. Geological Disposal of Nuclear Waste in Tuff: Yucca Mountain (USA). Elements 12, 263–268. doi:10.2113/gselements.12.4.263

Tanwar, P., Nandy, T., Ukey, P., Manekar, P., 2008. Correlating on-line monitoring parameters, pH, DO and ORP with nutrient removal in an intermittent cyclic process bioreactor system. Bioresour. Technol. 99, 7630–7635. doi:10.1016/j.biortech.2008.02.004

Tapia-Rodríguez, A., Luna-Velasco, A., Field, J. a., Sierra-Alvarez, R., 2012. Toxicity of Uranium to Microbial Communities in Anaerobic Biofilms. Water, Air, Soil Pollut. 223, 3859–3868. doi:10.1007/s11270-012-1154-0

Terry, L.R., Kulp, T.R., Wiatrowski, H., Miller, L.G., Oremland, R.S., 2015. Microbiological Oxidation of Antimony(III) with Oxygen or Nitrate by Bacteria Isolated from Contaminated Mine Sediments. Appl. Environ. Microbiol. 81, 8478–8488. doi:10.1128/AEM.01970-15

Tessier, A., Fortin, D., Belzile, N., DeVitre, R.R., Leppard, G.G., 1996. Metal sorption to diagenetic iron and manganese oxyhydroxides and associated organic matter: Narrowing the gap between field and laboratory measurements. Geochim. Cosmochim. Acta 60, 387–404. doi:10.1016/0016-7037(95)00413-0

Thayer, J.S., 2002. Review: Biological methylation of less-studied elements. Appl. Organomet. Chem. 16, 677–691. doi:10.1002/aoc.375

Thompson, A., Chadwick, O. a., Rancourt, D.G., Chorover, J., 2006. Iron-oxide crystallinity increases during soil redox oscillations. Geochim. Cosmochim. Acta 70, 1710–1727. doi:10.1016/j.gca.2005.12.005

Thorstenson, D.C., 1984. The concept of electron activity and its relation to redox potentials in aqueous geochemical systems.

Tournassat, C., Charlet, L., Bosbach, D., Manceau, A., 2002. Arsenic(III) Oxidation by Birnessite and Precipitation of Manganese(II) Arsenate. Environ. Sci. Technol. 36, 493–500. doi:10.1021/es0109500

Tournassat, C., Gaucher, E.C., Fattahi, M., Grambow, B., 2007. On the mobility and potential retention of iodine in the Callovian–Oxfordian formation. Phys. Chem. Earth, Parts A/B/C 32, 539–551. doi:10.1016/j.pce.2005.12.004

Tratnyek, P.G., Grundl, T.J., Haderlein, S.B., 2011. Aquatic Redox Chemistry. ACS Symposium Series; American Chemical Society: Washington, DC.

Tratnyek, P.G., Macalady, D.L., 2000. Oxidation-Reduction Reactions in the Aquatic Environment, in: Boethling, R.S., Mackay, D. (Eds.), Handbook of Property Estimation Methods for Chemicals. CRC Press LLC, pp. 383–415.

USEPA, 2000. Soil Sampling (Standard Operating Procedures No. SOP 2012).

USEPA, 1996. Method 3052 - Microwave Assisted Acid Digestion of Siliceous and Organically Based Matrices.

Van Cappellen, P., Wang, Y., 1996. Cycling of iron and manganese in surface sediments; a general theory for the coupled transport and reaction of carbon, oxygen, nitrogen, sulfur, iron, and manganese. Am. J. Sci. 296, 197–243. doi:10.2475/ajs.296.3.197

Van Cappellen, P., Wang, Y., 1995. Metal cycling in surface sediments: Modeling the interplay of transport and reaction, in: Allen, H. (Ed.), Metal Contaminated Aquatic Sediments. Ann Arbor Press, Chelsea.

Varanda, L.C., Morales, M.P., Jafelicci, J.M., Serna, C.J., 2002. Monodispersed spindle-type goethite nanoparticles from FeIII solutions. J. Mater. Chem. 12, 3649–3653. doi:10.1039/b207190h

Viollier, E., Inglett, P.., Hunter, K., Roychoudhury, A.., Van Cappellen, P., 2000. The ferrozine method revisited: Fe(II)/Fe(III) determination in natural waters. Appl. Geochemistry 15, 785–790. doi:10.1016/S0883-2927(99)00097-9

Vithanage, M., Rajapaksha, A.U., Dou, X., Bolan, N.S., Yang, J.E., Ok, Y.S., 2013. Surface complexation modeling and spectroscopic evidence of antimony adsorption on iron-oxide-rich red earth soils. J. Colloid Interface Sci. 406, 217–224. doi:10.1016/j.jcis.2013.05.053

Viti, C., Marchi, E., Decorosi, F., Giovannetti, L., 2014. Molecular mechanisms of Cr(VI) resistance in bacteria and fungi. FEMS Microbiol. Rev. 38, 633–659. doi:10.1111/1574-6976.12051

Vodyanitskii, Y.N., 2010. Status and behavior of natural and technogenic forms of As, Sb, Se, and Te in ore tailings and contaminated soils: A review. Eurasian Soil Sci. 43, 30–38. doi:10.1134/S1064229310010059

von Canstein, H., Ogawa, J., Shimizu, S., Lloyd, J.R., 2008. Secretion of Flavins by Shewanella Species and Their Role in Extracellular Electron Transfer. Appl. Environ. Microbiol. 74, 615–623. doi:10.1128/AEM.01387-07

Vorenhout, M., van der Geest, H.G., van Marum, D., Wattel, K., Eijsackers, H.J.P., 2004. Automated and continuous redox potential measurements in soil. J. Environ. Qual. 33, 1562–7.

Wang, X., He, M., Lin, C., Gao, Y., Zheng, L., 2012. Antimony(III) oxidation and antimony(V) adsorption reactions on synthetic manganite. Chemie der Erde - Geochemistry 72, 41–47. doi:10.1016/j.chemer.2012.02.002

Wang, Y., Frutschi, M., Suvorova, E., Phrommavanh, V., Descostes, M., Osman, A.A.A., Geipel, G., Bernier-Latmani, R., 2013. Mobile uranium(IV)-bearing colloids in a mining-impacted wetland. Nat. Commun. 4, 1–9. doi:10.1038/ncomms3942

Wang, Y., Van Cappellen, P., 1996. A multicomponent reactive transport model of early diagenesis: Application to redox cycling in coastal marine sediments. Geochim. Cosmochim. Acta 60, 2993–3014. doi:10.1016/0016-7037(96)00140-8

Wang, Z., Bush, R.T., Sullivan, L.A., Liu, J., 2013. Simultaneous Redox Conversion of Chromium(VI) and Arsenic(III) under Acidic Conditions. Environ. Sci. Technol. 47, 130529093223005. doi:10.1021/es400547p

Wang, Z., Ma, W., Chen, C., Zhao, J., 2008. Photochemical Coupling Reactions between Fe(III)/Fe(II), Cr(VI)/Cr(III), and Polycarboxylates: Inhibitory Effect of Cr Species. Environ. Sci. Technol. 42, 7260–7266. doi:10.1021/es801379j

Wareham, D.G., Hall, K.J., Mavinic, D.S., 1993. Real-Time Control of Aerobic-Anoxic Sludge Digestion Using ORP. J. Environ. Eng. 119, 120–136. doi:10.1061/(ASCE)0733-9372(1993)119:1(120)

Watts, M.P., Lloyd, J.R., 2012. Bioremediation via Microbial Metal Reduction, in: Gescher, J., Kappler, A. (Eds.), Microbial Metal Respiration. Springer Berlin Heidelberg, Berlin, Heidelberg, pp. 161–201.

Weckhuysen, B.M., Verberckmoes, A. a., Buttiens, A.L., Schoonheydt, R. a., 1994. Diffuse Reflectance Spectroscopy Study of the Thermal Genesis and Molecular Structure of Chromium-Supported Catalysts. J. Phys. Chem. 100, 579–584.

Weckhuysen, B.M., Verberckmoes, A. a., de Baets, A.R., Schoonheydt, R. a., 1997. Diffuse Reflectance Spectroscopy of Supported Chromium Oxide Catalysts: A Self-Modeling Mixture Analysis. J. Catal. 166, 160–171. doi:10.1006/jcat.1997.1518

Weigand, H., Mansfeldt, T., Bäumler, R., Schneckenburger, D., Wessel-Bothe, S., Marb, C., 2010. Arsenic release and speciation in a degraded fen as affected by soil redox potential at varied moisture regime. Geoderma 159, 371–378. doi:10.1016/j.geoderma.2010.08.014

Wersin, P., Leupin, O.X., Mettler, S., Gaucher, E.C., Mäder, U., De Cannière, P., Vinsot, A., Gäbler, H.E., Kunimaro, T., Kiho, K., Eichinger, L., 2011. Biogeochemical processes in a clay formation in situ experiment: Part A – Overview, experimental design and water data of an experiment in the Opalinus Clay at the Mont Terri Underground Research Laboratory, Switzerland. Appl. Geochemistry 26, 931–953. doi:10.1016/j.apgeochem.2011.03.004

Whitfield, M., 1974. Thermodynamic limitations on the use of the platinum electrode in Eh measurements. Limnol. Oceanogr. 19, 857–865. doi:10.4319/lo.1974.19.5.0857

Whitfield, M., 1969. Eh as an operational paramtere in esturine studies. Limnol. Oceanogr. 14, 547–558. doi:10.4319/lo.1969.14.4.0547

Willey, J.D., Mullaugh, K.M., Kieber, R.J., Avery, G.B., Mead, R.N., 2012. Controls on the redox potential of rainwater. Environ. Sci. Technol. 46, 13103–11. doi:10.1021/es302569j

Williams, K.H., Nevin, K.P., Franks, A., Englert, A., Long, P.E., Lovley, D.R., 2010. Electrode-based approach for monitoring in situ microbial activity during subsurface bioremediation. Environ. Sci. Technol. 44, 47–54. doi:10.1021/es9017464

Wilson, N., Webster-Brown, J., Brown, K., 2012. The behaviour of antimony released from surface geothermal features in New Zealand. J. Volcanol. Geotherm. Res. 247–248, 158–167. doi:10.1016/j.jvolgeores.2012.08.009

Wilson, S.C., Lockwood, P. V, Ashley, P.M., Tighe, M., 2010. The chemistry and behaviour of antimony in the soil environment with comparisons to arsenic: A critical review. Environ. Pollut. 158, 1169–1181. doi:10.1016/j.envpol.2009.10.045

Wittebroodt, C., Savoye, S., Gouze, P., 2008. Influence of initial iodide concentration on the iodide uptake by the argillite of Tournemire. Phys. Chem. Earth, Parts A/B/C 33, 943–948. doi:10.1016/j.pce.2008.05.020

Włodarczyk, T., Szarlip, P., Brzezińska, M., Kotowska, U., 2007. Redox potential, nitrate content and pH in flooded Eutric Cambisol during nitrate reduction. Res. Agric. Eng. 53, 20–28.

Wu, W.-M., Carley, J., Luo, J., Ginder-Vogel, M. a., Cardenas, E., Leigh, M.B., Hwang, C., Kelly, S.D., Ruan, C., Wu, L., Van Nostrand, J., Gentry, T., Lowe, K., Carroll, S., Luo, W., Fields, M.W., Gu, B., Watson, D., Kemner, K.M., Marsh, T., Tiedje, J., Zhou, J., Fendorf, S., Kitanidis, P.K., Jardine, P.M., Criddle, C.S., 2007. In Situ Bioreduction of Uranium (VI) to Submicromolar Levels and Reoxidation by Dissolved Oxygen. Environ. Sci. Technol. 41, 5716–5723. doi:10.1021/es062657b

Xi, J., He, M., Kong, L., 2016. Adsorption of antimony on kaolinite as a function of time, pH, HA and competitive anions. Environ. Earth Sci. 75, 136. doi:10.1007/s12665-015-4916-3

Xi, J., He, M., Lin, C., 2010. Adsorption of antimony(V) on kaolinite as a function of pH, ionic strength and humic acid. Environ. Earth Sci. 60, 715–722. doi:10.1007/s12665-009-0209-z

Xi, J., He, M., Wang, K., Zhang, G., 2013. Adsorption of antimony(III) on kaolinite in the presence of competitive anions. J. Geochemical Explor. 132, 201–208. doi:10.1016/j.gexplo.2013.07.004

Xie, X., Li, E.L., Tang, Z.K., 2010. Sudden Emergence of Redox Active Escherichia coli Phenotype : Cyclic Voltammetric Evidence of the Overlapping Pathways. Int. J. Electrochem. Sci. 5, 1070–1081.

Zhang, G., Samper, J., Montenegro, L., 2008. Coupled thermo-hydro-bio-geochemical reactive transport model of CERBERUS heating and radiation experiment in Boom clay. Appl. Geochemistry 23, 932–949. doi:10.1016/j.apgeochem.2007.09.010

Zhang, G., Senko, J.M., Kelly, S.D., Tan, H., Kemner, K.M., Burgos, W.D., 2009. Microbial reduction of iron(III)-rich nontronite and uranium(VI). Geochim. Cosmochim. Acta 73, 3523–3538. doi:10.1016/j.gca.2009.03.030

Zhang, H., Selim, H.M., 2008. Reaction and Transport of Arsenic in Soils: Equilibrium and Kinetic Modeling, in: Advances in Agronomy. pp. 45–115. doi:10.1016/S0065-2113(08)00202-2

Zhang, H., Selim, H.M., 2005. Kinetics of Arsenate Adsorption−Desorption in Soils. Environ. Sci. Technol. 39, 6101–6108. doi:10.1021/es050334u

Zhang, J., Stanforth, R., 2005. Slow Adsorption Reaction between Arsenic Species and Goethite (α-FeOOH): Diffusion or Heterogeneous Surface Reaction Control. Langmuir 21, 2895–2901. doi:10.1021/la047636e

Zhou, Y., Messier, N., Ouellette, M., Rosen, B.P., Mukhopadhyay, R., 2004. Leishmania major LmACR2 Is a Pentavalent Antimony Reductase That Confers Sensitivity to the Drug Pentostam. J. Biol. Chem.

279, 37445–37451. doi:10.1074/jbc.M404383200

Zhu, Y.-G., Yoshinaga, M., Zhao, F.-J., Rosen, B.P., 2014. Earth Abides Arsenic Biotransformations. Annu. Rev. Earth Planet. Sci. 42, 443–467. doi:10.1146/annurev-earth-060313-054942

Zotov, a. V., Shikina, N.D., Akinfiev, N.N., 2003. Thermodynamic properties of the Sb(III) hydroxide complex Sb(OH)3(aq) at hydrothermal conditions. Geochim. Cosmochim. Acta 67, 1821–1836. doi:10.1016/S0016-7037(00)01281-4

Zydorczak, B., May, P.M., Meyrick, D.P., Bátka, D., Hefter, G., 2012. Dissolution of Cr 2 O 3 (s) and the Behavior of Chromium in Concentrated NaOH Solutions. Ind. Eng. Chem. Res. 51, 16537–16543. doi:10.1021/ie302096e